Robust Multi-sensor Data Fusion for Practical Unmanned Surface Vehicles (USVs) Navigation

by

Wenwen Liu

A dissertation submitted in partial fulfilment
of the requirements for the degree of

Doctor of Philosophy

of

University College London

Department of Mechanical Engineering
University College London
2020

I, Wenwen Liu confirm that the work presented in this thesis is my own. Where information has been derived from other sources, I confirm that this has been indicated in the thesis.

Abstract

The development of practical Unmanned Surface Vehicles (USVs) are attracting increasing attention driven by their assorted military and commercial application potential. However, addressing the uncertainties presented in practical navigational sensor measurements of an USV in maritime environment remain the main challenge of the development. This research aims to develop a multi-sensor data fusion system to autonomously provide an USV reliable navigational information on its own positions and headings as well as to detect dynamic target ships in the surrounding environment in a holistic fashion. A multi-sensor data fusion algorithm based on Unscented Kalman Filter (UKF) has been developed to generate more accurate estimations of USV's navigational data considering practical environmental disturbances. A novel covariance matching adaptive estimation algorithm has been proposed to deal with the issues caused by unknown and varying sensor noise in practice to improve system robustness. Certain measures have been designed to determine the system reliability numerically, to recover USV trajectory during short term sensor signal loss, and to autonomously detect and discard permanently malfunctioned sensors, and thereby enabling potential sensor faults tolerance. The performance of the algorithms have been assessed by carrying out theoretical simulations as well as using experimental data collected from a real-world USV projected collaborated with Plymouth University. To increase the degree of autonomy of USVs in perceiving surrounding environments, target detection and prediction algorithms using an Automatic Identification System (AIS) in conjunction with a marine radar have been proposed to provide full detections of multiple dynamic targets in a wider coverage range, remedying the narrow detection range and sensor uncertainties of the AIS. The detection algorithms have been validated in simulations using practical environments with water current effects. The performance of developed multi-senor data fusion system in providing reliable navigational data and perceiving surrounding environment for USV navigation have been comprehensively demonstrated.

Impact Statement

USVs have emerged as viable tools for various military and commercial missions. However, most of the existing USVs are designed to perform delicate tasks in an environment subject to disturbances and uncertainties. Therefore, an effective and reliable navigation system is deemed essential to ensure the safe and reliable operation of USVs and cope with different mission requirements and varying environmental conditions.

Pursing this goal, this research presents a novel sensor system for autonomous USV navigation including a set of multi-sensor data fusion algorithms has been developed for practical applications focusing on four aspects: on-board navigational sensor measurement accuracy, navigation system robustness, sensor reliability as well as multiple dynamic targets detection. The system takes the practical environmental influence and potential sensor uncertainties into account to improve the practicality of proposed multi-sensor data fusion algorithms. The navigation algorithms employ Kalman filtering technology to process raw sensor measurements and provide more accurate and reliable navigational data for the USV in real-time. The dynamic multiple targets detection algorithm ensures the safety of the USV in practical operations.

The effectiveness of the developed system has been demonstrated through numerous simulations and experiments on a real-world USV (*Springer*). The results of USV estimated trajectories and heading determinations in sections 5.3 and 6.3.3 have been demonstrated to improve the overall performance of *Springer*. Consequently, this work has resulted in nine publications in journals and leading conferences contributing to the following areas: real-time positioning, sensor signal accuracy, sensor reliability and real-time target detection. The outputs have been absorbed by Office of Naval Research in conjunction with path planning algorithms developed by colleagues in the same research group (Liu et al, 2014; Liu et al, 2015; Song et al, 2015; Song et al, 2016). This research provides valuable insights on the design of autonomous navigation systems, which can inform the research and development for new USV applications.

Acknowledgement

I would like to express my deep gratitude to the following people for their contribution to this work:

- First and foremost I would like to thank my supervisor, Professor Richard Bucknall, for offering this PhD opportunity with financial support, for his patient guidance, enthusiastic encouragement and valuable and constructive suggestions during the development of this research. His generous and patience keep me away from giving up to make this study completed eventually.

- I would like to thank Mr Konrad Yearwood for his efforts on improving the English written expressions of my thesis and publications. Advice given by my colleague, Dr Yuanchang Liu has also been a great help in writing this thesis and publishing my very first journal paper.

- I would like to express my sincere gratitude to my parents for their financial support and generous love to me. I'm particular grateful for the companion of my dear husband, Dr Yujian Ye and my little bunny, Marshmallow. I could never finish this research without their patience, unconditional love and continuous support.

- I would like to thank my best friend, Dr Rui Song, who is also in our USV research group, for her companion in both work and daily life.

- My grateful thanks are also extended to the Autonomous Marine System Research Group, Plymouth University, for offering the opportunity to carry out experiments on a practical USV and giving me guidance at the early stage of my research.

- Finally, I would like to thank to the Atlantic Centre for the innovative design and Control of Small Ships (ACCeSS) group for granting me the studentship generously.

Table of Contents

List of Figures

List of Tables

Nomenclatures

Roman Symbols

A	State transition matrix
A_i	AIS measurements
a	Acceleration rate
a_o	Accelerometer Reading
a_i	Actual Acceleration
B	Control matrix
BC	Bhattacharyya coefficient
b_a	Accelerometer bias
b_g	Gyroscope bias
C_A	Actual covariance
C_T	Theoretical covariance
$CT1, CT2, \dots, CTj$	System model with specific ω
DoM	Degree of matching
D_B	Bhattacharyya distance
d	Distance between transmitter station and on-board receiver
$F,\ F_{CVM},\ F_{CTM}$	State matrix
G_1, G_2	Integrated association grades
g_1, g_2	Correlation grades
H	Observation matrix
K	Kalman filter gain
L_j	Likelihood
lat	Latitude
lon	Longitude
M	System models
m	Mean of system state
N	Moving size window
o_l, o_e, o_s	Output membership functions
P	Error covariance

p_0	Initial position
p_t	Position at time t
$p,\ p_x, p_y$	Position coordinate
Q	Processing noise covariance matrix
R	Measurement covariance matrix
RE	Radius of the earth
RM	Rotation Matrix
R_j	Radar measurement
r_m	Range
S	Predicted covariance
SMA	Simple Moving Average of Innovation Vectors
$SMAN$	Negative SMA Boundary
$SMAP$	Positive SMA Boundary
T	Sampling time
TS_m	Targets state vector
$\widehat{TS}_{Am}$	Estimation based on AIS measurements
$\widehat{TS}_{Am}$	Estimation based on Radar measurements
$\widehat{TS}_{Fm}$	Master fusion results
t	Time
t_a, t_f	Sample time
u	Control input
u_R, u_B, u_C, u_S	Difference of AIS and Radar Measurements
v_0	Initial velocity of the vehicle
v	velocity of radio waves in m/s
v, v_x, v_y	Velocity
w	System processing noise
w_a	Accelerometer random noise
w_g	Gyroscope random noise
W_0^m, W_i^m	Constant weight for system state
W_0^c, W_i^c	Constant weight for error covariance
w_i	Weights
X_j	Spread of the means

x	System State vector
z	Measurement vector

Greek Symbols

α	Adjustment coefficient
Δw	Weight Changing
δ_1, δ_2	Differences between measurements
ε	Measurement residual
ϵ	Innovation
μ_l, μ_e, μ_s	Input membership functions of Chapter 5
μ_N, μ_P, μ_Z	Input membership functions of Chapter 6
μ_p, μ_m	Predicted position and measured position
μ_j	Model probability
μ_x, μ_y	Estimated bias
ν	Measurement noise
π_{ij}	System probability matrix
Σ_p, Σ_m	Position error covariance matrix
$\sigma_0,\ \sigma_x,\ \sigma_Z$	Sensor error
σ_p, σ_m	Position error variance
Υ	Propagated Sigma Points
φ	Target course
ϕ	Frame rotation Angle
χ_0, χ_i	Sigma Points
ψ_0	Initial heading
ψ_t	Heading at time t
ψ	USV Heading
ω	Angular velocity
ω_o	Gyroscope reading
ω_i	Actual angular velocity

Abbreviations

AIS	Automatic Identification System
AMR	Anisotropic Magneto Resistance
AP	Access Point
API	Application Programming Interface
ARCS	Admiralty Raster Chart Service
ARPA	Automatic Radar Plotting Aid
ASC	Autonomous Surface Craft
AVCS	Admiralty Vector Chart Service
AUKF	Adaptive Unscented Kalman Filter
AUV	Autonomous Underwater Vehicle
BDS	BeiDou Satellite Navigation System
BIOS	Basic input/output system
CPU	Central Processing Unit
CTM	Coordinated Turn Model
CVM	Constant Velocity Model
DGPS	Differential Global Positioning System
DOM	Degree of Matching
DR	Dead Reckoning
EKF	Extended Kalman Filter
ENC	Electronic Navigation Chart
GLA	General Lighthouse Authorities
GLONASS	Global Navigation Satellite System (Russia)
GNSS	Global Navigation Satellite System
GPS	Global Positioning System
GUI	Graphical user interface
HD	High Definition
IKF	Interval Kalman Filter
IP	Internet protocol
IMMPDAF	Interacting multiple model probabilistic data association filter
IMU	Inertial Measurement Unit

INS	Inertial Navigation System
IP	Internet Protocol
KF	Kalman Filter
LCD	Liquid Crystal Display
LIDAR	LIght Detecting And Ranging
LoS	Line of Sight
MAST	Maritime Autonomy Surface Testbed
MBES	Multi-beam Echo sounder
MEMS	Micro-Electro-Mechanical System
MIT	Massachusetts Institute of Technology
MMSE	Minimum Mean Square Error
MMSI	Maritime Mobile Service Identity
MR	Magnetoresistive
MSDF	Multi-Sensor Data Fusion
MSE	Mean Square Error
NGC	Navigation, Guidance, Control
NMEA	National Marine Electronics Association
NN	Nearest Neighbours
ONR	Office of Naval Research
PC	Personal Computer
PCB	Printed Circuit Board
pdf	Probability Density Function
PPA	Path Planning Algorithm
PRN	Pseudo-random Noise
PTZ	Pan-tilt-zoom
R&D	Research and Development
RADAR	RAdio Detecting And Ranging
RF	Radio Frequency
RMS	Rooted Mean Square
RMSE	Rooted Mean Square Error
RNC	Raster Navigation Chart
RNSS	Regional Navigation Satellite System
SBC	Single Board Computer

SIMU	Strapdown Inertial Measurement Unit
SMA	Simple Moving Average
TS	Target Ship
UAV	Unmanned Ariel Vehicles
UGV	Unmanned Ground Vehicle
UKF	Unscented Kalman Filter
UKHO	UK Hydrographic Office
USBL	Ultra-Short Base Line
USV	Unmanned Surface Vehicle
UUV	unmanned underwater vehicle
VTS	Vessel Traffic Service
WLAN	Wireless Local Area Network

List of Achievements

Journal publications

- Liu W., Liu Y., Gunawan B. A. & Bucknall R. (2020). Practical moving target detection in maritime environments using fuzzy multi-sensor data fusion. *International Journal of Fuzzy Systems*. DOI: 10.1007/s40815-020-00963-1.

- Liu, W., Liu, Y. & Bucknall, R. (2019). A Robust Localization Method for Unmanned Surface Vehicle (USV) Navigation Using Fuzzy Adaptive Kalman Filtering. *IEEE Access*. 7, pp. 46071-46083, DOI: 10.1109/ACCESS.2019.2909151.

- Liu, Y., Liu, W., Song, R. & Bucknall, R. (2017). Predictive navigation of unmanned surface vehicles in a dynamic maritime environment when using the fast marching method. *International Journal of Adaptive Control and Signal Processing*. 31(4), pp. 464-488. DOI: 10.1002/acs.2561.

- Motwani, A., Liu, W., Sharma, S., Sutton, R., & Bucknall, R. (2016). An interval Kalman filter–based fuzzy multi-sensor fusion approach for fault-tolerant heading estimation of an autonomous surface vehicle. *Proceedings of the Institution of Mechanical Engineers, Part M: Journal of Engineering for the Maritime Environment*. 230(3), pp. 491-507. DOI: 10.1177/1475090215596180.

Conference publications

- Liu W., Liu Y., Song R. & Bucknall R. (2020). Towards intelligent navigation in future autonomous surface vessels: developments, challenges and strategies. In: *Proceedings of the International Naval Engineering Conference and Exhibition*. October 5th -9th, Virtual online.

- Liu, W., Liu, Y., Song, R. & Bucknall, R. (2018). The Design of an Embedded Multi-Sensor Data Fusion System for Unmanned Surface Vehicle Navigation Based on Real Time Operating System. In: *Proceedings of the MTS/IEEE OCEANS'18 Kobe / Techno-Ocean Conferences.* 28-31 May, 2018, Kobe, Japan. DOI: 10.1109/OCEANSKOBE.2018.8559352.

- Song, R., Liu, W., Liu, Y. & Bucknall, R. (2016). Aspect of a reliable autonomous navigation and guidance system for an unmanned surface vehicle. In: *Proceedings of MTS/IEEE OCEANS'16 Conferences*. 19-23 September, 2016, Montery, USA. DOI: 10.1109/OCEANS.2016.7761415.

- Song R., Liu, Y., Liu, W. & Bucknall, R. (2015). A two-layered fast marching path planning algorithm for an unmanned surface vehicle operating in a dynamic environment. In: *Proceedings of MTS/IEEE Oceans'15 Conferences*. 18-21 May, 2015, Genova/Italy. DOI: 10.1109/OCEANS- Genova.2015.7271405.

- Liu W., Liu Y., Song, R. & Bucknall, R. (2015). The design of an autonomous maritime navigation system for unmanned surface vehicles. In: *Proceedings of 14th International Conference on Computer and Information Technology Application in the Maritime Industries*. 11-13 May, 2015, Ulrichshusen, Germany. pp. 147-160.

- Liu W., Liu Y., Song, R. & Bucknall, R. (2015). Towards the development of an autonomous navigation system for unmanned vessels. In: *Proceedings of 13th International Navigation Conference (INC) 2015*. 24-26 February, 2015, Manchester, UK.

- Liu Y., Song R., Liu, W. & Bucknall, R. (2014). Autonomous navigation system for unmanned surface vehicles. In: *Proceedings of 13th International Conference on Computer and Information Technology Application in the Maritime Industries*, 12-14 May, 2014, Redworth, UK. pp. 123-135.

Other publications

- Liu, W., Motwani, A., Sharma, S., Sutton, R. & Bucknall, R. (2014). Fault Tolerant Navigation of USV using Fuzzy Multi-sensor Fusion. *MIDAS technical report*. MIDAS.SMSE.2014.TR.010.

- Liu, W. & Bucknall, R. (2013). Intelligent Navigation System for Unmanned Surface Vehicles. In: *The 5th UK Marine Technology Postgraduate Conference*. 9-10 June, 2014, Newcastle upon Tyne, UK

Chapter 1. Introduction

1.1. Motivation

The maritime industry is advancing with rapid development of autonomous unmanned surface vehicles (USVs), providing benefit in both civilian applications and military operations. With a reduced need to deploy human operators on-board, USVs offer the advantages of the reduction and elimination of risks to human crew, reduced power consumption and lower manufacturing and operating costs. As such, USVs exhibit superior performance compared to equivalent sized manned vessels in various marine surveillance missions, such as marine monitoring and surveying, marine waste detection, mapping bridges and waterside buildings and mining (Han et al., 2015; Vasilj et al., 2017). Furthermore, USVs also play a crucial role in military applications such as anti-terrorism operations, force protection, and electronic warfare (Yan et al., 2010; Embention, 2015).

An increasing research interest in further development of USVs has been witnessed worldwide, driven by their capabilities to perform a large range of missions. A variety of remotely controlled USVs have been constructed and are in service, such as the *CEE-USV* developed by CEE HydroSystems which is used to conduct mine tailings and bathymetry surveys in Arizona, USA (CEE HydroSystems, 2017). In the meantime, the research into USVs for autonomous operations is still undergoing active development where the key challenge resides in developing an autonomous navigation system for USVs. As shown in Figure 1.1, an autonomous navigation system, also refers to as the Navigation Guidance and Control (NGC) system, is composed of three modules: a data acquisition module (Navigation), a path planning module (Guidance), and an advanced control module (Control). First, the data acquisition module acquires information pertaining to the USV's own position, speed and heading (obtained using various navigation sensor). It also constructs the surrounding operational environment by detecting target ships (TSs). Based on this information, the path planning module is then tasked to generate a safe path, usually defined by a series of waypoints, for the USV to navigate. Finally, the advanced

control module uses the generated waypoints, which may be either predetermined as part of a mission or generated by the path planning algorithm, as reference points to guide the USV and help ensure that the USV adheres to the generated path by controlling its propulsion and steering system. While at sea, accurate measurements of positions, speeds, and headings are vital to ensure a vessel reaches its destination safely. The need for accurate positional information usually becomes more critical once the vessel is en route. Other vessels traffic and waterway hazards can increase the complexity of the required manoeuvring and the risk of accidents (National Coordination Office, 2014). Therefore, the data acquisition module responsible for obtaining and processing real time navigational data constitutes the fundamental component of an autonomous navigation system. This research focuses on the navigation and guidance function of USV operation, with particular focus on the improvement of reliability and resilience of the navigation function through use of data fusion methodologies applied to disparate navigation sensor and data gathering technologies. It will be through the reinforcement of such technologies that the author will seek to provide novel solutions to the problems that can affect the security and reliability of transit for USVs by failings to which standard navigation devices are prone. This work supports and complements work on path planning and fleet orientation of USVs that has been carried out by other colleagues in the marine research group of UCL.

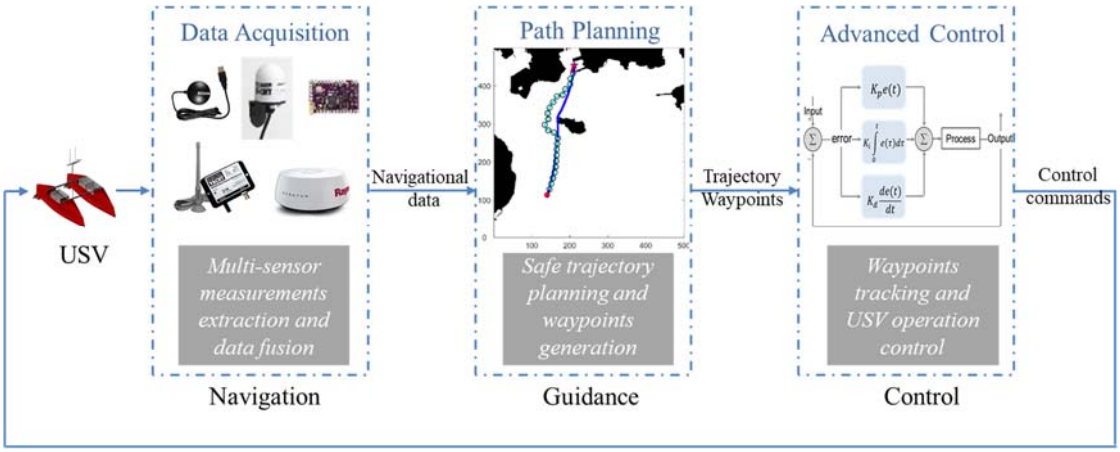

Figure 1.1 Autonomous navigation system (NGC system) of an Unmanned Surface Vehicle

Contemporarily, the most widely used navigation method is the Global Navigation Satellite System (GNSS), which is able to provide absolute positional information in

open area. However, it suffers from problems of signal reliability and continuity in harsh environments. If the GNSS fails the consequences for an autonomous USV could be disastrous. The ship has limited certainty as to its current position and other navigational instruments based on it may have their functionality degraded. Therefore, instead of relying solely on the satellite navigation system, the recent trend is to acquire continuous and precise navigational data by interfacing a dead-reckoning (DR) system and using the multi-sensor data fusion (MSDF) techniques (Appriou, 2014). For the safe navigation of an USV, understanding its interaction with the environment is vital. The USV's NGC system should have the knowledge of static obstacles (e.g. land masses, etc.), the impact off changes in weather, tides, as well as the changing dynamic situation of other vessels (which is referred to as TSs). Nowadays, existing nautical charts in the market can provide accurate positions of static obstacles and the environmental influences can be determined and accessed by online data. Therefore, the detection of neighbouring moving TSs becomes one of the salient issues that needs to be addressed in the navigation system. The Automatic Identification System (AIS) and marine radar are commonly used to determine positions of dynamic obstacles such as TSs. Marine radar is considered a primary perception sensor system that provides distances from and bearings to TSs, while AIS is a relatively new technology that could obtain the absolute position and course information of TSs from their on-board navigational sensors.

As mentioned earlier, the data acquisition module utilises multiple sensors on-board to process a range of measurements and obtain the information required for the USV's safe navigation. With a variety of sensors on-board, the research challenge is how to analyse their outputs and develop suitable data fusion algorithms to combine those data streams in an efficient and predictable manner to increase the system measurement accuracy. Ideally, the fusion results would allow the USV to identify and locate itself precisely and perceive the surrounding environment. However, due to equipment limitations and environmental influences, such as signal loss, unpredictable sensor failure and inaccurate measurements makes this a difficult goal to realise. This thesis details the development of the sensor data acquisition system as well as the algorithms and methodologies that have been designed to address the aforementioned issues.

1.2. Aims and Contributions

1.2.1. Aims

This research mainly aims at developing a practical robust multi-sensor data acquisition and fusion system for autonomous USV navigation by generating reliable navigational data. The work involves practical sensor system design, data fusion algorithms development as well as data fusion results analysis. Detailed objectives are outlined below to achieve the main aim of this research.

- Review up-to-date USV projects with regard to the designs of their navigational sensor systems. Review current technologies used in marine vessel navigation. Identify key research gaps in the solution options to practical situations a USV might encounter during operation and explore possible improvements to fill such gaps.

- Identify the types of sensors that are available and can be employed to obtain the necessary navigational information and implement a practical hardware system with applicable sensors using a cost-effective solution to extract raw sensor measurements.

- Develop multi-sensor data fusion algorithms to estimate more accurate navigational data as opposed to simply using raw sensor measurements, the accuracy of which are in practice susceptible to environmental disturbances, and thereby improve the navigational accuracy of USVs.

- Enhance the capability of the developed data fusion algorithms in dealing with unpredicted sensor error during practical operations.

- Analyse system reliability and design data fusion algorithms to manage and mitigate against possible sensor malfunction for autonomous USV navigation.

- Develop TS detection and tracking algorithms to enable and enhance USV perception capability of the surrounding environment to improve its collision avoidance capability.

- Demonstrate all the research findings and contributions to the work through conference and journal paper publications as well as the final thesis.

1.2.2. Contributions

In order to fulfil the research aims, a novel navigation system has been developed that operates effectively, reliably, and is also adaptable to new mission requirements as they evolve. The main contributions of this research are summarised as:

- A practical sensor system based on an embedded system has been installed to obtain raw measurements from multiple navigation sensors and communicate with the main control computer. The embedded system promises benefits such as improved cost-effectiveness, lower power consumption and heat production, is more reliable and portable. A conference paper regarding this work has been published in MTS/IEEE OCEANS'18 (Liu et al, 2018).

- A multi-sensor data fusion algorithm based on Unscented Kalman Filter (UKF) has been developed to improve the accuracy of the raw sensor measurements for an USV navigation in a complex environment. The algorithm is capable of dealing with practical environmental disturbances, such as water current, which may alter the planned trajectory of the USV and introduce non-linearity to the data fusion system. This work led to publications in proceedings of International Conference on Computer and Information Technology (Liu et al, 2014; Liu et al, 2015).

- A Fuzzy logic based adaptive estimation algorithm has been designed in addition to the developed multi-sensor data fusion algorithm to deal with issues caused by unpredicted sensor error during practical operations. The algorithm has significantly improved the performance of the data fusion system that is based on the conventional UKF. This work led to a journal paper published in the IEEE Access (Liu et al., 2019).

- Quantitative analysis of the sensor data uncertainties and USV operation risks

has been provided to express the reliability of the fused sensory information. An algorithm has been designed to generate a number to represent the reliability of the data fusion system to inform the path planning module regarding the level of trust residing in the fusion results. This work has been partly published in the Proceedings of MTS/IEEE OCEANS'16 Conference (Song et al, 2016).

- A fuzzy multi-sensor data fusion algorithm based on Kalman filtering technology has been developed to detect and automatically recover sensor malfunctions during operation. The fuzzy estimation provides an efficient and smooth method to discard the false measurements of the failed sensor. This work has been published in the Proceedings of 13th International Navigation Conference (Liu, et al, 2015) and the Journal of Engineering for the Maritime Environment (Motwani et al, 2016).

- A target ship detection system has been developed for the USV to perceive the surrounding environment. The system employs a two stage fuzzy data association algorithm to allocate measurements from both AIS and radar to the associated TS track and an IMM based multiple manoeuvring TS detection and prediction algorithm to generate more accurate fusion results in TSs' navigational data. This work has been published in the International Journal of Adaptive Control and Signal Processing (Liu et al, 2015), the Proceedings of 13th International Navigation Conference (Liu et at, 2015) and the International Journal of Fuzzy System (Liu et al, 2020).

1.3. Scope and structure of thesis

This thesis has been divided into 8 chapters.

Chapter 2 provides a literature review of various USV projects and their navigation sensors, different modern electronic navigation systems and target ship detection systems as well as related data fusion techniques. A critical review is provided to analyse the development requirements of today's USVs and the main challenges and gaps in autonomous navigational sensor systems.

Chapter 3 introduces the *Springer* USV and presents a practical, low-cost and low power consumption navigation sensor system. The hardware system is built on an embedded Linux platform and is capable of extracting raw measurements from various navigational sensors and communicating with a control computer in real-time.

Chapter 4 demonstrates how Kalman filtering technology benefits the estimation of the USV's own navigational data. The environmental disturbance is taken into account when developing the nonlinear, multi-sensor data fusion system for the USV navigation.

Chapter 5 considers the influences caused by unpredictable sensor errors, which is common in practical applications. A novel adaptive multi-sensor data fusion algorithm has been developed to deal with such situations and the impracticability that conventional Kalman Filter algorithms are unable to process.

Chapter 6 analyses the outcomes of the developed algorithms to provide sufficient information of the fusion results obtained by the designed reliability monitoring system for the path planning system to take corresponding actions. The rest of the chapter also discusses the fault detection as well as monitoring algorithms that can be applied to USV navigation. The details of the novel fuzzy multi-sensor data fusion system used to detect the simulated malfunction of an electronic compass and recover its faulty measurements while the USV is conducting autonomous missions are presented.

In Chapter 7, a development of the dynamic TS detection system is presented. First, an AIS aided TS detecting and prediction algorithm has been developed to process the simulated AIS measurements to locate the TSs and predict their short term movements. Then, a marine radar has been integrated in the multiple TSs detection and tracking algorithm, which involves multi-sensor data association and fusion.

The research findings and outcomes are summarised in Chapter 8, together with a future plan to enhance the practicability of the proposed data acquisition system.

Chapter 2. Literature review

This chapter provides a comprehensive literature review of the current research related to USV navigation. The review has been divided into three sections. First, a survey of the background and current development progress of unmanned surface vehicles has been provided. This is followed by a review of the marine navigation technologies that can be applied to USVs applications. The final section is the review of the related sensor data processing and fusion techniques together with the analysis of existing research in USVs navigation.

2.1. Unmanned Surface Vehicle

2.1.1. Background of USVs

It has been thousands of years since human beings started to exploit the sea with most of the early activity was fishing and trade. The development of ship construction has enabled further exploration of the ocean and has led the ocean engineering growing rapidly. However, the environmental conditions at sea differ greatly from those on land. Even with the advanced technologies available today, people still encounter unpredictable weather and harsh environmental conditions that can prove to be hazardous while working at sea. It can also be very demanding and fatiguing for people to work on vessels and platforms influenced by the motions at the surface of the water. In certain industries there is growing interest and demand for marine robotics to reduce risks to humans and potential casualties. Unmanned Surface Vehicles (USVs) are vessels that operate on the surface of the water with no human operators on board. Although researchers have tried to build USVs that could be controlled remotely using radio control in the past, significant development of remotely controlled USVs by navies took place after the Second World War (Corfield, 2006; Motwani, 2012). Most of the early naval USVs were simple, radio-controlled drone boats for specific tasks such as clearing dangerous mine, assessing battle damage, etc. (Shurliff, 1947). After the war, USVs were used and developed mainly for military operations for the next two decades. The US navy used drone boats to

collect radioactive water samples after atomic bomb tests on Bikini Atoll in 1946 (Bertram, 2008). Within ten years, remotely controlled minesweeping boats had been developed and are still in use today. By 1960, the US navy used remotely-controlled target drone boats for missile firing practice. Universities and commercial companies started to develop an interest in USVs thereafter. Various USV projects were then constructed throughout the world in the 1990s, such as *MIMIR* (Robert and Sutton, 2006), *Roboski* (Bremer et al 2007), and *Owls WK II* USV (Motiwani, 2012). The early educational applications can be traced back to the Massachusetts Institute of Technology's (MIT) Sea Grant program established in 1970 (Manley, 2008). The aim was to develop educational marine robotics to solve real world problems and a set of autonomous surface craft (ASC) were produced including *ARTEMIS*, *ACES* and *AutoCat* as shown in Figure 2.1 (Manley, 1997).

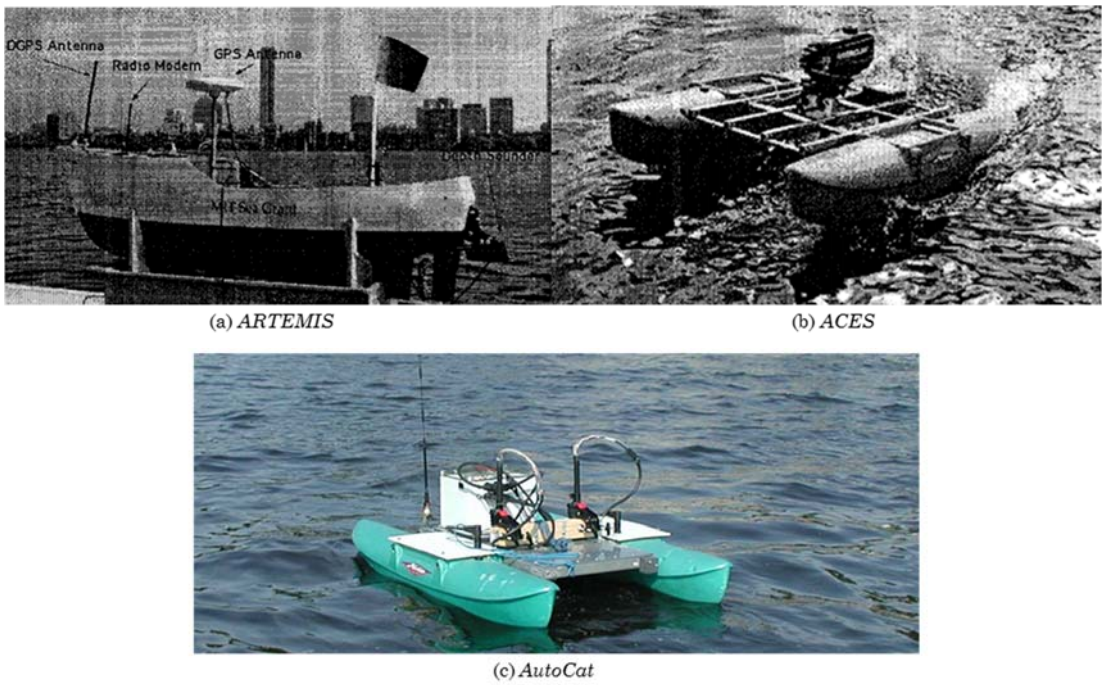

(a) *ARTEMIS* (b) *ACES*

(c) *AutoCat*

Figure 2.1 ASCs produced by Sea Grant of Massachusetts institute of Technology. (a) *ARTEMIS* was developed to collect simple bathymetry data in the Charles River in Boston; (b) *ACES* was equipped with upgraded sensors for more detailed survey of Boston harbour; (c) *AutoCat* is the newest ASC developed by MIT sea grant and it is an upgrade of *ACES* and equipped with DGPS for navigation. (Source: Manley, 2008)

2.1.2. Current USV applications and development (post 2000)

In the past two decades, with the rapid development of marine electronic navigation

technology, especially the Global Positioning System (GPS), in addition to the navies USVs are attracting increasing attention from academic and commercial companies, driven by their capability to undertake various maritime missions, which are listed in Table 2.1.

Table 2. 1 Various examples of missions that USVs can accomplish

Commercial missions	**Military missions**
Marine monitoring	Anti-terrorism forces
Marine waste detection	Protection forces
Mapping the marine funds and mining	Electronic warfare
Shipping	Mine Countermeasure
Cooperate with UUVs and UAVs	Anti-submarine warfare
Sea surveillance	Post explosion assessment
Environmental monitoring	Threat identification and classification
Water sampling	Harbour patrol

In order to complete a mission, an autonomous USV must be able to determine its location, detect the surrounding environment, as well as other dedicated abilities for the specific tasks. Some missions require a high autonomy within the USV's functionality, therefore, researchers are keen to improve USV autonomy. According to Liu et al (2016), USV development is focused on four main aspects: USV hull and auxiliary structural elements; propulsion and power system; Navigation, Guidance and Control (NGC) system; communication system and ground station. In order to increase USVs' level of autonomy, improvement in the NGC system is core to that development. This type of navigation system should have the ability to accurately determine the location of the USV itself as well as perceiving the surrounding environment so that a safe path of operation can be generated along which the USV would need to transit.

Since the Second World War, the USA has been the leading country for USV development. In addition, the US Navy has increased its focus on USVs since 2002. They have announced a master plan for the navy unmanned surface vehicle in 2007, which has accelerated the research and development (R&D) of USVs. Since then,

various advanced naval applications have been developed. For reasons of security and secrecy within the navy, a few notable military applications are outlined as follows:

The *Blackfish* USV was developed by QinetiQ North America as one of the Office of Naval Research (ONR) projects in 2008 (Sonnenburg, 2012). The design was based on a jet-ski hull platform and its main missions are maritime force protection and patrol in harbours and ports. It features a 360 degree high resolution Pan-tilt-zoom (PTZ) camera for situation awareness and a satellite compass for local navigation. A high-resolution 2D sonar and an underwater video camera are also available for diver and swimmer threat response missions.

Figure 2. 2 *Blackfish* USV (Source: QinetiQ, 2018)

The US navy uses a remotely controlled USV called *Protector*, as shown in Figure 2.3, to conduct mine countermeasure and reconnaissance operations. It was developed and produced by Rafael Advanced Defence Systems of Israel in 2003. Its design is based on a rigid hull inflatable boat (Naval Technology, 2014) and the suite of navigational sensors includes a GPS receiver, a navigation Radar and several video cameras (Hanlon, 2006).

Figure 2.3 *Protector* USV (Source: Naval Technology, 2014)

The military are often keen to develop and build additional features in addition to the base design, such as the extra green power source for long term operation. The *Wave Glider* from Liquid Robotics is a single hull hybrid wave and solar propelled USV. It can also be used as an unmanned underwater vehicle (UUV) (Liquid Robotics, 2014). The *Wave Glider* is equipped with a GPS receiver as the primary navigation sensor, along with a tilt-compensated compass with three-axis accelerometers and a water speed sensor. It also has an on-board Radar and an AIS module to enable obstacle detection and collision avoidance capability (Carragher et al, 2013).

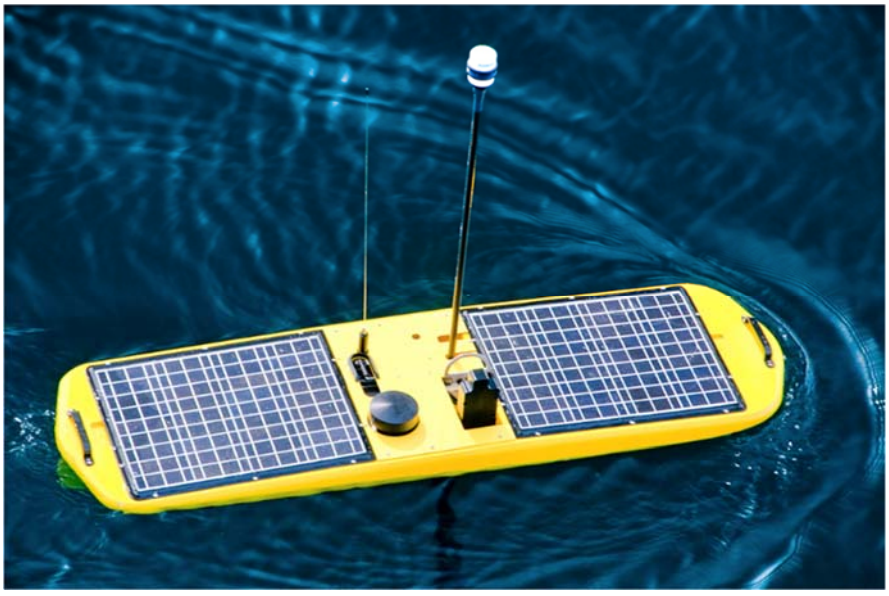

Figure 2.4 METOC *Wave Glider SV3* (Source: Liquid Robotics, 2014)

Today, the MIT have shifted their focus to software development of USVs. They stopped developing their own USVs and have started using commercial USVs instead, for example the *Heron M300* USV and *WAM-V* USV (MIT Marine Autonomy Bay, 2018). As shown in Figure 2.5, *Heron M300* USV is a portable sized, catamaran design USV. It is equipped with built-in GPS for navigation (Clearpath Robotics, 2018). Other sensors, such as PTZ camera, Lidar, IMU and higher resolution GPS modules, are available for upgrade.

Figure 2. 5 *Heron* USV (Source: Clearpath Robotics, 2018)

The *WAM-V* USVs were first designed for research and scientific purposes. Figure 2.6(a) illustrates the first 12-foot *WAM-V* USV. It was delivered as a pure remote control vehicle to universities for research in 2009 (Marine Advanced Research INC., 2014). Its navigation sensor suite contains a Differential GPS (DGPS), an Inertial Measurement Unit (IMU) and an electronic compass. In 2012, the 14-foot *WAM-V* USV was constructed and delivered to Florida Atlantic University for research on autonomous operation and tasked to perform autonomous launch and recovery of an Autonomous Underwater Vehicle (AUV). Unlike the remote control USV (12-foot *WAM-V*), it can accomplish way-point tracking tasks via heading guidance (Pearson et al. 2014). The navigational sensor suite of the 14-foot *WAM-V* USV consists of an XSENS MTi-G INS/GPS and an Ocean Server OS5000 electronic compass package. The 16-foot *WAM-V* was developed in 2014 and was used to map the coast view of the San Francisco waterfront by both Marine Advanced Research, INC. and Google. The largest *WAM-V* USV is 33 feet long and is able to carry a person, as shown in

Figure 2.6(d). It was constructed in 2010 and is used for other applications such as port and riverine operations and surveillance, deploying oceanographic sensors and instruments, protecting passage and acting as a sea shield. With the 9 years of development, smaller size *WAM-V*s can also conduct commercial missions when mounting proper mission sensors (Pearson et al. 2014).

Figure 2.6 *WAM-V* USVs (Source: Marine Advanced Research INC., 2014)

European researchers have also shown interest in USVs. Figure 2.7 presents the *Catarob* USV and *Cat Surveyor* USV developed by Subsea Tech in France. *Catarob* has been especially designed to carry out tele-operated or autonomous inspections, survey and modelling missions in shallow inland waters and harbour areas. It is equipped with front and rear facing HD colour video cameras, electronic compass and GPS for gathering data regarding the surrounding environment and navigation. The Cat Surveyor is of larger size and includes a DGPS module for more precise localisation. It can be employed to acquire hydrographic data for inland waters, harbours and coastal areas (Subsea Tech, 2019).

Figure 2.7 *Catarob USV and Cat Surveyor* USV (Source: Subsea Tech, 2019)

A world leading USV development company, Autonomous Surface Vehicles (ASV) Global Ltd, is located in the UK. The company has developed a range of USVs. Figure 2.8(a) shows the *C-Worker 6*. The *C-Worker* series are of single hull design carrying surveying sensors such as the Ultra-Short Base Line (USBL), multi-beam echo sounder (MBES) and multi-beam sonar to conduct a range of tasks such as marine construction survey, metocean data collection, environmental and site survey. *C-Cat* USV was designed in smaller size for the University of Southampton for research and experiments in autonomous development. It can also conduct simple maritime missions such as water sampling and monitoring. ASV Global is also working with the Royal Navy, where the *C-Target* series was designed in various sizes to support military missions, such as naval gunnery training, weapons and platform trials. The *C-Sweep* features a robust glass fibre reinforced plastic hull, twin diesel engines and ASV's own design of control system. It provides direct control, semi-autonomous and autonomous modes, complete with real time video, Radar, AIS and payload feedback, vehicle sensor data channels and safety systems. It is designed to offer a high degree of directional stability, substantial towing capacity for long-endurance mine sweeping missions and sufficient electrical generating capacity to support modern mine sweeping equipment requirements (ASV Global, 2018).

(a) *C-Worker 6* (b) *C-Cat 3*

(c) *C-Target 3* (d) *C-Sweep*

Figure 2.8 USVs from ASV Global: (a) *C-Worker 6* USV; (b) *C-Cat 3* USV; (c) *C-Target 3* USV; (d) *C-Sweep* (Source: ASV Global, 2018)

Maritime Autonomy Surface Testbed (*MAST*), is another project for the Royal Navy. It was designed and developed by the Defence Science and Technology Laboratory together with ASV Global and Roke Manor Research. In October 2016, it participated at an unmanned Warrior event in Ministry of Defence exercise areas around Wales and Scotland for the Royal Navy to observe and assess current and future operations with naval USVs. During the event, *MAST* has demonstrated its ability to operate at various levels of autonomy from remote control to fully autonomous navigation. The *MAST* USV equips a 360-degree camera and a marine Radar which provide tactical situational awareness to support wider picture compilation (ASV Global, 2018; Defence Science and Technology Laboratory, 2016).

Figure 2. 9 *MAST* USV (Source: Defence Science and Technology Laboratory, 2016)

China is now paying increasing attention to USV development. Back in 2009, USVs in China were still in the conceptual design phase. Now, the market for USVs is growing rapidly and a number of USV applications have been developed and have come into service. Oceanα (Chinese name: Yunzhou) is a leading company in China for USV development. They have different designs for environmental measurement and hydrographic surveying. Figure 2.10 shows some existing USVs that have already been deployed and are in use. The *ESM30* is a smaller sized design that is mainly used for water sampling and monitoring. It is equipped with a standalone GPS module for navigation and can operate in autonomous mode for simple missions on calm water. *ME70* is a catamaran design survey vehicle with built-in GPS for navigation. It is also equipped with an ultrasound sensor to detect and avoid surrounding obstacles. *L30* USV is designed for on the water fire control and rescue. *M80* USV is designed for autonomous navigation and obstacle avoidance research so it has several navigation and perception sensors (e.g. GPS, marine Radar, camera) installed. It can also be used to conduct commercial missions such as underwater exploration of inland and coastal waters. (Oceanα, 2019). The company is keen to work with the Chinese navy to develop USVs with increased autonomous capability (Gain, 2019).

(a) *ESM30* (b) *ME70*

(c) *L30* (d) *M80*

Figure 2.10 Oceanα USVs (Source: Oceanα, 2019)

The Chinese navy has also funded a number of USV projects. *SeaFly-01* USV, developed by the Beijing Sifang Automation Company's Wuhan branch, is made of carbon fibre for ultralight weight and a tougher body. It is equipped with BeiDou, the satellite navigation system developed in China for navigation. It has its own autonomous navigation system with path planning and obstacle avoidance features and can be used to conduct missions such as detecting submarines, harbour and coastline patrol, and armed intervention (Jane's International Defence, 2018).

Figure 2.11 *SeaFly -01* USV (Source: Jane's International Defence, 2018)

After reviewing the number of applications developed in the US, Europe and China, it is noticeable that the military applications are much more advanced than those in the commercial and academic sectors. Table 2.2 lists the reviewed USVs and their navigation sensors. Remote control has been implemented for the majority of the commercial and academic USV applications. On the other hand, military USVs have been designed with autonomous control systems. Military applications also display more features, such as the use of wave and solar energy, precise localisation systems, etc. In addition, they are more focused on comprehending the state of the surrounding environment to enable collision avoidance. In the commercial market, smaller size USVs that are mainly used for surveying are representative of the more mature applications. Therefore, research on autonomous navigation and collision avoidance for commercial and academic USVs is still an area that could benefit from further research and development.

Table 2. 2 Reviewed USVs and their navigational sensors

USVs	**Hull design**	**Navigation sensors**
Blackfish	Jet-ski single hull	360 degree PTZ camera and satellite compass
Protector	Single hull	GPS, Radar and cameras
Wave Glider SV3	Single hull with solar panel	GPS, compass, accelerometer and water speed sensor AIS and Radar
Heron	Catamaran	GPS, can be upgraded by PTZ camera, Lidar, IMU, higher resolution GPS
WAM-V	Catamaran	Differential GPS, IMU, and electronic compass
Catarob	Catamaran	GPS, HD colour video cameras, electronic compass
Cat Surveyor	Catamaran	Differential GPS
C-sweep	Single hull	GPS, video camera, Radar and AIS
MAST	Single hull	360 degree camera and marine Radar
ME70	Catamaran	Built-in GPS
M80	Single hull	GPS, video camera and Radar
SeaFly-01	Single hull	BeiDou

2.1.3. USV challenges and future directions in development

Although USVs have developed rapidly in the last two decades and various applications exist on the market, USV development still lags behind other branches of robotics and autonomous control. Apart from the naval USVs, the existing USV applications on the market are mainly for educational use and survey missions. To widen the range of applications and development of USVs, practical NGC systems with higher degrees of autonomy could prove beneficial. Two main challenges of such development are detailed below.

- Navigation: Of the current USVs reviewed, especially the latest ones, high resolution sensors are employed for precise navigation, which leads to higher construction costs of the USV. Using lower cost sensors with relatively erroneous measurements and applying data fusion algorithms to increase the accuracy of the measurements could be one solution to reduce the cost. Low cost sensors often consume less power, which can bring benefits such as increasing the USV's endurance. Therefore, developing data fusion algorithms to mitigate against limitations in reliability of sensors and/or accuracy of sensor signals is the first challenge towards the development of a low cost USV NGC system to overcome the equipment limitations and mitigate against environmental effects.

- Guidance: Path planning with collision avoidance feature is important to increase the level of autonomy of USV. Most of the existing commercial and academic USVs are in their early phase of development. They are either remotely controlled or simply designed to track a few pre-set GPS coordinates. Efficient path planning algorithms are another aspects of USV development that needs further investigation to enable fully autonomous USV navigation. The accurate detection of obstacles is a key requirement of the path planning algorithm to help generate a safe path.

The future of USV applications offers a wide range of prospects, driven by their high potential in marine engineering. Considering that USVs are entering the test phase, it deems feasible that in future marine vessels and cargo ships soon could be

operating autonomously. It is envisaged that the incorporation of a USV NGC system could play a vital role in improving autonomy of those vessels. Therefore, the future NGC system for such a purpose should be self-contained and universally adaptable to standard on-board equipment.

2.2. Overview of marine navigation technologies

Navigation technique is the method by which an object's navigational data such as position, velocity, and some or all of the attitudes are determined (Groves, 2013). Modern navigation technique employs navigation sensors to provide measurements to compute the object's navigational data. This section reviews available navigation technologies for USVs in the marine environment.

2.2.1. Satellite navigation

Satellite navigation systems are in wide use today, especially in vessel navigation. From the review of current USV applications in Section 2.1.2, it can be seen that most USVs are equipped with a GPS receiver for navigation. Satellite navigation uses a system of satellites that provide autonomous geo-spatial positioning each with a certain coverage. They allow small electronic receivers to determine their location (longitude, latitude and altitude) with reasonably high precision (to within a few metres) using time signals transmitted along a line of sight (LoS) by radio from satellites as the signals will not penetrate most solid objects, such as dense clouds and mountains (Sabatini et al, 2017). From Figure 2.12, it can be seen that at least four satellites are required to calculate the position of the signal receiver. The distance between the satellite and receiver is computed as in Equation 2.1 and the exact location of the receiver can then be determined based on the computed distances and the known positions of the satellites by applying the triangulation method (Darrozes, 2016; Hapgood, 2018; Giorgi et al, 2019; Grewal et al, 2020).

$$distance = travel\ time * speed\ of\ light \tag{2.1}$$

According to Croslow, 2013, satellite navigation systems can be classified as one of two types: the Global Navigation Satellite System (GNSS) and the Regional Navigation Satellite System (RNSS). As USVs are developed to operate and conduct

missions on the ocean surface, GNSS with wider coverage is a more suitable solution for their navigation. Four major GNSS systems are currently in use and in development throughout the world.

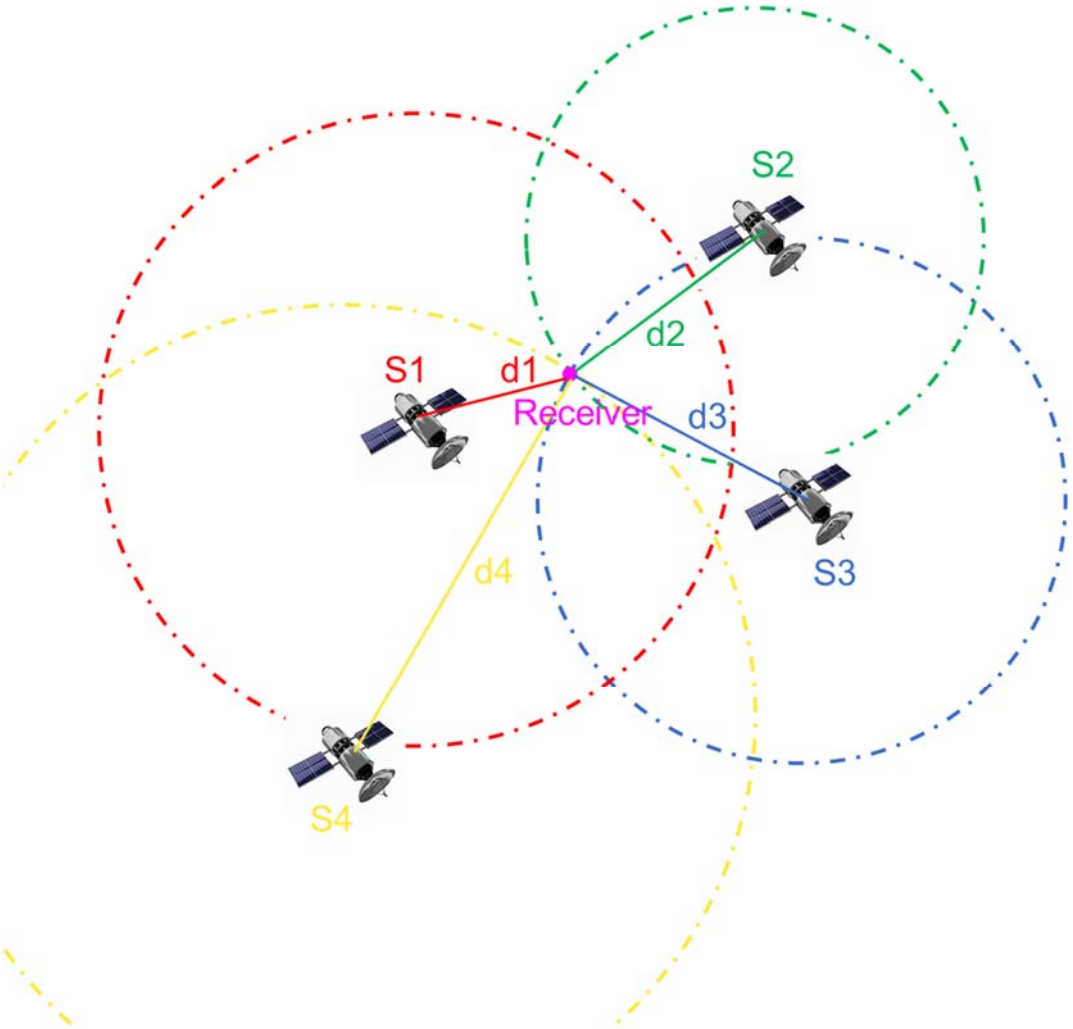

Figure 2.12 Principle of GNSS localisation

- The Global Positioning System (GPS) service is provided by a network of US satellites called Navstar. The system is composed of 24 satellites and was created by the US Department of Defense. GPS was originally intended for military applications, but in the 1980s, the government made the system available for civilian use. GPS works in all weather conditions, anywhere in the world, 24 hours a day (Garmin, 2014).
- Global Navigation Satellite System (GLONASS) is also composed of 24 satellites but was developed in the Soviet Union and is operated by Russian Aerospace Defense Forces. This satellite navigation system is the only other

navigational system in operation with global coverage and of comparable precision to that of GPS (Darrozes et al, 2016).

- Galileo is a 30-satellite global navigation system currently being developed by the European Union and European Space Agency. One of the goals of this system is to provide a high-precision positioning system for European nations that is independent from the Russian GLONASS and US GPS (EGSA, 2019).
- Compass/BeiDou Navigation Satellite System (CNSS) is a global geolocation network system being developed by China and is expected to be completed in 2020. (GPS Daily, 2019). It is the third generation of its regional BeiDou Satellite Navigation System (BDS), also known as BeiDou-3. It currently has 38 satellites in orbit.

Navstar GPS was the most widely used GNSS but it is now facing competition from the Russian GLONASS and will do so shortly from the European Galileo and Chinese CNSS. Therefore Navstar engineers are concentrating on improving the accuracy of the system's positioning to enable Navstar to compete. Today's civilian GPS systems are accurate to within 12 metres, according to the Federal Aviation Administration, 2014. Military systems are even more precise to within a few decimetres. The fast development of GPS offers more applications and also reduces the price of GPS receivers. It is now the primary navigation method for ships as it offers the benefits of relatively accurate real-time positioning data (National Coordination Office, 2014). Therefore, GNSS is an effective navigation solution for USVs since they operate in the open water area where more satellites can be "viewed" by the onboard receiver.

2.2.2. Inertial navigation

Inertial navigation is a dead-reckoning navigation system. Dead-reckoning (DR) is not a new technique in navigation. It has been used by mariners since the fifteenth century (Penobscot marine museum, 2012). The principle of DR navigation is to determine the current position of the vessel based on knowledge of its previous position and velocity. In modern electronic navigation systems, the inertial navigation system (INS) uses electronic sensors to measure the motion of the operating platform. The main sensors of an INS are the accelerometer and the

gyroscope, which measure the acceleration and angular velocity respectively. With a fixed start point and direction, the DR positions and headings can be determined using the following equations (Grewal et al, 2020).

$$p_t = p_0 + v_0 t + \frac{1}{2} a t^2 \tag{2.2}$$

where p_t is the position at time t, p_0 is the initial position, v_0 is the initial velocity and a is the acceleration rate for time t.

$$\psi_t = \psi_0 + \omega t \tag{2.3}$$

where ψ_t is the heading at time t, ψ_0 is the initial heading and ω is the angular velocity.

In marine navigation, DR positions and headings are approximate as the methodology makes no direct allowance or correction for the effects of leeway, current, or equipment limitations. Consequently, the DR technique is vulnerable to drift error and is not able to replicate the accuracy of GNSS, especially when used in isolation (Grewal et al, 2020).

2.2.3. Dynamic obstacle detection

In order to navigate safely, autonomous USVs would require the ability to sense its surrounding environment by detecting and avoiding both static and dynamic obstacles. Avoiding a static obstacle is relatively straightforward while a dynamic obstacle, such as a target ship, poses a more complex hazard. Therefore, an USV would need to differentiate the type of and risk posed by each obstacle and predict the movements of the dynamic obstacles to eliminate the potential risk of collision. A large number of the USVs reviewed in Section 2.1 employ long range digital cameras (PTZ camera, video camera) to perceive the surrounding environment since the camera can provide real-time precise images of obstacles with the benefits of small size and light weight. Other sensors, like marine Radar (Radio detection and ranging), Lidar (Light detection and ranging) and AIS are also available for larger sized USVs (ASV Global, 2018; Oceanα, 2019). Marine Radar has been regarded as a prime solution to perceive the surrounding environment in maritime vessel navigation for many decades. It determines positions and courses of target ships by measuring the relative distances and bearings to the Radar. Other range based sensors

such as the Lidar and ultrasonic sensors have similar operating function as marine Radar and the difference is the transmitted signal (Onunka et al, 2013; Hermann, et al, 2015; Liu et al, 2018). Automatic Identification System (AIS), that is employed by both mariners and the vessel traffic services (VTS) for identifying and locating surrounding vessels to improve maritime safety, has been developed over the last few decades and can provide reasonably accurate navigational data of a target ship that is equipped with an AIS transmitter (Chaturvedi, 2019). According to Pallotta (2013), a simple AIS receiver can be powered at similar low-voltage levels that are also adequate for the navigation sensor system of an autonomous USV. The detection ranges of above mentioned detection sensors are listed in the Table 2.3 (Tang et al, 2015; Mousazadeh et al, 2018).

Table 2. 3 Different detection sensors and their detection range

Detection sensors	**Detection range**
Radar	48 nautical miles (appx. 88896 meters)
Lidar	Up to 200 meters
Ultrasonic	Up to 10 meters
AIS	20 nautical miles (appx. 37040 meters)
Long range Camera	About 2000 meters

2.2.4. Simultaneous Localisation and Mapping (SLAM)

Simultaneous localisation and mapping (SLAM) is a combination of the inertial navigation and the dynamic obstacle detection. It can be defined as a process to build a map of the environment surrounding a robot and keep determining its position in the map without any *a priori* knowledge of its position (Whyte, 2006). Spatial sensors are required to map the environment with unknown landmarks. Range based sensors such as Lidar and vision based sensors such as PTZ cameras are the two primary spatial sensors employed in SLAM approaches (Chong et al, 2015; Huang et al, 2019; Jiang et al, 2019). They detect and measure distances and bearings between the robot and surrounding landmarks so that a real-time map can be constructed. An inertial navigation system is employed to measure the motion of the robot so that the real-time position of the robot can be calculated. SLAM algorithms can then be applied to fuse the raw measurements of spatial sensors and the

calculated robot positions (Zhang et al, 2017).

Table 2.4 lists all the reviewed modern electronic navigation technologies s as well as their features.

Table 2. 4 Various navigation methods and their features

Navigation methods	**Features**
Satellite navigation	Use satellites to provide absolute navigational data; signal loss and blockage occur without LoS to the space
Inertial navigation	Calculate current information based on prior information and motion, large errors occur if using standalone
Dynamic Target detection	Use detection sensors such as range based sensors, AIS and visual sensors to calculate target's navigational data based on own navigational data
SLAM	Build a map of surrounding environment and keep tracking own position within the map

Integrated systems involving multiple sensors are popular in modern navigation for providing more comprehensive and accurate navigational data. The recent trend to enable the USV to determine its location is to integrate the inertial navigation system into the satellite navigation system as a complementary system (Xia et al, 2016; Ccolque-Churquipa et al, 2018; Mousazadeh et al, 2018;). Multiple sensors are also used in dynamic target detection for more reliable navigational data of surrounding target ships (Kazimierski, 2013; Habtemariam et al, 2014; Kalsen et al, 2015; Chaturvedi, 2019). The integrated system is sufficient for guaranteeing satisfactory performance in USV navigation. SLAM is not necessary for USV navigation since satellite navigation is available, but it can be effective in a GNSS denied environment. SLAM also relies on the surrounding landmarks, which makes it unserviceable when USVs conduct missions in the open sea surface that is far from the shore.

2.3. Gap analysis of multi-sensor integrated system in USV navigation

As detailed in the literature review of the history of USVs in Section 2.1, the majority of the existing USVs are of small size and light weight and are usually dedicated to specialised missions. The operating conditions of USVs are often hazardous and unpredictable. Therefore, accurate and reliable navigational data is primary demand demanded to ensure the safety of the USV. Integrated navigation systems that involve multiple sensors are normally employed to provide more accurate, continuous and reliable navigational data (Paulino et al., 2019; Groves, 2013; Stateczny and Kazimierski, 2011; Allerton and Jia, 2005). It has many advantages, such as improving system reliability and robustness, extending measurment coverage, increasing data confidence and improving resolution (Xie and Wan, 2011; Varshney, 1997). With multiple sensors, the system will gather a large amount of navigational data. Therefore, the optimal estimation techniques applied to fuse the data obtained are the core of a multi-sensor navigation system. A well-known definition of data fusion was provided by Hall and Llinas, 1997: "*data fusion techniques combine data from multiple sensors, and related information from associated databases, to achieve improved accuracies and more specific inferences than could be achieved by the use of a single sensor alone.*" It can be briefly described as a combination of multiple sources to obtain improved information.

2.3.1. Integrated satellite and inertial navigation system

Integrated satellite and inertial navigation systems use multiple sensors to locate an USV. Large amounts of navigational data that are associated with different coordinate frames will be fed into the navigation system. Coordinate frames are used to express the position of a point in relation to some fixed reference. According to Noureldin et al. (2013), there are four kinds of coordinate frames (listed in Table 2.5) related to a USV's integrated satellite and inertial navigation system: inertial frame (i-frame), Earth frame (e-frame), body frame (b-frame) and navigation frame (n-frame). As illustrated in Figure 2.13, satellite navigation systems normally provide the measured object's coordinates along the e-frame. Inertial sensors measure the object's motion along the sensors i-frame, but these motions can be approximated or

converted to the object's b-frame when the inertial sensors are placed near the centre of gravity of the object. In order to combine and fuse these measurements, a local n-frame has to be designed and all the sensor measurements have to be converted to match the designed navigation frame.

Table 2. 5 Different reference coordinate frames related to USV navigation

Coordinate Frames	Description
Inertial-frame	Determined by the inertial sensors' sensitive axis
Earth-frame	With the centre of mass of earth as its origin
Body-frame	With the gravity centre of the hosting platform as its origin
Navigation-frame	With a fixed point on the earth surface as reference

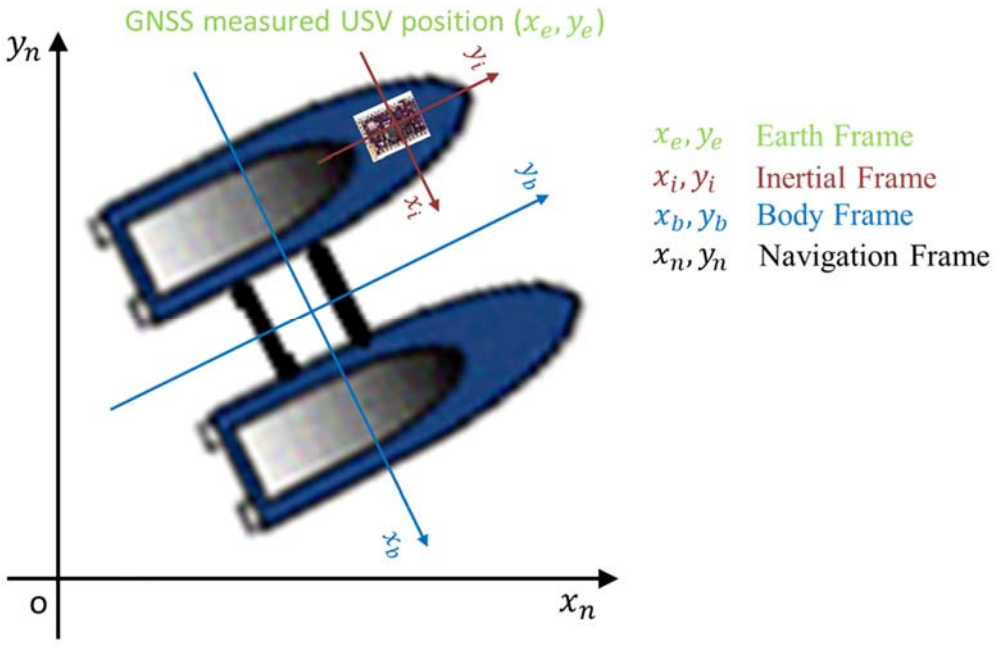

Figure 2.13 Navigation frames related to USV navigation

After converting raw sensor measurements into the pre-designed navigation frame, multi-sensor data fusion algorithms can be developed to provide useful navigation data for the path planning module of an USV's autonomous navigation system. Kalman Filter (KF), a linear recursive data processing algorithm, is extensively used in vehicle navigation. It processes all available measurements, regardless of their precision, to estimate the current value of the variables of interest, using knowledge

of the system and measurement device dynamics; the statistical description of the systems noise, measurement errors, and uncertainty in the dynamics models; as well as available information regarding initial conditions of the variables of interest (Maybeck, 1979). If the input data fits the predefined linear dynamics and statistical models and *a priori* knowledge is known, the KF can provide an optimal estimate of the state vector, in a minimum variance sense (Gelb, 1974). As a result, the KF has become the most common technique for estimating the state of a linear system, particularly in navigation systems. Rodriguez and Gomez (2009) developed three sensor fusion algorithms based on Kalman Filtering to locate an agricultural land vehicle by trying different combinations of existing navigation sensors. The first KF algorithm takes measurements from a GPS module and a steering angle sensor and outputs fused navigational data i.e. position, heading and speed of the vehicle. The second KF algorithm they developed was used to provide corrections to GPS measurements from an electronic compass. They integrated an IMU to a GPS system with an extra steering angle sensor in the final algorithm for system linearisation. They concluded that combining a complementary sensor is an effective way to improve GPS signals. However, a practical application of a KF to a specific problem requires correct configuration of its parameters. Li et al (2014) used the KF to process the measurements from a conventional strapdown inertial navigation system to track a vehicle's attitude. They applied the developed algorithm to a practical vehicle with a rocking base and the repeated alignment achieved a precision of 0.04° over 180 seconds. Most of the other approaches using conventional KFs in navigation that can be found in published sources only deal with sensor sample integration in linear systems, or pre-processes the sensor signals to linearise the integrated system (Jose and White, 2001; Sazdovski et al., 2005; Baselga et al, 2009; Xie and Wan, 2011; Chu et al., 2013; Maklouf et al, 2013).

In practice, most systems are non-linear and the KF is incapable of making estimations with sufficient accuracy. Therefore, variant KFs are developed to accommodate non-linear applications in the real world. Bijker and Steyn (2008) designed an IMU/GPS integrated system with two minor extended Kalman Filters (EKFs) to determine an unmanned airship's navigational data, i.e. attitude, velocity and position. They found that using one major EKF with all the navigational data as inputs generates more accurate estimations but requires higher processing power.

The trade-off between the accuracy and processing power has been mitigated by splitting the single EKF into two minor EKFs namely the attitude estimator and position estimator. Saderzadeh et al (2009) proposed an EKF algorithm to handle the navigation error of a mobile robot. It was demonstrated that the estimation at primary state would introduce error into the system and the convergence speed of the EKF algorithm is slow. Mousazadeh et al (2017) used the EKF to estimate an USV's state and position. Although the authors did not provide the computational time of the EKF based algorithm, it necessitates the computation of a complex Jacobian matrix at each time step, hindering its adaptation in real time applications. Zhang et al (2005) implemented an Unscented Kalman Filter (UKF) to improve the GPS, the IMU and the electronic compass measurements. The authors implemented both UKF and EKF and tested them on a practical land vehicle. The results showed that UKF is able to produce estimated navigational data with greater accuracy than those generated by EKF. The superior performance of UKF over EKF was further proved by Zhai et al (2012) for GPS/INS integrated navigation, Choi et al (2010) for on-board orbit determination using GPS observations, Lee et al (2017) for nanosat attitude estimation and Gao et al (2018) for INS/GNSS/CNS integration. The reason that UKF is able to provide more stable and accurate estimations over EKF is explained in their operational details as follows.

For a nonlinear system with a state vector $x \sim N(m, P)$ and a stochastic difference equation as below:

$$x(k) = f(x(k-1), w(k-1)) \tag{2.4}$$

the EKF firstly linearises the system by using the first order of the Taylor expansion of $f(x)$ to approximate the mean m and covariance P:

$$f(x) \approx f(m) + \frac{\partial f(m)}{\partial x}(x - m) = f(m) + F_x(m)(x - m) \tag{2.5}$$

where F_x is the Jacobian matrix of f. This process has limitations when working in systems with considerable non-linearities. In addition, the computation of the Jacobian matrix is complex and can be quite error prone (Sarkka, 2013). On the contrary, UKF does not linearise the system, but forms a set of (so-called) Sigma points to capture the mean and covariance of the original distribution of the state x exactly and propagates them through the actual non-linear function. The mean and

covariance are then recalculated from the propagated points, yielding more stable and accurate results (Julier and Uhlmann, 2004; Sarkka, 2013; Khamseh et al, 2019).

Another variant of KF used for unmanned vehicle navigation was proposed by Motwani et al (2013). They developed an Interval Kalman Filter (IKF) based algorithm to estimate the yaw dynamics of an uninhabited surface vehicle called *Springer* during operation. The system to determine *Springer's* yaw dynamic is linear, but the authors improved the conventional KF by adding the boundaries of system uncertainties to the algorithm using interval system models (Motwani et al, 2013). In recent years, a growing interest in developing mathematical techniques to deal with the impracticality of the conventional KF and its variants, such as fuzzy logic, adaptive estimations (Liu et al, 2019; Meng et al, 2016; Gao et al, 2015; Motwani et al, 2016; Li et al , 2014; Malleswaran et al, 2013) has been witnessed.

Table 2. 6 Comparison of current sensor data fusion algorithms

Sensor fusion algorithms	**Feature**
Kalman Filter	Used in linear system
Extended Kalman Filter	Linearise the non-linear system using Taylor expansion
Unscented Kalman Filter	Generates several Sigma points and propagate them through the non-linear state function directly
Interval Kalman Filter	Add boundaries to system uncertainty

2.3.2. Multi-sensor data fusion for target ship detection

Multiple target ship tracking presents two main challenges: data association and state estimation. When detecting multiple dynamic target ships, all detection sensor measurements are gathered which results in the autonomous system not being capable of distinguishing the measurements associated to each target. Therefore, data association algorithms would need to be employed. Hall and Llinas (1997) provided the definition of the data association as: "*a process by which the closeness of sensor measurements is completed.*" The data association problem corresponds to correctly identifying multiple measurements to its target. Poor match between a measurement and its target will in turn lead to poor estimation. Failure of data association could

occur in certain situations, such as multiple targets, false alarms, ambiguities or detection uncertainty (Appriou, 2014). While researchers were pursuing basic data association algorithms such as Nearest Neighbour (NN), K-means, etc. (Guerriero, 2008; Kazimierski, 2011; Kazimierski and Stateczny, 2015; Zahra et al, 2015), Hu and Lin (2011) proposed a preliminary study on data association algorithms for Radar and AIS using neural networks and achieved effective performance. However, the proposed algorithm converges slowly and readily falls into local minima, which is impractical for USV target detection. Jan and Kao (2013) developed an interacting multiple model probabilistic data association filter (IMMPDAF) for Radar tracking systems, which has been demonstrated to outperform the conventional NN filter. However, this algorithm exhibits a high computational burden due to the consideration of real-time target detection. More robust methodologies especially in highly cluttered environments are widely recognised probabilistic approaches that include Multiple Hypothesis Tracking (MHT) and Joint Probabilistic Data Association (JPDA) where various probable association hypotheses are considered instead of direct individual assignment (Svensson et al, 2011; Habtemariam et al, 2014; Ning et al, 2016; Siegert, 2017). By spending more computational effort, these algorithms perform reliably even when observations are likely to agree on more than one target ship.

It has been well regarded that Interactive Multiple Model (IMM) is a highly effective method for estimating a manoeuvring target ship (Blom et al, 1998). IMM is a suboptimal recursive filter and its ability to adaptively switch between different kinematic models using Markovian coefficient appeals to many practical tracking scenarios. Many combinations of state estimation and data association algorithms have been proposed to yield robust multitarget tracking. IMM-JPDA, introduced by Bar-Shalom et al. (1991), has been broadly accepted due to the blending of IMM's renowned performance and JPDA's dependable association in cluttered environments. This maritime oriented work was then extended further by Gregor et al (2017), where radar-based IMM-JPDA is employed in a multitarget scenario, providing substantial improvement in the state estimation aspect. However, here the data association aspect still indicates room for improvement in terms of reducing computational expense by using alternative techniques. Additionally, JPDA-based tracking tends to merge tracks together when separation distance between objects are

close (Blackman, 2004). Another related work was also done by Liu et al. (2019) in using IMM with AIS for ship tracking. Although it complements UKF-JPDA's limitation in state estimation by using a multiple model system, the work was focused on single-target tracking using AIS.

Table 2. 7 Comparison of current data association algorithms

Data association algorithms	**Feature**
Nearest neighbour	Simple and straightforward, unreliable in highly cluttered environments
Neural network	converges slowly and readily falls into local minima
PDAF	Large computational burden
MHT & JPDA	Reliable with more computational efforts

2.3.3. Problems in practical USV applications

The unique environment of the water's surface makes USVs different from unmanned ground vehicles (UGVs), unmanned aerial vehicles (UAVs) and even unmanned underwater vehicles (UUVs). The current, wind and tide at the water surface could cause the USV to drift from its designed path and lead to unpredictable risks in operation. Navigation in unknown, harsh environments requires effective data processing to improve the accuracy of sensor signals. Real-time navigation with a robust and reliable system is key in the research and development process of an USV. As the basis of the system, problems may occur to the navigational sensors in practice and are analysed as follows.

- Real time positioning: Different sensors have different updating intervals. For safe operation, the navigation system should be aware of the USV's position at all times and have a real time update at short pre-set intervals. Therefore, the computational time of the navigation system must be comparatively short (Bremer et al, 2007).

- Sensor signal accuracy: Sensor measurements are not ideal and can never be fully relied on in the real world. There are many effects that introduce errors

into the sensor measurements, especially equipment limitations and environmental disturbances. For a particular USV application, water currents can have large impact on the USV's operation that should be considered when developing algorithms to improve sensor signal accuracy (Manley, 2008; Ma et al, 2014; Xia et al, 2016; Ccolque-Churquipa, 2018).

- Sensor reliability: A practical navigation system may accidentally generate unreliable navigational data for the USV during operation. In an autonomous system without human intervention, one failed sensor could result in disastrous consequences. By failing to take such a scenario into account, the USV will lose its current navigational information and the whole system may start to fail. Therefore, an effective method of detecting and recovering the failed sensor must be considered. Monitoring algorithms should also be developed to protect the whole sensor system (Caccia et al, 2008; Liu et al, 2016; Wang et al, 2018).

- Target ship detection: Obstacle avoidance is a very important feature of the autonomous USV that allows safe operation. Accurate detection of both static and dynamic obstacles is the first step towards successful obstacle avoidance. Unlike the static obstacles that can be found on existing maps, dynamic obstacles, such as target ships, should be detected and tracked by own ship to avoid possible collisions. As a primary device for detecting obstacles, marine Radar can only detect the distance between the obstacle and the USV. AIS data is more reliable and provides more extensive information regarding the target ship, albeit an AIS transponder is not equipped on every ship. Therefore, a combination of the two sensors could provide a complementary solution to detect a dynamic target ship (Liu et al, 2018; Wang et al, 2018)).

Most of the current research in USV navigation focuses on using variant filtering techniques to fuse raw sensor measurements without considering practical uncertainties associated with sensors themselves and varied environments (Xia et al, 2016; Mousazadeh et al, 2018; Ccolque-Churquipa et al, 2018; Wang et al, 2018). There is a knowledge gap in developing a practical autonomous navigation system to address the above practical problems in real-life USV developments.

2.4. Summary

This chapter reviews a number of different USV projects. The development of USVs has grown rapidly in recent decades and has increased demand for the development of effective and robust autonomous navigation systems. The capabilities of current navigation systems for commercial and academic USVs are still limited. After reviewing the mainstream modern electronic navigation methods, it has been demonstrated that the use of multiple sensors plays a vital role in designing an accurate and robust navigation system. Such systems should not only provide accurate position data of USV but should also include the feature to perceive the surrounding environment. The problems that may be encountered during the development have been proposed with suitable solution techniques. They are discussed in details in the following chapters.

Chapter 3. Practical Navigation Sensor System

With the benefit of the advances of navigational devices such as the GPS and other marine electronic navigational aids, essential navigational data, such as position, velocity and heading of an USV can be measured to a reasonably high degree of accuracy for relatively low capital investment. The literature review identified that there was a gap in developing a practical autonomous navigation system to address the practical problems in Section 2.3.3 regarding real-life USV developments. This chapter first introduces the navigation sensor system of a practical USV called *Springer*. Then a practical, cost-effective and universally competitive on-board navigation sensor system for USV navigation has been designed and implemented to extract practical sensor data so that data fusion algorithms can be further developed to fill this technology gap.

3.1. The *Springer* USV

UCL and Plymouth University have a collaboration program to jointly explore the improvement of the autonomous navigation system of a practical USV, *Springer*. The *Springer* USV, developed by Marine and Industrial Dynamic Analysis Research (MIDAS) group (now known as Autonomous Marine Systems Research Group) from the Department of Marine Engineering, Plymouth University, is a double hull designed USV as shown in Figure 3.1. Each hull carries a watertight Pelican case to house electronic equipment. The navigation sensor hardware system is housed in the Pelican case on the starboard side. It originally contained three electronic compasses, which are not themselves waterproof, together with a hosting computer. A low cost water-proof GPS receiver is connected to the system on the mast outside the Pelican case. Two motors are mounted at the stern, one on each hull, and the *Springer*'s manoeuvring is achieved by independent and differential control of the speeds of each motor (MIDAS Group, 2014; Sutton et al. 2011).

Figure 3.1 *Springer* USV developed by MIDAS group from Plymouth University

The main research of the navigation system of the *Springer* USV was estimating accurate heading information by electronic compasses to guide the USV on way-point tracking missions. (Motwani et al. 2013; Motwani et al. 2014). In an electronic compass, the magnetic field sensor is the core. The principle of magnetic sensors is based on the measurement of the Earth's magnetic field. The Earth's magnetic field, generated by the core of the Earth, flows out of the magnetic South Pole and back in through the magnetic North Pole. The Earth's magnetic field therefore has a component parallel to the Earth's surface that always points toward the magnetic North. By resolving this component, the direction of the magnetic sensor with respect to the magnetic North can be determined (Caruso, 1997). Today, there are various types of electronic compass available. The most commonly used magnetic field sensors for electronic compasses are based on the anisotropic magneto resistive (AMR) effect, on the fluxgate effect or on magneto inductive effect (Racz et al. 2004). Three independent electronic compasses each using different working principles, TCM2, HMR3000 and KVH C100, were employed by the *Springer* to provide raw heading measurements.

- The TCM2 compass is based on the magneto-inductive effect. It combines a two-axis inclinometer to measure the tilt and roll (PNI, 2014).
- The HMR3000 compass uses the Anisotropic Magneto Resistance (AMR) effect; it includes three perpendicular sensors and a fluidic tilt sensor to provide a tilt-compensated heading (Honeywell, 2014).
- The KVH C100 compass is a flux-gate compass that offers modules incorporating both rate gyros that compensate for error from acceleration, as well as inclinometers that provide accurate readings of heading, pitch, and roll (KVH, 2014).

Table 3. 1 Compasses Specifications

Compass Model	**TCM2**	**HMR3000**	**KVH C100**
Dimension (mm)	73.5*50.8*32.75	74.9*30.5*25.0	114.0*46.0*28.0
Weight (kg)	0.0454	0.0213	0.0638
Baud Rate	38400	1200-19200	300-9600
Voltage (VDc)	+5	+12	+5
Current (mA)	15-20	35	30
Frequency (Hz)	1-30	20	1
Accuracy (°RMS)	±1	±0.5	±0.5
Manufacturer	PNI	Honeywell	KVH Industries

The TCM2 compass is of simple design with low operating power, however it is very sensitive to electrical and environmental disturbances. The AMR compass HMR3000 can output accurate heading information, but it has greater power consumption. Among these three compasses, the flux-gate compass KVH C100 is the most accurate with disturbance resistant capability.

Raw GPS signals from the BU353 GPS receiver were used to locate the *Springer* when conducting the missions. A small size fan-less general purpose PC, the Intense PC pro, was chosen to extract raw measurement data from each sensor. The measurements and errors of the sensors employed are listed in Table 3.1 and the

original hardware system inside the starboard-side Pelican case is shown in Figure 3.2.

Table 3. 2 *Springer* navigational sensors and their measurements and errors

Sensors	**Measurements**	**Error**
TCM2 electronic compass	Heading	1° RMS
HMR3000 electronic compass	Heading	0.5° RMS
KVH C100 electronic compass	Heading	0.5° RMS
BU353 GPS receiver	Longitude/latitude	Up to 5 m 2D

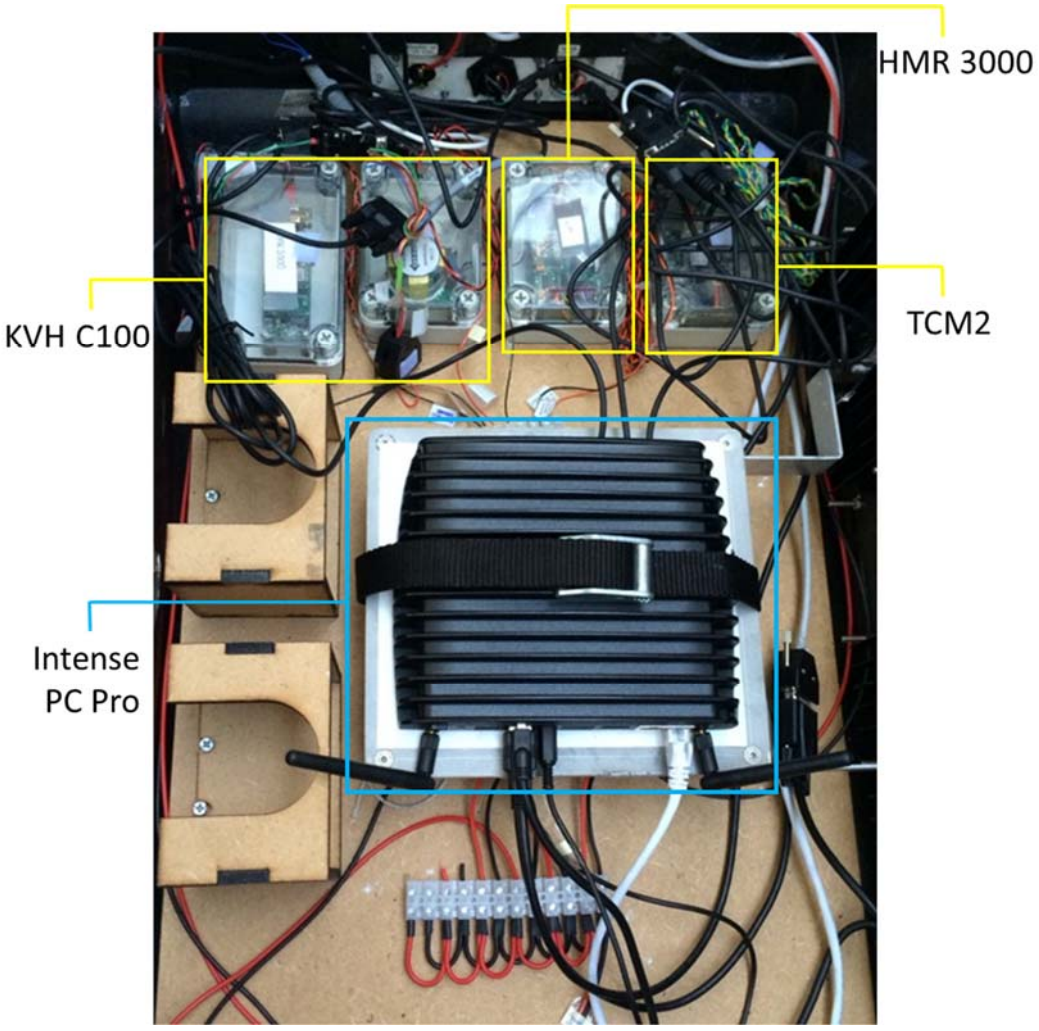

Figure 3.2 Inside system of the peli-case on the starboard-side of the *Springer* USV

The aim of the cooperation program was to improve the performance of the existing navigation and guidance system. A low cost gyroscope chip from Tinker kit has been integrated to the system to measure the angular velocity of the

Springer USV that was fused with absolute sensor measurements obtained from the three electronic compasses to improve their measurement accuracy (Liu et al, 2014). The gyroscope chip generates voltages that are proportional to the angular velocity while moving. A microcontroller board called Arduino Mega 2560 was employed so that the hosting computer can read the measurements of the gyroscope via serial a communication link. The connection of the gyroscope chip and the microcontroller is shown in Figure 3.3 and the schematic drawing is shown in Figure 3.4. The signal pins of the gyroscope chip are connected to the analogue pins on the Arduino board so that the Arduino could convert the analogue signal to the angular velocity.

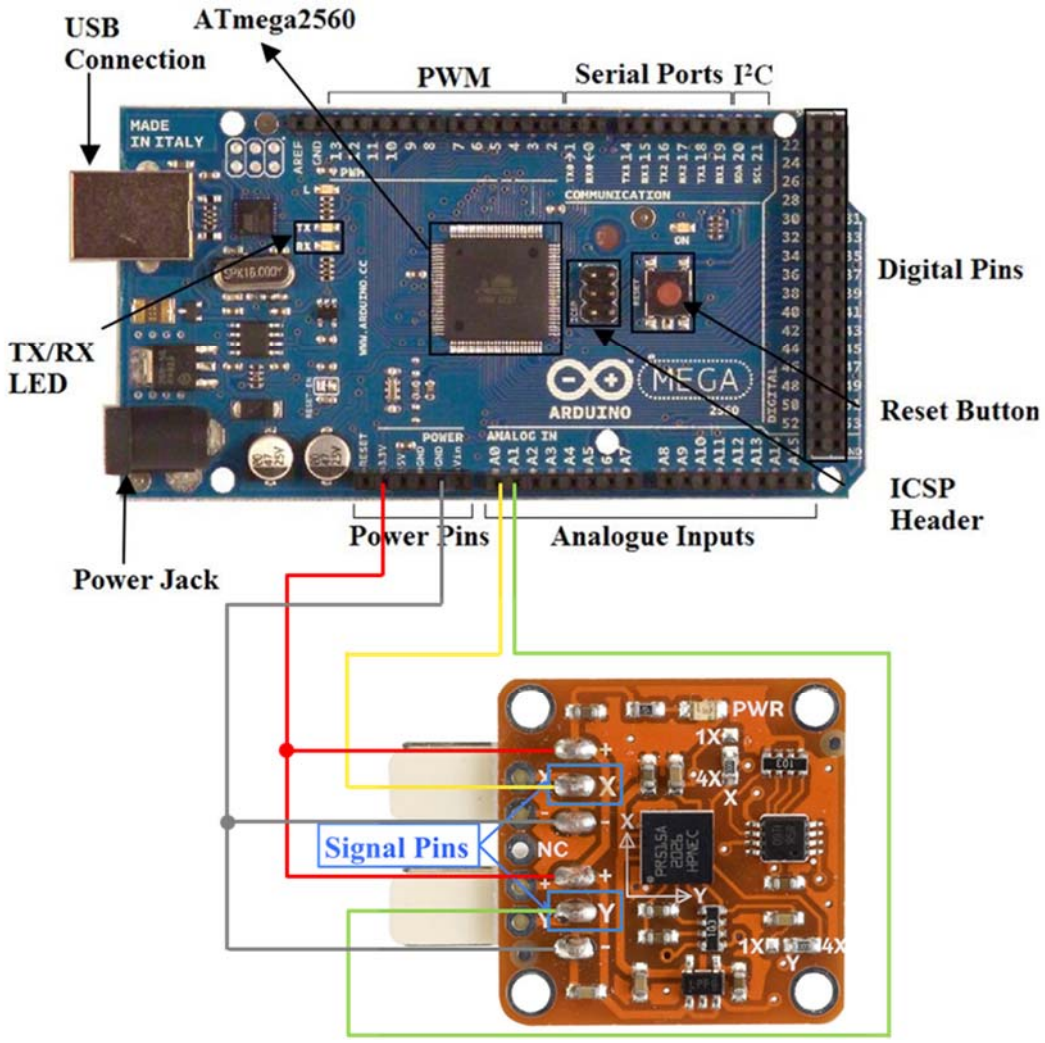

Figure 3.3 Connection of Arduino Mega 2560 and TinkerKit gyroscope chip

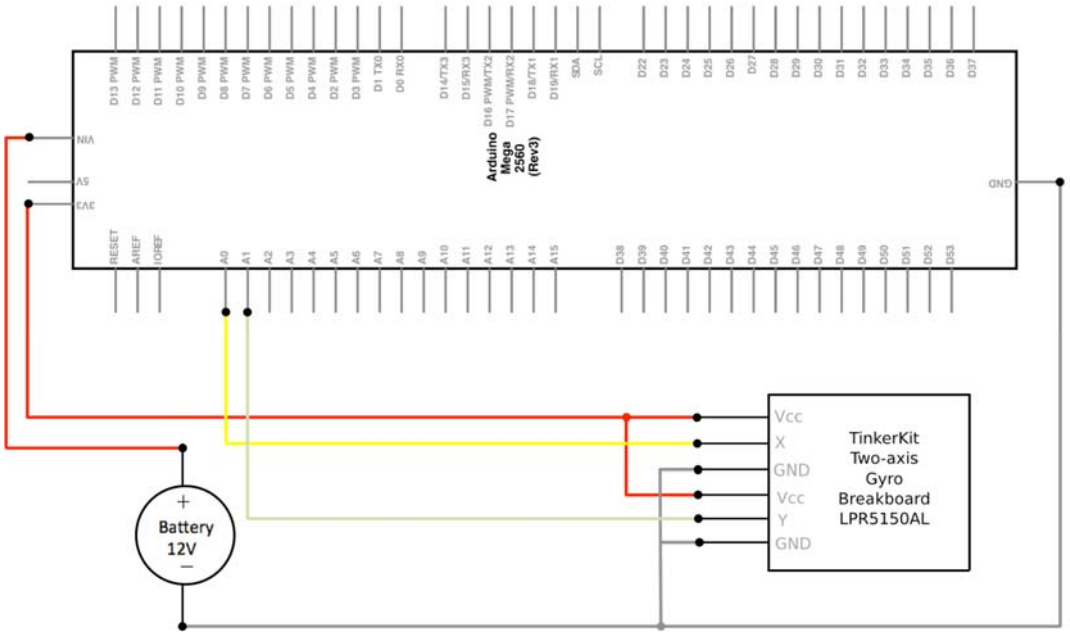

Figure 3. 4 Schematic Drawing of the Arduino/Gyro Connection

After the implementation of the hardware and software connections of the integrated navigation sensor system, several trials were carried out to validate the performance of the improvement. The details of the trials and results will be presented in Chapter 6.

3.2. Proposed navigation sensor system

For an unmanned surface vehicle like the *Springer* USV, a number of sensors are included in its navigation sensor system, which require a navigation processor to acquire and process the raw sensor measurements. The navigation processor normally runs on an on-board hosting platform, such as a computer that can be exploited for its adaptability and high computational processing capability. Modern navigational sensors, such as a GPS receiver and an electronic compass are normally employed to provide the absolute measurements of a vehicle's positions, velocities and headings throughout its operation. Inertial Measurement Units (IMUs) that are composed of both accelerometer and gyroscope are used to measure a vehicle's motions (Appriou, 2014; Maklouf et al, 2013; Yang et al, 2018). A marine Radar and an Automatic Identification System (AIS) module are commonly employed to perceive the surrounding environment in maritime applications (Yang et al. 2013; Habtemariam et al. 2014). The combination of

various on-board sensors and a hosting platform form a typical yet complete navigation sensor system for an USV as shown in Figure 3.5.

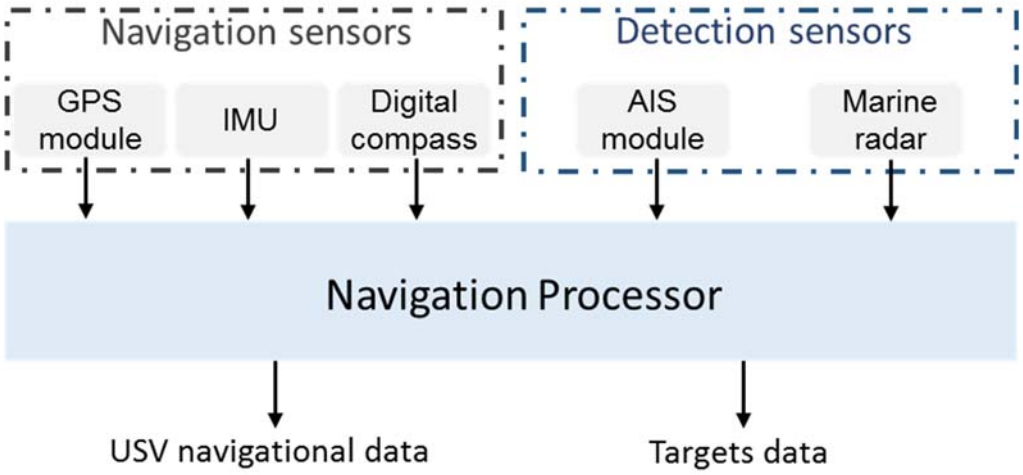

Figure 3.5 Navigation sensor system

Similar to the *Springer* USV, typical USVs are of small size and relatively light weight (Clearpath Robotics, 2018; Pearson et al, 2014; ASV Global, 2018). Therefore, compact sized sensors and a main control unit with relatively low power consumption are ideal for the navigation sensor system. A low cost and low power consumption hardware system has been proposed as a practical navigation sensor system in this section. A set of hardware constraints are applied when designing the system as referenced to the *Springer* USV. Low cost navigational sensors with encapsulated packaging are employed rather than PCB chips for reduced complexity in hardware implementation and better waterproofing features. The processing rate of the navigation processor needs to be high enough such that it is able to run a main loop for the raw sensor data extraction and conversion within the predefined sampling time. The details of each component of the proposed navigation sensor system are demonstrated in the following sections.

3.2.1. Navigation processors

The main function required of a navigation processor is extracting valuable data from sensor signals and communicating with the control PC so as to achieve autonomous navigation in real time. When installed on a practical USV for operations on the water, the whole sensor suite needs to be housed in a waterproof case that may be without adequate airflow. This could lead to issues allied to a

limited ability to dissipate the heat generated by the electronic devices. Therefore, with consideration towards the reduction of power consumption and cost, a single board computer (SBC), with high computational efficiency running a dedicated embedded software program, is chosen over an expensive computer as the hosting platform. An SBC is a microprocessor with a number of programmable communication interfaces that allow connection to peripheral functions. It also brings benefits such as small size and light weight to a modular system. Embedded processors are special-purpose devices that are a combination of hardware and software. The general definition of the embedded systems is that they are standalone computing devices and are usually designed to perform limited but specific computing functions reliably, securely and often with real-time computing constraints while minimising the equipment costs (Kamal, 2003). Advantages of an embedded system include reliability, stability, modularisation, low cost, low power consumption and minimum maintenance. (Ma et al. 2006).

PandaoBoard ES is a low-cost, low-power SBC development platform that allows users to develop applications using its hardware and software. It integrates an OMAP4460 system on a chip that is widely used in wireless mobile applications. The OMAP4460 contains a dual-core ARM Cortex-A9 MPCore CPU clocked at 1.2 GHz, and a 384 MHz PowerVR-SGX540 GPU, which meets the hardware constraints of the proposed system. According to Pang (2011), the energy efficiency of the ARM processor of the PandaBoard ES is eight times that of an Intel CPU's energy consumption. Using the OMAP4460 processor, which provides high calculation efficiency, the PandaBoard ES can support high-level operating systems such as Android, Windows^{TM} CE and various versions of Linux. As shown in Figure 3.6, in addition to the OMAP4460 processor, there are other major components, such as the TPS62361 switching power supply, HDMI connector, and two USB host ports together with one USB on-the-go port, supporting USB 2.0. A wired 10/100 Ethernet as well as wireless local area network (WLAN) and Bluetooth connectivity are also equipped on the PandaBoard ES. These high specifications of the PandaBoard ES ensure that the board satisfies the computing requirement of a navigation platform. In addition, it is also a device of relatively small size at about 114.3 x 101.6 mm and light weight at 74g (Farnell, 2014).

PandaBoard ES also has the advantages of vibration and shock resistance to ensure a stable and reliable on-board navigation sensor system for the USV's operation.

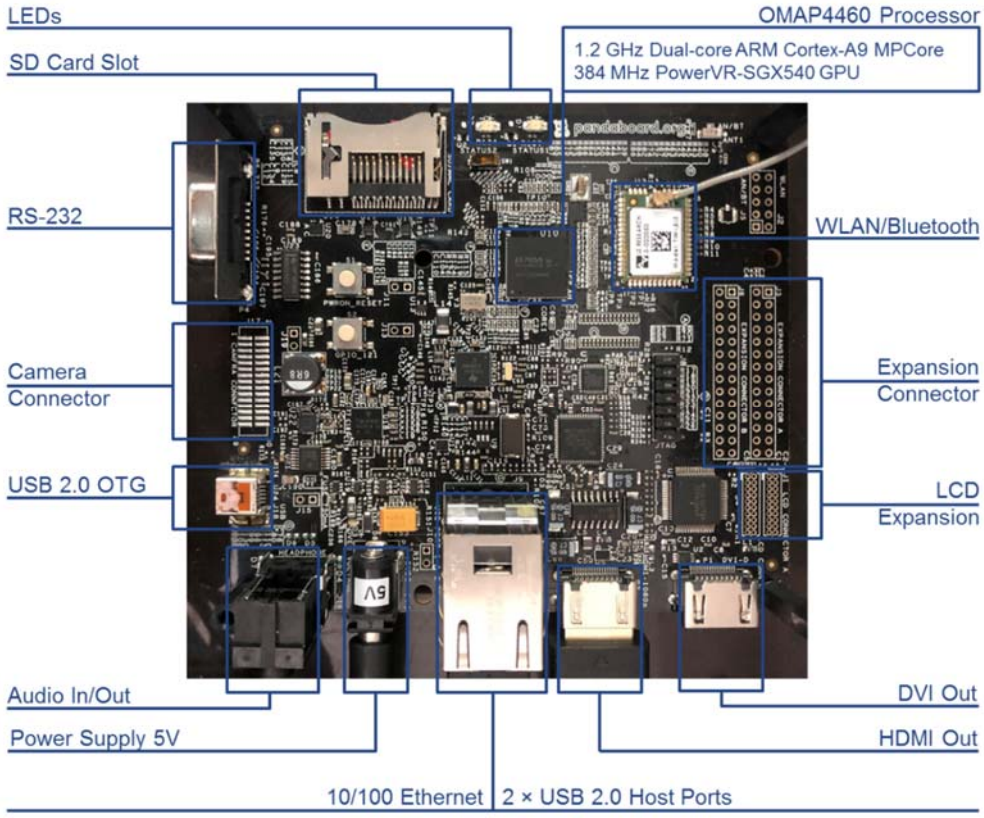

Figure 3.6 PandaBoard ES Layout

3.2.2. Navigational sensors

For a more comprehensive navigation sensor system than that on the *Springer* USV, real-time position estimations should also be included in the development of the navigation sensor system. Learning from the joint program of the *Springer* USV's improvement, an electronic compass and a GPS receiver are able to provide absolute measurement of an USV's headings and positions. An inertial measurement unit that measures both the USV's acceleration and rotation rate can be integrated to accomplish the hybrid compensation system to provide more accurate and robust navigational data. The ability to detect dynamic target ships in the surrounding environment could further enhance the practicability of an USV. This section provides details of employed navigation and detection sensors and their error modelling for future development of data fusion algorithms.

3.2.2.1. GPS receiver

As shown in Figure 3.7, GPS satellites circle the earth twice per day in very precise orbits and transmit two low power radio signals to earth, designated L1 and L2. Civilian GPS uses the L1 frequency of 1575.42 MHz in the UHF band (Darrozes, 2016).

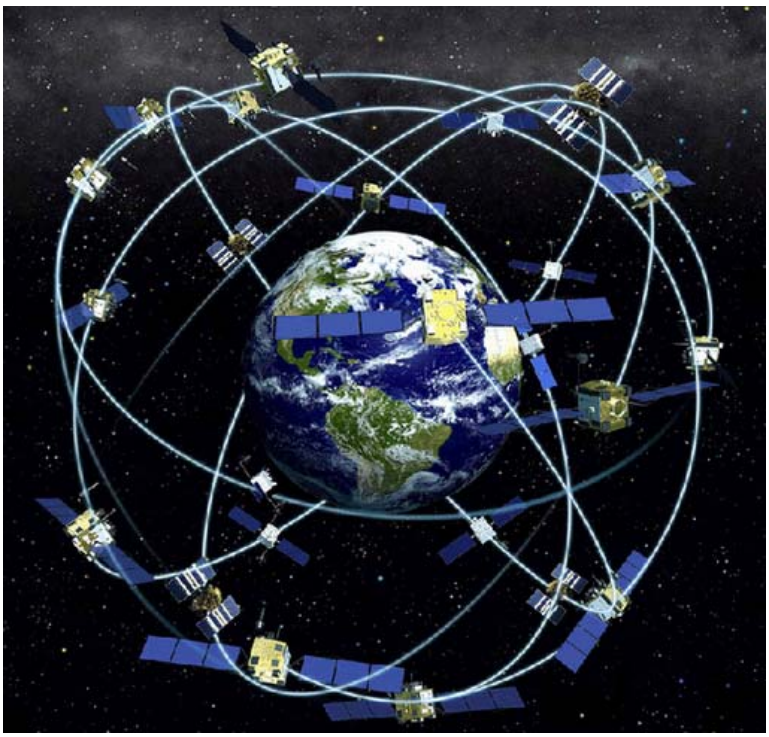

Figure 3. 7 The orbits of GPS satellites (Source: Howell, 2013)

In the navigation sensor system of the *Springer* USV, the BU-353 S4 by USGlobalSat (Figure 3.8) is used to provide raw measurements of its latitude and longitude. It is a low cost, waterproof GPS receiver based on the SiRF Star IV using the L1 frequency. The SiRF Star IV, developed and manufactured by SiRF Technology Inc., is able to provide continuous location updates with a signal augmentation system. The BU-353 S4 completes the sensor design with a universal USB interface and an integrated highly sensitive GPS aerial to the SiRF Star IV chip to maximise reception quality. In addition, the whole package of the GPS receiver is compact with a diameter of only 53mm, thickness of 19.2mm, and weight of 62.37g. (USGlobalSat Inc., 2016).

Figure 3. 8 GPS BU353 S4 receiver

The BU353 S4 supports several types of NMEA 0183 sentences that provide absolute measurements of its latitude and longitude. The extraction and the conversion of the latitude and longitude to the coordinates in the designed navigation frame are demonstrated in Appendix B.

Table 3. 3 Common errors of GPS signals

Error type	**Description**	**Margin of error**
Receiver clock error	Receiver's built-in clock has slight timing error with the atomic clocks on-board the GPS satellites	3-10 m
Number of satellites visible	GPS signal travels Line of Sight, less satellites leads more errors	5 m
Satellite geometry	When the satellites are located at wide angles relative to each other, the GPS accuracy is high	5 m
Signal multipath	Signal can be reflected off surfaces during transmission, which increase travel time and cause errors in distance	5 m
Ionosphere effects	Signal may be attenuated as it travels through the charged plasma of ionosphere	5-10 m
Troposphere delays	Signal may be changed slightly when passing through the water particles in the upper atmosphere	2 m

The absolute measurements are associated with random noises, which are described as Rooted Mean Square (RMS) errors in the sensor manuals. RMS error indicates that at 68% probability the measurement lies within the range of the error from the true position and twice the range at 95% probability. The Table 3.3 lists the common errors that impact on the accuracy of GPS signals (McWilliam et al. 2005). Therefore, the sensor model of the GPS receiver can be defined with an additive random noise component as following:

$$p_o = p_i + v_g \tag{3.1}$$

where p_i is the true position; p_o is the noisy measurements; and v_g is the uncertainty normally distributed with the standard deviation of its RMS error value r_g.

3.2.2.2. Inertial Measurement Unit

Although raw GPS measurements were used to determine *Springer's* positions in the trials of the cooperation program, an IMU called ArduIMU V3 from Sparkfun was also integrated into the *Springer* navigation sensor system for further development. The ArduIMU V3 is a low cost, smart orientation solution that measures a vehicle's acceleration and angular velocity and its outputs can be read via the serial communication. Unlike the TinkerKit gyroscope chip that requires an additional Arduino board in the *Springer* navigation sensor system, the ArduIMU V3 is a complete module that incorporates motion processing unit, MPU-6000 together with an ATmega328 microprocessor itself as shown in Figure 3.9. Its size is only 38.1 mm * 25.4 mm. The MPU-6000, which consists of three embedded 3-axis MEMS (Micro Electro Mechanical System) gyroscopes, a 3-axis MEMS accelerometer and a 3-axis magnetometer, is widely used for mobile communication handsets and other portable applications. According to Faulkner et al., 2002, Micro Electro Mechanical System (MEMS)-based sensors exploit the benefits of high volume manufacturing techniques, flexible and rugged packaging options, which provides cost effective and small sized sensors. The gyroscopes in the MPU-6000 detect rotation along the x, y and z axes of its inertial frame. When the gyroscope is rotated, vibration caused by the Coriolis Effect is first detected by a capacitive pickoff. The resulting signal is then amplified, demodulated, and filtered to produce a voltage output. This voltage output is proportional to the

angular rate and will be digitised using an individual on-chip 16-bit Analog-to-Digital Converter (ADC). In terms of the accelerometer, it uses separate proof masses for each axis. The acceleration induces a displacement on the proof masses and each displacement is detected differentially by a corresponding capacitive sensor . The scaling factor is calibrated at the factory and is independent of supply voltage. The ATmega328 microprocessor processes the voltages generated by both gyroscope and accelerometer and outputs associated measurements at 20Hz (Ardu-imu, 2014).

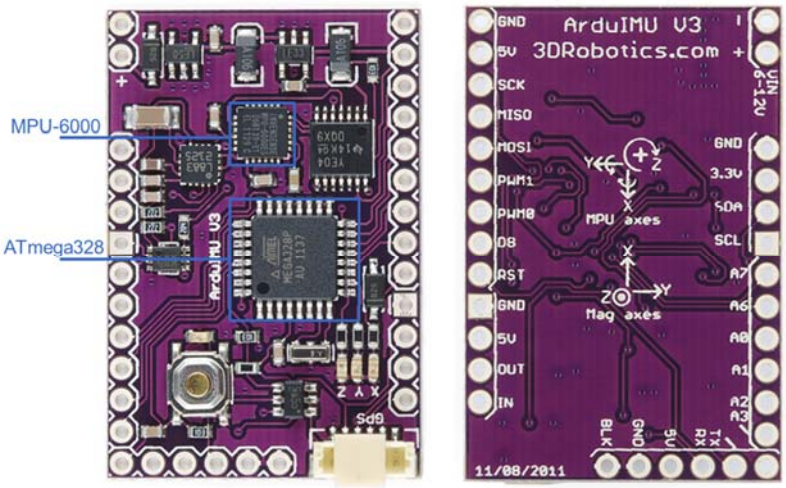

Figure 3. 9 ArduIMU V3 from Sparkfun

The MEMS inertial sensors are sensitive to dynamic changes and vibrations. Inertial sensors are often subject to bias, scale factor, and cross-coupling errors with the former two being the major sources of the error. The inertial sensor bias is defined as the average over a specified time of the sensor output measured at specified operating conditions that are independent of input acceleration or rotation (IEEE Std 528-2001, 2001). A scale factor is the ratio of a change in output to a change in the input to be measured. Both errors include some or all of the following components: fixed terms, temperature induced variations, turn-on to turn-off variations and in-run variations (Titterton et al., 1997). The fixed component of the error is present when the sensor is turned on and can be predicted. A large fraction of the temperature induced variations can be corrected with suitable calibration. The turn-on errors vary from sensor turn-on to turn-on but remain constant without powering off. They can be obtained from laboratory calibrations or estimated during the navigation process. The in-run random errors

are unpredictable and vary throughout the periods when the sensor is powered on. As a result, the in-run random errors cannot be removed from measurements using deterministic models and should be modelled by a stochastic process such as a random walk process or a Gaussian Markov process (Farrell, 2005). The cross-coupling error is the error due to sensor sensitivity to inputs about axes normal to an input reference axis (IEEE Std 528-2001, 2001). For low-cost MEMS inertial navigation systems, the cross-coupling error is relatively small and negligible compared to other sources of errors. As a result, the bias has the largest impact on the INS navigation performance.

The measurements of the inertial sensors therefore contain a random noise component and a constant bias, which can be modelled as Equation 3.2 and Equation 3.3.

$$a_o = a_i + b_a + w_a \tag{3.2}$$

$$\omega_o = \omega_i + b_g + w_g \tag{3.3}$$

where a_o & ω_o are raw sensors readings, a_i & ω_i are the true acceleration and true rotation, respectively, b_a & b_g are the constant bias errors and w_a & w_g are the random noise. Both the accelerometer and the gyroscope are associated with a constant bias factor, which can be estimated by a calibration process prior to testing. The process is demonstrated in detail in Appendix B. But the estimated bias component cannot be removed due to the sensitivity of the MEMS sensors.

3.2.2.3. Compass

Comparing the three independent electronic compasses with different working principles in the navigation sensor system of the *Springer* USV, the fluxgate compass KVH C100 outperformed the other two electronic compasses. However, the KVH C100 is not itself waterproof. Therefore, a low cost, waterproof electronic compass, the HSC100 electronic compass sensor from Digital Yacht (Figure 3.10), is employed in the proposed navigation sensor system. It can be placed outside the sensor box, thus the effects of the magnetic fields generated by other electronic devices can be reduced. It is also a fluxgate compass and is of similar working principle to *Springer's* KVH C100. It is a complete package and weighs about 0.12 kg. The centre of the HSC100 is a fluxgate compass with a ring style core,

which helps concentrate the magnetic field being measured. The core is magnetically saturated in opposing directions along two axes x and y respectively using an excitation coil driven by a sine or square waveform. Before saturation, the ambient field is conducted through the core producing a high flux. When saturation occurs, the flux will collapse. During the next half cycle of excitation, the core recovers from saturation and the flux returns to a high level until the core saturates in the opposite polarity. This cycle iterates the process while operating. A sense coil placed around the core detects these flux changes by means of induced voltages indicating flux collapse or recovery. The compass measures direction in terms of an electric current, and this current is used as a signal to be translated by other electronic devices. It also features an automatic calibration mode. According to the installation and quick start guide of the HSC100 compass sensor, general accuracies can be achieved to within 0.5 degrees after automatic calibration. It can tolerate up to a 45 degree gimbaled angle when the USV rolls and pitches on the water surface.

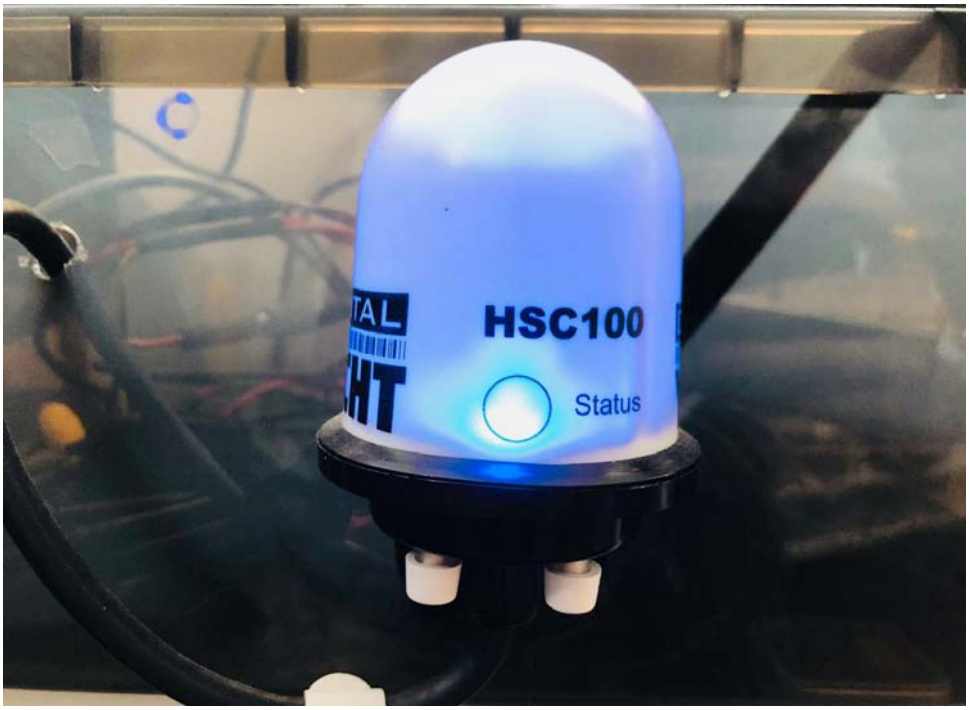

Figure 3.10 HSC100 electronic compass by Digital Yacht

The major magnetic measurement error results from the distortion of the Earth's magnetic field by nearby ferrous effects, sensor noise and magnetic interference. In practical applications, compasses are mounted in vehicles and platforms that usually have ferrous materials nearby. These nearby ferrous materials will generate

permanent magnetic fields (hard irons) or varying magnetic fields (soft irons) to distort the Earth's magnetic field (Caruso, 1997). Soft irons affect the magnetometer output by varying amounts depending on the compass orientation. This varying bias effect will distort the shape of the 2D magnetic field locus from a circle into an ellipse. Hard and soft iron distortions are the major error sources for magnetic compasses and compensating for these effects is essential to their application (Langley, 2003). Normally, a calibration process is conducted to remove the bias after installation since the bias is constant without change of installation environment. In a similar manner to the GPS module, the electronic compass also provides absolute measurements of vehicle's headings with an additive random noise that can be expressed as Equation 3.4.

$$\psi_o = \psi_i + \nu_h \tag{3.4}$$

where ψ_i is the true heading; ψ_o is the noisy measurement and ν_h is the uncertainty with a normal distribution with the standard deviation of the compass's RMS error value r_h.

3.2.2.4. Automatic Identification System

A practical USV that is designed to conduct missions over the sea should also have that ability to perceive its surrounding environment for safe operation. The *Springer* USV is still in the early stage of its development, therefore detection sensors such as marine Radar and AIS are not included in its navigation sensor system. AIS is an automatic tracking system that is employed by both mariners and the vessel traffic services (VTS) for identifying and locating surrounding vessels. The AIS signal normally provides static, dynamic, voyage related and short safety information. Static information, such as the ship's call sign, name and its Maritime Mobile Service Identity (MMSI) is permanently stored in an installed AIS transponder. Dynamic information that contains the ship's position, speed and course, is collected from the ship's own navigational sensors, e.g. GPS receivers, speed log and electronic compasses. Voyage related information that includes the ship's destination, cargo type, etc. is inputted at the beginning of the voyage (Lin, et al. 2008). As AIS is an intermediary to transmit navigational data obtained by on-board sensors' measurements (mainly GPS), its accuracy can be assumed to be similar to a conventional GPS receiver and its measurement modelling can be

expressed as Equations 3.5 to 3.7. However, AIS cannot be used in isolation to detect dynamic obstacles as it only works with ships that are equipped with an AIS transponder (Lloyd's List Intelligence, 2017; IMO, 2019).

$$p_{Ao} = p_{Ai} + \nu_{Ap} \tag{3.5}$$

$$v_{Ao} = v_{Ai} + \nu_{Av} \tag{3.6}$$

$$\varphi_{Ao} = \varphi_{Ai} + \nu_{A\varphi} \tag{3.7}$$

where p_{Ao}, v_{Ao} and φ_{Ao} are the position, velocity and course of the detected vessel obtained from AIS signal, respectively; p_{Ai}, v_{Ai} and φ_{Ai} are the true position, velocity and course of the detected vessel, respectively; and ν_{Ap}, ν_{Av} and $\nu_{A\varphi}$ are the uncertainties that are normally distributed within the standard deviation of the AIS's RMS error value r_{Ap}, r_{Av} and $r_{A\varphi}$, respectively.

3.2.2.5. Marine Radar

Radar is a device that measures the distance and bearing of the surrounding obstacles relative to the vessel with Radar onboard. The principal of Radar is similar to sound-wave echo reflection. The Radar set transmits the electromagnetic wave pulse and receives returns (reflections) from the reflecting object. A portion of the radio-frequency (RF) energy is reflected and the returned pulse is detected by the Radar set. This reflected pulse is called a return. Radar sets use the return to determine the direction and distance of the reflecting object (Brattebo, 2014; Bole et al. 2005). Figure 3.11 illustrates the main components of a typical Radar set.

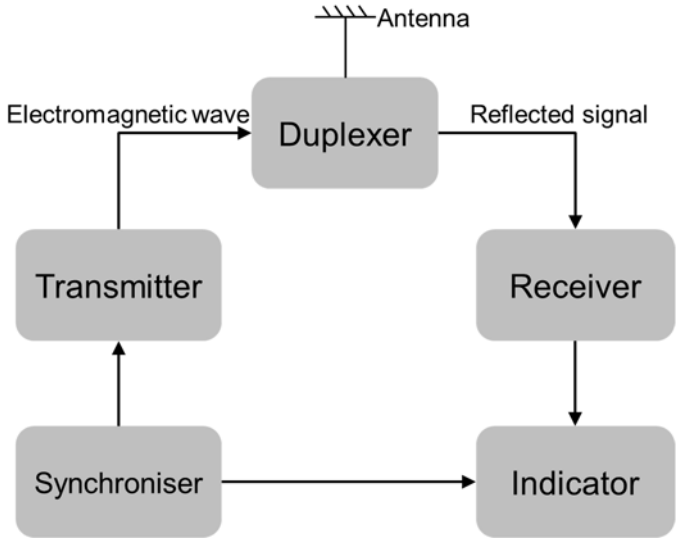

Figure 3.11 Radar set and fundamental components

The main components are described below:

- The SYNCHRONISER supplies the synchronising signals of the transmitted pulses, the indicator, and other associated circuits.
- The TRANSMITTER generates electromagnetic energy in the form of short, powerful pulses.
- The DUPLEXER allows the same antenna to be alternately switched between transmitting and receiving modes.
- The ANTENNA routes the electromagnetic energy from the transmitter, radiates it in a highly directional beam, receives any returning echoes, and routes those echoes to the receiver.
- The RECEIVER amplifies the weak RF signal returned from the reflecting object and generates video pulses as the output.
- The INDICATOR presents a visual indication of the return pulses to the observer with relative positions of the targets.

The index error, beamwidth error and attenuation error affect the accuracy of Radar's measurements (Rohde & Schwarz, 2012). These errors bring a random noise component of the raw Radar measurements and the sensor's measurements can be modelled as Equations 3.8 to 3.11.

$$d_{Ro} = d_{Ri} + \nu_{Rd} \tag{3.8}$$

$$B_{Ro} = B_{Ri} + \nu_{RB} \tag{3.9}$$

$$v_{Ao} = v_{Ai} + \nu_{Av} \tag{3.10}$$

$$\varphi_{Ao} = \varphi_{Ai} + \nu_{A\varphi} \tag{3.11}$$

where d_{Ro} and B_{Ro} are the range and bearing to the detected vessel, respectively; v_{Ro} and φ_{Ro} are the measured velocity and course of the detected vessel, respectively; d_{Ri} and B_{Ri} are the true range and bearing to the detected vessel, respectively; v_{Ri} and φ_{Ri} are the true velocity and true course of the detected vessel, respectively; and ν_{Rd}, ν_{RB}, ν_{Rv} and $\nu_{R\varphi}$ are the uncertainties that are normally distributed within the standard deviation of the Radar's RMS error value r_{Rd}, r_{RB}, r_{Rv} and $r_{R\varphi}$, respectively.

Most of the early marine Radar models are too expensive and large in size so that they were not included in the initial development of USVs. With the development of the technology, lower cost and smaller sized Radar are available for unmanned vehicles. The main advantage of marine Radar is its capability to detect obstacles in all environments at relatively long range, which enables vessels to operate safely at sea. However, the accuracy of Radar measurements is relatively low when compared with AIS data. It may suffer from beam width error, attenuation error, double or multiple echoes and indirect wave error. Therefore, multiple sensors need to be integrated to provide more accurate and continuous estimations of a target ship's position (Xu et al., 2017; Kalsen et al. 2015).

In summary, functionality of each sensor employed by the proposed navigation sensor system and their RMS errors are outlined in Table 3.4. The value of the sensor noise will be used in the simulations throughout Chapter 4 to Chapter 7.

Table 3. 4 Employed and simulated navigational sensors and their measurements with errors

Sensor	**Measurement**	**Noise**	
		Bias	**Variance**
IMU	Acceleration a_x	$0.03\ m/s^2$	$0.0042\ m/s^2$
	Acceleration a_y	$0.02\ m/s^2$	$0.0042\ m/s^2$
	Rotation rate ω	$0.28\,°/s$	$0.036\,°/s$
GPS	Position p_x	-	$8m$
	Position p_y	-	$7m$
Electronic Compass	Heading ψ	-	0.5°
AIS (Simulated)	Position p_A	-	$0.01\ nautical\ mile$
	Speed v_A	-	$0.07\ knot$
	Course φ_A	-	0.5°
Marine Radar (Simulated)	Range d_R	-	$0.05\ nautical\ mile$
	Bearing B_R	-	1.2°
	Speed v_R	-	$0.013\ knot$
	Course φ_R	-	1°

3.3. Implementation of the proposed system

3.3.1. Hardware Connections

In this section, a practical hardware system has been implemented using the sensors detailed in Section 3.2 to obtain and convert raw sensor measurements to a pre-designed navigation frame so that they can be used in a data fusion system. Practical AIS module and marine Radar are not included since their measurements are not useful inland and they will be simulated in this research.

The BU353 S4 GPS receiver, the ArduIMU V3 IMU and the HSC100 electronic magnetic compass, that all support USB interfaces, are integrated in the proposed navigation sensor system. The embedded Linux board, PandaBoard ES, which is capable of supporting USB and RS232 serial interfaces, is used to connect to all the aforementioned navigational sensors. Therefore, working as the on-board hosting platform, the PandaBoard ES's tasks include interfacing to each sensor, acquiring and converting each sensor's raw measurements and communicating with the monitoring control computer.

The connections of the hardware system are illustrated in Figure 3.12. The on-board navigation sensor suite is composed of on-board navigational sensors, a navigation processor, as well as complimentary accessories, such as Liquid Crystal Display (LCD) screen and the battery. The on-board sensors, including a GPS module, an IMU module and an electronic compass, are connected to the PandaBoard ES via serial communication ports. Digital interfaces are required to enable the hosting platform to access the navigational sensor measurements. The control PC is the interface used to monitor on-board sensor measurements and runs the developed data fusion and path planning algorithms. The communication between the control PC and on-board hosting platform employs the wi-fi, 2.4 GHz 802.11b/g/n protocol due to its longer working range and more stable signal transmission. The software design to achieve the connections is demonstrated in the next section.

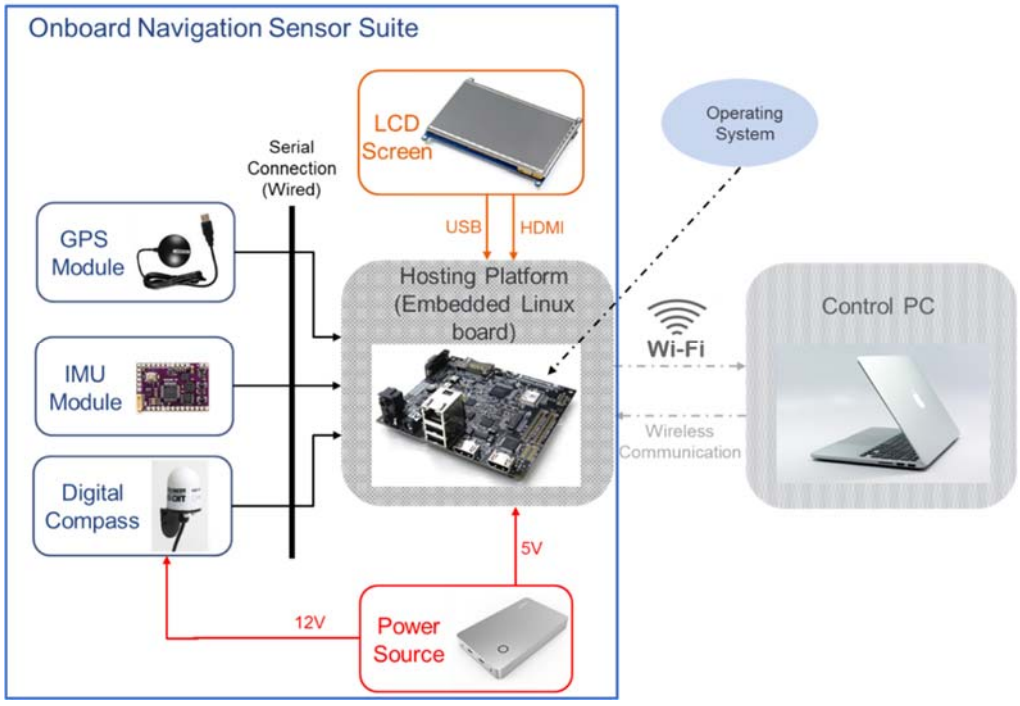

Figure 3. 12 Hardware installations

3.3.2. Software connections

With a variety of navigational sensors that have different functions and different sampling rates on-board the USV, the navigation sensor system needs to be capable of synchronising all the sensors, acquiring different sensor measurements, and processing the measurements for further use. As mentioned, the PandaBoard ES features an OMAP4460 processor that supports Linux kernel, therefore embedded Linux has been used to perform these assigned tasks. Embedded Linux is a general term for using Linux kernel and various open source components in embedded systems (Bootlin, 2017). Embedded Linux has the advantages of reduced power consumption and increased processing speed. The embedded Linux system has five generic properties: Diskless media for booting and storage, lack of BIOS, footprint (500 KB) and runtime memory restrictions, memory management and dedication to a small number of tasks (Tucker, 2015). Like desktop computers, some embedded Linux systems are now adopting graphical user interface (GUI) rather than text-based interface, such as ARM Ubuntu. Ubuntu, the most widely used Linux operating system, releases several distributions that support various ARM processors. For PandaBoard ES, there is an Ubuntu 12.04 release for the Texas Instruments OMAP4 processor that delivers a desktop with GUI and supports

various programming languages such as C, Python, Java, etc., which makes it easier to design the on-board software to meet the system requirements.

From Figure 3.6, it can be seen that the PandaBoard ES has two USB 2.0 interfaces that could connect to navigational sensors. The on-board software should have the ability to communicate with the connected sensors for incoming sensor signals, which are called the digital interfaces. The digital interfaces have been built based on Java according to the formats of the sensor outputs described in Section 3.2. PandaBoard ES also features the Tiwi-BLE WLAN/Bluetooth transceiver that provides a Bluetooth interface and a 2.4 GHz WLAN 802.11b/g/n interface, where 802.11 is the IEEE Wi-fi Standard. Therefore, wireless connectivity between the on-board hosting platform and the offshore control computer can be established using Wi-fi by building a wireless base station, called an access point (AP).

In the ARM Ubuntu operating system, a user space daemon called Hostapd can be used to create the AP and authentication servers. After enabling the PandaBoard as a wireless AP and assigning a static internet protocol (IP) address, the control PC can connect to it and establish bi-directional wireless communication via socket programming. A socket program involves at least a pair comprising a client and a server. Here the PandaBoard ES acts as the Server that awaits a connection request from the control PC (Client) and transmits the sensor data when requested. Benefiting from the ARM Ubuntu system, the PandaBoard ES is able to use its own wireless module to transmit acquired sensor measurements when set up as a wireless AP automatically, and the server program starts as soon as the board powers up. Figure 3.13 shows the flowchart of the server socket as well as the digital interfaces to each navigational sensor. When the server starts, it waits for the connection request from the client. Once the wireless connection is established, the PandaBoard ES connects to all the sensors using a serial communication protocol and sends a “connected” flag to the client. The server then waits for new commands and an iteration number. As soon as the loop number is received, the server starts to read data from the sensors and parse them to create a new sentence, which contains all the available information. The new sentence is sent to the client via the wireless connection and the server enters the next cycle. Once the iteration

number equals to that of the received number m, the server socket is closed automatically.

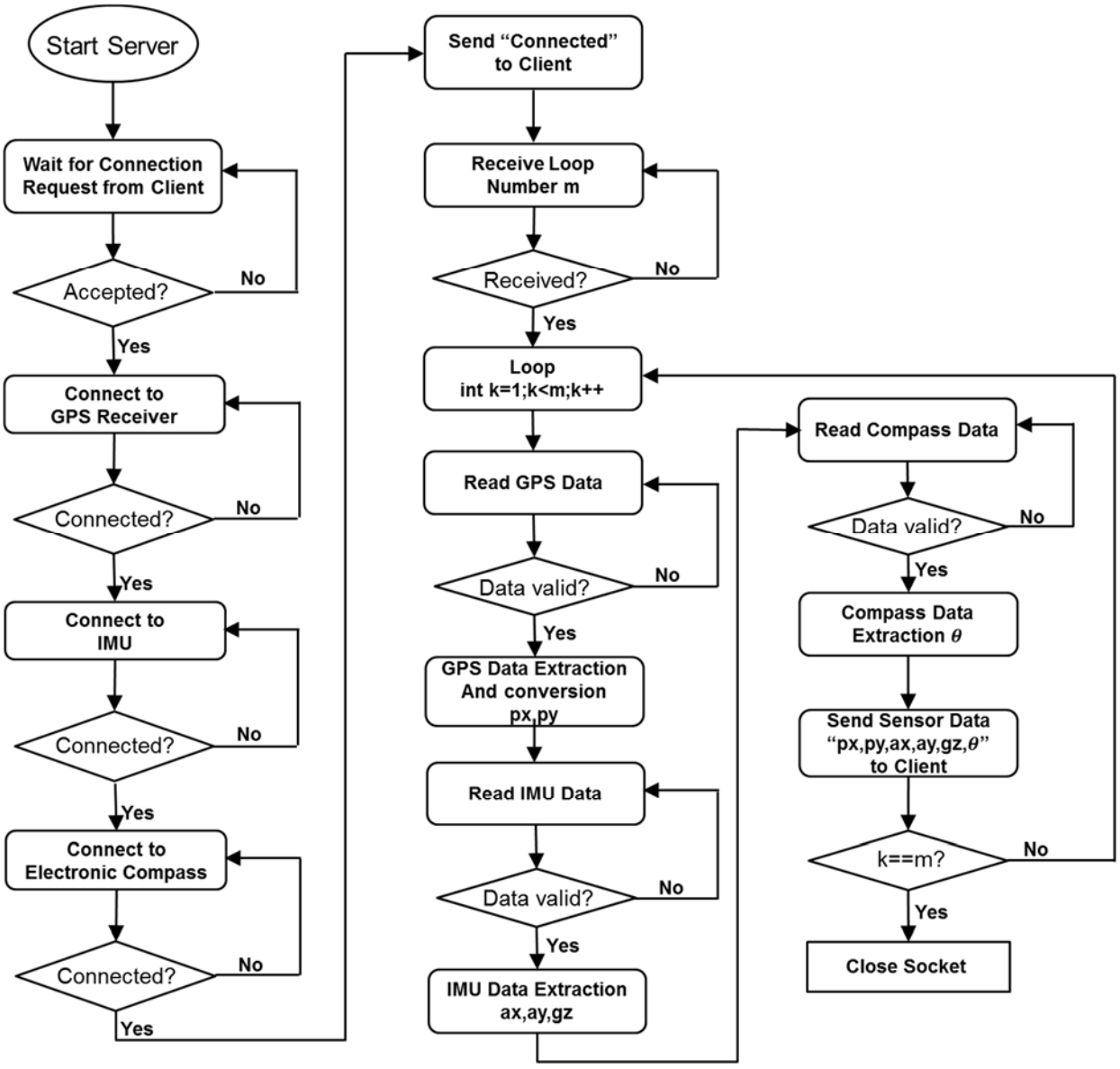

Figure 3.13 Flowchart of the Server Socket

The ARM Ubuntu on PandaBoard ES has the computational ability to be able to complete all the assigned tasks in a relatively short time period. It uses time sharing architecture where each task is assigned a specific time interval to allow the tasks to be executed before switching to the next task in order to allow multi-tasking. The switching process is fast enough such that the user is unable to discern the individual task actions and treat it as a simultaneous real time process.

Correspondingly, the control PC acts as the client. Figure 3.14 illustrates the flowchart of the client socket. It sends the connection request to the server via the predefined port and the server's static IP address. Then it sends the loop number once it receives the "connected" flag. The next step for the client is to apply the parsed raw sensor data into data fusion algorithms, which will be detailed in the next four chapters. Likewise, the client socket is closed when the loop number is reached.

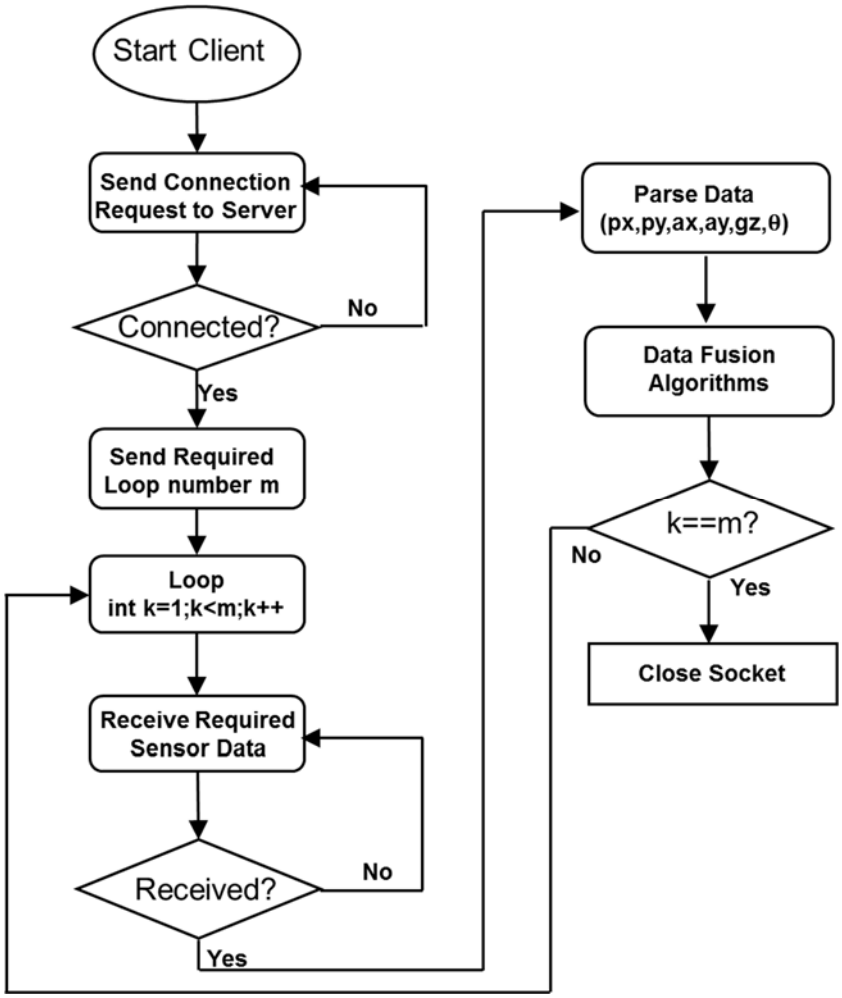

Figure 3. 14 Flowchart of Client Socket

3.4. Summary

In this chapter, a practical USV called *Springer* has been introduced and a practical navigation hardware sensor system has been implemented based on the *Springer's* navigation sensor system. The implemented system employs an embedded Linux board as the main on-board navigation processor to extract and convert raw sensor measurements from a GPS receiver, an IMU module and an electronic magnetic compass as well as establishing the wireless communication with a control computer. The proposed compact navigation sensor system is able to provide real-time raw sensor measurements, which will be used by the data fusion algorithms (as detailed in Chapter 4 to 6) to estimate more accurate navigational data, when such sensor system is incorporated in any practical USV platforms. Detection sensors such as AIS and marine Radar have been demonstrated and will be simulated in Chapter 7 encompassing their error models as detailed in this Chapter to develop a more comprehensive navigation sensor system to improve those USVs, such as the *Springer,* that are in early stages of development.

.

Chapter 4. Multi-sensor Data Fusions for USV Navigation

Knowing real-time USV's navigational data, i.e. position, velocity and heading, is important for autonomous USV operation since these data are required for the path planning and control modules to generate a safe path and appropriate control commands autonomously. Considering the working conditions under which an USV operates, i.e. the navigational sensors have inherent associated with uncertainties and environment influences have effects on USV trajectory, multi-sensor data fusion algorithms will be developed in this chapter to deal with the raw sensor measurements from the three kinds of sensors described in the preceding chapter and calculate improved navigational data for USV operation in a practical environment.

4.1. Bayesian approaches to data fusion

In an ideal world, sensors are supposed to provide exact measurements with complete certainty. However, such measurement accuracy and reliability are difficult to attain in practice due to equipment limitations and environment influences. As discussed in Chapter 2, a low cost IMU is normally a Micro Electro Mechanical System (MEMS) based sensor, which is sensitive to the surrounding environment, such as dynamic changes, noise and vibrations. The GPS measurements are relatively accurate as long as the receiver is placed in an open and clear area, where it has access to more satellites. However, it could suffer signal loss and return inaccurate measurements under harsh environmental conditions. In addition, the distortion of the Earth's magnetic field by nearby ferrous effects, sensor noise and magnetic interference have a large impact on the measurements of an electronic compass. The noisy measurements obtained from those sensors would deliver inaccurate navigational data to an autonomous USV trying to determine its own position and could lead to unsafe operation through increased collision risks. Multi-sensor data fusion, the process of combining the measurements from different sensors and reduce

possible sensor errors, to provide a reliable and complete description of an environment or process of interest, should then be employed to model and reduce sensor uncertainties.

4.1.1. Probabilistic methods on data fusion

After the discussion of why multiple sensors should be included to produce a more robust and accurate navigation system, there needs to be a clear understanding as to what data fusion is and how data fusion works with the sensors. Probability underlies most data fusion methods. It can provide a powerful and consistent means of describing sensor uncertainties and estimating the true value of the measured variable (Klein, 2004; Roth, 2017). Here follows a statistical interpretation for the data fusion to estimate the position of an USV. Before an USV operates on the water surface, it might be parked at the port or be held at the start point waiting to be launched, a guess of its position can be made based on a map or historic data of that position, and this guess is associated with uncertainties. It is assumed that the guess is a normally distributed random position as variable x with mean m_0 and standard deviation σ_0,

$$P(x) \sim N(m_0, {\sigma_0}^2) \tag{4.1}$$

where $P(x)$ is the prior belief of the USV's position, according to which, the best belief of the USV's position $\hat{x}$ is given by the mean of the distribution, $\hat{x} \stackrel{\text{def}}{=} E[x] = m_0$. At this time, a GPS sensor that is installed on the static USV can provide an observation of the USV's position that is associated with uncertainties as to the USV's true position X. The observation can be described as a conditional random variable $z|x = X$ with mean m_z and standard deviation σ_z:

$$P(z|x = X) \sim N(m_z, {\sigma_Z}^2) \tag{4.2}$$

Bayes' rule provides a solution that makes inferences about the USV's position described by the state x, given an observation z. Given the prior belief and the value derived from the observation, the posterior distribution that is treated as a correction of the prior belief of the system can be derived by Bayesian inference (Sarkka, 2013):

$$P(x|z) \sim N(m_x, {\sigma_x}^2) \tag{4.3}$$

where

$$m_x = {\sigma_x}^2({m_0}{\sigma_z}^{-2} + m_z{\sigma_0}^{-2}) \tag{4.4}$$

$${\sigma_x}^2 = \frac{1}{\frac{1}{{\sigma_0}^2} + \frac{1}{{\sigma_z}^2}} \tag{4.5}$$

The best estimation of the USV's position is then updated in accordance as following:

$$\hat{x}_{new} \overset{\text{def}}{=} E[x|z] = m_x = {\sigma_x}^2({m_0}{\sigma_z}^{-2} + m_z{\sigma_0}^{-2}) \tag{4.6}$$

The posterior probability on x given observation z is proportional to the prior probability on x and individual likelihoods from each information source (Charles, 2017). The correction can then be expressed as Equations (4.7) and (4.8).

$$\hat{x}_{new} = \hat{x} + K(z - \hat{x}) \tag{4.7}$$

$${\sigma_x}^2 = {\sigma_0}^2(1 - K) \tag{4.8}$$

where $K \overset{\text{def}}{=} {\sigma_0}^2/{\sigma_0}^2 + {\sigma_z}^2$, is the gain to adjust the prior belief based on the observation.

The on-board GPS sensor can constantly make observations of the USV's position. With a number of observations $z = [z_1 \quad z_2 \quad \cdots \quad z_n]^{-1}$, Equation (4.7) can be reorganised as Equation (4.9) to compute the USV's estimated position recursively and make more corrections to reduce the uncertainty to provide more accurate estimations.

$$\hat{x}_n = \hat{x}_{n-1} + K_n(z_n - \hat{x}_{n-1}) \tag{4.9}$$

This section details how the Bayesian inference works on the data fusion of a random position where an USV is located statically and a set of GPS observations to obtain its posterior probability of the best belief of the USV's location. In this case, the system probability distribution does not evolve with time. But when the USV travels on the water surface, the prior distribution would vary with time. Therefore, Bayesian optimal filtering, the methodology based on the above probabilistic approach that

can be used for estimating the state of a time-varying system should be employed to compute the best belief of the USV's real-time navigational data (Sarkka, 2011).

4.1.2. Kalman Filtering

Kaman filtering was first introduced by Rudolf E. Kalman in his paper that describes a recursive solution to a discrete-data linear filtering problem (Kalman, 1960). It is essentially a set of mathematical equations that implement a prediction-correction type estimator that is optimal in the sense that it minimizes the estimated error covariance – when some presumed conditions are met. As a Bayesian optimal estimator for linear stochastic systems, KF is ideal for systems with time-varying states. It does not require a memory to keep tracking all historical system states, but rather the last state, rendering it well suitable for real-time problems and embedded systems. Furthermore, if the input data fits the predefined linear dynamics and statistical models and *a prior* knowledge is known, the KF can provide an optimal estimate of the state vector, in a minimum variance sense (Gelb, 1974). As a result, Kalman filtering has become a particularly popular technique and is widely applied to autonomous navigation (Hu et al. 2003; Jwo and Chang, 2007; Loebis et al. 2004).

Developing a KF requires *a priori* knowledge of the system state, initial settings and noise models. In the examined application, the state of the system refers to the collection of dynamic variables such as position, velocities and accelerations or orientation and rotational motion parameters, which describe the physical state of the USV navigation system.

When a USV is operating on the water surface, its state $\boldsymbol{x} \in \Re^n$ varies by time, which is governed by the linear stochastic difference equation

$$\boldsymbol{x}(k) = \boldsymbol{A}\boldsymbol{x}(k-1) + \boldsymbol{B}\boldsymbol{u}(k) + \boldsymbol{w}(k-1) \tag{4.10}$$

with a measurement $\boldsymbol{z} \in \Re^n$:

$$\boldsymbol{z}(k) = \boldsymbol{H}\boldsymbol{x}(k) + \boldsymbol{v}(k) \tag{4.11}$$

where $\boldsymbol{u}(k)$ is the input, $\boldsymbol{A}, \boldsymbol{B}, \boldsymbol{H}$ are the state-transition matrix, the input matrix and the observation matrix respectively. The system is subject to the following assumptions: (Shimkin, 2009)

- process noise $w(k)$ is white noise with normal distribution with zero mean and variance $\boldsymbol{Q}$, $\boldsymbol{P}(\boldsymbol{w}) \sim N\ (0, \boldsymbol{Q})$
- measurement noise $\nu(k)$ is also white, normally distributed with zero mean and variance $\boldsymbol{R}$, $\boldsymbol{P}(\boldsymbol{v}) \sim N\ (0, \boldsymbol{R})$
- there is no correlated noise, i.e. $E[\boldsymbol{\omega}(l)\boldsymbol{v}(k)] = 0\ \forall l, k$;
- each noise is uncorrelated to the time steps $E[\boldsymbol{w}_k \boldsymbol{w}_i] = \begin{cases} \boldsymbol{Q}_k, i = k \\ 0, i \neq k \end{cases}$ and $E[\boldsymbol{v}_k \boldsymbol{v}_i] = \begin{cases} \boldsymbol{R}_k, i = k \\ 0, i \neq k \end{cases}$

Charles (2017) derived the whole process of Kalman Filter using the Bayesian approach. Kalman filtering has two steps, prediction and correction. Equations (4.12) and (4.13) makes predictions of the system state and its covariance according to the system transition model. The predicted state is the prior belief of the navigation system.

$$\hat{\boldsymbol{x}}^{-}(k) = \boldsymbol{A}\,\hat{\boldsymbol{x}}(k-1) + \boldsymbol{B}\,\boldsymbol{u}(k) \tag{4.12}$$

$$\boldsymbol{P}^{-}(k) = \boldsymbol{A}\,\boldsymbol{P}(k-1)\,\boldsymbol{A}^{T} + \boldsymbol{Q} \tag{4.13}$$

The Kalman Filter gain to correct the prior belief by reducing the mean square error is computed by Equations (4.14) and (4.15):

$$\boldsymbol{K}(k) = \boldsymbol{P}^{-}(k)\,\boldsymbol{H}^{T}\boldsymbol{S}(k)^{-1} \tag{4.14}$$

$$\boldsymbol{S}(k) = \boldsymbol{H}\,\boldsymbol{P}^{-}(k)\,\boldsymbol{H}^{T} + \boldsymbol{R} \tag{4.15}$$

Similar to the standstill USV example, the posterior belief of the navigation system given observation $\boldsymbol{z}(k)$ can be obtained by applying the Kalman Filter gain to the prior belief as shown in Equations (4.16) and (4.17).

$$\hat{\boldsymbol{x}}(k) = \hat{\boldsymbol{x}}^{-}(k) + \boldsymbol{K}(k)\,[\boldsymbol{z}(k) - \boldsymbol{H}\,\hat{\boldsymbol{x}}^{-}(k)] \tag{4.16}$$

$$\boldsymbol{P}(k) = (I - \boldsymbol{K}(k)\,\boldsymbol{H})\,\boldsymbol{P}^{-}(k) \tag{4.17}$$

After the correction, the system then enters the next state and makes new predictions. This prediction-correction process iterates the navigation system and generates real-time navigational data for each state, which is shown in the block diagram in Figure 4.1.

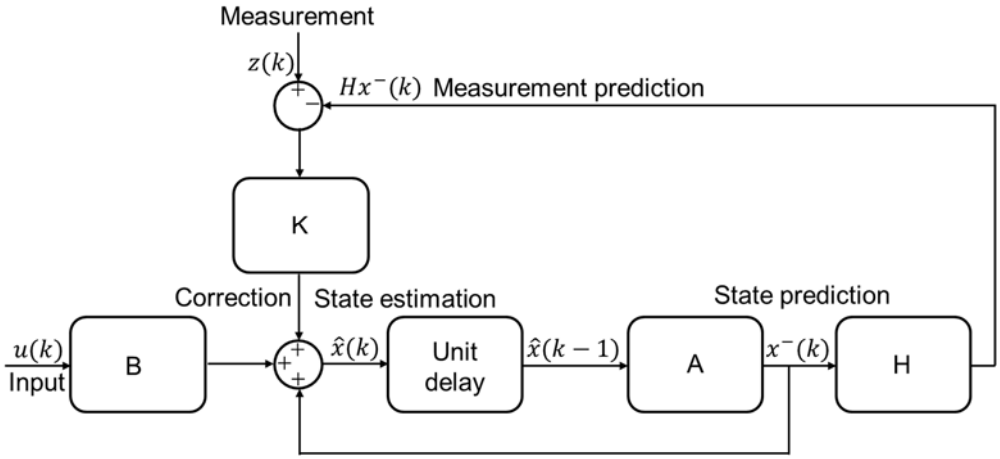

Figure 4. 1 Block diagram of a discrete Kalman Filter

The KF estimates the optimal state of a system given the measurement by minimising the mean square error in Equation (4.18), in which the expectations are shown in Equations (4.19) to (4.21):

$$\hat{\boldsymbol{x}} = \arg\min_{\hat{x}} E\{(\hat{\boldsymbol{x}} - \boldsymbol{x})(\hat{\boldsymbol{x}} - \boldsymbol{x})^{T}\} \tag{4.18}$$

$$E[\boldsymbol{x}(k)] = \hat{\boldsymbol{x}}(k) \tag{4.19}$$

$$E[(\boldsymbol{x}(k) - \hat{\boldsymbol{x}}(k))(\boldsymbol{x}(k) - \hat{\boldsymbol{x}}(k))^{T}] = \boldsymbol{P}(k) \tag{4.20}$$

$$P(\boldsymbol{x}(k)|\boldsymbol{z}(k)) \sim N(E[\boldsymbol{x}(k)], E[(\boldsymbol{x}(k) - \hat{\boldsymbol{x}}(k))\big(\boldsymbol{x}(k) - \hat{\boldsymbol{x}}(k)\big)^{T}]) = N(\hat{\boldsymbol{x}}(k), \boldsymbol{P}(k)) \tag{4.21}$$

4.2. Kalman Filter for multi-sensor data fusion

4.2.1. Discrete USV navigation model

After explaining how the probability method works on the data fusion of the positions of a standstill USV, the time-varying working conditions of an USV should

be considered. The state of an autonomous navigation system incorporates the required USV's navigational data, i.e. position (p), velocity (v) and heading (ψ), which are governed by a discrete time state-space model of the USV dynamic system in a two-dimensional navigation frame. Instead of fully relying on the system model, the acceleration rate (a) and rotation rate (ω), which can be measured by inertial sensors, are used to compute each of the modes of navigational data using discrete integration. The integration of the inertial measurements brings a more accurate ship motion model that can then be expressed as:

$$\boldsymbol{p}(k) = \boldsymbol{p}(k-1) + T \times \boldsymbol{v}(k-1) + \frac{1}{2}T^2 \times \boldsymbol{a}(k-1) \tag{4.22}$$

$$\boldsymbol{v}(k) = \boldsymbol{v}(k-1) + T \times \boldsymbol{a}(k-1) \tag{4.23}$$

$$\psi(k) = \psi(k-1) + T \times \omega(k) \tag{4.24}$$

where T is the processing time between two consecutive sampling steps.

Equations (4.22) to (4.24) can be viewed as the transition state models with $p, v \; and \; \psi$ being the state of the system, which are the estimation objects of the Kalman Filter. Therefore, the state vector $\boldsymbol{x}$ with required data can be defined as

$$\boldsymbol{x} = \begin{bmatrix} p_x & p_y & v_x & v_y & \psi \end{bmatrix}^T \tag{4.25}$$

where p_x and p_y represent the positions in a north-east navigation frame, v_x and v_y are velocities and ψ is the heading of the USV. By adding the system processing error ($\boldsymbol{w}$) and substituting into Equations (4.22) to (4.24), the system state equation (Equation (4.10)) can be further expressed as following:

$$\begin{bmatrix} p_x(k) \\ p_y(k) \\ v_x(k) \\ v_y(k) \\ \psi(k) \end{bmatrix} = \begin{bmatrix} 1 & 0 & T & 0 & 0 \\ 0 & 1 & 0 & T & 0 \\ 0 & 0 & 1 & 0 & 0 \\ 0 & 0 & 0 & 1 & 0 \\ 0 & 0 & 0 & 0 & 1 \end{bmatrix} \begin{bmatrix} p_x(k-1) \\ p_y(k-1) \\ v_x(k-1) \\ v_y(k-1) \\ \psi(k-1) \end{bmatrix} + \begin{bmatrix} \frac{1}{2}T^2 & 0 & 0 \\ 0 & \frac{1}{2}T^2 & 0 \\ T & 0 & 0 \\ 0 & T & 0 \\ 0 & 0 & 1 \end{bmatrix} \begin{bmatrix} a_x(k) \\ a_y(k) \\ \omega(k) \end{bmatrix} + \boldsymbol{w}(k-1) \tag{4.26}$$

where the acceleration and rotation rate form the control input $\boldsymbol{u} = [a_x \; a_y \; \omega]^T$.

From the start of USV operation, the on-board IMU starts to measure the motions of the USV, that is, the accelerometer measures the accelerations and the gyroscope measures the angular velocity of the USV. As mentioned in Chapter 3, the acceleration rates provided by the IMU are along the inertial frame, which can be approximated as the body frame; whereas, other navigation information has been presented in the navigation frame. It therefore should convert the IMU data from the inertial frame to the navigation frame by using the rotation matrix:

$$\begin{bmatrix} a_{nx} \\ a_{ny} \end{bmatrix} = \begin{bmatrix} cos\emptyset & -sin\emptyset \\ sin\emptyset & cos\emptyset \end{bmatrix} \begin{bmatrix} a_{ix} \\ a_{iy} \end{bmatrix} \tag{4.27}$$

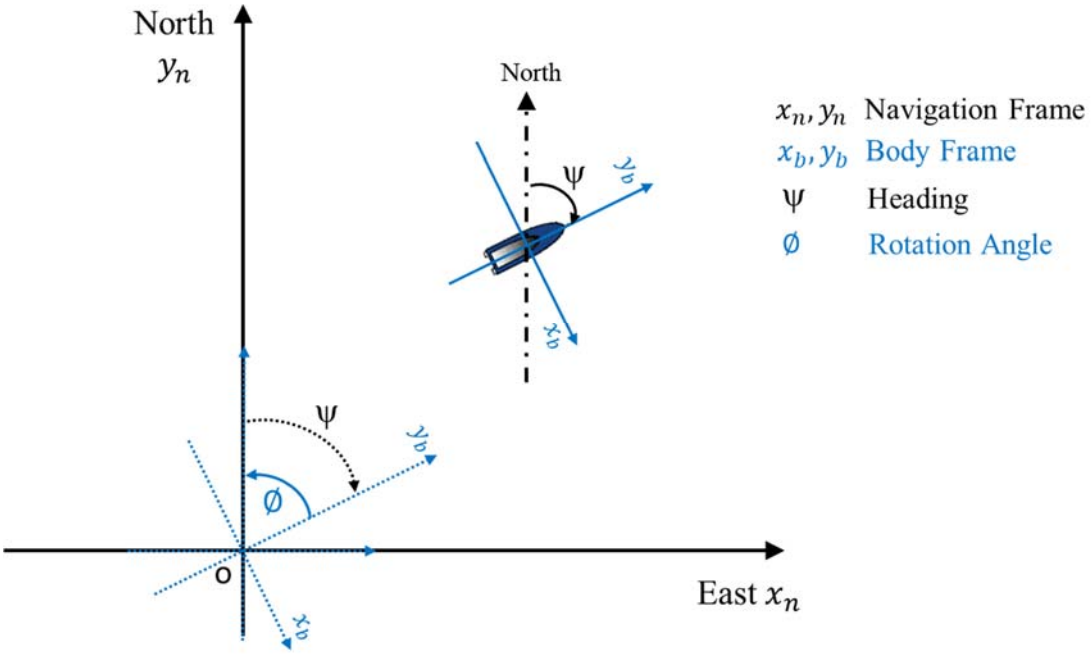

Figure 4.2 Conversion from i-frame to n-frame

As shown in Figure 4.2, the heading ψ that can be obtained from the compass is the clockwise angle referenced to the North. Therefore, the anti-clockwise rotation angle from the i-frame to the n-frame is equal to the heading:

$$\begin{bmatrix} a_{nx}(k) \\ a_{ny}(k) \end{bmatrix} = \begin{bmatrix} cos\psi(k) & -sin\psi(k) \\ sin\psi(k) & cos\psi(k) \end{bmatrix} \begin{bmatrix} a_{ix}(k) \\ a_{iy}(k) \end{bmatrix} \tag{4.28}$$

When implementing the KF based algorithm, the IMU, which can provide the acceleration and rotation rate, is used to create the predictive model for the estimation of the position and heading of the USV. As stated in Section 3.2.2, the IMU does not provide precise measurements due to equipment limitations. Hence, the

measurements of the IMU are modelled as in Equations (3.2) and (3.3). The bias factors can be predicted by applying the calibration, which is explained in detail in Appendix B. The unknown random noise vector $\boldsymbol{w}$ comprises the processing noise in Equation (4.10), which is assumed to be the white noise sequence with zero mean and standard deviation given by q_1 and q_2, respectively. The q_1 and q_2 refer to the root-mean-square (RMS) values of the accelerometer and gyroscope's unpredictable measurement errors respectively. The covariance matrix $\boldsymbol{Q}$ of the processing noise $\boldsymbol{w}$ can then be expressed as:

$$\boldsymbol{Q} = cov(\boldsymbol{w}) = \begin{bmatrix} \left(\frac{1}{2}T^2 q_1\right)^2 & 0 & \frac{1}{2}T^3 {q_1}^2 & 0 & 0 \\ 0 & \left(\frac{1}{2}T^2 q_1\right)^2 & 0 & \frac{1}{2}T^3 {q_1}^2 & 0 \\ \frac{1}{2}T^3 {q_1}^2 & 0 & (T q_1)^2 & 0 & 0 \\ 0 & \frac{1}{2}T^3 {q_1}^2 & 0 & (T q_1)^2 & 0 \\ 0 & 0 & 0 & 0 & {q_2}^2 \end{bmatrix} \tag{4.29}$$

It can be observed that the conversion of the frames generates the non-linearity of the system. However, in order to obtain real-time results, during the simulation or practical trials, the sampling time is normally selected to be short. Over a short time period, the change in heading experienced by the USV could be considered negligible, which can be viewed as a constant value. Thus, the rotation angle can be assumed to be the prior estimated heading in the last time step, which allows the system's non-linearity to be ignored.

4.2.2. System measurement model

As described in Chapter 3, the sensor models of GPS and electronic compass can be defined with an additive noise component as following:

$$p_o = p_i + \nu_g \tag{4.30}$$

$$\psi_o = \psi_i + \nu_h \tag{4.31}$$

where p_i and ψ_i are the true position and heading respectively; p_o and ψ_o are the noisy measurements; and ν_g and ν_h are the uncertainty with a normal distribution with the standard deviation of their RMS error value r_g and r_h.

Therefore, the measurement model z can be denoted as:

$$\boldsymbol{z}(k) = \begin{bmatrix} p(k) \\ \psi(k) \end{bmatrix} + \begin{bmatrix} v_g(k) \\ v_h(k) \end{bmatrix} \tag{4.32}$$

By substituting Equation (4.32) into Equation (4.11), the measurement equation can be rewritten as:

$$\boldsymbol{z}(k) = \begin{bmatrix} 1 & 0 & 0 & 0 & 0 & 0 \\ 0 & 1 & 0 & 0 & 0 & 0 \\ 0 & 0 & 0 & 0 & 0 & 1 \end{bmatrix} \begin{bmatrix} p_x(k) \\ p_y(k) \\ v_x(k) \\ v_y(k) \\ \psi(k) \end{bmatrix} + \boldsymbol{\nu}(k) \tag{4.33}$$

where $\boldsymbol{\nu}$ represents additive system measurement noise, which is also assumed to be white noise with zero mean and standard deviation given by r_g and r_h referring to as the RMS errors of GPS sensor and electronic compass, respectively. $\boldsymbol{R}$, the covariance of measurement noise $\boldsymbol{\nu}$ is then given by:

$$\boldsymbol{R} = cov(\boldsymbol{\nu}) = \begin{bmatrix} {r_g}^2 & 0 & 0 \\ 0 & {r_g}^2 & 0 \\ 0 & 0 & {r_h}^2 \end{bmatrix} \tag{4.34}$$

By giving the initial state estimate $\hat{\boldsymbol{x}}(0)$ and the initial covariance about this estimate, $\boldsymbol{P}(0) = cov\{(\hat{\boldsymbol{x}}(0) - \boldsymbol{x}(0))(\hat{\boldsymbol{x}}(0) - \boldsymbol{x}(0))^T\}$, the Minimum Mean Square Error (MMSE) estimate of the state vector $\boldsymbol{x}(k)$ can be obtained according to the recursive KF algorithm (Equations (4.12) to (4.17)).

4.2.3. Simulations of KF based multi-sensor data fusion algorithm

In order to evaluate the performance of the Kalman Filter based multi-sensor data fusion algorithm on USV navigation, the operations of an USV that is equipped with the aforementioned sensors (Chapter 3) have been simulated in a quiet two dimensional environment without obstacles. The simulated USV is considered as a mass point. Without considering the environment effects such as wind or tidal current, USVs normally operate in straight line trajectories at constant velocity and make turns at a predesigned angular velocity. Therefore, its motion movements can be described by a discrete motion model as follows:

$$\boldsymbol{x}(k+1) = \boldsymbol{F} \times \boldsymbol{x}(k) \tag{4.35}$$

where, $\boldsymbol{x} = [p_x \quad p_y \quad v_x \quad v_y]^T$ is the system state including the position and velocity information. $\boldsymbol{F}$ is the state matrix and has different expressions depending upon specific motion models.

The proposed algorithm has been implemented and verified using Matlab simulations during development. Measurements obtained from different navigational sensors including a GPS, an electronic compass and an IMU have been simulated by adding noises to the true values using sensor models presented in Chapter 3 (Equations 3.1 to 3.4). Sensor noises are used as the same value in Table 3.4. The presenting of the noise model of each sensor to implement the Kalman Filter based multi-sensor data fusion algorithm is shown in Table 4.1.

Table 4. 1 The KF characteristics

Accelerometer noise model	$q_{1x} = 0.0039^2(m/s^2)^2$ $q_{1y} = 0.0039^2(m/s^2)^2$
Gyroscope noise model	$q_2 = 0.033^2(deg/s)^2$
GPS noise model	$r_{1x} = 3^2(m)^2$ $r_{1y} = 2.5^2(m)^2$
Compass noise model	$r_2 = 0.5^2(deg)^2$

4.2.3.1. Simulation Scenario 4.1: Line trajectory

An autonomous USV usually maintains a constant velocity during operations in order to move efficiently through water. Therefore, the vehicle can be simulated by the Constant Velocity Model (CVM) with the following state matrix $\boldsymbol{F}$:

$$\boldsymbol{F}_{CVM} = \begin{bmatrix} 1 & 0 & T & 0 \\ 0 & 1 & 0 & T \\ 0 & 0 & 1 & 0 \\ 0 & 0 & 0 & 1 \end{bmatrix} \tag{4.36}$$

and ideally its heading does not change and there is no rotation rate ($\omega = 0$) in this case, i.e.:

$$\psi_x(k+1) = \psi_x(k) \tag{4.37}$$

An area of 800 m * 800 m with North as the y-axis and East as the x-axis has been simulated for an USV to navigate. In simulation Scenario 4.1, the mission of the USV is to start steering from point (125 m, 628 m) at the speed of 1 m/s on a heading of 135° for 700 time steps. The sampling time is 1s and all the sensors generate one measurement at each time step. The initial values of the system state vector (Equation (4.25)) and its covariance are defined as below:

$$\boldsymbol{x}(1) = [125 \quad 628 \quad 0.7071 \quad -0.7071 \quad 135]^T \tag{4.38}$$

$$\boldsymbol{P}(1) = \begin{bmatrix} 1 & 0 & 0 & 0 & 0 \\ 0 & 1 & 0 & 0 & 0 \\ 0 & 0 & 0.01 & 0 & 0 \\ 0 & 0 & 0 & 0.01 & 0 \\ 0 & 0 & 0 & 0 & 0.25 \end{bmatrix} \tag{4.39}$$

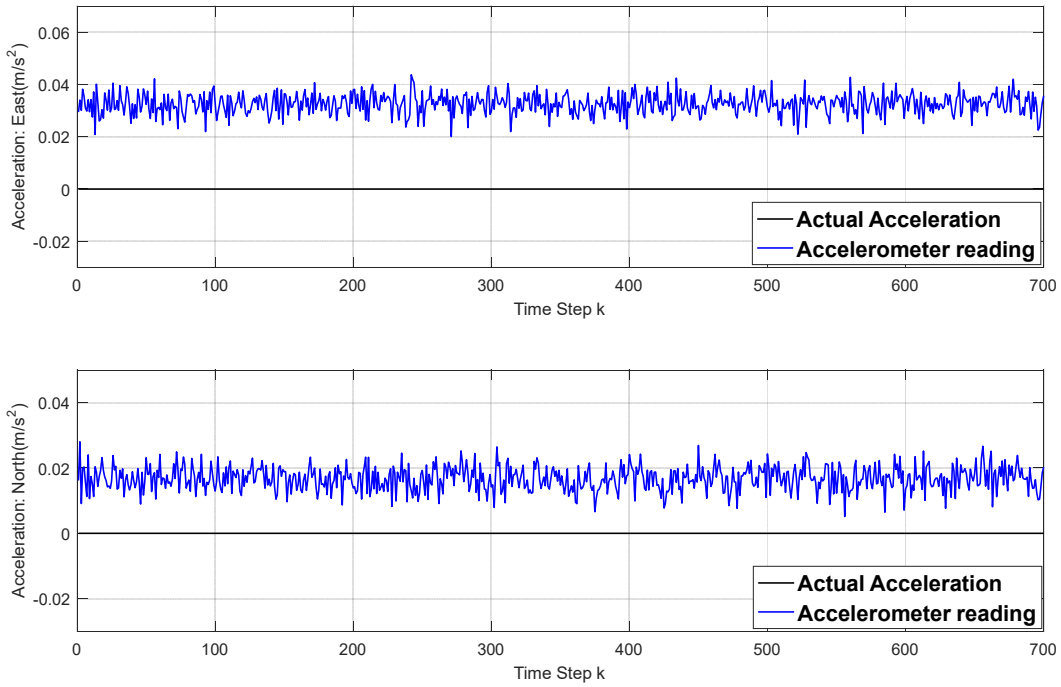

Figure 4. 3 Simulation Scenario 4.1: the simulated actual and measured acceleration

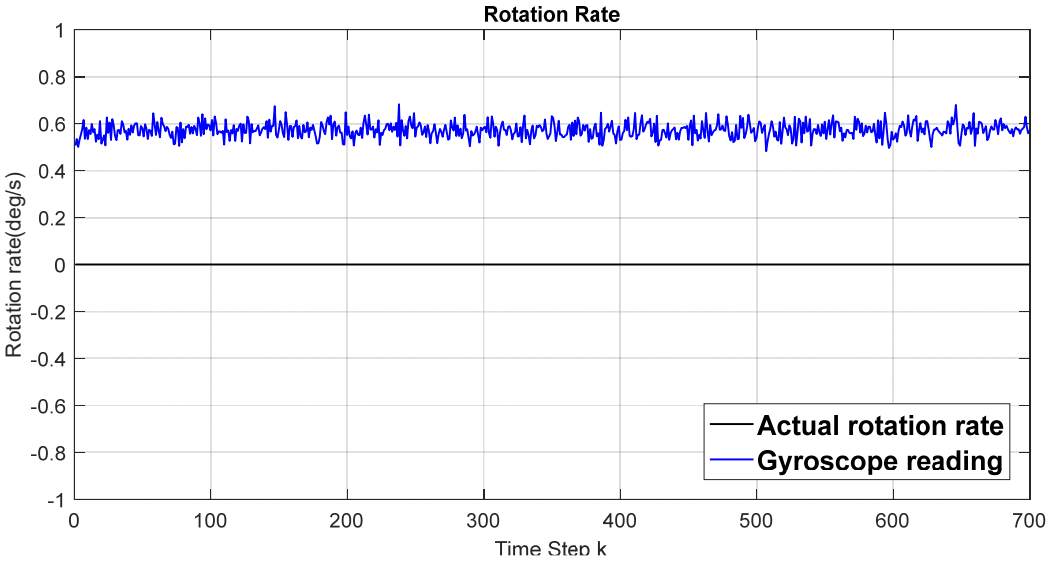

(b)

Figure 4. 4 Simulation Scenario 4.1: the simulated actual and measured rotation rate

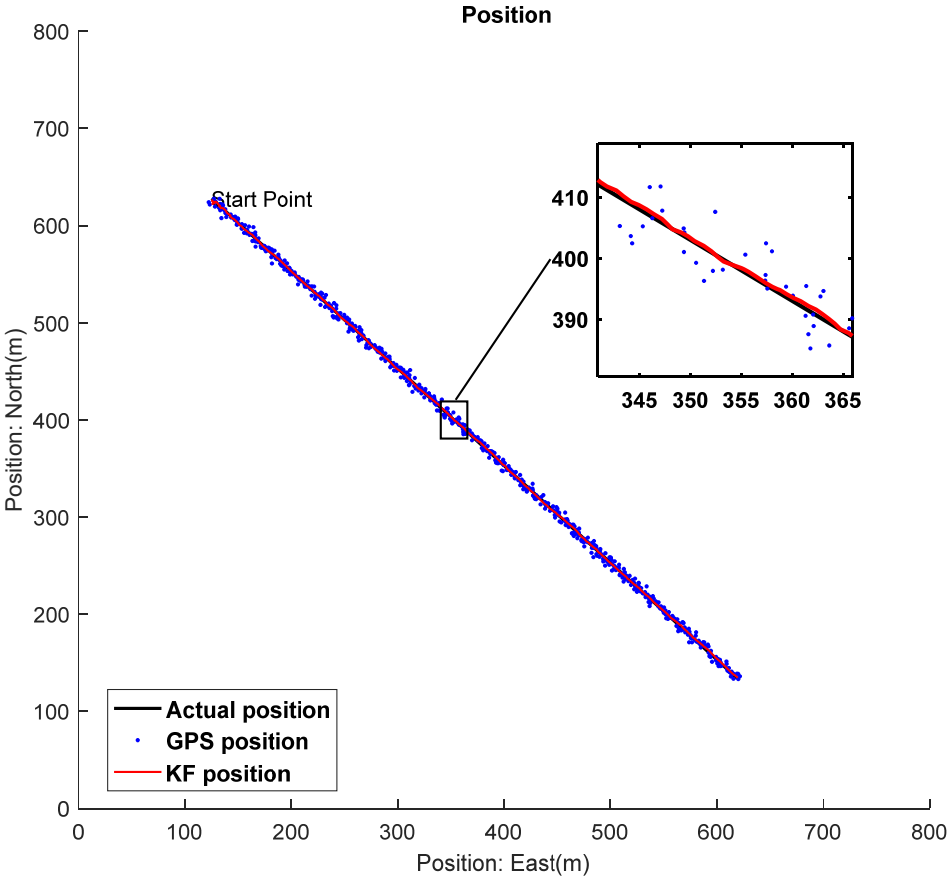

Figure 4. 5 Simulation Scenario 4.1: the fused position result

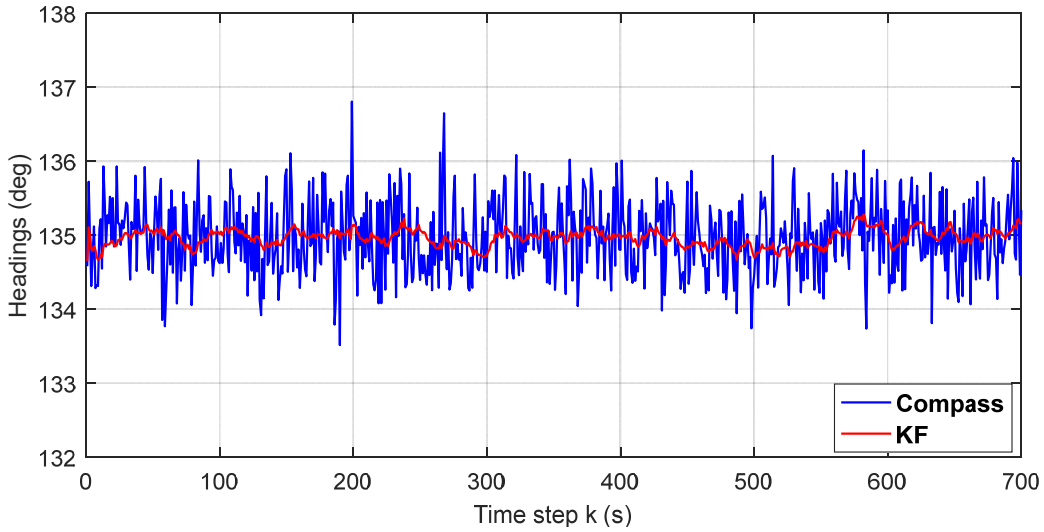

Figure 4. 6 Simulation Scenario 4.1: the fused heading results

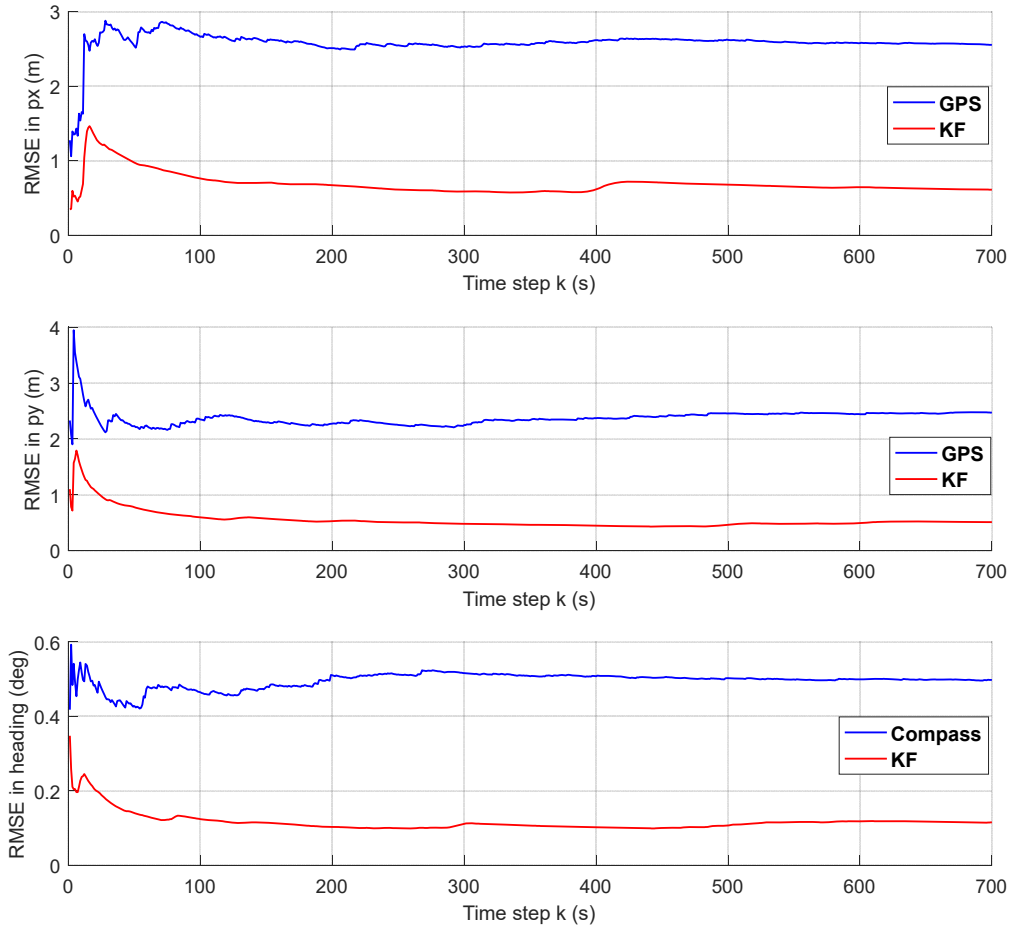

Figure 4.7 Simulation Scenario 4.1: the RMS errors of the USV's position and heading

From the simulation results, it is clear that the Kalman Filter (KF) improves the accuracy of raw measurements from both GPS and electronic compass. Figure 4.5 illustrates the simulated actual USV trajectory, shown as the black line and the GPS

raw measurements as the blue dots scattered around the actual trajectory by the predefined variance. The red line indicates the fused results of the USV's positions by applying the KF based data fusion algorithm. As can be seen the red line is very close to the actual trajectory, especially from the enlarged inset. In this simulation, the USV is meant to operate in a straight line trajectory without any heading changes. In Figure 4.6, the heading estimations (red) are also closer to the set heading of 135° than the raw compass measurements. These improvements are confirmed by Figure 4.7, which presents the RMS error of the fused results and raw sensor measurements. The figure clearly shows the RMS error of the fused positions in both x-axis and y-axis are reduced to less than one meter and the RMS error of the fused heading is reduced to less than 0.2°. Table 4.2 lists the mean square errors after the USV completes its mission that provides numerical proofs.

Table 4. 2 Mean Square Errors for KF algorithm in Simulation Scenario 4.1

Method	***MSE***	***Units***
KF_position $\boldsymbol{p_x}$	0.4846	m^2
KF_position $\boldsymbol{p_y}$	0.5703	m^2
GPS position $\boldsymbol{p_{gpsx}}$	6.1069	m^2
GPS position $\boldsymbol{p_{gpsx}}$	5.8936	m^2
KF_heading $\boldsymbol{\psi}$	0.0361	deg^2
Electronic Compass $\boldsymbol{\psi_c}$	0.4145	deg^2

4.2.3.2. Simulation Scenario 4.2: Two turning manoeuvres

In the simulation Scenario 4.1, the CVM is used to design the trajectory of the USV, which can only model a simple line trajectory and cannot provide a model sufficient enough for complex USV manoeuvres such as heading changes. Thus another model called the Coordinated Turn Model (CTM) is employed to simulate the heading changes of the vehicle (Yuan et al. 2014). It is assumed the rotation rate is constant while turning and the state matrix can be expressed by Equation (4.40) with the heading changes in terms of turning time in Equation (4.41).

$$\boldsymbol{F}_{CTM} = \begin{bmatrix} 1 & 0 & \frac{\sin \omega T}{\omega} & \frac{-(1-\cos \omega T)}{\omega} \\ 0 & 1 & \frac{1-\cos \omega T}{\omega} & \frac{\sin \omega T}{\omega} \\ 0 & 0 & \cos \omega T & -\sin \omega T \\ 0 & 0 & \sin \omega T & \cos \omega T \end{bmatrix} \tag{4.40}$$

$$\psi_x(k+1) = \psi_x(k) + \omega * \mathrm{T} \tag{4.41}$$

The mission for the USV in this simulation is to make two turns. The USV is simulated to start at point (250 m, 280 m) with constant speed of 1 m/s and initial heading of 70° for 300 time steps. It is then assigned to turn anti-clockwise at k= 115~150 and 225~255. When turning the angular velocity is constant at 3 °/s. The initial values of the system state vector (Equation (4.25)) and its covariance are predefined as:

$$\boldsymbol{x}(1) = [250 \quad 280 \quad 0.9397 \quad 0.3420 \quad 70]^T \tag{4.42}$$

$$\boldsymbol{P}(1) = \begin{bmatrix} 1 & 0 & 0 & 0 & 0 \\ 0 & 1 & 0 & 0 & 0 \\ 0 & 0 & 0.01 & 0 & 0 \\ 0 & 0 & 0 & 0.01 & 0 \\ 0 & 0 & 0 & 0 & 0.25 \end{bmatrix} \tag{4.43}$$

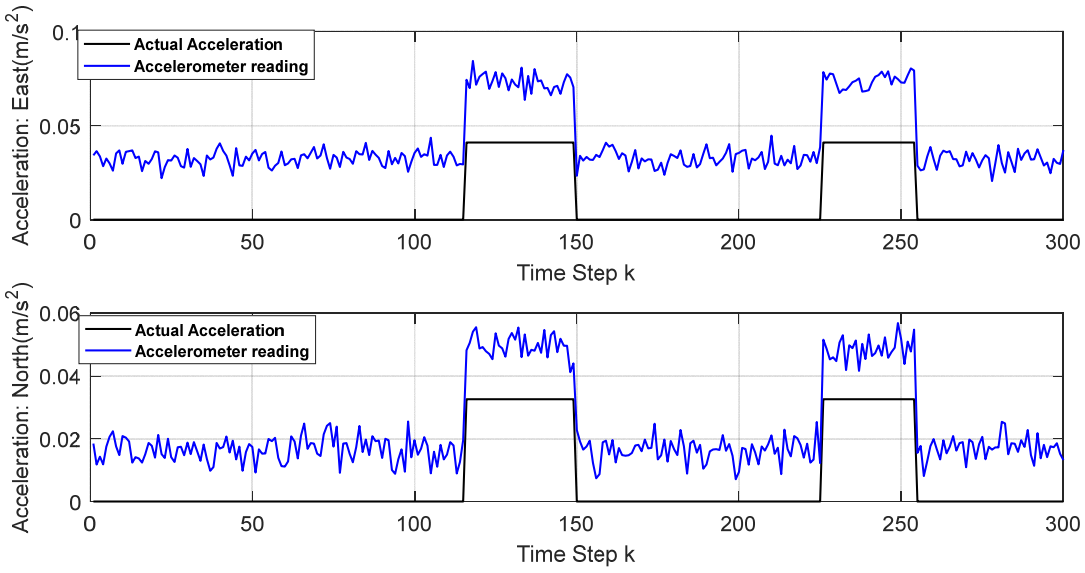

Figure 4.8 Simulation Scenario 4.2: the simulated actual and measured acceleration

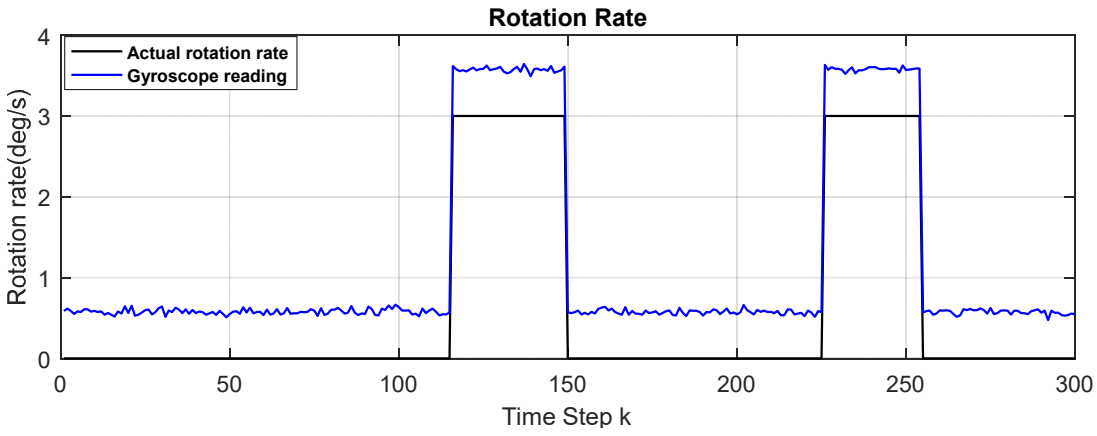

(b)

Figure 4.9 Simulation Scenario 4.2: the simulated actual and measured rotation rate

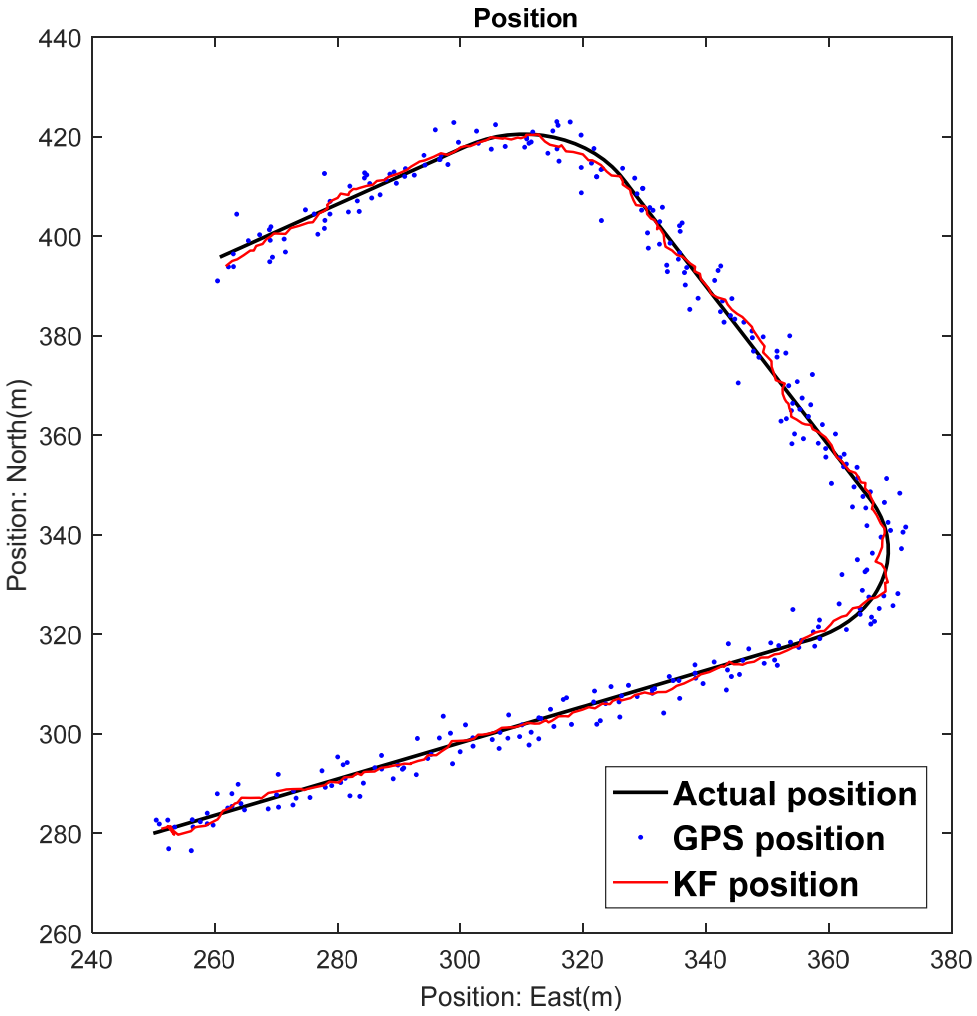

Figure 4. 10 Simulation Scenario 4.2: the fused position result

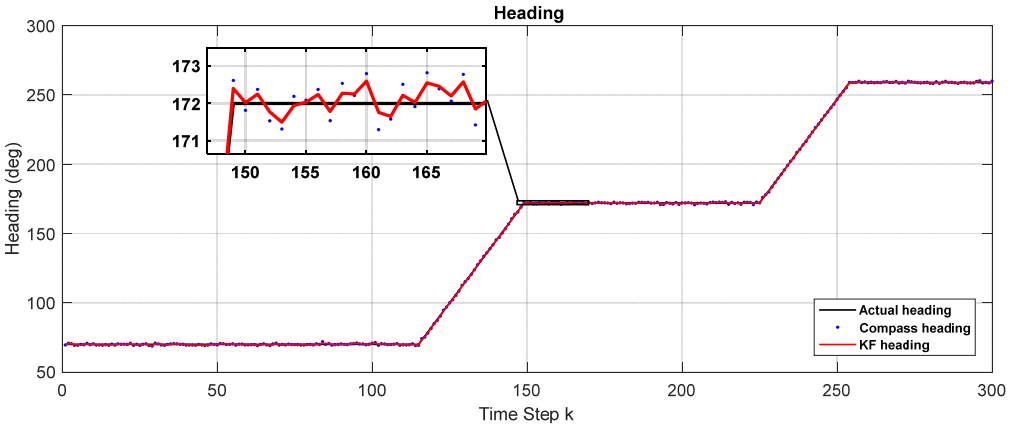

Figure 4. 11 Simulation Scenario 4.2: the fused heading results

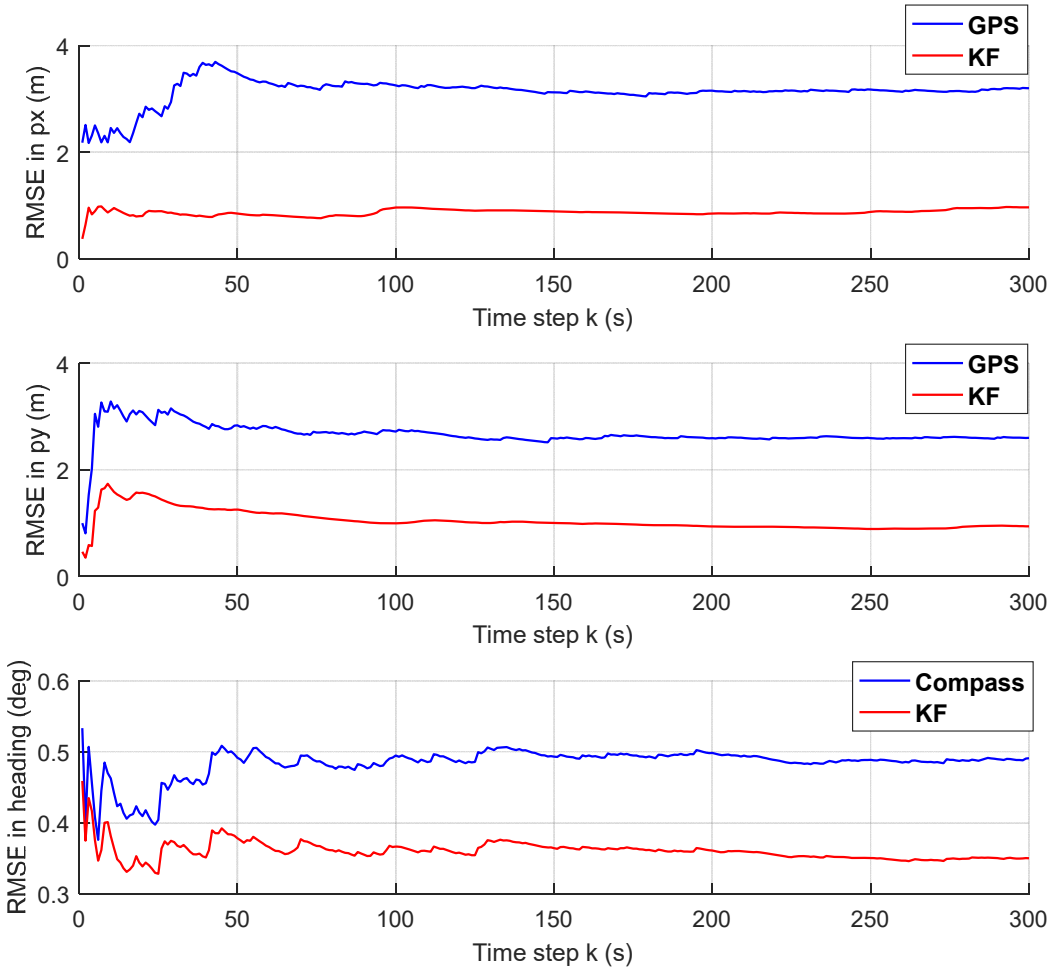

Figure 4. 12 Simulation Scenario 4.2: the RMS errors of the USV's position and heading

In simulation Scenario 4.2, a more complex mission is assigned to the USV to model the possible manoeuvres during operation. The data fusion algorithm is still able to reduce the error of raw measurements from the GPS and electronic compass. Figure 4.10 illustrates that the red line that represents the fused trajectory is closer to the

actual trajectory than the GPS measured positions, but with degraded performance during heading changes. The heading results are shown in Figure 4.11. There are two changes of heading. From the enlarged inset, it can be seen that the fused headings fluctuate around the actual heading with less improvement than those in simulation Scenario 4.1. Figure 4.12 compares the RMS error of the fused results and raw sensor measurements to display the improvement in navigational data accuracy and Table 4.3 lists the mean square errors for the whole mission. It is noticeable that the performance of the developed algorithm in simulation Scenario 4.2 is worse than in Scenario 4.1 due to the more complex motions of the USV. Therefore, deeper research on the data fusion algorithm must be carried out to achieve levels of accuracy that are sufficient enough to allow it to be adapted for practical USV applications.

Table 4. 3 Simulation Scenario 4.2: Mean Square Errors

Method	***MSE***	***Units***
KF_position $\boldsymbol{p_x}$	1.5635	m^2
KF_position $\boldsymbol{p_y}$	0.8454	m^2
GPS position $\boldsymbol{p_{gpsx}}$	10.1532	m^2
GPS position $\boldsymbol{p_{gpsx}}$	5.4936	m^2
KF_heading $\boldsymbol{\psi}$	0.1365	deg^2
Electronic Compass $\boldsymbol{\psi_c}$	0.2643	deg^2

4.3. Multi-sensor data fusion for practical USV navigation

4.3.1. Environment influences

The Marine environment is uncertain and complex for USV navigation. There are various aspects that could cause position offset, especially environmental influences. Tidal current, wind and waves are the most significant effects that would cause drifting of a vessel moving on the water surface. In this context, the trajectory of an USV is complicated and cannot be simply characterized as operating on a straight line or a curved line of fixed radius in practice. If using a conventional Kalman Filter, the system has to be linear, and in the previous section the non-linearity caused by

the frame conversion was neglected by assuming that only minimal heading change can occur during each time step. However, such an approximation may cause large errors in practical applications, especially when the USV is following a non-straight line. Thus, Kalman Filter variants such as the Extended KF (EKF) and the Unscented KF (UKF) have been developed and used to deal with non-linear systems. As discussed in Chapter 2, the UKF can provide more accurate results at reduced computational cost. In this section, an UKF based multi-sensor data fusion algorithm has been developed to deal with issues that might occur in a practical environment when estimating the navigational data of the USV.

4.3.2. Unscented Kalman Filtering

Unscented Kalman filtering, uses an unscented transform to propagate designed Sigma points and calculates the mean of the propagated point to compute the optimal estimation of the input data. It has been used increasingly in vehicle navigation in recent years (Zhang, 2005; Hide et al, 2007; Pardal et al, 2013; Ma, 2015; Meng et al, 2016; Liu, 2019). As stated in the previous section, when the frame rotation angle is equal to the heading of the USV, the non-linear dynamic model can then be obtained by combining Equation (4.28) and Equations (4.22) to (4.24) as below:

$$f'(x) = \begin{pmatrix} \dot{p}_x \\ \dot{p}_y \\ \dot{v}_x \\ \dot{v}_y \\ \dot{\psi} \end{pmatrix} = \begin{pmatrix} v_x \\ v_y \\ cos\psi a_{ix} - sin\psi a_{iy} \\ sin\psi a_{ix} + cos\psi a_{iy} \\ \omega \end{pmatrix} \tag{4.44}$$

Based on the measurements, the observation model is the same linear equation as Equation (4.33). For an n dimensional random variable $\boldsymbol{x}$ with mean $\boldsymbol{m}$ and covariance $\boldsymbol{P}$, the UKF employs the unscented transformation to form a set of 2n+1 weighted points, which are also called Sigma points (Wan and Merwe, 2000). The working procedures of the UKF are also composed of the prediction and estimation steps as the conventional KF. In the autonomous navigation system with the above dynamic model and measurement model, the mean and covariance of the required navigational data are computed using the following steps (Sarkka, 2011):

Step 1: Form 2n+1 sigma points around the $\boldsymbol{x}$ at the last state ($n = 5$ where the dimension of state vector $\boldsymbol{x}$ is 5) using Equations (4.45) to (4.47):

$$\boldsymbol{\chi_0}(k-1) = \boldsymbol{m}(k-1) \tag{4.45}$$

$$\boldsymbol{\chi_i}(k-1) = \boldsymbol{m}(k-1) + \sqrt{n+\lambda}\left[\sqrt{\boldsymbol{P_i}(k-1)}\right] \tag{4.46}$$

$$\boldsymbol{\chi_{i+n}}(k-1) = \boldsymbol{m}(k-1) - \sqrt{n+\lambda}\left[\sqrt{\boldsymbol{P_i}(k-1)}\right],\ i = 1, \dots, n \tag{4.47}$$

The constant weights W_i^m and W_i^c that are associated to each sigma point are computed as follows:

$$W_0^m = \lambda/(n+\lambda) \tag{4.48}$$

$$W_0^c = \frac{\lambda}{(n+\lambda)} + (1 - \alpha^2 + \beta) \tag{4.49}$$

$$W_i^m = W_i^c = 1/2(n+\lambda),\ i = 1, \dots, 2n \tag{4.50}$$

where $\lambda = \alpha^2(n+\kappa) - n$. The parameters α and κ determine the spread of the sigma points around the mean. β describes the distributed information, of which the optimal value is 2 for Gaussian distribution.

Step 2: Propagate the calculated sigma points through the dynamic model

$$\hat{\boldsymbol{\chi}}_{\boldsymbol{i}}(k) = f(\boldsymbol{\chi_i}(k-1)),\ i = 0, \dots, 2n \tag{4.51}$$

Step 3: Compute the predicted mean $\boldsymbol{m}^-(k)$ and the predicted covariance $\boldsymbol{P}^-(k)$ by multiplying each weight to the associated Sigma point as following:

$$\boldsymbol{m}^-(k) = \sum_{i=0}^{2N} W_i^m\, \hat{\boldsymbol{\chi}}_{\boldsymbol{i}}(k) \tag{4.52}$$

$$\boldsymbol{P}^-(k) = \sum_{i=0}^{2N} W_i^c\, (\hat{\boldsymbol{\chi}}_{\boldsymbol{i}}(k) - \boldsymbol{m}^-(k))(\hat{\boldsymbol{\chi}}_{\boldsymbol{i}}(k) - \boldsymbol{m}^-(k))^T + \boldsymbol{Q}(k-1) \tag{4.53}$$

where N is the dimension of the expended state space, which equals to $N_x + N_w + N_{\boldsymbol{v}}$. N_x is the dimension of the original state that equals to n; N_w and $N_{\boldsymbol{v}}$ are the dimensions of the white noise $\boldsymbol{w}$ and $\boldsymbol{v}$.

Step 4: For a linear observation model, sigma points are not required at the correction stage that results in reduced computational cost and higher accuracies (Briers et al, 2003). The update process is the same as with the conventional Kalman Filter (Equations (4.14) to (4.17)).

4.3.3. Simulations of UKF based multi-sensor data fusion algorithm

In order to simulate an USV operation in a practical environment, waypoint tracking missions have been simulated according to the map of the environment. The simulated USV calculates its distance and bearing to the next waypoint from the start. Once it researches proximity to the predesigned waypoint, which is termed waypoint clearance, it then searches for the next waypoint and steers to it until it reaches the final destination (Gursoy et al, 2013). The condition for a waypoint clearance is

$$\left|p_{USV} - p_{wp}\right| = \sqrt{(p_{xUSV} - p_{xwp})^2 + (p_{yUSV} - p_{ywp})^2} < d \qquad (4.54)$$

where, $p_{USV} = \left(p_{xUSV}, p_{yUSV}\right)$ is the current position of the USV, $p_{wp} = (p_{xwp}, p_{ywp})$ is the position of the target waypoint, d is the predesigned minimum radius around the waypoint. The USV can be considered as having reached the waypoint by entering the circle of radius d around the waypoint.

According to the waypoint clearance condition, the operation of the USV is adjusted by changing its headings to track the target waypoint as follows:

if $heading - bearing < \omega * T$, then USV turns clockwise at the angular velocity ω, $heading = heading + \omega * T$;

if $heading - bearing > \omega * T$, then USV turns anti-clockwise at the angular velocity ω, $heading = heading - \omega * T$;

if $heading - bearing = \omega * T$, then USV remains its current direction, $heading = heading$,

where ω is the angular velocity of the USV and T is the sampling time of the system.

In a practical environment, sensor measurements accuracy could degrade. In this section, the simulated sensor noise settings may be larger than those in the sensors' manuals and differ to the UKF predefined noise models that are based on the manuals. The sensor noise settings are listed in Table 4.4 and the noisy sensor readings are simulated by generating random errors from a normal distribution with zero mean and corresponding variance using the sensor models demonstrated in Chapter 3. In this section, the UKF uses the same noise models as described in Table 4.1.

Table 4. 4 predefined sensor noises for simulations in practical environment

Sensor	**Measurement**	**Noise**	
		Bias	**Variance**
IMU	Acceleration a_x	$0.03\ m/s^2$	$0.004\ m/s^2$
	Acceleration a_y	$0.02\ m/s^2$	$0.004\ m/s^2$
	Rotation rate ω	$0.28\,°/s$	$0.033\,°/s$
GPS	Position p_x	0	$8\ m$
	Position p_y	0	$7\ m$
Electronic Compass	Heading ψ	0	1°

4.3.3.1. Simulation Scenario 4.3: Line trajectory

The simulation area is based on a practical environment in Southampton east Cowes as shown in Figure 4.12 (a). Variable water currents that affect the USV's trajectory and heading are classified as an environmental disturbance. According to the environment agency Defra (Defra, 2018), in the Southampton Water area, the tidal current at the mouth peaks at a speed of 0.7 m/s on the flood and 1.0 m/s on the ebb. The estuary flow rates are up to 0.5 m/s and up to 0.25 m/s towards the head of the rivers. The two main components of currents are the speed and direction. In this simulation, a constant current at speed v_c along the direction of the water flows that causes drifting of the USV's position has been simulated as in Figure 4.13. The velocity of the USV, with respect to the shore-based reference, can then be calculated as:

$$\begin{bmatrix} v_{rx} \\ v_{ry} \end{bmatrix} = \begin{bmatrix} v_{ux} + v_c \times \cos\alpha \\ v_{uy} + v_c \times \sin\alpha \end{bmatrix} \tag{4.55}$$

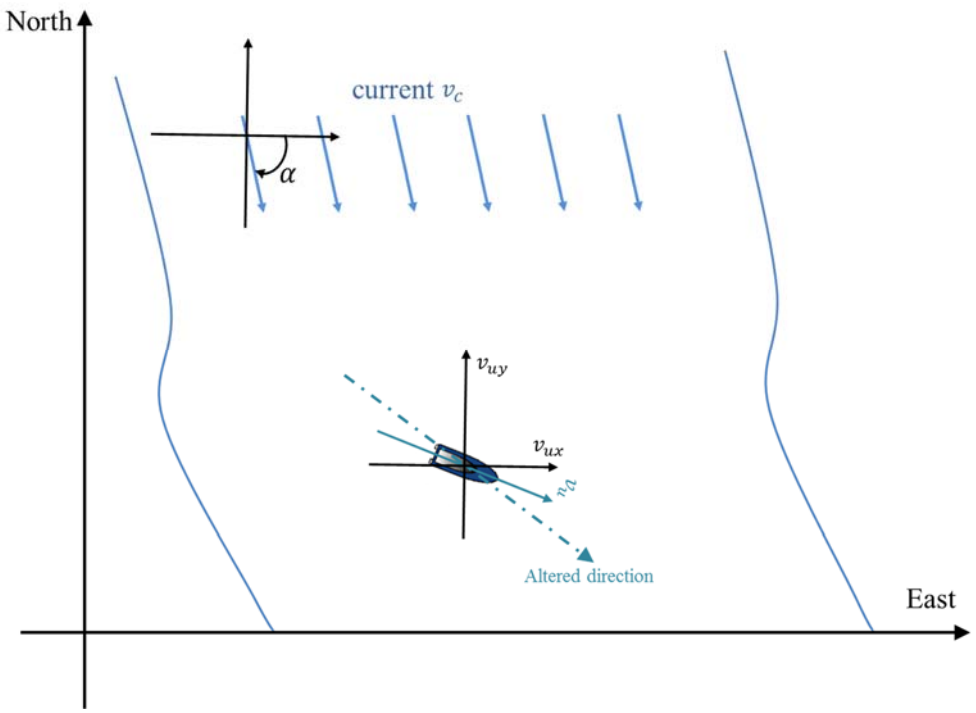

Figure 4. 13 Calculation of Tidal effect to the USV speed

The start and end points of the USV's trajectory are chosen to cross the water according to the satellite map to avoid the collision with the land as illustrated in Figure 4.14. The actual length of the map is 4000 m * 4000 m, and scaled to 800 m * 800 m in this simulation. The mission of the USV is to track to the end point (517 m, 125 m) from the start point (365 m, 728 m) by following a straight line trajectory. Three simulations were conducted each with the water current at a different but constant speed but in the same direction on the ebb. The data of the currents was chosen according to the previous recorded information (National coastwatch, 2018) and tide tables (Dolby, 2018) for the currents in the Solent and Southampton Water. As shown in Figure 4.14 (b), the planned straight line trajectory is altered by the influence of the water current. The blue line represents the altered trajectory by a current speed of 0.15 m/s. The black line (in the middle) represents the altered trajectory with a current oft 0.3 m/s. The green line that shows the most deviation from the ideal straight line represents the trajectory altered by a current of 0.5 m/s . As would be expected the greater the velocity of the influencing current the greater the drift effect from the ideal path. The initial state of the system is:

$$\boldsymbol{x}(1) = [365 \quad 728 \quad 0.5 \quad -0.866 \quad 150]^T \tag{4.56}$$

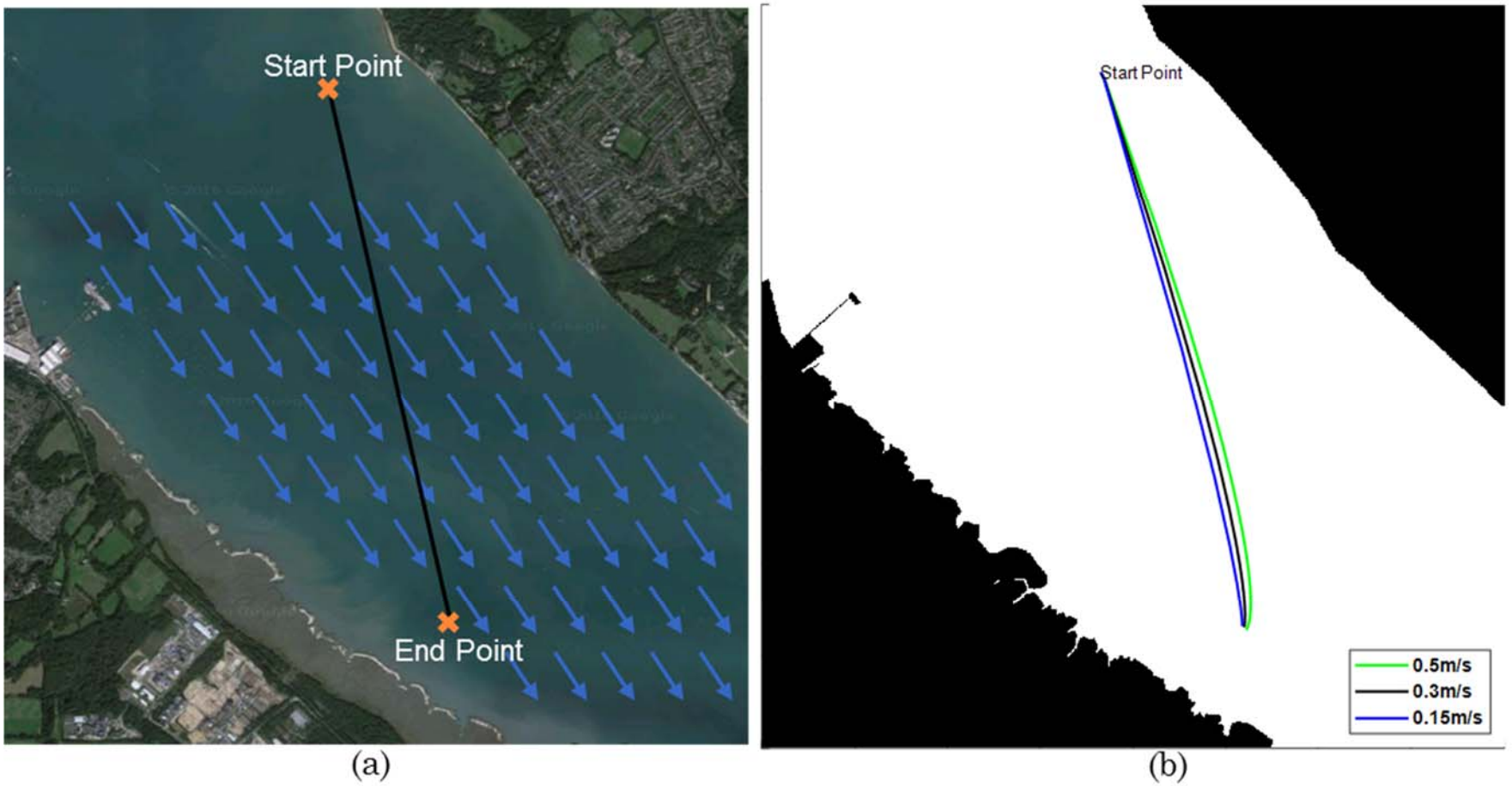

Figure 4. 14 Simulation Scenario 4.3: testing environment in Southampton east Cowes. (a) shows the satellite map with planed line trajectory of the USV, a constant current is also simulated along the water flow; (b) gives the binary map that converted from the satellite map with the drifted trajectory of the USV caused by three different currents

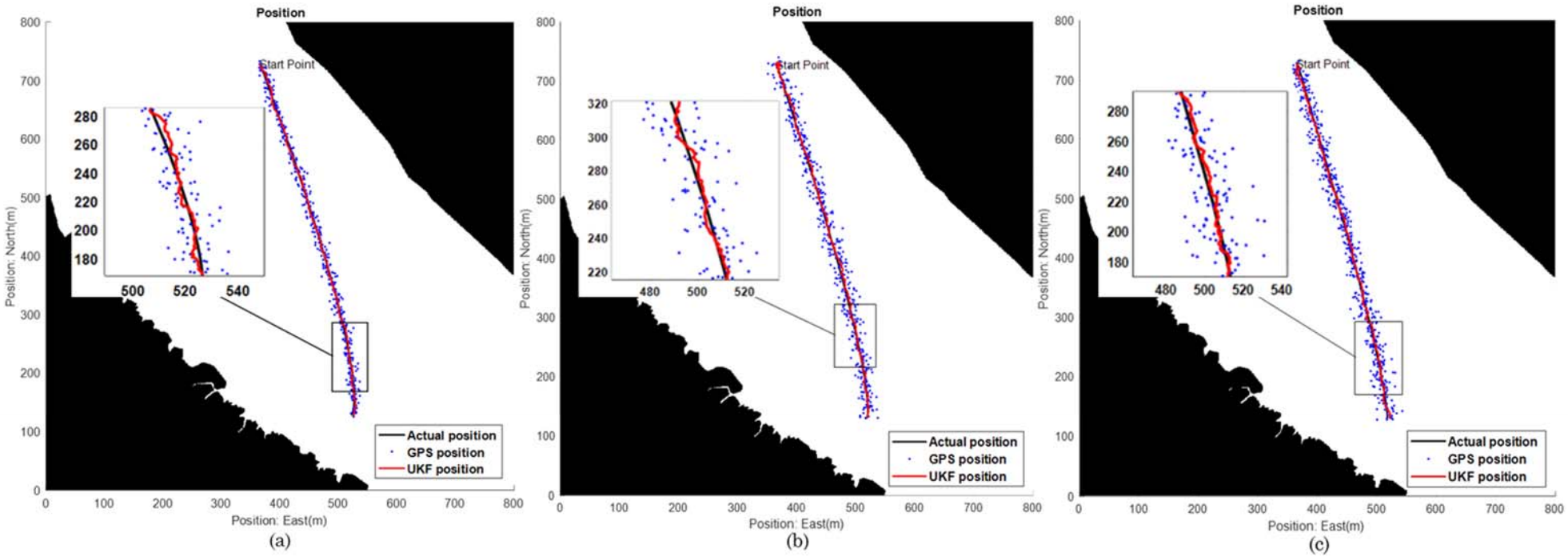

Figure 4. 15 Simulation Scenario 4.3: the converted binary map with the simulated GPS measurements and fused position results: (a) current: 0.5 m/s; (b) current: 0.3 m/s; (c) current: 0.15 m/s

In the simulations, the USV completed all three missions by tracking the predesigned end points using the methodology demonstrated earlier in this section and reached the end point in the environments with three different water current speeds, 0.5 m/s, 0.3 m/s and 0.15 m/s respectively. The trajectory results are displayed in the converted binary maps shown in Figures 4.15(a), (b) and (c). In each figure, the actual drift affected trajectories of the USV that are displayed in Figure 4.12(b) are represented by black lines. The simulated GPS measurements are denoted as blue dots. The red lines represent the trajectories formed by the estimated positions of the developed UKF based multi-sensor data fusion algorithm. The insets in each figure that are enlargements of part of the trajectories demonstrate the details of the simulation results. It can be seen that the red lines are very close to the black lines. The blue dots are more noisy for all three simulations, which indicates the developed UKF based multi-sensor data fusion algorithm is able to provide more accurate estimations of the USV's positions and reduce the error from the raw GPS measurements in a practical environment with water currents effects.

The estimated results of the USV headings in the environments with three different currents are illustrated in Figures 4.16 (a), (b) and (c). The effects on the USV's navigational data are more clearly shown in these three figures. When the speed of the water current is higher, the USV has to make more heading corrections to mitigate against the current influence, but it takes less time for the USV to reach the end point because the direction of the water current is generally coincident to USV's planned direction. Regardless of the speed of the current, it is clear that the red lines representing the fused headings closely adhere to the actual headings (black lines) with less obvious error than the compass raw measurements (blue lines) as shown in the enlarged inset.

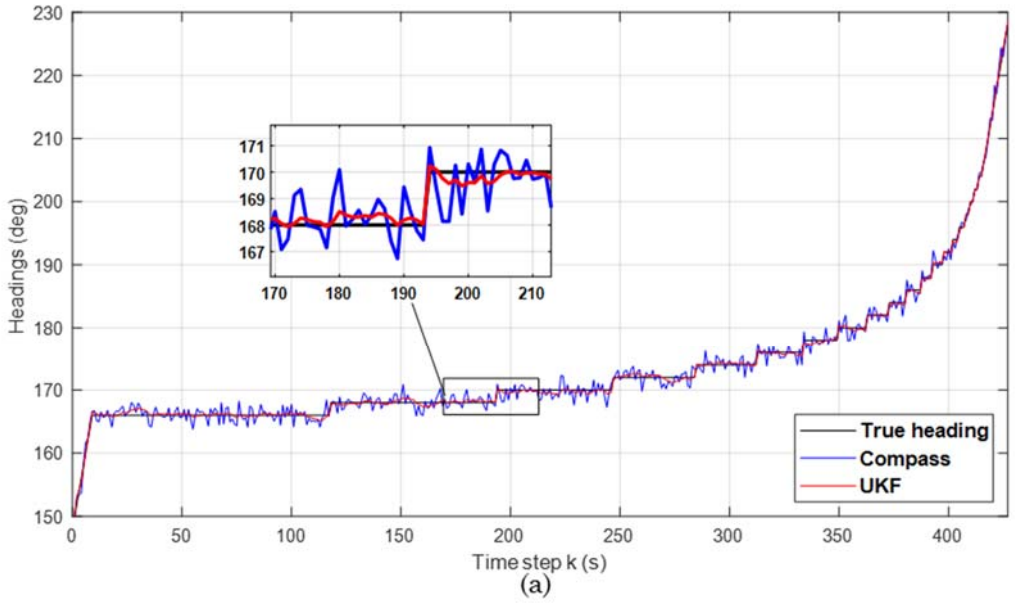

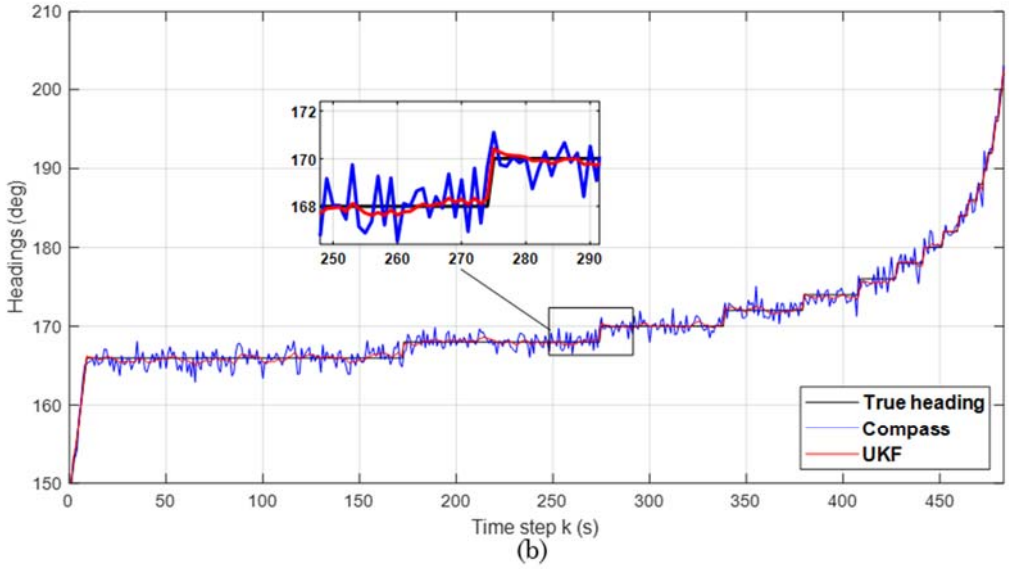

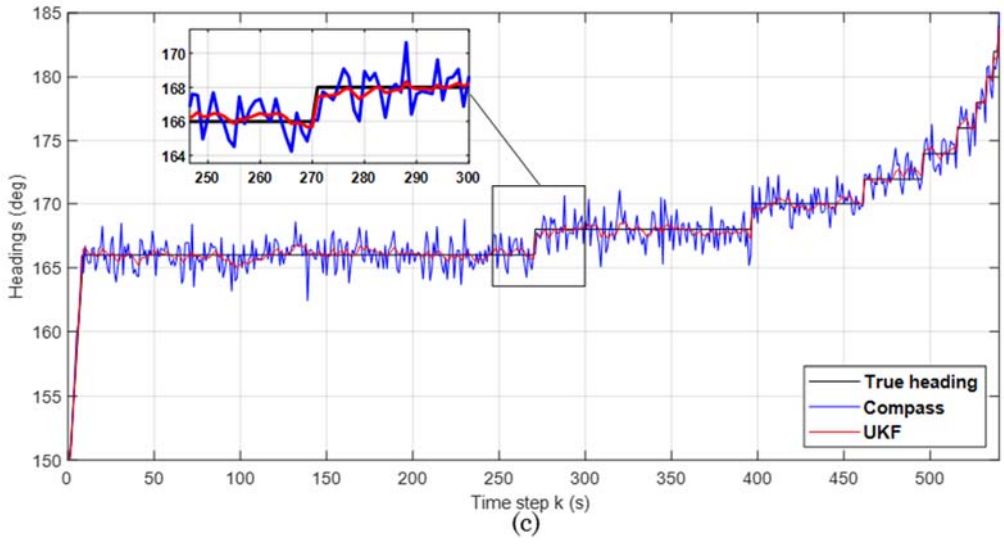

Figure 4. 16 Simulation Scenario 4.3: Actual headings, compass measurements and fused heading results: (a) current: 0.5 m/s; (b) current: 0.3 m/s; (c) current: 0.15 m/s

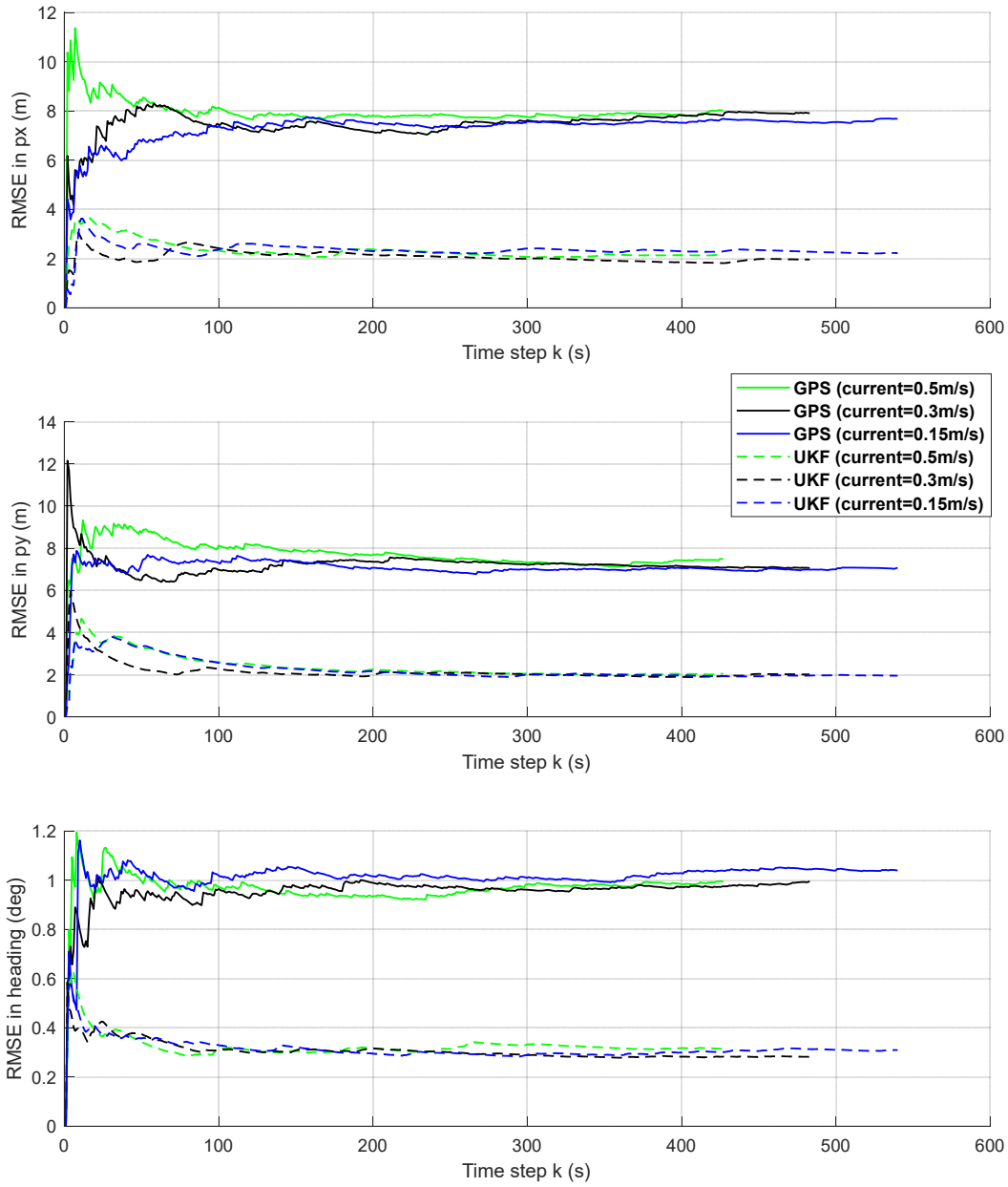

Figure 4. 17 Simulation Scenario 4.3: Rooted mean square errors (RMSEs) of the USV's positions and headings for the environment with three different currents

The improved performance of the algorithm is further exemplified in Figure 4.17, in which the rooted mean square errors (RMSEs) of the USV's positions in the x-axis and y-axis and USV headings are demonstrated. The figure clearly shows the RMS error of the fused positions in both x-axis and y-axis are reduced to around 2 meters and the RMS error of the fused heading is reduced to less than 0.4° regardless of the water current speed. Table 4.5 lists the mean square errors after the USV completes its mission that provides numerical proofs.

Table 4. 5 Simulation Scenario 4.3: Mean Square Errors

Method	***MSE 0.5m/s***	***MSE 0.3m/s***	***MSE 0.15m/s***	***Units***
UKF_position $\boldsymbol{p_x}$	4.972	4.746	3.8618	m^2
UKF_position $\boldsymbol{p_y}$	4.4747	4.2782	3.7013	m^2
GPS position $\boldsymbol{p_{gpsx}}$	66.6812	56.5433	63.4131	m^2
GPS position $\boldsymbol{p_{gpsx}}$	51.0834	48.0087	48.4819	m^2
UKF_heading ψ	0.1109	0.0926	0.0892	deg^2
Electronic Compass ψ_c	0.9261	0.9469	1.0015	deg^2

4.3.3.2. Simulation Scenario 4.4: Two turning manoeuvres

After proving the effectiveness of the developed UKF based multi-sensor data fusion algorithm in a simple mission with a straight line trajectory in a practical marine environment with three different constant current speeds, Scenario 4.4 simulates a more complex environment with varied water currents and assigns manoeuvring missions to the USV instead of following a straight line. Two waypoints were set for the USV to conduct manoeuvres. The initial state is shown in Equation (4.57) and the planned start point, manoeuvring waypoints and the end point are shown in Table 4.6.

$$\boldsymbol{x}(1) = [765 \quad 728 \quad -0.5 \quad -0.866 \quad 210]^T \tag{4.57}$$

Table 4. 6 Waypoint settings in Simulation Scenario 4.4

Planned Trajectory	**Start point**	**Waypoint 1**	**Waypoint 2**	**End point**
T1	(765,728)	(650,385)	(320,190)	(30,250)
T2	(765,728)	(580,385)	(380,190)	(30,250)
T3	(765,728)	(650,200)	(320,260)	(30,250)

Figure 4.18 (a) shows three planned manoeuvring trajectories and the water current at the speed of 0.5 m/s in varied directions. The drifted trajectories are illustrated in Figure 4.18 (b).

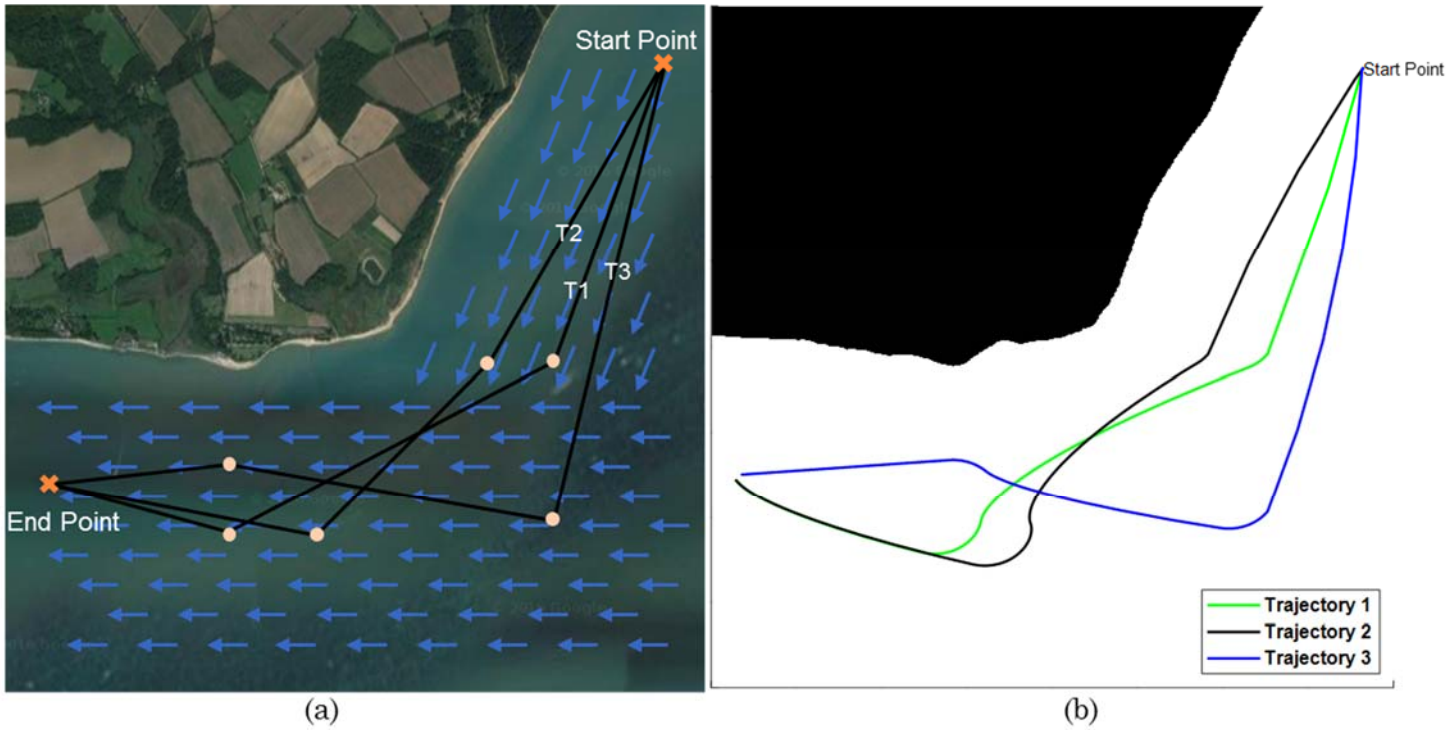

Figure 4. 18 Simulation Scenario 4.4: testing environment in Solent. (a) shows the satellite map with planed waypoint tracking trajectory of the USV, a varying current is simulated along the coastline; (b) gives the binary map that converted from the satellite map with the drifted trajectory of the USV caused by the varying current

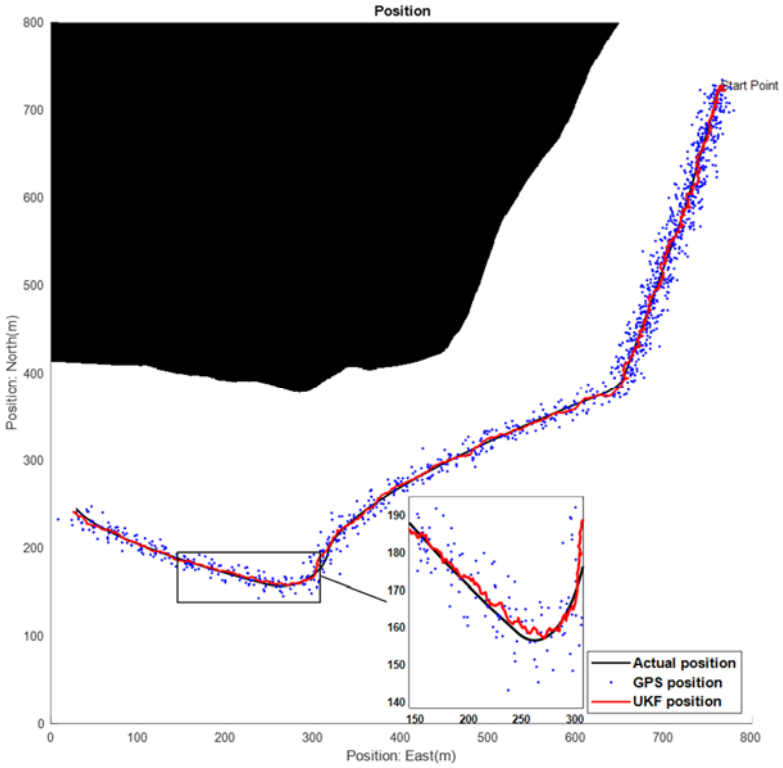

Figure 4. 19 Simulation Scenario 4.4: the converted binary map with the simulated GPS measurements and fused position result of planned trajectory 1

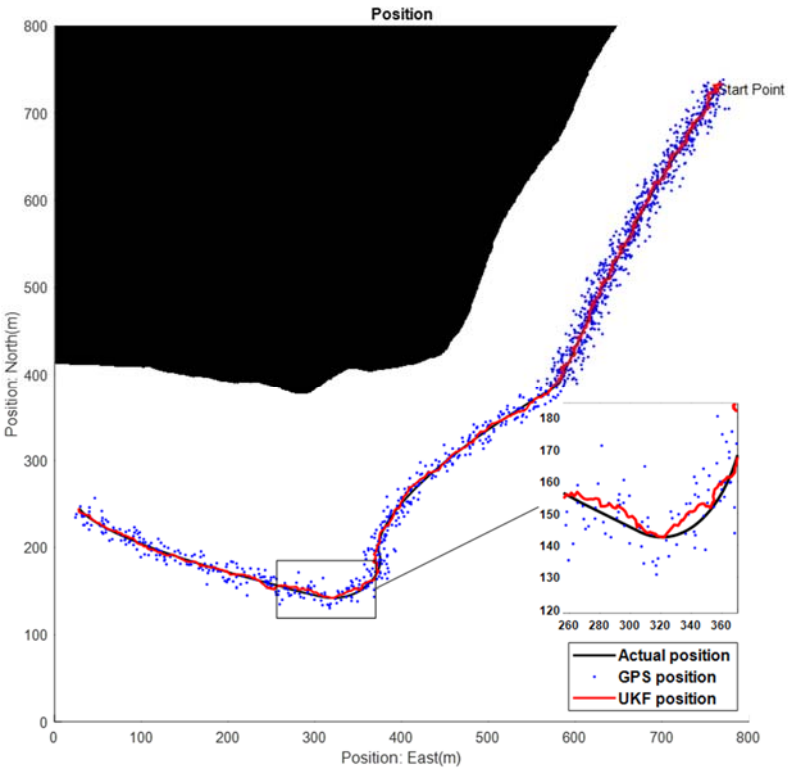

Figure 4. 20 Simulation Scenario 4.4: the converted binary map with the simulated GPS measurements and fused position result for planned trajectory 2

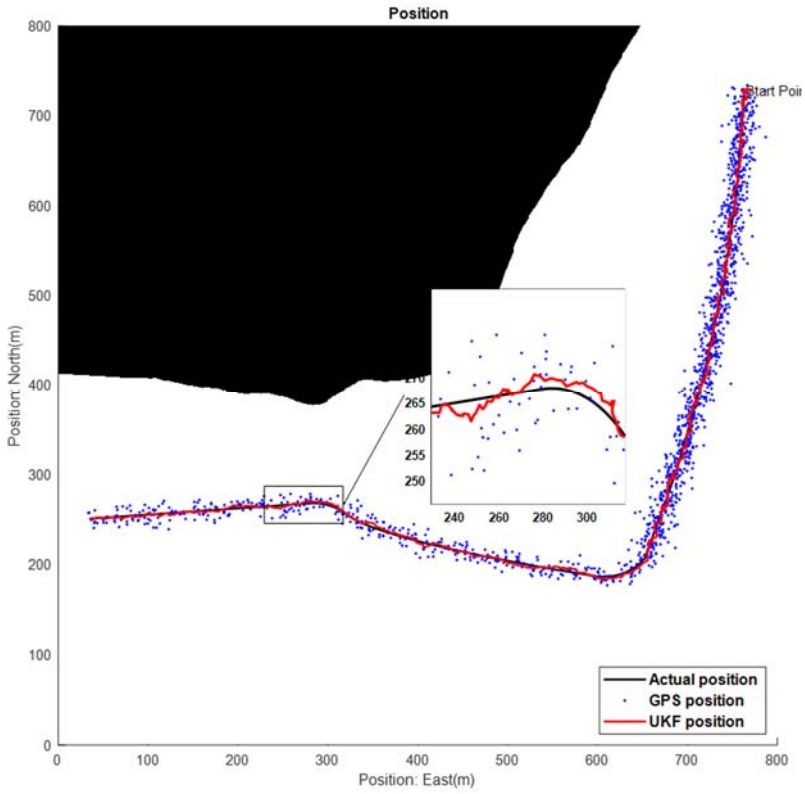

Figure 4. 21 Simulation Scenario 4.4: the converted binary map with the simulated GPS measurements and fused position results for planned trajectory 3

In a similar fashion to the Simulation Scenario 4.3, Figures 4.19 to 4.21 display the drift influenced trajectories (the black lines) of the USV for the three different missions denoted as Simulation Scenario 4.4. The speed of the current imposes different alterations to each trajectory. The GPS measurements denoted as blue dots are scattered around the altered trajectories and the fused trajectories are represented as red lines. From the enlarged insets of all three figures, it can be seen that the red lines are closer to the black lines while the blue dots indicate increased noise. The error reduction of the fused position results prove that the developed UKF based data fusion algorithm works well when the USV is assigned more complex missions that require turning manoeuvres and is able to provide more accurate estimations of USV's position in a practical environment with more complex disturbances.

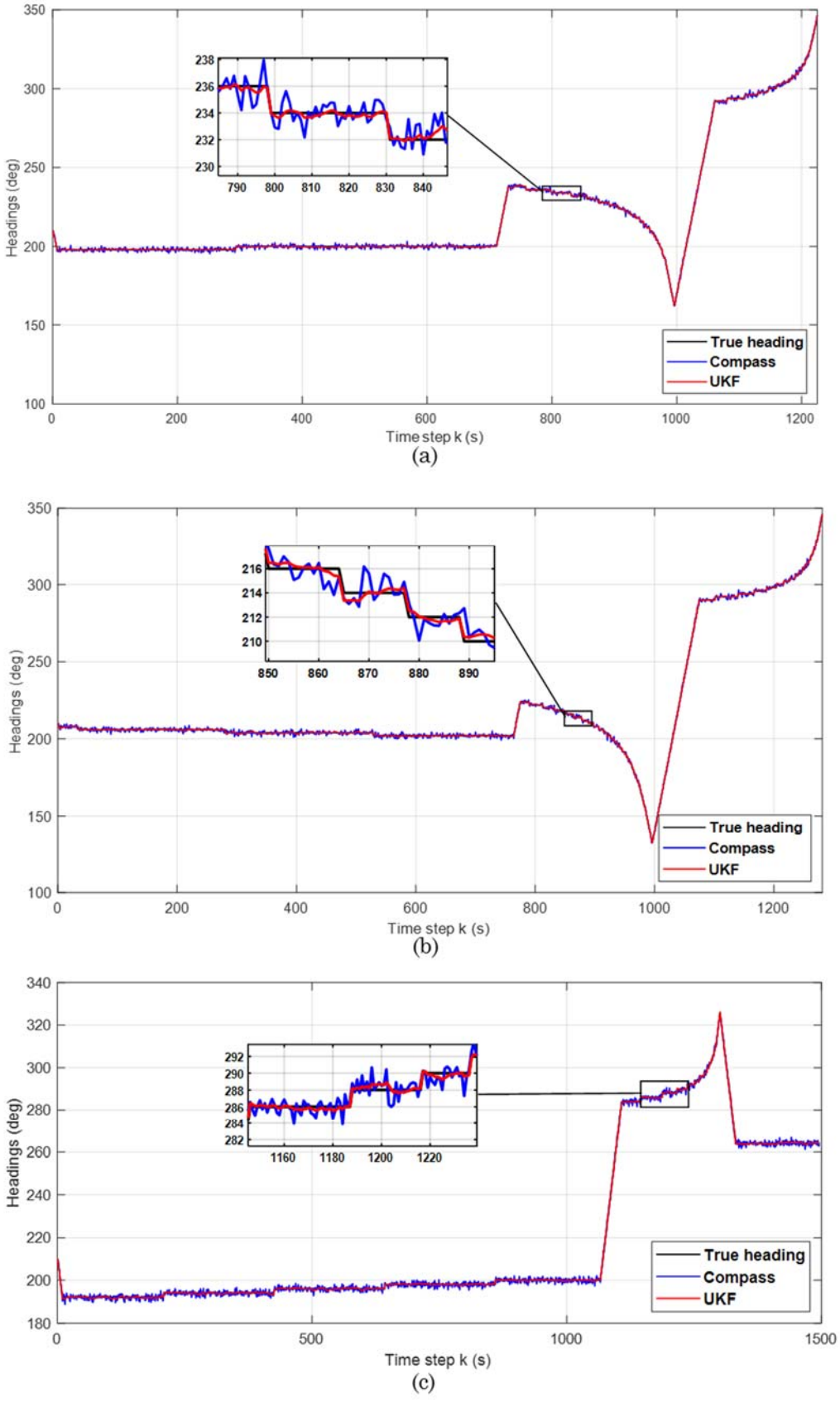

Figure 4. 22 Simulation Scenario 4.4: actual headings, compass measurements and fused heading results (a) planned trajectory 1; (b) planned trajectory 2; (c) planned trajectory 3

Figure 4.22 (a), (b) and (c) demonstrate the actual headings (black line), raw compass measurements (blue dots) and fused heading results (red lines) of each mission. From the enlarged insets, it can be seen clearly that no matter where the manoeuvring waypoints are, the fused headings are much closer to the actual headings than the compass measurements, which again confirms the developed data fusion algorithm's ability to reduce raw sensor measurement errors.

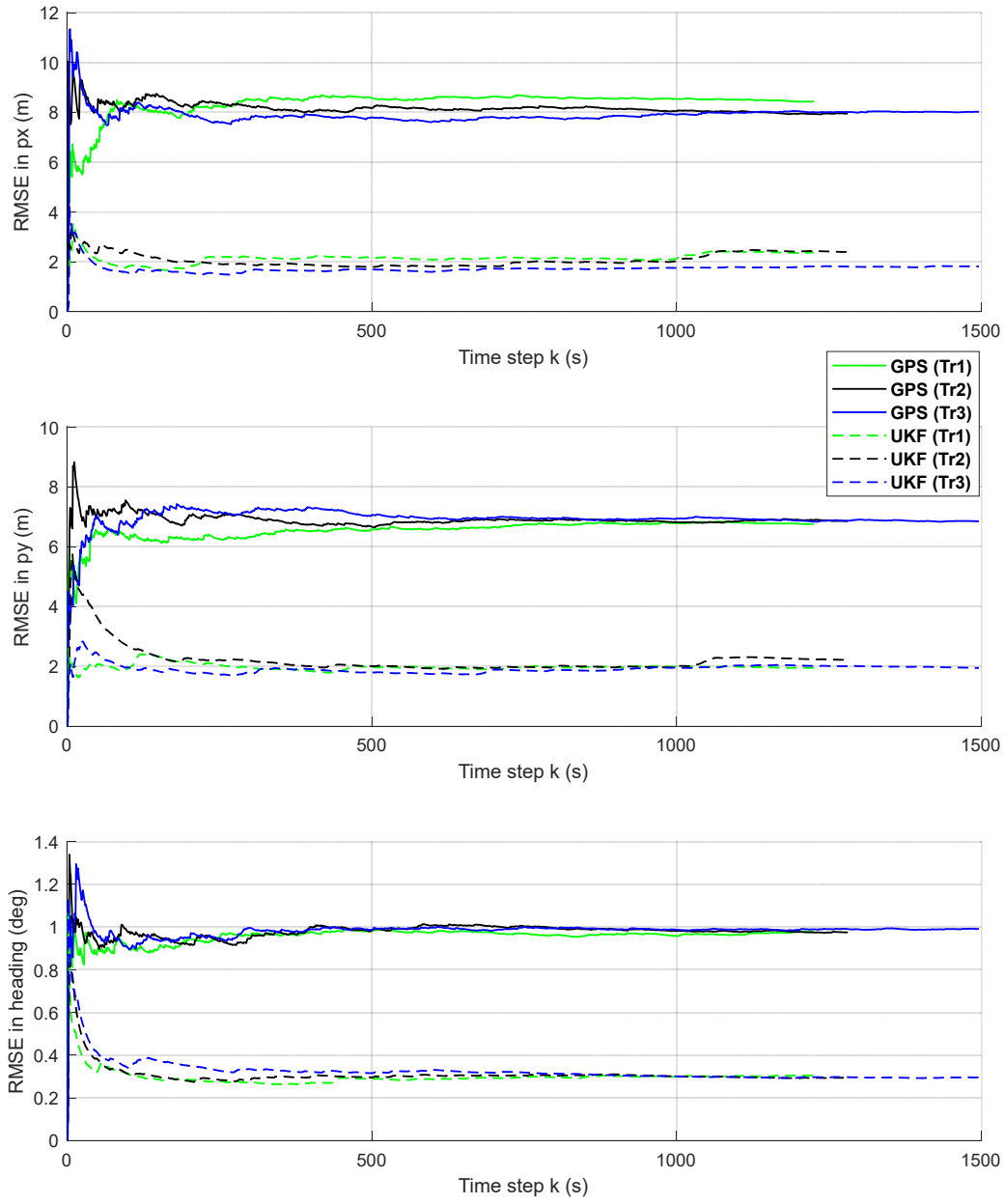

Figure 4. 23 Simulation Scenario 4.4: Rooted mean square errors (RMSEs) of the USV's positions and headings for three different planned trajectories

Even though the USV conducts more complicated manoeuvres in a more complex environment, the developed algorithm still performs satisfactorily in estimating the navigational data for each mission. The RMS errors and MSEs shown in Figure 4.23 and Table 4.7 provide further evidence of the algorithm's capability in reducing raw sensor measurement errors for USV navigation. It can be concluded that the UKF based multi-sensor data fusion algorithm can generate good results for USV navigation in a practical environment with no restrictions on path planning.

Table 4. 7 Simulation Scenario 4.4: Mean Square errors

Method	***MSE (Tr1)***	***MSE (Tr2)***	***MSE (Tr3)***	***Units***
UKF_position $\boldsymbol{p_x}$	5.1926	5.7334	3.2977	m^2
UKF_position $\boldsymbol{p_y}$	3.7565	4.8809	3.7728	m^2
GPS position $\boldsymbol{p_{gpsx}}$	60.1971	63.1284	64.2108	m^2
GPS position $\boldsymbol{p_{gpsx}}$	46.8124	47.041	46.8535	m^2
UKF_heading $\boldsymbol{\psi}$	0.0956	0.0863	0.0876	deg^2
Electronic Compass $\boldsymbol{\psi_c}$	0.9799	0.9473	0.9822	deg^2

4.4. Summary

In this chapter the effect of the inherent accuracies of navigational sensors on USV navigation was examined. Initially the use of multiple sensors to overcome such inaccuracies was posited when it was determined that USV positional uncertainty would still exist and this uncertainty was quantified. To improve positional certainty data fusion techniques were investigated, primarily for the statically positioned USV.

It was found that although the predictive-corrective iterative methodology improved positional estimation certainty, the results conversion was still affected by each particular sensors' bias and inaccuracy. To reduce the effects of the sensor noise Kalman Filtering was investigated as a means to improve the accuracy of the navigational data. A system measurement model was developed and tested by simulations with manufacturer's data on sensor noise performance applied. The

simulations using the KF based data fusion algorithm displayed improved accuracy for both the static and moving USV.

The next stage was to move from a quiet environment to one where there the environment itself was subject to disturbances. Although the KF methodology provided credible results the environmental noise was noticeable and would mean that the fused sensor data results would not be satisfactory for practical USV autonomous navigation in highly disturbed environments. It was with this in mind that the UKF based data fusion algorithm was developed and applied.

Navigational positioning results using the UKF showed close correlation between the actual USV position and that of the predicted UKF position and improved upon the raw sensor data indication of position. Based on this improvement performance further development of the UKF algorithm and application will be examined in Chapter 5.

Chapter 5. Robust Kalman Filtering

In the previous chapter, Unscented Kalman Filter (UKF) based multi-sensor data fusion algorithms were developed for USV navigation in a practical environment. Multiple simulations showed that the algorithm is able to reduce the error of raw sensor measurements and provide more accurate estimations of the USV's navigational data even though the USV is conducting manoeuvres and is being influenced to drift from its planned trajectory. However, apart from environmental effects, practical applications could apply more interference to the data fusion algorithm. For example, sensor measurement errors may vary during operation, which could lead to inaccurate *a priori* knowledge of system measurement noises. This chapter will discuss situations in practical applications when the system lacks accurate *a priori* system measurement noises and subsequent effects on navigation in an influenced environment.

5.1. Adaptive estimation for robust Kalman filtering

The Unscented Kalman Filter (UKF) employs the unscented transform to form sigma points and propagate the points through a non-linear equation to approximate the mean and covariance of the system state. Theoretically, it is therefore able to provide more accurate results when working in such a non-linear system. However, conventional UKF largely relies on accurate *a priori* knowledge of the characteristics of system process noise (Q) and system measurement noise (R), which can be easily altered by practical environment effects. In practice, sensor noise is not guaranteed to be close to the RMS error stated in the sensor manual. According to Hightower and President (2008), in a dynamic environment, the GPS receiver provides constantly changing measurements and therefore increases its measurement error.

Driven by the nature of Kalman filtering, data fusion algorithms based on conventional UKF require accurate *a priori* knowledge on the characteristics of system noise (Hu et al, 2003). When constructing a conventional UKF, the *a priori*

system noise is commonly based on best knowledge of system noises from previous data. However, in practical applications this approach is normally associated with uncertainties. In particular, the uncertainties in system processing noise and measurement noise have a large impact on the conventional UKF, and thereby result in degraded performance (Tseng, 2016 and Zheng, 2018). An adaptive estimation algorithm to match the system processing noise covariance Q and measurement noise covariance R is a solution to accommodate the influences caused by inaccurate *a priori* knowledge of the characteristics of system noise and contributes to a more robust system. The adaptive estimation algorithm is able to determine the system noise covariance of the dynamic system in real time so that the UKF data fusion algorithm can approximate the system state, based upon the determined real-time statistical parameters together with the observed data.

Wang et al. (2015) proposed a fuzzy logic based adaptive KF algorithm to adapt the two noise parameters to determine the attitudes of a satellite. The algorithm defines an adjustment coefficient according to the designed fuzzy logic system to update the processing error covariance and measurement error covariance for the next state. Jin et al. (2014) proposed a fuzzy logic based adaptive estimation method to correct the measurement noise covariance in the KF operation for the inertial motion capture system. Rahimi et al. (2015) extended the adaptive research into the conventional UKF and detailed the matching between the theoretical and actual processing and measurement error covariance for reaction wheels application. These studies on a range of practical applications validate and demonstrate the effectiveness of the adaptive estimation for conventional KF/UKF based algorithms.

Previous effort has also been made in the field of navigation. Almagbile et al. (2010) demonstrated the performance of covariance matching based adaptive KF methods with three different adaptive methods: processing error covariance matrix Q estimation; innovation based measurement error covariance matrix R estimation; and residual based R estimation in improving GPS measurements. They compared the RMS errors of the estimated positions under these adaptive methods. Results have demonstrated that although all adaptive methods exhibit stable estimation characteristics, Q adaptation corresponds to larger RMS error and lower

convergence speed when compared to both innovation based and residual based R adaptations. Meng et al. (2016) deduced an adaptive estimating algorithm based on the UKF for both Q and R adaptation simultaneously and applied it to the Global Navigation Satellite System (GNSS) and Inertial Navigation System (INS) hybrid navigation system. However, their method to determine the real-time R matrix was achieved by simply adjusting its theoretical value to the calculated actual value. Compared to the processing error, measurement noise, which is prone to alteration, has a greater impact on the performance of data fusion algorithms since the practical condition of the sensors is difficult to predict and evaluate, detrimentally affecting the data fusion algorithms.

5.1.1. Covariance matching adaptive estimation

The innovation-based adaptive estimation has been mainly used to match the noise covariance. Based on the operation of the conventional UKF process (Equations (4.14) to (4.17) and (4.45) to (4.53)), the system innovation $\boldsymbol{\epsilon}$, which is defined as the difference between the measurement $\boldsymbol{z}$ and system prediction $\boldsymbol{x}^{-}$, and its theoretical covariance $\boldsymbol{C_T}$ can be computed as below:

$$\boldsymbol{\epsilon}(k) = \boldsymbol{z}(k) - \boldsymbol{H}\boldsymbol{x}^{-}(k) \tag{5.1}$$

$$\boldsymbol{C_T}(k) = \boldsymbol{H}\,\boldsymbol{P}^{-}(k)\,\boldsymbol{H}^{T} + \boldsymbol{R} \tag{5.2}$$

In the meantime, for a dynamic system, the actual covariance of innovation $\boldsymbol{C_A}(k)$ is obtained from sensor observations and can be calculated as the mean of previous innovations over a moving window size N in a recursive manner (Rahimi, et al, 2015; Yang et al, 2018):

$$\boldsymbol{C_A}(k) = \frac{1}{N}\sum_{j=k-N+1}^{k}\big(\boldsymbol{\epsilon}(j)\big)\big(\boldsymbol{\epsilon}(j)\big)^{T} \tag{5.3}$$

$$\boldsymbol{C_A}(k) = \boldsymbol{C_A}(k-1) + \frac{1}{N}\Big(\big(\boldsymbol{\epsilon}(k)\big)\big(\boldsymbol{\epsilon}(k)\big)^{T} - \big(\boldsymbol{\epsilon}(k-N+1)\big)\big(\boldsymbol{\epsilon}(k-N+1)\big)^{T}\Big) \tag{5.4}$$

Now match the theoretical covariance $\boldsymbol{C_T}(k)$ to the actual covariance $\boldsymbol{C_A}(k)$

$$\boldsymbol{C_T}(k) = \boldsymbol{C_A}(k) \tag{5.5}$$

So that the measurement noise covariance $\boldsymbol{R}$ can be updated as

$$\widehat{\boldsymbol{R}}(k) = \boldsymbol{C_A}(k) - \boldsymbol{H}\,\boldsymbol{P}^{-}(k)\,\boldsymbol{H}^{T} \tag{5.6}$$

The subscription equation may generate a negative outcome that would lead to system errors. Therefore, the residual sequence has been considered to replace the innovations.

$$\boldsymbol{\varepsilon}(k) = \boldsymbol{z}(k) - \widehat{\boldsymbol{x}}(k) \tag{5.7}$$

$$\boldsymbol{C_{AR}}(k) = \frac{1}{N}\sum_{j=k-N+1}^{k}\big(\boldsymbol{\varepsilon}(k)\big)\big(\boldsymbol{\varepsilon}(k)\big)^{\boldsymbol{T}} \tag{5.8}$$

$$\widehat{\boldsymbol{R}}(k) = \boldsymbol{C_{AR}}(k) + \boldsymbol{H}\,\boldsymbol{P}^{-}(k)\,\boldsymbol{H}^{T} \tag{5.9}$$

Covariance matching is widely used in adaptive estimations. The theoretical measurement covariance is made to be equal to the actual measurement covariance (Meng et al, 2016).

5.1.2. Improved fuzzy logic based adaptive estimation

As stated in the last section, the innovation based estimation cannot guarantee that the outcomes are always positive. Therefore, an improved UKF is proposed to assist with robust USV navigation. The novelty of this method lies in the fact that a fuzzy logic based noise covariance adaptive estimation is developed to compensate sensors' noises and improve overall localisation performance. The framework of this algorithm is illustrated in Figure 5.1, where the working process of the UKF has been divided into two parts, namely the UKF prediction module and UKF estimation module. Different navigational sensors are employed to provide raw sensor measurements, i.e. the inertial measurement unit (IMU) is able to measure a USV's acceleration and rotation so that the UKF prediction module can calculate and predict the vehicle's position and heading, while the GPS and electronic compass provide absolute measurements of the USV's position and heading, which are then fed into the UKF estimation module to make optimal estimations. Apart from the standard operation of the UKF, the proposed fuzzy logic based adaptive estimation has been added to the algorithm to correct the measurement noise covariance. The theoretical covariance $\boldsymbol{C_T}$ and the actual covariance $\boldsymbol{C_A}$ of the innovation sequence $\boldsymbol{\epsilon}$, which is defined as the difference between the measurement $\boldsymbol{z}$ and system prediction $\boldsymbol{x^-}$ in Equation (5.1) are calculated and their similarity is the input to the fuzzy logic system (Jin et al, 2014). The system

then adjusts the $\boldsymbol{C_T}$ to match the $\boldsymbol{C_A}$ by tuning the UKF measurement noise covariance R. This newly developed algorithm delivers a more practical solution to solve the problem of the robust localisation of an USV.

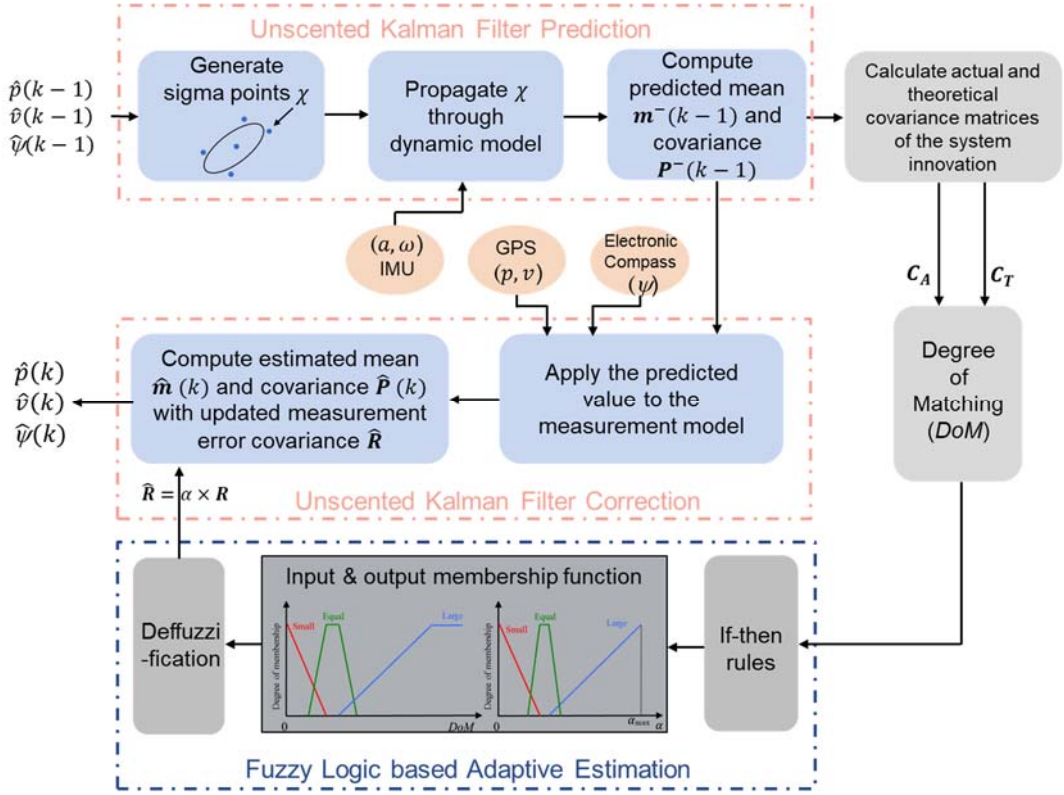

Figure 5.1 Framework of the proposed Adaptive Unscented Kalman Filter Algorithm

If the fixed value of the measurement noise covariance matrix $\boldsymbol{R}(k)$ is close to that of the actual measurement noise covariance, it makes the theoretical covariance of innovation $\boldsymbol{C_T}(k)$ equal to the actual covariance of innovation $\boldsymbol{C_A}(k)$. However, in real applications, sensor disturbances could make $\boldsymbol{C_A}(k)$ differ from $\boldsymbol{C_T}(k)$, and to improve the performance of the UKF, $\boldsymbol{R}(k)$ should be adjusted according to the similarity of $\boldsymbol{C_A}(k)$ and $\boldsymbol{C_T}(k)$, which is expressed as multi-factor Degree of Matching ($\boldsymbol{DoM}$) in this paper which is defined as:

$$\boldsymbol{DoM}(k) = \boldsymbol{C_A}(k)/\boldsymbol{C_T}(k) \tag{5.10}$$

Based upon $\boldsymbol{DoM}$, the fuzzy logic based algorithm is developed to adapt the system measurement noise covariance matrix $\widehat{\boldsymbol{R}}(k)$, which can be updated by an adjustment coefficient $\boldsymbol{\alpha}(k)$ as:

$$\widehat{\boldsymbol{R}}(k) = \boldsymbol{\alpha}(k) \times \boldsymbol{R}(k) \tag{5.11}$$

where $\boldsymbol{\alpha}(k)$ is determined by the $\boldsymbol{DoM}(k)$ using fuzzy logic.

In general, the relationship between each element of the coefficient $\boldsymbol{\alpha}(i,k)$ and each element of $\boldsymbol{DoM}(i,k)$ can be described as

If $\boldsymbol{DoM}(i,k) > 1$, $\boldsymbol{C_A}(i,k)$ is larger than $\boldsymbol{C_T}(i,k)$, $\boldsymbol{R}(i,k)$ should be increased to reduce the two innovation covariances, then $\boldsymbol{\alpha}(i,k)$ should be greater than 1;

If $\boldsymbol{DoM}(i,k) \sim = 1$, $\boldsymbol{C_A}(i,k)$ is similar to $\boldsymbol{C_T}(i,k)$, then $\boldsymbol{\alpha}(i,k)$ should equal to 1 to maintain $\boldsymbol{R}(i,k)$ unchanged;

If $\boldsymbol{DoM}(i,k) < 1$, $\boldsymbol{C_A}(i,k)$ is smaller than $\boldsymbol{C_T}(i,k)$, $\boldsymbol{R}(i,k)$ should be deceased, then $\boldsymbol{\alpha}(i,k)$ should be reduced to be less than 1.

The fuzzy rules with thresholds ($ep1$ and $ep2$) can then be defined based on the relationship between $\boldsymbol{\alpha}$ and $\boldsymbol{DoM}$ as in Table 5.1.

Table 5.1 Fuzzy rules

Rule 1: If $\boldsymbol{DoM > 1 + \varepsilon 2}$, then $\boldsymbol{\alpha}$ is large;
Rule 2: If $\boldsymbol{1 - \varepsilon 1 \leq DoM \leq 1 + \varepsilon 1}$, then $\boldsymbol{\alpha}$ is equal;
Rule 3: If $\boldsymbol{DoM < 1 - \varepsilon 2}$, then $\boldsymbol{\alpha}$ is small.

The fuzzy rules with thresholds ($ep1$ and $ep2$) can then be defined based on the relationship between each element of $\boldsymbol{\alpha}$ and $\boldsymbol{DoM}$ in Table 5.1. The thresholds $ep1$ and $ep2$ are two small values used to create intersections between each fuzzy rule that allows the algorithm to compute the adjustment coefficient $\boldsymbol{\alpha}$ in a fuzzy way.

The range of each element of $\boldsymbol{DoM}$ at each time step k is divided into six bands to define the following input membership functions of the fuzzy system, which are also illustrated in Figure 5.2.

Large:

$$\mu_l = \begin{cases} 1 & \boldsymbol{DoM}(i,k) > max \\ \frac{1}{max-1-ep2} \times \boldsymbol{DoM}(i,k) + \frac{1+ep2}{ep2+1-max} & 1+ep2 < \boldsymbol{DoM}(i,k) \leq max \end{cases} \quad (5.12)$$

Equal:

$$\mu_e = \begin{cases} \frac{1}{ep2-ep1} \times \boldsymbol{DoM}(i,k) + \frac{1+ep1}{ep1-ep2} & 1+ep2 < \boldsymbol{DoM}(i,k) \leq 1+ep1 \\ 1 & 1-ep2 < \boldsymbol{DoM}(i,k) \leq 1+ep2 \\ \frac{1}{ep1-ep2} \times \boldsymbol{DoM}(i,k) + \frac{ep1-1}{ep1-ep2} & 1-ep1 \leq \boldsymbol{DoM}(i,k) \leq 1-ep2 \end{cases} \quad (5.13)$$

Small:

$$\mu_s = \frac{1}{ep2-1} \times \boldsymbol{DoM}(i,k) + 1 \quad \boldsymbol{DoM}(i,k) < 1-ep2 \quad (5.14)$$

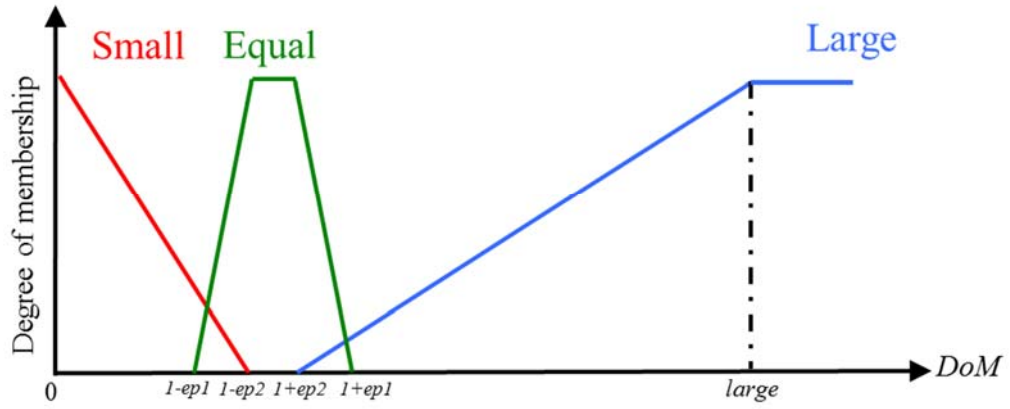

Figure 5.2 Input membership functions

Based on the fuzzy rules, the output membership functions can then be determined using Equations (5.15) to (5.17), which are also expressed in Figure 5.3.

Large:

$$o_l = \frac{1}{al\_large-1-al\_ep2} \times \boldsymbol{\alpha}(i,k) + \frac{1+al\_ep2}{al\_ep2+1-al\_large} \quad \boldsymbol{\alpha}(i,k) > 1+al\_ep2 \quad (5.15)$$

Equal:

$$o_e = \begin{cases} \frac{1}{al\_ep2-al\_ep1} \times \boldsymbol{\alpha}(i,k) + \frac{1+al\_ep1}{al\_ep1-al\_ep2} & 1+al\_ep2 < \boldsymbol{\alpha}(i,k) \leq 1+al\_ep1 \\ 1 & 1-al\_ep2 < \boldsymbol{\alpha}(i,k) \leq 1+al\_ep2 \\ \frac{1}{al\_ep1-al\_ep2} \times \boldsymbol{\alpha}(i,k) + \frac{al\_ep1-1}{al\_ep1-al\_ep2} & 1-al\_ep1 \leq \boldsymbol{\alpha}(i,k) \leq 1-al\_ep2 \end{cases} \quad (5.16)$$

Small:

$$o_s = \frac{1}{al\_ep2-1} \times \boldsymbol{\alpha}(i,k) + 1 \quad \boldsymbol{\alpha}(i,k) < 1-al\_ep2 \quad (5.17)$$

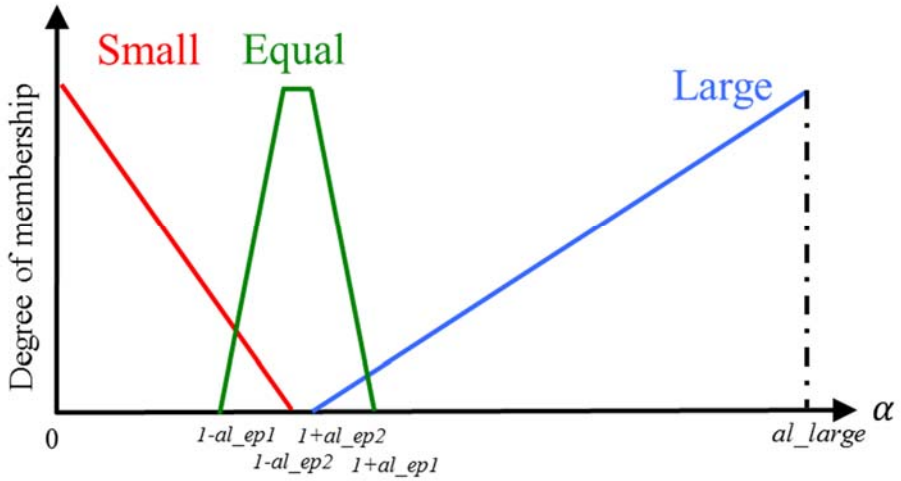

Figure 5.3 Output membership functions

Then, at each sampling time step k, the adjustment coefficient $\boldsymbol{\alpha}$ is de-fuzzified by applying Centroid methodology where multiple rules can be applied as:

$$\boldsymbol{\alpha}(i,k) = \int o_i(\boldsymbol{\alpha}(i,k))\, \boldsymbol{\alpha}(i,k)\, d\boldsymbol{\alpha}(i,k) / \int o_i(\boldsymbol{\alpha}(i,k))\, d\boldsymbol{\alpha}(i,k) \quad (5.18)$$

The following cases that are distributed by the ranges within which the DoM lies are analysed to determine the calculation of the adjustment coefficient α:

Case 1: $\boldsymbol{DoM}(i,k) < 1-ep1$, *rule 3* solely applies, and $\boldsymbol{\alpha}(i,k)$ is given by the horizontal projection of the centroid of the Small output membership function (Equation 5.19):

$$\boldsymbol{\alpha}(i,k) = (\mu_s(\boldsymbol{DoM}(i,k)) - 1) \times (\text{al\_ep2} - 1) \quad (5.19)$$

Case 2: $1 - al\_ep1 \leq \boldsymbol{\alpha}(i,k) \leq 1 - al\_ep2$, both *rule 2* and *rule 3* apply. As shown in Figure 5.4, according to the each element of $\boldsymbol{DoM}$, the degree of membership of the small and equal input membership function can be determined as $\mu_s(\boldsymbol{DoM}(i,k))$ and $\mu_e(\boldsymbol{DoM}(i,k))$, respectively. Then the corresponding α_s and α_e can be computed by the horizontal projection to the Small and Equal output membership functions using each element of $\boldsymbol{DoM}$ and $\boldsymbol{\alpha}$ is the centroid point of the orange area shown in Figure 5.4, which is determined by α_s and α_e.

$$\boldsymbol{\alpha}(i,k) =$$

$$\left(\int_{1-al_{ep1}}^{\alpha(\mu_e(DoM))} o_e \alpha d\alpha + \int_{\alpha(\mu_e(DoM))}^{\alpha(\mu_s(DoM))} \mu_e(DoM)\alpha(i,k)d\alpha(i,k) + \int_{\alpha(\mu_s(DoM))}^{1-al_{ep2}} o_s \alpha d\alpha\right) /$$

$$\left(\int_{1-al_{ep1}}^{\alpha(\mu_e(DoM))} o_e d\alpha + \int_{\alpha(\mu_e(DoM))}^{\alpha(\mu_s(DoM))} \mu_e(DoM) d\alpha + \int_{\alpha(\mu_s(DoM))}^{1-al_{ep2}} o_s d\alpha\right) \quad (5.20)$$

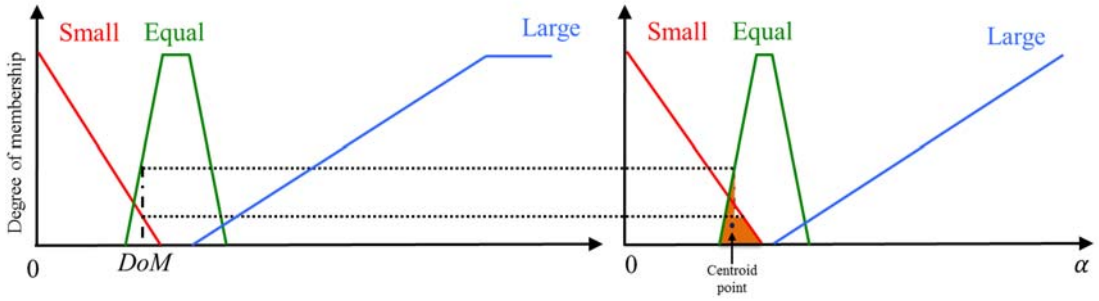

Figure 5.4 Calculation of the output α

Case 3: $1 - al\_ep2 < \boldsymbol{\alpha}(i,k) \leq 1 + al\_ep2$, only *rule 2* applies. $\boldsymbol{\alpha}(i,k)$ is determined by the horizontal projection to the Equal output membership function.

$$\boldsymbol{\alpha}(i,k) = 1 \quad (5.21)$$

Case 4: $1 + ep2 < \boldsymbol{DoM}(i,k) \leq 1 + ep1$, both *rule 1* and *rule 2* apply. The degree of membership of the Equal and Large input membership function can be determined as $\mu_e(\boldsymbol{DoM}(i,k))$ and $\mu_l(\boldsymbol{DoM}(i,k))$ and corresponding α_e and α_l can be computed by the horizontal projection to the Equal and Large input membership functions. $\boldsymbol{\alpha}$ is then calculated by the centroid method using each element of $\boldsymbol{DoM}$ as Equation (5.22).

$$\boldsymbol{\alpha}(i,k) = \left(\int_{1+al_{ep2}}^{\alpha(\mu_l(DoM))} o_l \alpha d\alpha + \int_{\alpha(\mu_l(DoM))}^{\alpha(\mu_e(DoM))} \mu_e(DoM)\alpha d\alpha + \int_{\alpha(\mu_e(DoM))}^{1+al_{ep1}} o_e \alpha d\alpha\right) / \left(\int_{1+al_{ep2}}^{\alpha(\mu_l(DoM))} o_l d\alpha + \int_{\alpha(\mu_l(DoM))}^{\alpha(\mu_e(DoM))} \mu_e(DoM) d\alpha + \int_{\alpha(\mu_e(DoM))}^{1+al_{ep1}} o_e d\alpha\right) \quad (5.22)$$

Case 5: $\boldsymbol{DoM}(i,k) > 1 + ep1$, *rule 1* applies solely, and $\boldsymbol{\alpha}(i,k)$ is given by the horizontal projection of the centroid of the Large output membership function (Equation (5.23)):

$$\boldsymbol{\alpha}(i,k) = \left(\mu_l(\boldsymbol{DoM}(i,k)) - \frac{1+al_{ep2}}{al_{ep2}+1-al_{large}}\right) \times \left(al_{large} - al_{ep2} - 1\right) \quad (5.23)$$

Once the adjustment coefficient α has been computed at time step k, the corrected measurement noise $\hat{R}(k)$ can be obtained and fed into the KF update process to make more accurate estimations. The terms in the adaptive fuzzy logic based UKF data fusion algorithm are summarised in Table 5.2.

Table 5.2 Terms in UKF and fuzzy adaptive settings

UKF settings	$\boldsymbol{x_0}$: Initial value of the state vector
	$\boldsymbol{P}_0$: Initial value of the error covariance
	$\boldsymbol{Q}$: Covariance of process noise
	$\boldsymbol{R}$: Covariance of measurement noise
Adaptive settings	$\boldsymbol{N}$: Moving window size
	$\boldsymbol{R_0}$: Initial covariance of measurement noise
	$\boldsymbol{ep1}$ and $\boldsymbol{ep2}$**:** Defined small ranges of input membership functions
	$\boldsymbol{max}$**:** Defined largest value of input membership functions
	$\boldsymbol{al\_ep1}$ and $\boldsymbol{al\_ep2}$ **:** Defined small ranges of output membership functions
	$\boldsymbol{al\_max}$ **:** Defined largest value of output membership functions

5.2. Simulations of improved adaptive UKF data fusion algorithm

Simulations are carried out to verify the proposed fuzzy adaptive UKF data fusion algorithm. The same simulation environment as detailed in simulation Scenario 4.4, where the USV carries out a mission with two turning manoeuvres in a complex marine environment with varied tidal current, is used. As detailed in Figure 4.9, which is re-displayed as Figure 5.5, the start point of the USV is at (765 m, 728 m) at the top right corner of the environment map and the end point (30 m, 250 m) is at the lower left of the map. Two waypoints (650 m, 385 m), (320 m, 190 m) have been assigned for the USV to follow and make manoeuvres to avoid any collision with the coastline. The varied tidal currents influence the planned straight line trajectories of the USV between each navigation point and the drift affected actual trajectory of the USV is shown in Figure 5.5(b).

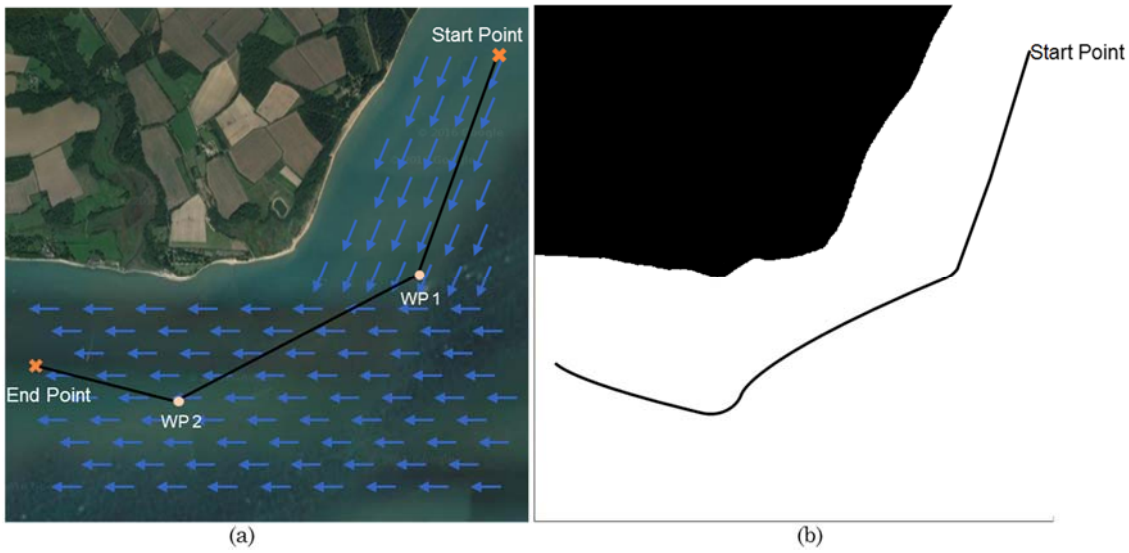

Figure 5.5 Simulation testing environment in Solent: (a) shows the satellite map with planed waypoint tracking trajectory of the USV, a varying current is simulated along the coastline; (b) gives the binary map that converted from the satellite map with the drifted trajectory of the USV caused by the varying current

In order to verify the working performance of the modified fuzzy adaptive UKF algorithm, three scenarios are considered: 1) a system with good knowledge of the *a priori* measurement noise; 2) a system with poor knowledge of the *a priori* measurement noise; 3) a system with good initial knowledge of the *a priori* measurement noise but with the actual sensor noise changes part way through the

operation. The UKF noise characteristics and the fuzzy adaptive estimation algorithm thresholds listed in Table 5.3 remain the same for all the three simulations.

Table 5.3 UKF characteristics and fuzzy system threshold

Accelerometer noise	$q_{1x} = 0.0039^2\ (m/s^2)^2$ $q_{1y} = 0.0039^2\ (m/s^2)^2$
Gyroscope noise	$q_2 = 0.033^2\ (deg/s)^2$
GPS noise	$r_{1x} = 6^2\ (m)^2$ $r_{1y} = 7^2\ (m)^2$
Compass noise	$r_2 = 0.5^2\ (deg)^2$
Input Membership Function Thresholds	$ep1 = 0.25$ $ep2 = 0.15$ $max = 7$
Output Membership Function Thresholds	$al\_ep1 = 0.2$ $al\_ep2 = 0.08$ $al\_max = 5$

5.2.1. Simulation Scenario 5.1: Good *a priori* system noise

In this simulation, the noise of the sensors' measurements are assumed to be predictable and are close to the predefined UKF error characteristics in Table 5.3. The simulated sensor errors for the sensor measurement models, which are expressed in Equations (4.30) and (4.31), during USV operation are listed in Table 5.4.

Table 5.4 Simulated sensor noise characteristics

Sensor	**Measurement**	**Noise**	
		Bias	**Variance**
IMU	Acceleration a_x	$0.03\ m/s^2$	$0.0042\ m/s^2$
	Acceleration a_y	$0.02\ m/s^2$	$0.0042\ m/s^2$
	Rotation rate ω	$0.28\,°/s$	$0.036\,°/s$
GPS	Position p_x	0	$8m$
	Position p_y	0	$7m$
Electronic Compass	Heading ψ	0	0.8°

Figures 5.6 to 5.9 show how the conventional UKF and fuzzy adaptive UKF improve raw measurements of the GPS and subsequently provide robust localisation

capability. A converted binary map of the simulation area is displayed in Figure 5.6 with the complete simulated USV actual trajectory shown as the black line. The GPS raw measurements as indicated as blue dots which are scattered around the true trajectory subject to the predefined variance. The fused position results of the conventional UKF and adaptive UKF are indicated as green and red lines respectively. From the enlarged inset in Figure 5.6, it can be seen that the red line (adaptive UKF result) is slightly closer to the black line than the green line (conventional UKF result), which indicates that the proposed adaptive UKF data fusion algorithm offers better performance as regards estimating the USV's real-time positions than the conventional UKF algorithm.

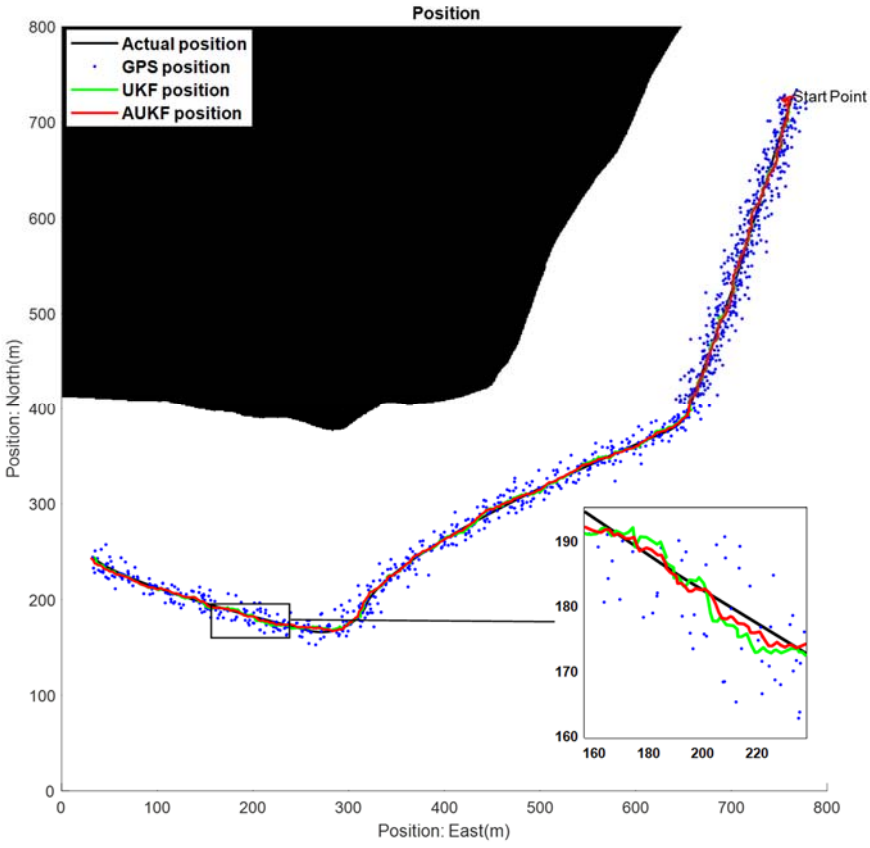

Figure 5. 6 Simulation Scenario 5.1: the trajectories of the USV

Figure 5.7 demonstrates the USV's heading results, where both conventional and adaptive UKF algorithms are able to reduce the raw compass measurement noises. Again the adaptive UKF algorithm offers marginal improvements in performance. This is also supported by Figure 5.8, which records the real time RMSEs of the measured and estimated positions and headings. The RMSEs of the adaptive UKF

estimations (red line) are slightly lower than those of the conventional UKF (green line) and they both are much lower than those of the raw sensor measurements.

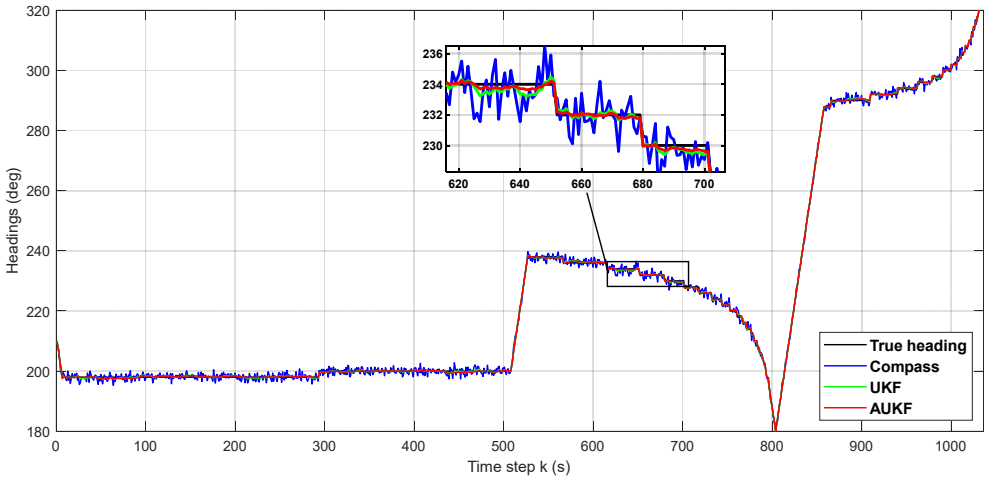

Figure 5. 7 Simulation Scenario 5.1: Measured and estimated USV headings

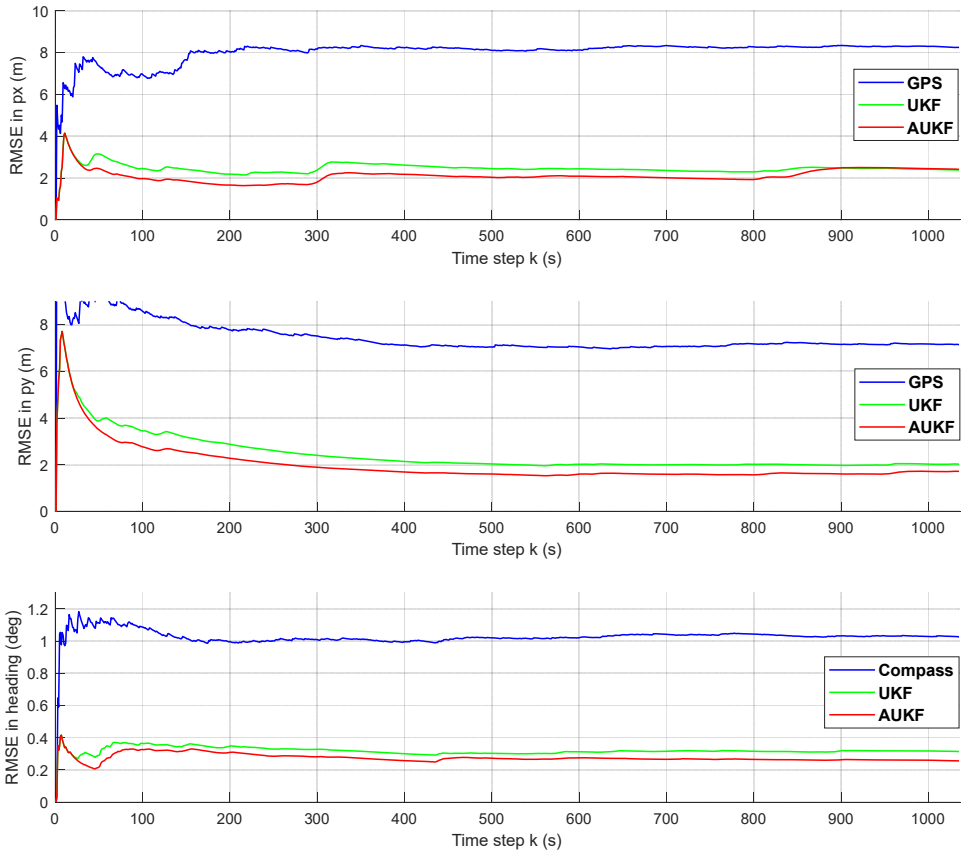

Figure 5. 8 Simulation Scenario 5.1: Rooted Mean Square Error (RMSE) of the USV's position

The diagonal elements of the measurement noise covariance matrix $\boldsymbol{R}$ are illustrated in Figure 5.9. The actual value of the measurement covariance $\boldsymbol{R_a}$ is obtained using Equations (5.24) and (5.25) and used to be compared with the estimated adaptive in the simulation results:

$$\boldsymbol{R}_a(k) = \frac{1}{N}\sum_{j=k-N+1}^{k}\big(\boldsymbol{v}(j)\big)\big(\boldsymbol{v}(j)\big)^T \tag{5.24}$$

where $\boldsymbol{v}$ is the measurement noise that can be computed as the difference between the sensor measurements $\boldsymbol{z}$ and actual USV navigational data $\boldsymbol{x_a}$ in Equation (5.25).

$$\boldsymbol{v}(k) = \boldsymbol{z}(k) - \boldsymbol{H}\boldsymbol{x}_a(k) \tag{5.25}$$

Since the simulated sensors noises are close to the predefined UKF noise characteristics, the actual value of R (black line) is close to the fixed value of R (blue line) used in the conventional UKF algorithm. The adjusted R (red line) by the fuzzy adaptive UKF algorithm fluctuates around the actual R. This simulation proves the effectiveness of the proposed fuzzy adaptive UKF data fusion algorithm. As long as the system has a good *a priori* knowledge of the sensor measurement noise characters, the conventional UKF algorithm is also able to provide accurate estimations of the USV's navigational data even when the USV is operating in a complex environment with turning manoeuvres. To further compare the results, the overall Mean Square Error (MSE) of the position estimations have been calculated and shown in Table 5.5. The smallest MSE value is generated using the fuzzy adaptive UKF with the MSE in x direction being 0.4989 m^2 and 0.2288 m^2 in y direction.

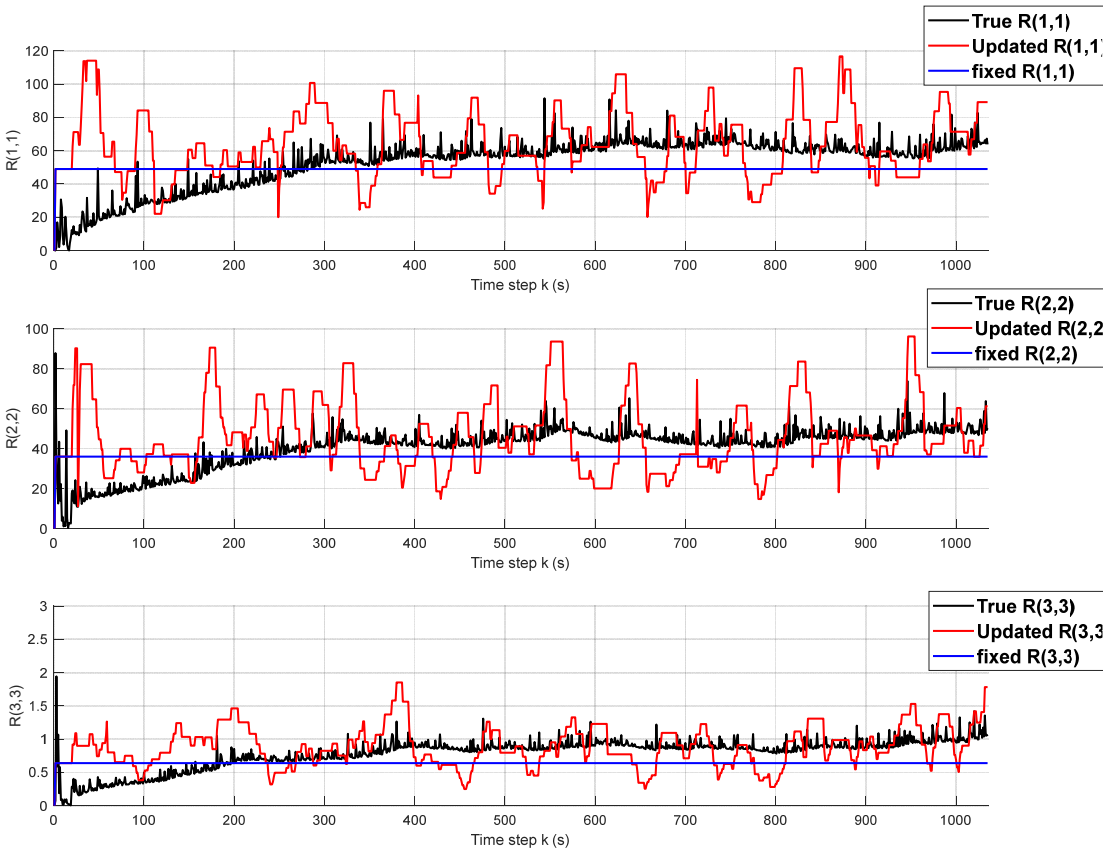

Figure 5. 9 Simulation Scenario 5.1: The two elements of measurement covariance ***R*** that related to position estimation

Table 5. 5 Simulation Scenario 5.1: Overall Mean Square Errors

Method	***MSE_px*** (m^2)	***MSE_py*** (m^2)	***MSE_ψ*** (deg^2)
GPS module	61.0478	50.1697	-
Electronic Compass	-	-	1.1112
Conventional UKF	4.6139	2.7207	0.1054
Adaptive UKF	4.0837	2.5523	0.0011

5.2.2. Simulation Scenario 5.2: Poor *a priori* system noise

In a practical environment, sensor measurement accuracy could degrade. The sensor noise may be larger than those listed in the sensors' manuals during operation and will therefore differ to the UKF predefined noise models that are based on the manuals. In this simulation, the knowledge of the *a priori* GPS and compass measurement noise is unknown and an inaccurate assumption of measurement noise

covariance parameter $\boldsymbol{R}$ has been assigned to the system to examine the performance of the improved fuzzy logic based adaptive estimation algorithm. The RMSE of the raw GPS measurements increases to 20m in both the x and y axes and the RMSE of the raw compass measurements increases to 5° while the settings of the UKF noise characteristics are unchanged, as shown in Table 5.2. Such a configuration indicates that the conventional UKF uses incorrect measurement noise characteristics to make estimations without any updates during the process.

Figures 5.10 to 5.13 present the simulation results of simulation Scenario 5.2. Similar to the Simulation Scenario 5.1, Figure 5.10 and Figure 5.11 represent the position and heading results from the proposed algorithms together with raw sensor measurements. However, in this simulation, the proposed fuzzy adaptive UKF algorithm performs much better than the conventional UKF. According to the real-time RMSEs for the navigational data shown in Figure 5.12, the error of the adaptive UKF estimations are much lower than those of the conventional UKF estimations, providing at least a 30% improvement. Such an improvement is a result of the fuzzy adaptive UKF's capability to intelligently calculate the measurement covariance $\boldsymbol{R}$ to facilitate improving the accuracy of the filtered data. Figure 5.13 demonstrates the diagonal elements of the actual, updated and fixed measurement covariance $\boldsymbol{R}$. The adapted R in this simulation is convergent to the actual $\boldsymbol{R}$ when compared to the fixed settings.

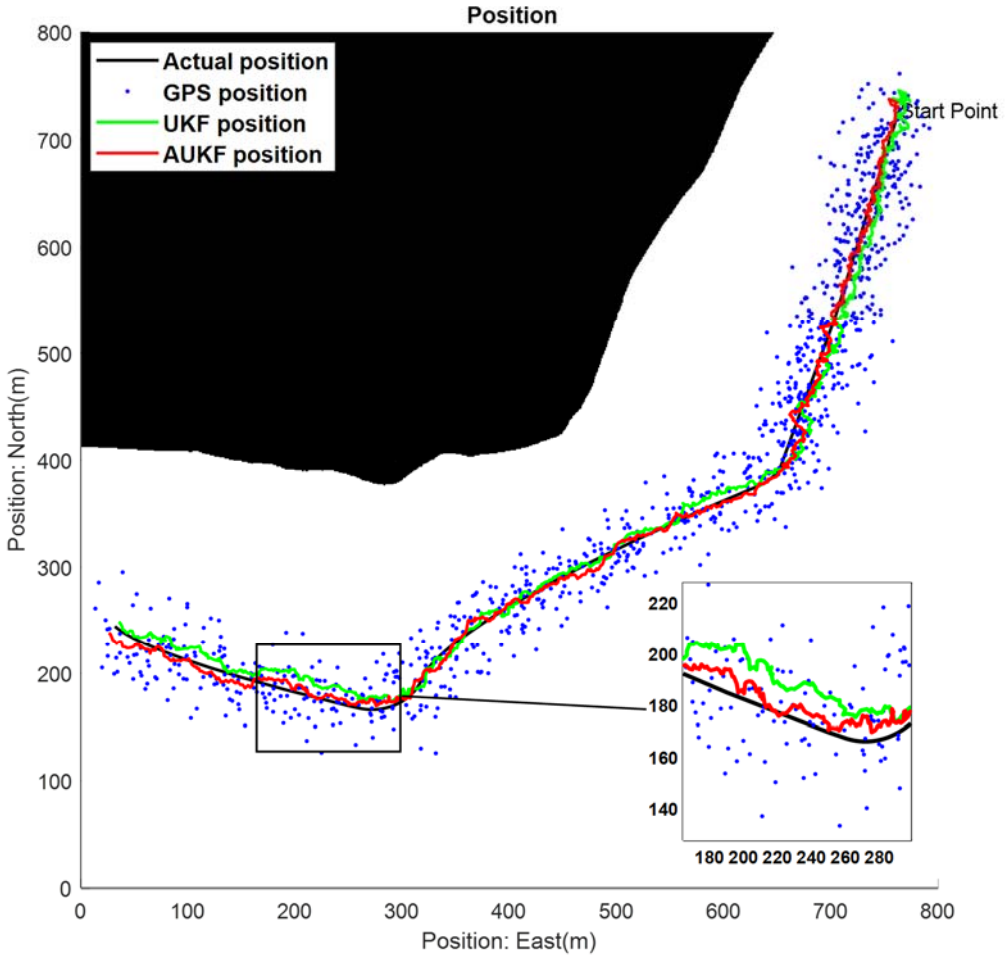

Figure 5. 10 Simulation Scenario 5.2: the simulated environment and the trajectories of the USV

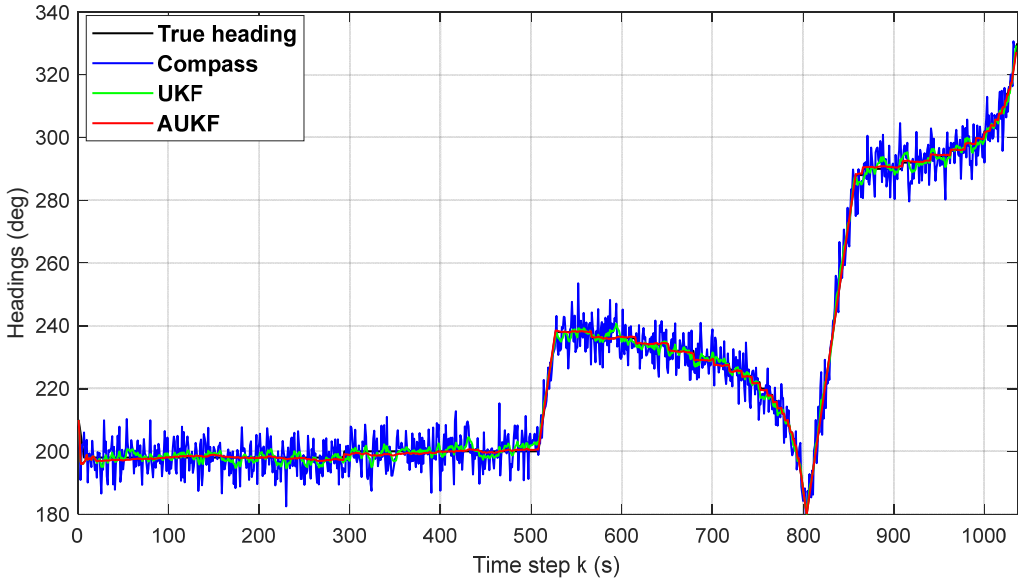

Figure 5. 11 Simulation Scenario 5.2: measured and estimated USV headings

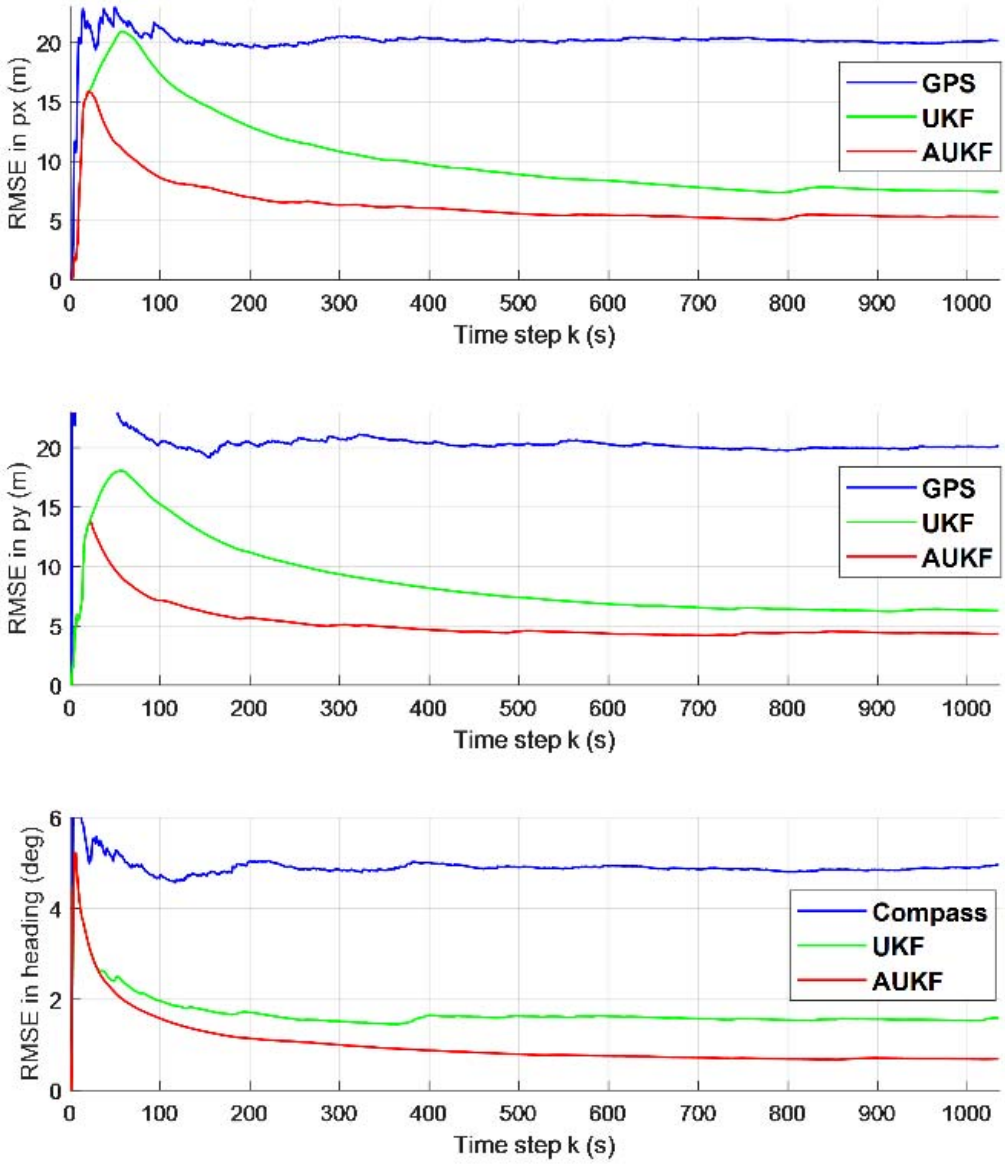

Figure 5. 12 Simulation Scenario 5.2: Real time Rooted Mean Square Error (RMSE) of the USV's position and heading

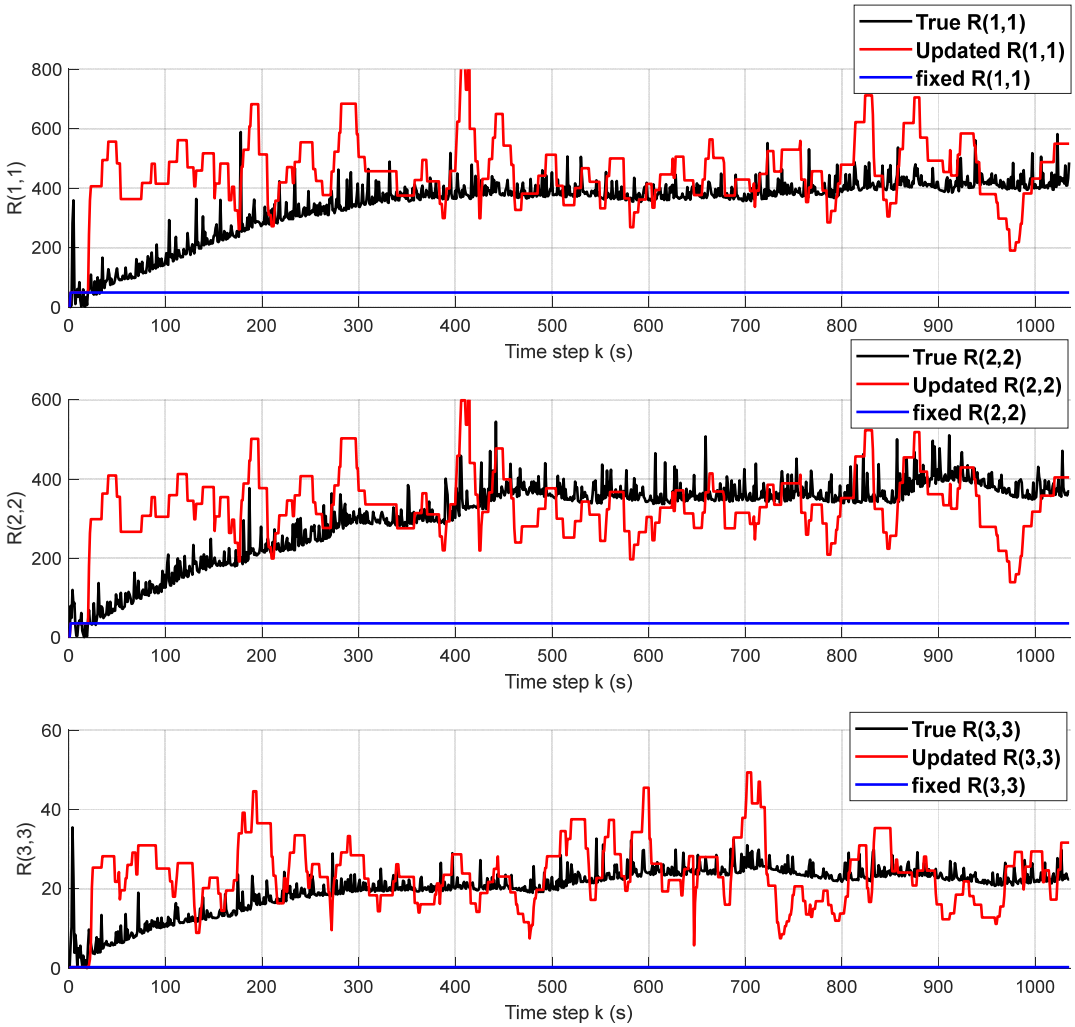

Figure 5. 13 Simulation Scenario 5.2: The two elements of measurement covariance R that related to position estimation

Table 5. 6 Simulation Scenario 5.2: overall Mean Square Errors

Method	***MSE_px (m^2)***	***MSE_py (m^2)***	***MSE_ψ (deg^2)***
GPS module	402.2386	395.6904	-
Electronic Compass	-	-	20.1516
Conventional UKF	62.8698	47.0732	3.2428
Adaptive UKF	26.6514	18.0436	0.6988

5.2.3. Simulation Scenario 5.3: Variable measurement noise

In Simulation Scenario 5.3, the noise of raw sensor measurements is assumed to increase during USV operation. During the first 300 time steps, the sensor noises are assumed to be at the same values as used in Simulation Scenario 5.1. Then a sudden change of sensor noises occurs due to some unexpected influences on the sensors. The noises increase to the values used in Simulation Scenario 5.2.

Figures 5.14 to 5.17 demonstrate the performance of both the conventional UKF algorithm and the proposed fuzzy adaptive UKF algorithm under these conditions. From Figure 5.14, it can be seen that the GPS measurements become noisier before the USV reaches the first waypoint. The green line that represents the conventional UKF estimated positions starts to fluctuate significantly from the true trajectories (black line) while the adaptive UKF still provides much closer estimations. The improved performance of the adaptive UKF algorithm is again shown to be apparent from the enlarged inset in the heading estimations (Figure 5.15). The conventional UKF estimated headings (green line) generates larger errors when the compass error increases, whereas the fuzzy adaptive UKF estimated headings (red line) still maintain their accuracy and stay close to the true values. The real-time RMSE values for each of the navigational data in Figure 5.16 further supports that the proposed fuzzy adaptive UKF data fusion algorithm achieves better accuracy when the system lacks appropriate *a priori* knowledge of system measurement noise characteristics, even when the sensor noises change suddenly. The reason for this is the proposed fuzzy adaptive UKF data fusion algorithm is able to tune the predefined measurement covariance R close to the actual value in real-time, which is also shown in Figure 5.17, instead of fixing it as in the conventional UKF algorithm.

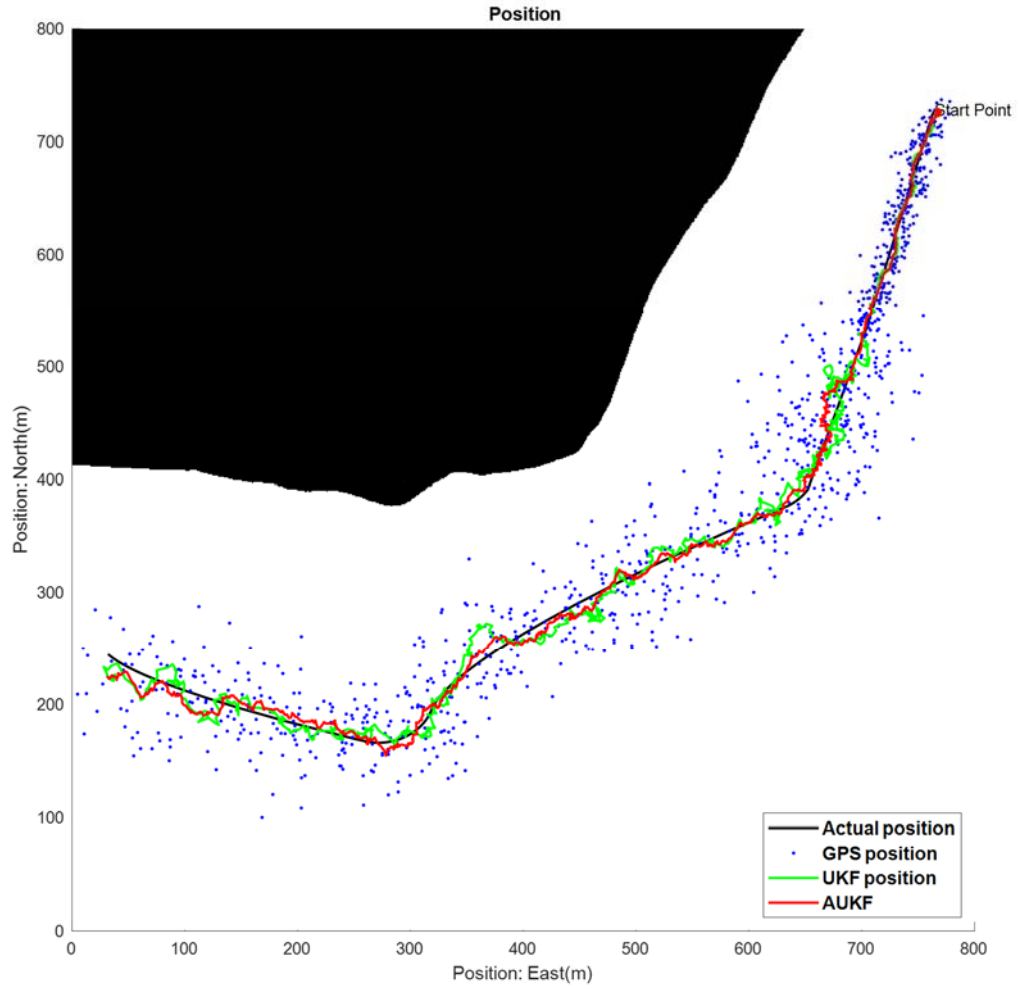

Figure 5. 14 Simulation Scenario 5.3: the simulated environment and the trajectories of the USV

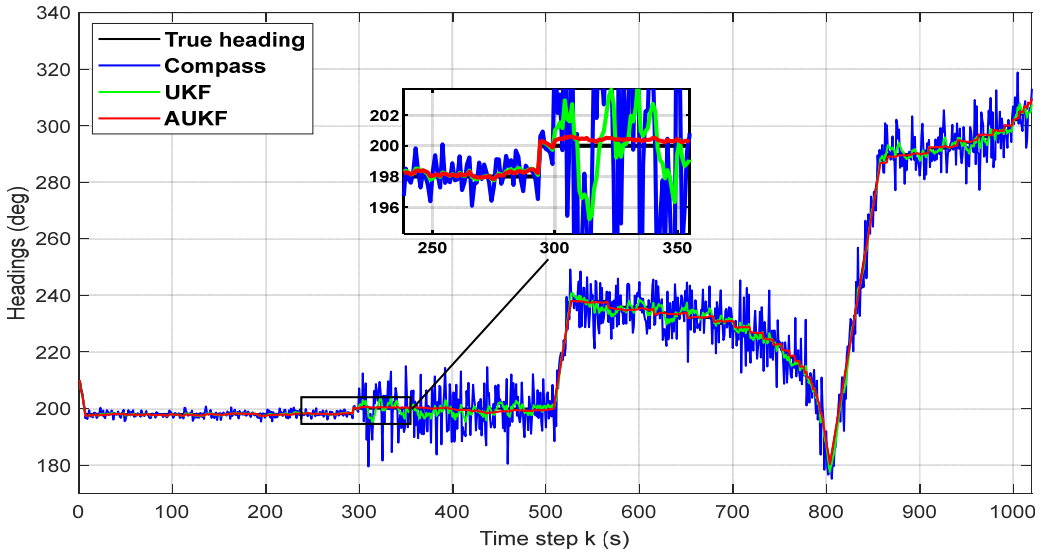

Figure 5. 15 Simulation Scenario 5.3: measured and estimated USV headings

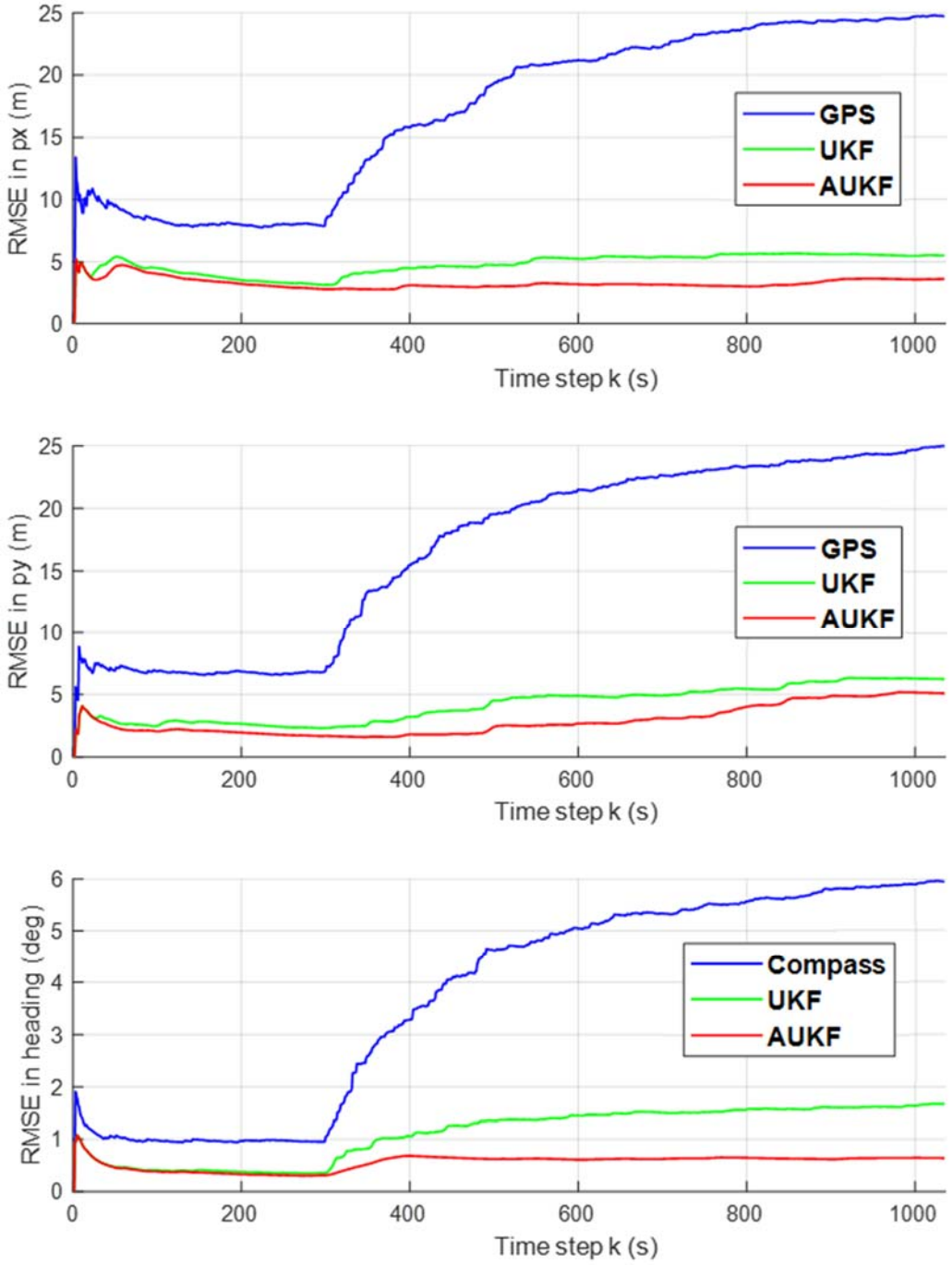

Figure 5. 16 Simulation Scenario 5.3: rooted Mean Square Error (RMSE) of the USV's position

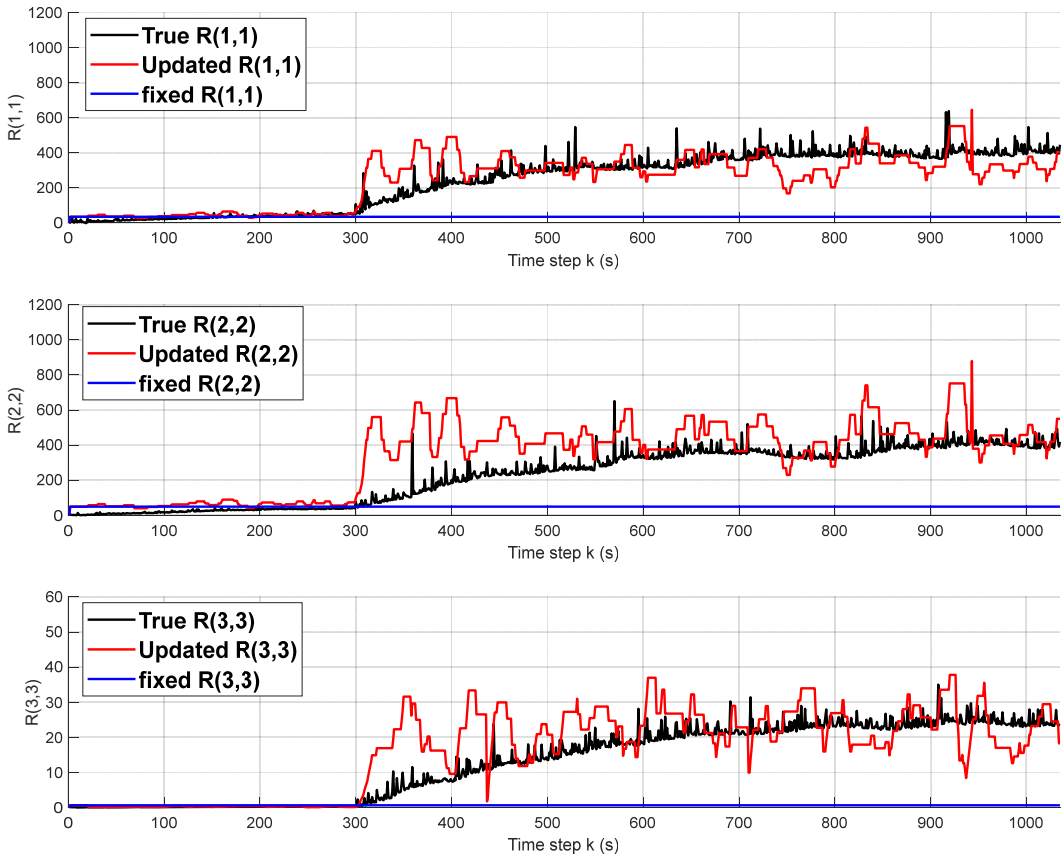

Figure 5. 17 Simulation Scenario 5.3: the diagonal elements of measurement covariance ***R*** that related to position estimation

Table 5. 7 Simulation Scenario 5.3: overall Mean Square Errors

Method	***MSE_px (m^2)***	***MSE_py (m^2)***	***MSE_ψ (deg^2)***
GPS module	413.2008	387.5966	-
Electronic Compass	-	-	19.7812
Conventional KF	28.5974	22.5572	1.8318
Adaptive KF	12.3998	11.1658	0.5234

At this juncture, it can be summarised that in the first simulation, the proposed fuzzy adaptive UKF shows marginal improvement in reducing the raw sensor measurement errors over the conventional UKF. In the second simulation, when the *a priori* information of the sensor noise is poor and varies significantly from the UKF's settings, the proposed fuzzy adaptive UKF provides more accurate results than the conventional UKF. The improved performance has been demonstrated again in Simulation Scenario 5.3, where the sensor noise changes suddenly during USV

operation. The computational time of the proposed multi-sensor data fusion algorithm at each time step in all three simulations is approximately 0.0023 seconds. It is far below the simulated sampling time of the navigation system, which is 1 second. Therefore, the proposed algorithm is capable of conducting data fusion missions in real-time applications. The results are summarised in Table 5.8.

Table 5. 8 Summary of the three simulations

Simulations	Results
Simulation Scenario 5.1: UKF based algorithm: good *a priori* information, sensors noise unchanged	Both conventional UKF and proposed fuzzy adaptive UKF algorithms work well in reducing sensor measurement noises.
Simulation Scenario 5.2: UKF based algorithm: poor *a priori* information, sensors noise unchanged	The proposed fuzzy adaptive UKF algorithm improves the results about 30% than conventional UKF algorithm.
Simulation Scenario 5.3: UKF based algorithm: good *a priori* information initially, sensors noise changed suddenly during operation	The estimation error of the conventional UKF algorithm increases when the sensor noise changes suddenly, whereas the proposed fuzzy adaptive UKF algorithm still maintains its estimation accuracy.

5.3. Practical Trials

5.3.1. Experiment platform and environment conditions

To further demonstrate the effectiveness of the proposed method, a field trial using an actual USV has been carried out on *Springer* USV, which is introduced in Chapter 3. The *Springer* USV was equipped with a GPS receiver, an IMU, and three independent electronic compasses. All the collected raw measurement data was stored during practical trials. The trials were held at the Roadford Lake in Devon, UK (Figure 5.18) on a cloudy day with drizzle and wind speeds of between 1 and 3.2 m/s blowing in a westerly direction. Three buoys were set up as the waypoints constituting a waypoint-

tracking path for the *Springer* USV. The actual GPS locations of the start point and buoys are listed in Table 5.9, which were input to the Path Planning Module as waypoints. The start point of Springer is used as the reference point of the navigational frame and the GPS locations of the three buoys are converted into meters. The USV has to make three turning maneuvers to complete the designed mission, from the start, tracking the three buoys in sequence and then heading back to the first buoy designated as the end of the journey (Figure 5.19). The sampling time for sensors to take measurements was 1 second. The duration for each trial was around 20 minutes and the USV was operated at a speed of approximately 1.5 m/s.

Table 5. 9 Summary of the three simulations

Way points	**GPS Location (Lat, Lon)**	**Converted position (m, m)**
Start point	(5041.7226, -414.1994)	(0, 0)
Buoy 1	(5041.8085, -414.0430)	(289.8315,158.7534)
Buoy 2	(5041.9728, -413.9645)	(435.3104, 462.4119)
Buoy 3	(5041.9330, -414.1790)	(37.7889, 388.8520)

Figure 5. 18 Experimental environment- Roadford lake, Devon

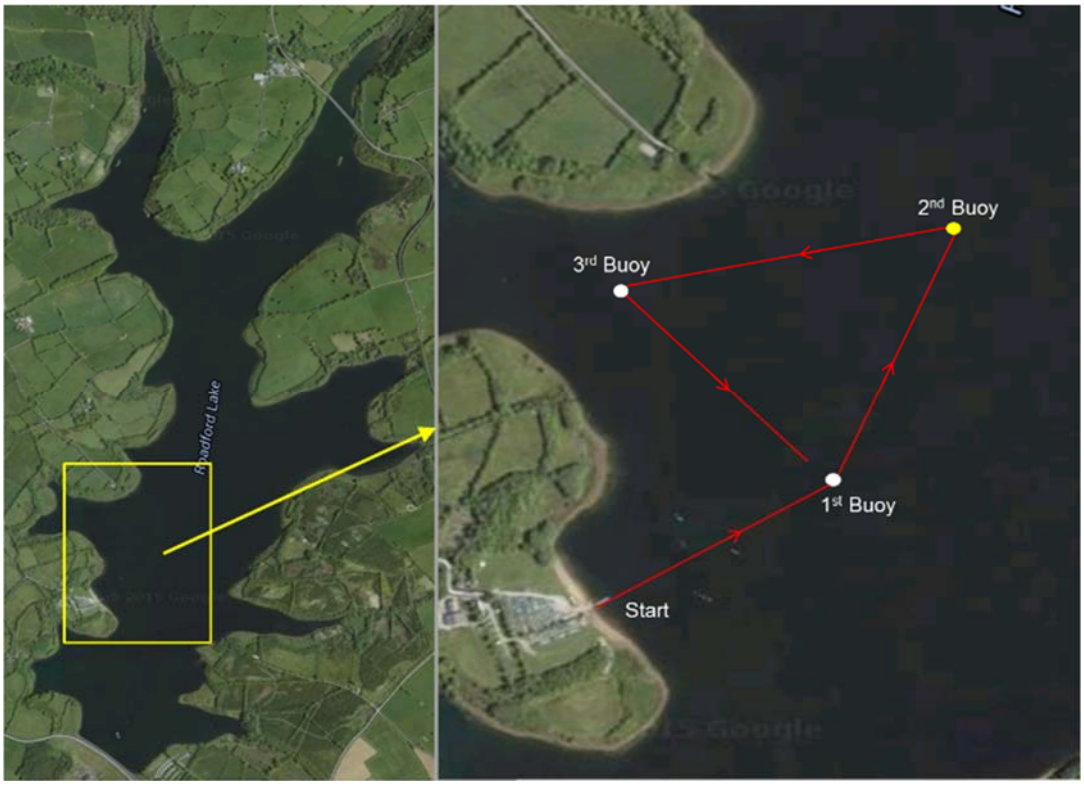

Figure 5. 19 The satellite map of the Roadford lake and the planned trajectory for the Springer USV to follow

5.3.2. Trial results

The actual environmental influences, such as the wind and water current, altered the trajectory of the *Springer* USV, which is shown in Figure 5.20. The blue line represents the raw GPS measurements that have been extracted from the trial. As illustrated in Figure 5.20, the USV successfully transited the three waypoints in sequence and returned to the first waypoint as planned, but the water surface currents pushed the vehicle towards the northwest and made large impacts on its trajectory when the USV was travelling northeast. As a result, the *Springer* USV had to turn right towards the second buoy then circumnavigate the buoy to alter its direction towards the third buoy instead of directly turning left after it reached the second buoy. This kind of unpredictable event increases the complexity of practical USV operations.

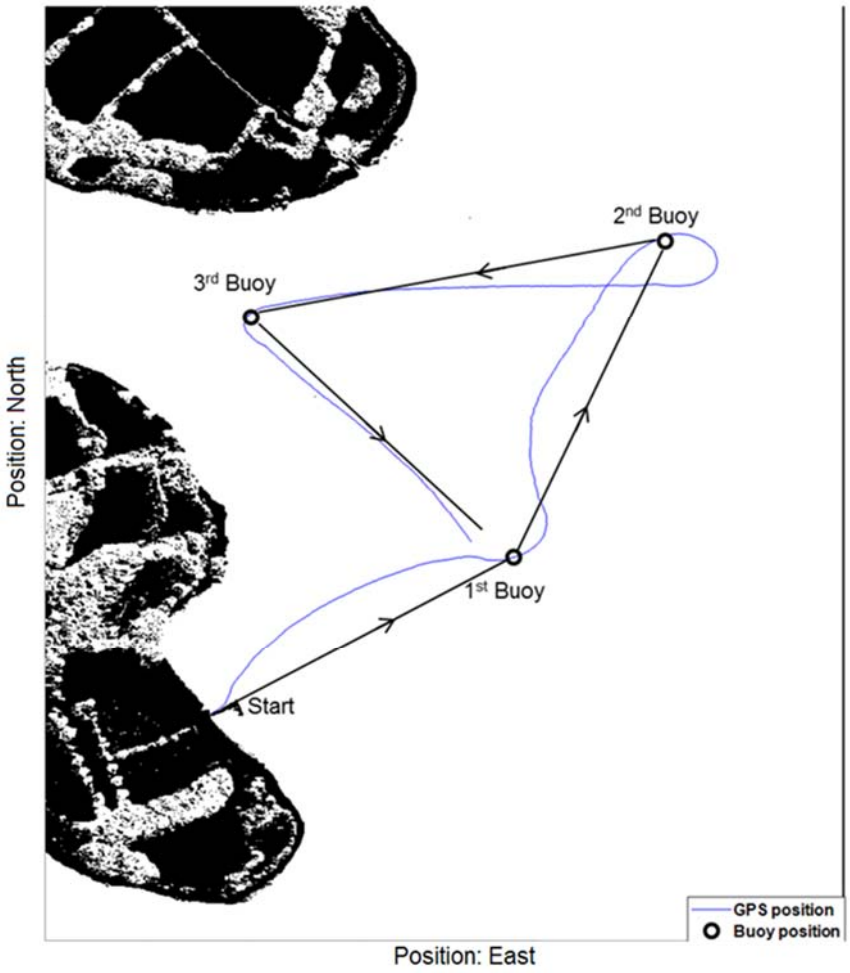

Figure 5. 20 The converted binary map with USV's planned trajectory and recorded GPS measurements during the practical experiment

The conventional UKF and the proposed fuzzy adaptive UKF data fusion algorithms were then applied to the raw sensor measurements recorded from the practical trial. The average computational time for each cycle of the algorithm is 0.0017 s while the actual sensor measurements are sampled at 1 second intervals, which confirms the proposed algorithm can be applied to this real-time navigation system. The fusion results are plotted in Figure 5.21 and Figure 5.22. As shown in Figure 5.21, the red line that denotes the fuzzy adaptive UKF estimated trajectory, is close to the GPS measurements that are represented by the blue line, whereas the green line that denotes the conventional UKF estimated trajectory deviates significantly from the other two trajectories. Figure 5.22 demonstrates the heading results. It can be seen that the headings estimated by the proposed fuzzy adaptive UKF algorithm (red line) are more coincident with the compass measurement (blue line). Again, the conventional UKF estimations (green line) are associated with deviations from the

other two headings. The results verify the feasibility of the proposed fuzzy adaptive UKF data fusion algorithm whereas the conventional UKF algorithm is prone to error in a practical application. In the simulations, despite the improved performance of the proposed fuzzy adaptive UKF algorithm, the conventional UKF can also reduce raw sensor measurement errors. Similar performance that has not been achieved in practice, states the conventional UKF is a theoretical optimal algorithm that proves less satisfactory in practical applications. In the meantime, the real-time adaption of the measurement noise covariance enhances the ability of the proposed fuzzy adaptive UKF algorithm to overcome the unexpected uncertainties in practical applications. Although the true positions and headings of the *Springer* USV are not available in a practical trial, the benefits obtained from the proposed algorithm can still be revealed by its smoother estimations with less pinnacles than from the raw sensors' measurements, which are presented in the enlarged insets in both Figure 5.21 and Figure 5.22.

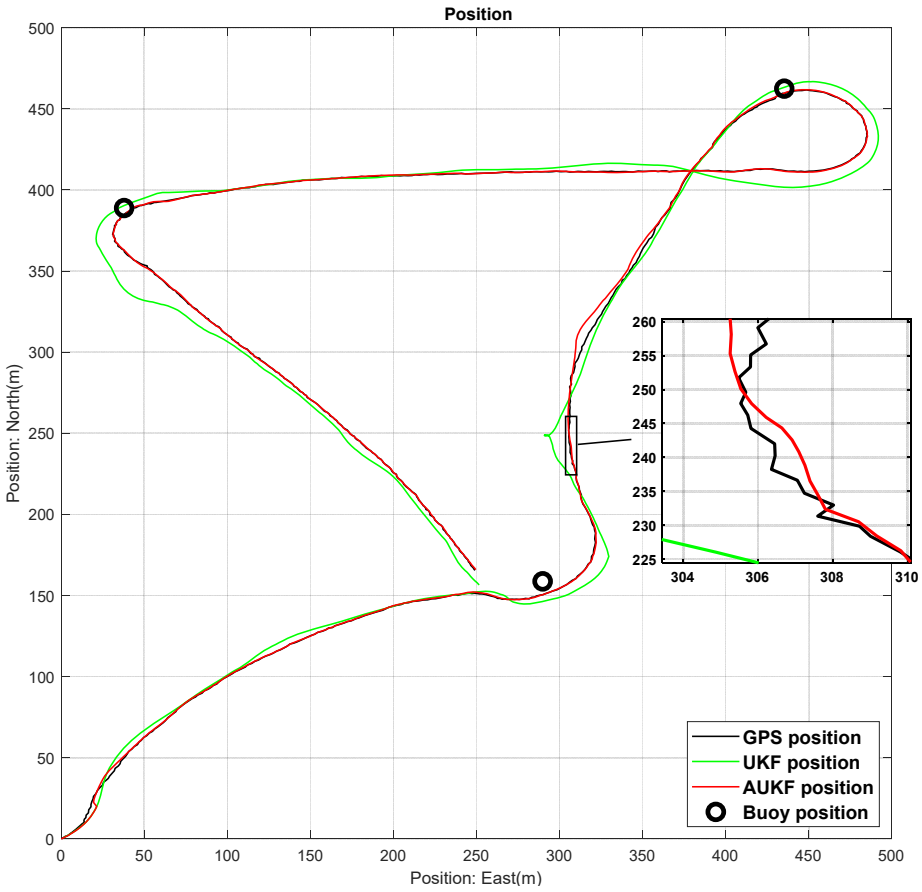

Figure 5. 21 The raw GPS measurements, waypoints positions and estimated positions generated by conventional UKF and adaptive UKF respectively

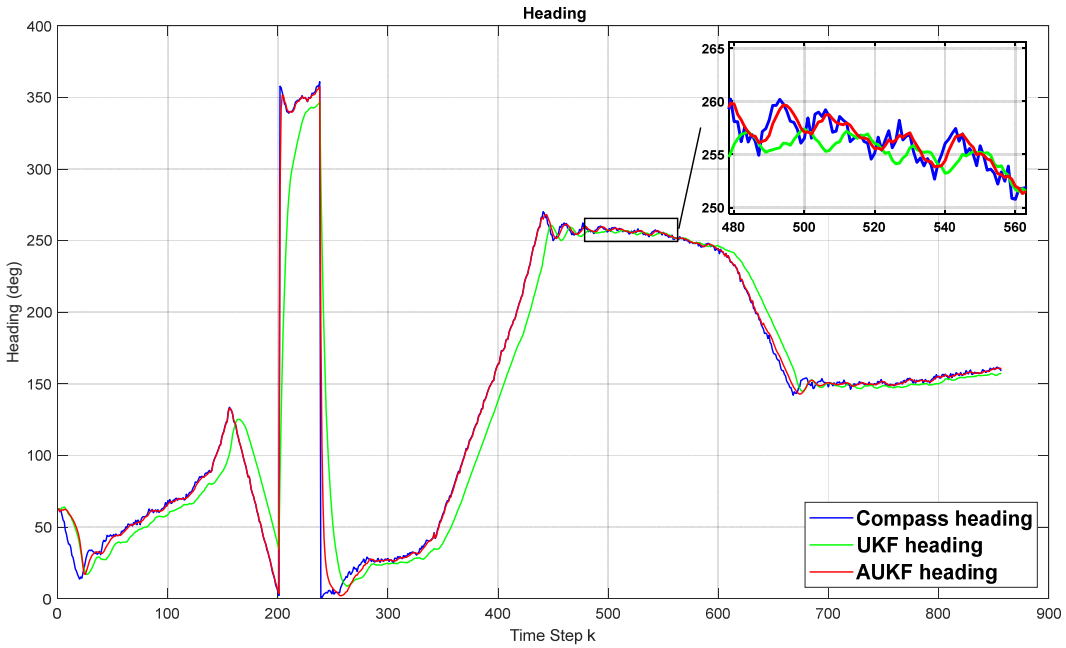

Figure 5. 22 The raw compass measurements and estimated headings generated by both conventional UKF and adaptive UKF

5.4. Summary

In the previous chapter the Unscented Kalman Filter based multi-sensor data fusion algorithms were applied to determine USV navigational data. Throughout it was assumed that the *a priori* measurement data was deemed reliable. However, it is an accepted fact that the measurement and system can be affected by interference, instrument performance and environmental issues and the UKF's performance is heavily reliant on good *a priori* noise measurement data.

To overcome this deficiency an adaptive estimation methodology and algorithm was developed and investigated. The area of concern was the measurement noise covariance (R). In effect best known data of R updated in real time would be for the correction thus catering for the effects of noise variation not in line with manufacturer's data. The system was augmented by an Adaptive UKF (AUKF). The main elements of the AUKF are covariance matching and adaptive estimation, applied to the UKF algorithm and using fuzzy logic as the control medium.

In simulation tests where uncertainty of system and measurement noise were applied the AUKF provided improved performance above that of the UKF. Further to these verification simulations, practical validation trials were conducted using the *Springer* USV and the results confirmed the performance improvement and navigational accuracy reliability offered by the AUKF.

In the following chapter, possible malfunctions of navigational sensors and reliability of the navigation system will be discussed.

Chapter 6. Reliable USV Navigation

The previous two chapters demonstrated how the developed Kalman filtering based multi-sensor data fusion algorithms improved raw sensor measurements and dealt with unknown *a priori* system noises in practical USV applications. Even though the algorithms are able to provide optimal estimations of the USV's navigational data in various situations, their performance may degrade when problems such as sensor signal loss or malfunctions occur in real life. So, apart from dealing with lost or faulty sensor measurements, knowledge of the system reliability could provide a measure of the level of assurance that could be assigned to the USV's safe operation. In this chapter, a level of confidence has been determined to express the system reliability so that the path planning module is able to adjust the planned trajectory of the USV. In addition, fault tolerance methods have been developed to deal with sudden changes in the sensor measurements reliability.

6.1. Navigation system reliability determination

In this research, the reliability of the developed USV autonomous navigation system is discussed in two aspects, the level of trust in the system's estimated navigational data and solutions to sudden faults of the practical sensors during operation. Using multiple sensors instead of using a single standalone sensor to compute real-time navigational data of an USV can increase the level of trust of the navigation system. In this section, a probabilistic method to express the level of trust of the estimated USV's position is demonstrated.

6.1.1. Probability distribution of sensor measurements

The sensor measurements of a continuous physical quantity are often associated with noise and uncertainties and are not, in principle, absolutely precise. In the navigation data fusion system, absolute sensor measurements, i.e. GPS and electronic compass

measurements are assumed to be Gaussian, which means the measurements are normally distributed around the true value with a variance (Feng, 2014). The IMU that is composed of an accelerometer and a gyroscope to measure the USV's motions is used to calculate the predicted position of a USV. Due to the nature of Kalman filtering, prior belief of the USV's position (predicted) is also assumed to be Gaussian. At each iteration time step k, the predicted position and measured position vectors are expressed as:

$$\boldsymbol{\mu_p} = [\hat{\boldsymbol{x}}^{-}(1,k) \quad \hat{\boldsymbol{x}}^{-}(2,k)]^T \in \Re^2 \tag{6.1}$$

$$\boldsymbol{\mu_m} = [\boldsymbol{z}(1,k) \quad \boldsymbol{z}(2,k)]^T \in \Re^2 \tag{6.2}$$

The Gaussian probability density function (pdf) of the two position vectors are defined in Equations (6.3) and (6.4), where $\boldsymbol{x}$ denotes the unknown position vector of the USV (Hertzmann et al, 2015).

$$f(\boldsymbol{\mu_p}) \triangleq \frac{1}{2\pi\sqrt{|\boldsymbol{\Sigma_p}|}} exp\left(-\frac{1}{2}(\boldsymbol{x}-\boldsymbol{\mu_p})\boldsymbol{\Sigma_p}^{-1}(\boldsymbol{x}-\boldsymbol{\mu_p})^T\right) \tag{6.3}$$

$$f(\boldsymbol{\mu}_m) \triangleq \frac{1}{2\pi\sqrt{|\boldsymbol{\Sigma_m}|}} exp\left(-\frac{1}{2}(\boldsymbol{x}-\boldsymbol{\mu_m})\boldsymbol{\Sigma_m}^{-1}(\boldsymbol{x}-\boldsymbol{\mu_m})^T\right) \tag{6.4}$$

where $\boldsymbol{\Sigma_p}$ is the predicted position error covariance matrix before fusion, $\boldsymbol{\Sigma_m}$ is the covariance matrix representing the uncertainty associated with the measurements. $\boldsymbol{\Sigma_p}$ and $\boldsymbol{\Sigma_p}$ are expressed in the form of Equation (6.5) and Equation (6.6), where $\boldsymbol{\sigma_p}$ and $\boldsymbol{\sigma_m}$ are the corresponding variances with $\boldsymbol{x}$.

$$\boldsymbol{\Sigma_p} = \begin{bmatrix} \boldsymbol{\sigma_p}^2(1,1) & 0 \\ 0 & \boldsymbol{\sigma_p}^2(1,2) \end{bmatrix} \tag{6.5}$$

$$\boldsymbol{\Sigma_m} = \begin{bmatrix} \boldsymbol{\sigma_m}^2(1,1) & 0 \\ 0 & \boldsymbol{\sigma_m}^2(1,2) \end{bmatrix} \tag{6.6}$$

According to the pdf functions, the system has 68% confidence that the error of the predicted/measured position is within $|\boldsymbol{\Sigma_p}|/|\boldsymbol{\Sigma_p}|$, and 96% confidence that the error of the predicted/measured position is within $2|\boldsymbol{\Sigma_p}|/2|\boldsymbol{\Sigma_p}|$. The confidence reaches 99.7% when the error is within three times of the accuracy ($3|\boldsymbol{\Sigma_p}|/3|\boldsymbol{\Sigma_p}|$) and any

predicted/measured positions with errors larger than that should not be trusted (Feng, 2014).

6.1.2. Level of confidence

In an autonomous navigation system as described in Figure 6.1, the path planning module and control module largely rely on accurate navigational data obtained by the data acquisition module. Although the higher the accuracy the better the USV can behave, the acceptance of inaccuracy is allowed when operating over the sea. Therefore, knowing how accurate the estimated navigational data is and to what level the data can be trusted would be useful for the path planning module to determine the safe area required around the USV to generate safe paths. When both IMU and GPS sensor can provide good measurements, the positions calculated should be highly consistent. The consistency degrades once either sensor makes inaccurate measurements so that the level of confidence in the estimated position based on the inaccurate measurements decreases. Therefore, the level of confidence of the USV's estimated position is quantified as the measurement consistency of two different sensors and the process has been added into the block diagram of the adaptive UKF data fusion algorithm developed in Chapter 5 as detailed in Figure 6.1.

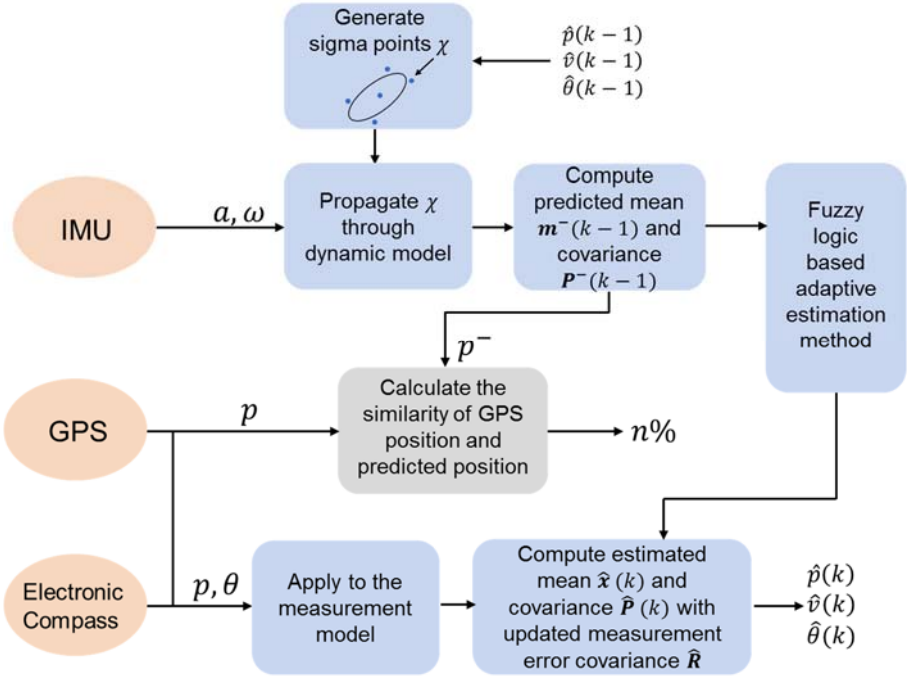

Figure 6. 1 The block diagram of the data fusion algorithm with system reliability (n%) determination

The similarity between the two distributions of predicted position vector and measured position vector are measured by the Bhattacharyya distance D_B, and the Bhattacharyya coefficient BC can represent the reliability of the system estimations (Patra et al, 2015).

$$D_B = \frac{1}{2}\ln\left(\frac{|\Sigma_p|^2+|\Sigma_m|^2}{2\sqrt{|\Sigma_p|^2|\Sigma_m|^2}}\right)+\frac{1}{4}\frac{(\mu_p-\mu_m)^2}{|\Sigma_p|^2+|\Sigma_m|^2} \tag{6.7}$$

$$BC = e^{-D_B}\times 100\% \tag{6.8}$$

6.2. Fault tolerance for multi-sensor navigation system

Sensor malfunction is another issue that could reduce the reliability of an autonomous system. Improper handling of faulty measurements can also result in an unreliable navigation solution. This section discusses how the system detects possible sensor failures and recovers from such failures automatically.

6.2.1. Autonomous recovery of temporary signal loss

GPS sensors suffer from sudden signal losses when the Line of Sight (LoS) to satellites is blocked (McWilliam et al, 2005). The blockage may disappear after the USV travels further to an wide open environment. This should be less hazardous for ships navigation with human operators on-board. However, for an unmanned autonomous system, the data fusion algorithm may fail to estimate navigational data for lack of GPS measurements.

In the multi-sensor data fusion algorithm already developed, the IMU is used together with the GPS to obtain better estimations of the USV's positions. The data analysis in the two preceding chapters shows that GPS measurements are very noisy, especially when the USV is travelling. The navigational data calculated by the IMU's measurements are prone to drift for long time durations because of the bias of the inertial sensors. Therefore, as they are complementary sensors, the fluctuations of the GPS measurements caused by sensor errors can be compensated with the

inertial sensors and the inertial sensor biases can be compensated with the GPS receiver. When a short-time blockage of the GPS sensor occurs, the data fusion algorithm has to temporarily switch to pure inertial navigation, in accordance with the rules in Table 6.1, to provide continuous estimations and recover the USV's trajectory.

Table 6. 1 Rules to switch the multi-sensor navigation to pure inertial navigation when GPS signal is null

Rule 1: When GPS signal is null, GPS measurement equals to (0,0)
Rule 2: Measurement matrix $\boldsymbol{H} = [\mathbf{0} \quad \mathbf{0} \quad \mathbf{0} \quad \mathbf{0} \quad \mathbf{1}]$
Rule 3: Mean Square Error (MSE) at $\boldsymbol{k}$ equals to $\boldsymbol{MSE(k-1)}$

6.2.2. Autonomous fault detection and tolerance

The sensor redundancy may appear wasteful, but in practice, sensor failure is a common occurrence, especially where low cost hardware is involved. The KF based data fusion algorithms developed previously are only capable of improving raw sensor measurements and recover the trajectory within short time periods but cannot deal with sensor malfunctions. Normally, once a sensor fails, the best solution is to manually switch to another sensor of the same type. However, during an autonomous mission, such a luxury does not normally exist and the occurrence of hardware failure would most likely result in forced abortion of the mission. A cold standby system can be used to replace the manual control in an autonomous system. It is an idle back up system that can be turned on and turned off as required. Although it can be employed on failure of the primary system, such a configuration could take some time to perform initialisation to be functional and the autonomous navigation system will lose real-time data during the gap if such a method is employed. There is also risks that the turn on may not be successful or the backup system may itself have already failed with there being no indication or knowledge that such a failure had already occurred. A hot standby system is more suitable for USV navigation since it is running simultaneously with the identical primary system. On failure of the primary system, the hot standby system immediately takes over to replace the faulty sensor. In such a setup, the data is mirrored in real time and both systems have identical data. However, the use of the identical sensors would also increase the cost

and it is a waste to use the hot standby system solely for backup purpose. In this research, a fuzzy multi-sensor data fusion algorithm is proposed to further improve the hot standby system and make use of the backup data.

The proposed system combines heading estimates from three separate Kalman Filters (KFs) using the measurements from three independent electronic compasses to construct a robust, fault tolerant heading estimator for the navigation of the USV. It improves the accuracy and continuity of raw measurements of the electronic compasses as well as further fuses the improved headings and detects and discards failed sensors automatically. The newly designed fuzzy logic based multi-sensor data fusion algorithm, employing the Federated filter architecture, is shown in Figure 6.2. A single, low-cost MEMS gyroscope and three independent electronic compasses are used to acquire data on-board the USV, where the electronic compasses represent local sensors and the gyroscope is used as the reference. The inertial data from the gyroscope, which is prone to sporadic bias drifts, is fused individually with measurements from each of the compasses via a conventional KF which is robust to gyroscope bias drifts. The three ensuing KFs that estimate the heading angle of the USV are identical in their predictive models (Equation 6.9), but with different heading measurement noise covariance, are then fused via a fuzzy logic algorithm designed to provide an accurate heading even in the face of a failure of up to two of the compasses at the same time.

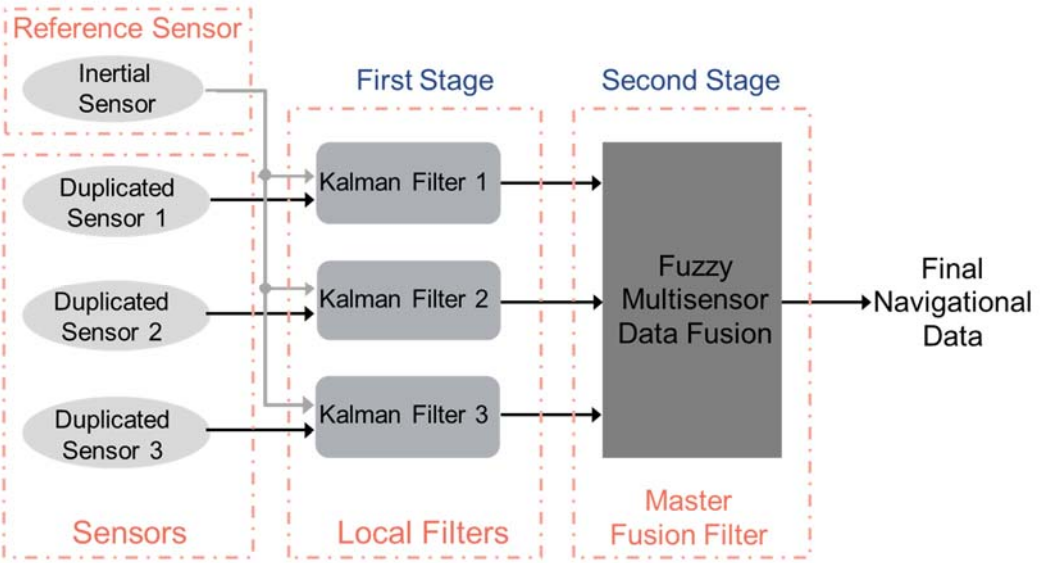

Figure 6. 2 Federated Filter Architecture for the Fuzzy MSDF Algorithm

$$\psi(k) = \psi(k-1) + T \times \omega(k) \tag{6.9}$$

where T is the sampling time between two consecutive time steps.

The fuzzy system is based on observation of the residual sequence of each KF, which is the difference between the measurement and the prediction. The reflected discrepancy is defined as follows:

$$\boldsymbol{\varepsilon}(k) = \boldsymbol{z}(k) - \boldsymbol{H}\,\hat{\boldsymbol{x}}(k) \tag{6.10}$$

It is the difference between the absolute measurement and the optimal estimated state at each time step k. It is well established that under an ideal scenario, the residual sequence should be comprised of a zero-mean, white noise sequence (Subramanian et al. 2009, Bijker et al. 2008). Therefore this sequence could be monitored to detect a failure in the correct estimation by one of the KFs.

In order to monitor the residual sequence, which in general is a random process and thus whose individual values are meaningless, a simple moving average (SMA) of the residual sequence of each KF is computed:

$$SMA(k) = \varepsilon_{\psi}(k) + \varepsilon_{\psi}(k-1) + \cdots + \varepsilon_{\psi}(k-N+1)/N \tag{6.11}$$

where N is the number of samples considered in the moving average. Since the SMA is, in the ideal case, a sum of zero-mean independent random variables, it is in itself a zero-mean random variable, tending to be normally distributed by the Central Limit Theorem. However, its variance is N times smaller than that of the residuals random variable. Thus, sporadic high values of the SMA are more improbable than for the residual, and will almost only occur when the residual stops being a white sequence. Hence it is this value that is chosen to indicate a compass fault in the KF estimate and it is also the input to the fuzzy system, as shown below:

Figure 6. 3 Designed Fuzzy Multi-sensor Data Fusion System

The final fused state estimate is then computed as:

$$\hat{\psi}(k) = \sum_{i=1}^{3} w_i(k)\, \hat{\psi}_{KF_i}(k) \tag{6.12}$$

A. Crisp decision algorithm

The crisp decision algorithm updates the SMA of each KF at each sampling instant and then accepts or rejects the filter by assigning it a weight of 1 or 0 according to whether the SMA lies within a predefined minimum and maximum threshold value:

IF ($SMA(k) < SMA_{min}$) OR ($SMA(k) > SMA_{max}$)

$w_i(k) = 0$

ELSE

$w_i(k) = 1$

END

after which the weights are normalised so that their sum equals one.

B. Fuzzy sensor fusion algorithm

The problem with the crisp decision algorithm is the choice of the threshold values, and the sudden change in the fused estimate that occurs when a change of decision is made regarding the inclusion or exclusion of some of the filters. In order to obtain a smoother decision process, the following fuzzy membership functions are defined (Figures 6.4):

Input membership functions:

Negative function: $\mu_N = \begin{cases} 1 & if\ SMA < SMAN \\ SMA/SMAN & if\ SMAN \leq SMA < 0 \\ 0 & if\ SMA \geq 0 \end{cases}$ (6.13)

Zero function: $\mu_Z = \begin{cases} 1 - SMA/SMAN & if\ SMAN \leq SMA < 0 \\ 1 - SMA/SMAP & if\ 0 \leq SMA \leq SMAP \end{cases}$ (6.14)

Positive function: $\mu_P = \begin{cases} 0 & if\ SMA < 0 \\ SMA/SMAP & if\ 0 \leq SMA < SMAP \\ 1 & if\ SMA \geq SMAP \end{cases}$ (6.15)

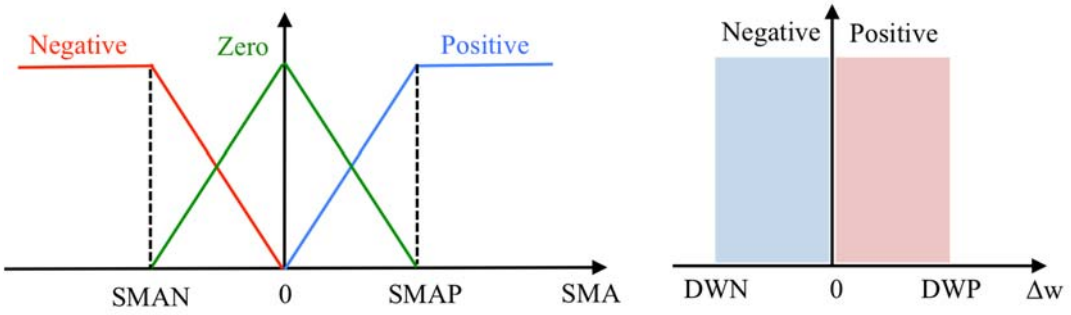

Figure 6. 4 Input and output membership functions

As indicated by the output fuzzy membership functions, the output to the fuzzy logic inference system is chosen to be a change in the weight of the filter, Δw, rather than the weight itself. This is to avoid brusque transitions in the overall estimate.

If-then rules:

Based on the aforementioned membership functions, the following fuzzy rules are established:

Table 6. 2 If-then rules

Rule 1: If SMA negative then $\boldsymbol{\Delta w}$ is negative
Rule 2: If SMA is zero then $\boldsymbol{\Delta w}$ is positive
Rule 3: If SMA is positive then $\boldsymbol{\Delta w}$ is negative

De-fuzzification:

Then, at each sampling time k, depending upon the value of the SMA, Δw is defuzzified by applying the Centroid method (Sameena et al. 2011) as follows:

$$\Delta w^* = \int \mu_i \, \Delta w \, d\Delta w / \int \mu_i \, d\Delta w \quad (6.16)$$

The following cases are chosen based on where the SMA lies in and explain the computation process of the Δw.

- *Case 1*: SMA < SMAN

  Rule 1 applies and Δw is given by the horizontal projection of the centroid of the negative output membership function, i.e. $\Delta w = DWN/2$.

- *Case 2*: SMAN < SMA ≤ 0

  Both *Rule 1* and *Rule 2* apply. Let μ_N represent the degree of membership of the input to the Negative input membership function (*Rule 1*), and μ_Z its degree of membership to the Zero input membership function (*Rule 2*). Then Δw is computed as the horizontal projection of the centroid of the area comprising the portions of the Negative and Positive output membership functions below the values μ_N and μ_Z respectively (Figure 6.5):

$$\Delta w = -\frac{1}{2} DWN^2 \times \mu_N + \frac{1}{2} DWP^2 \times \mu_Z / -DWN \times \mu_N + DWP \times \mu_Z \quad (6.17)$$

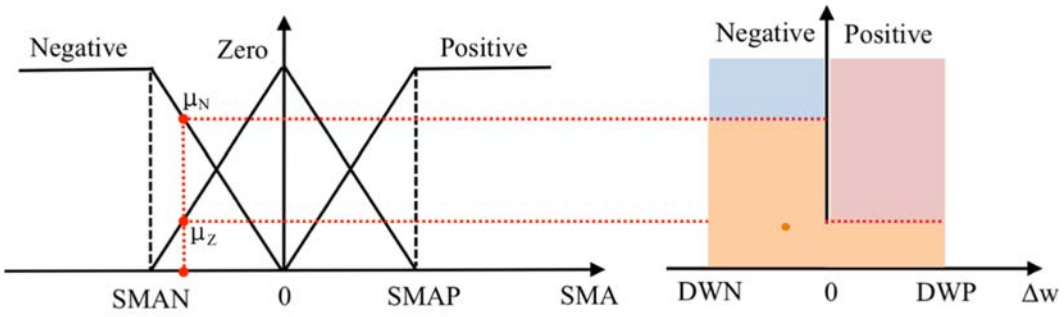

Figure 6. 5 Calculation of the output Δw for Case 2 (SMAN < SMA ≤ 0)

- *Case 3*: 0 < SMA < SMAP

  Both *Rule 2* and *Rule 3* apply. Let μ_Z represent the degree of membership of the input to the Zero input membership function (*Rule 2*), and μ_P its degree of membership to the Positive input membership function (*Rule 3*). Then Δw is computed as the horizontal projection of the centroid of the area

comprising the portions of the Positive and Negative output membership functions below the values μ_Z and μ_P respectively:

$$\Delta w = -\frac{1}{2} DWN^2 \times \mu_P + \frac{1}{2} DWP^2 \times \mu_Z / -DWN \times \mu_P + DWP \times \mu_Z \quad (6.18)$$

- *Case 4*: SMAP ≤ SMA

  Rule 3 solely applies, and Δw is given by the horizontal projection of the centroid of the Positive output membership function, i.e. $\Delta w = DWP/2$.

Once the Δw has been calculated at time step k for each KF estimated heading ($\Delta w_i(k),\ i = 1,2,3$), these values can be normalised so that their sum equals zero to ensure that the sum of the weights themselves will remain equal to one, as the weights are initialised equally at 1/3 for k = 0,

$$\Delta w_i^*(k) \coloneqq \Delta w_i(k) - \alpha,\ i = 1,2,3 \quad (6.19)$$

with α such that $\sum_{i=1}^{3}(\Delta w_i - \alpha) = 0$, i.e. $\alpha = \frac{1}{3}\sum_{i=1}^{3} \Delta w_i$ and resulting in the updated weights of each filter given by

$$w_i(k) = w_i(k-1) + \Delta w_i^*(k)\ ,\ i = 1,2,3 \quad (6.20)$$

However, direct application of Equation (6.20) might result in updated values of the weights not restricted to the interval [0, 1]. To restrict the values of the weights to this interval, the following procedure is carried out. Instead of directly updating all the weights according to Equation (6.20), these are tentatively updated in some auxiliary variables:

$$w_i^* = w_i(k-1) + \Delta w_i^*(k),\ i = 1,2,3 \quad (6.21)$$

Three possibilities exist:

- If all w_i^*'s are between 0 and 1 (inclusive), then these are taken directly as the updated weights $w_i(k)$; (Equation (6.20)).

- If (only) one of the w_i^* is less than zero, e.g. $w_j^* < 0$, then Δw_j^{**} is defined as

$\Delta w_j^{**} \coloneqq -w_j(k-1)$, i.e. the part of $\Delta w_j(k)$ that is actually used to make the corresponding updated weight equal to zero. Then the remaining two weight increments are normalised again: $\Delta w_i^{**}(k) \coloneqq \Delta w_i^*(k) - \alpha,\ i = 1,2,3\ \&\ i \neq j$, with α such that $\Delta w_j^{**}(k) + \sum_{\substack{i=1 \\ i \neq j}}^{3}(\Delta w_i^* - \alpha) = 0$, whereby $\alpha = \frac{1}{2}[\Delta w_j^{**}(k) + \sum_{\substack{i=1 \\ i \neq j}}^{3} \Delta w_i^*]$. The new prospective weights are then given by $w_i^{**} \coloneqq w_i(k-1) + \Delta w_i^{**}(k), i = 1,2,3$, where in particular $w_j^{**} \coloneqq w_j(k-1) + \Delta w_j^{**}(k)$=0. If none of the resulting w_i^{**} are negative, then these are the updated weights $w_i(k)$; however, if one of them is negative, e.g. $w_l^{**} < 0$, then the updated weights are $w_j(k) \coloneqq 0$, $w_l(k) \coloneqq 0$, and $w_i(k) \coloneqq 1, i \in \{1,2,3\}\ \&\ i \neq j, l.$;

- If two of the w_i^* obtained using Equation (6.21) are negative, e.g. w_j^*<0 and $w_l^* < 0$, this implies that the third weight, $w_i^*, i \in \{1,2,3\}\ \&\ i \neq j, l$, will be larger than one, since the sum of the three is always equal to unity. Therefore it suffices to take $w_j(k) \coloneqq 0$,$w_l(k) \coloneqq 0$, and $w_i(k) \coloneqq 1$.

This scheme allows for weights that at some point devolve to a zero value, signifying complete rejection of the corresponding KF, to start recovering if and when they are subsequently prescribed positive weight increments. A similar scheme without recovery is easily implemented by flagging down a KF that is assigned a zero weight at any given time, thenceforth permanently assigning it a zero weight and carrying out the weight redistribution process among the remaining filters.

For both the crisp and fuzzy data fusion algorithms, the initial weights are assumed equal ($w_i = \frac{1}{3}, i = 1,2,3$) and they are not modified until time instant K has been reached, which is the number of samples required to compute the SMA.

6.3. Results and discussions

6.3.1. Simulation of the reliability determination and autonomous temporary recovery of signal loss

This simulation adds the reliability determination Equations (6.7) and (6.8) as well as the rules to recover the short time GPS signal loss to the UKF based multi-sensor data fusion algorithm in Section 4.3.3.2. Recalling the Simulation 4.4 with planned trajectory 1, the USV started from the start point (765 m, 728 m) and was conducting a mission to track two waypoints (650 m, 385 m) and (320 m, 190 m) with an end point (30 m, 250 m) along the coastline of The Solent with a variety of current influences. In this simulation, the sensor data are simulated again based on their modelling in Chapter 3 and their noise characteristics as given in Table 4.5. In order to test the reliability of the system, the GPS signals are set to be blocked during the time steps $k = 200\ to\ 230\ s$ and $k = 700\ to\ 750\ s$. The trajectory results are shown in Figure 6.6. The two green circles highlight the periods when the GPS signal is blocked. As can be observed in Figure 6.6, the GPS measured positions are missing during the two highlighted periods whereas the fusion results using the developed data fusion algorithm (red line) are still close to the actual trajectory (black line), which confirms that the algorithm can provide accurate estimations of the USV's position and recover the USV's trajectory during blockage of the GPS signal.

The percentage value determined to represent system reliability is shown in Figure 6.7. It fluctuates with the mean around 75% and reduces to zero when the GPS signal is blocked. The value of the reliability is obtained by calculating the consistency of the GPS measured positions and IMU predicted positions. When the GPS signal is missing, the system assigns the GPS measured position as (0, 0) and the difference between the GPS measured position (0, 0) and IMU predicted position is numerically high, which reduces the consistency of the two positions and generates a very low reliability measure.

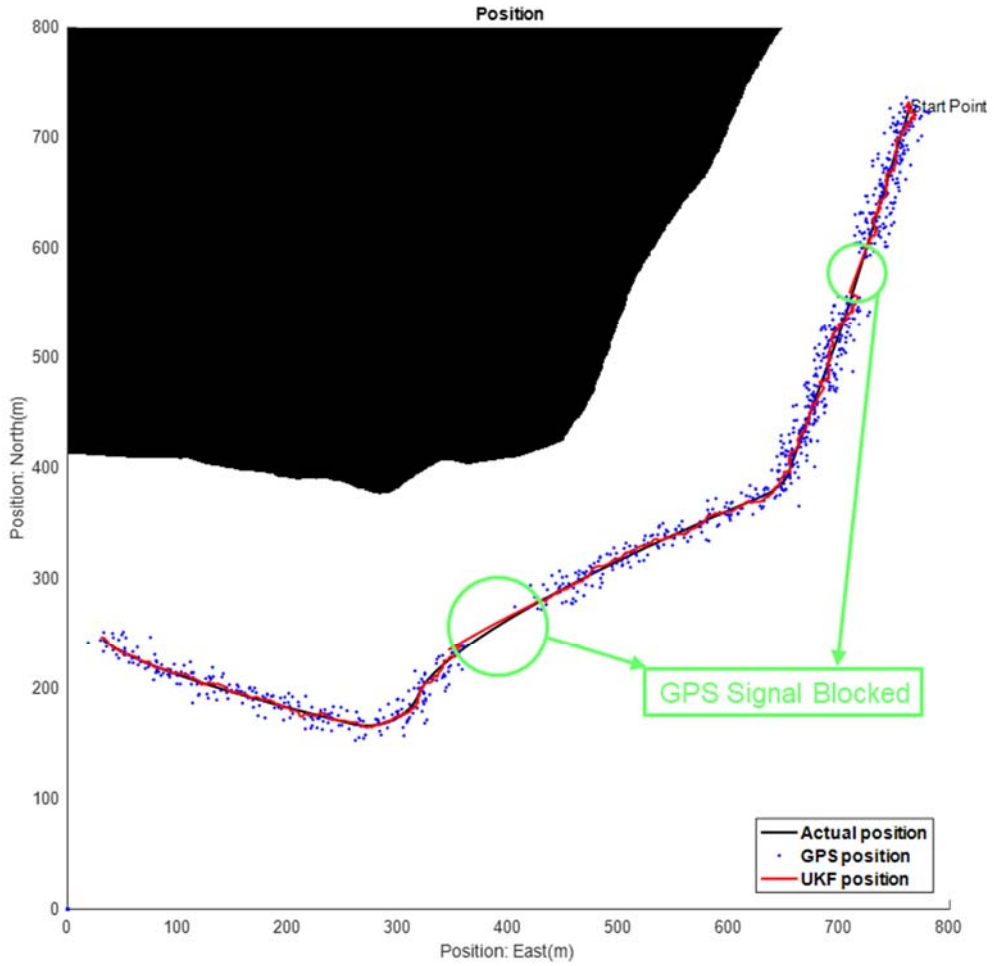

Figure 6. 6 Simulation Scenario 6.1: Recovered trajectory of USV navigation with two short term GPS blockage

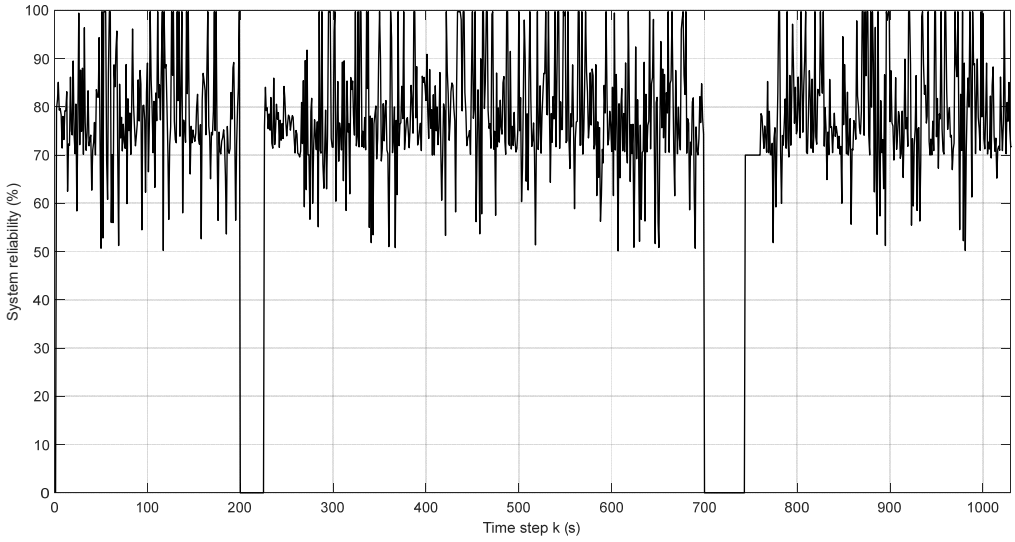

Figure 6. 7 Simulation Scenario 6.1: The determined system reliability based on the consistency of GPS positions and IMU predicted positions

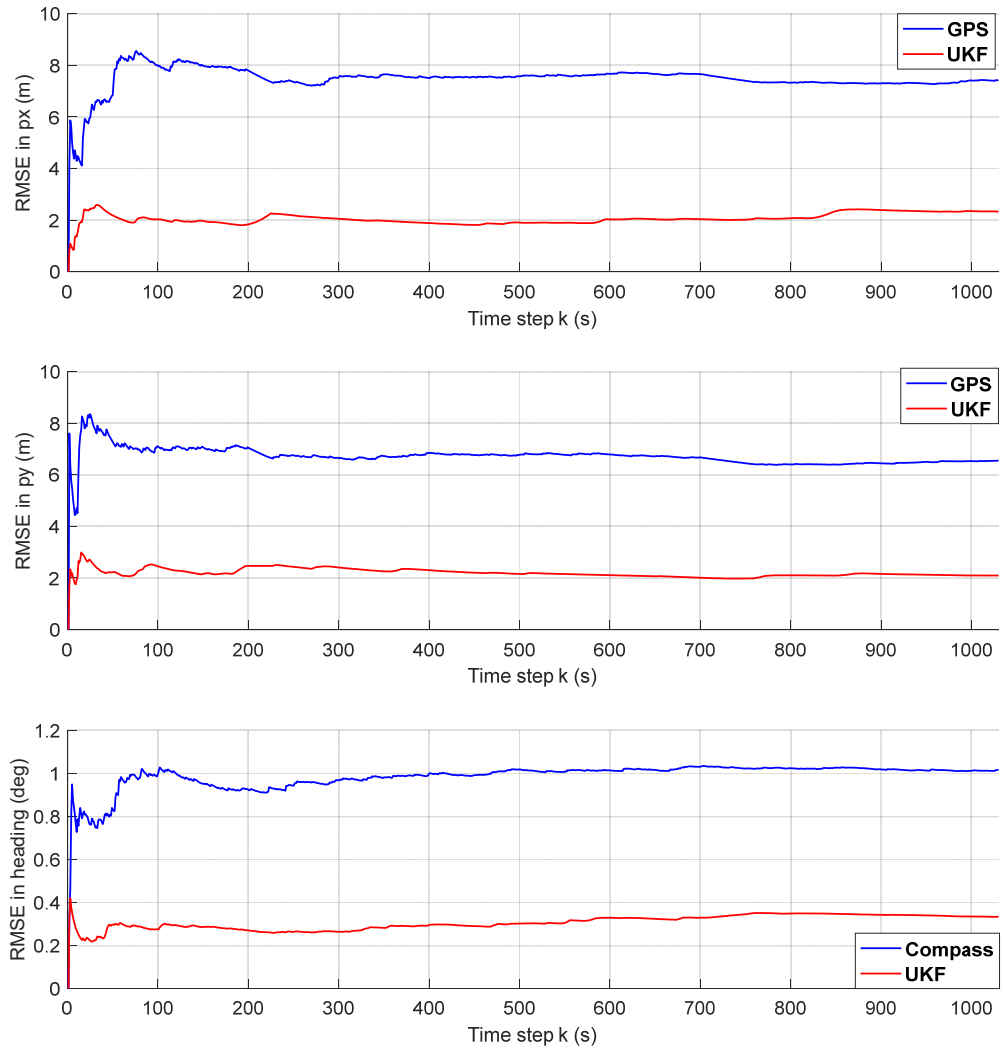

Figure 6. 8 Simulation Scenario 6.1: Rooted mean square errors of USV positions and headings with GPS signal blockage

The accuracy of the developed data fusion algorithm is demonstrated by the RMS errors displayed in Figure 6.8. According to Rule 2 in Table 6.1, the RMS error of the GPS measurements during the period when the signal is blocked remains the same as at the last time step before the signal is blocked. The red line in the top two figures in Figure 6.8 that denotes the RMS errors of the fused positions are stabilised with reduced values over the raw GPS RMS errors.

6.3.2. Simulation of Fuzzy logic based data fusion algorithm

The fuzzy logic based data fusion algorithm is implemented and compared to a crisp decision-making algorithm, both of which attempt to fuse data from the three KFs in such a way as to disregard erroneous estimates caused by faulty compass readings. This simulation study (Simulation 6.2) uses simulated gyroscope and compass readings, based on a prescribed turning rate of the vehicle. The turning rate of the vehicle, in °/s, is prescribed according to:

$$\omega_i(k) = \sin(k) + \sin\left(\frac{k}{10}\right) + \sin\left(\frac{k}{100}\right) \tag{6.22}$$

to allow excitation at different frequencies. The gyroscope measurements are simulated based on this actual turning rate plus the noise vectors according to Equation (3.4), with a constant bias of 3 °/s, and a white, normally distributed random measurement noise with variance $q = (0.5°/s)^2$. The actual heading angle of the USV is calculated from integration of $\omega_i(k)$, based on which three different compass readings are simulated using Equation (6.23) with three different measurement noise sequences ν_i with variances $R_1 = (1.5\ °)^2, R_2 = (5.5\ °)^2, R_3 = (9.5\ °)^2$ for each one, respectively.

$$z_\theta = \theta + \nu_i \tag{6.23}$$

A KF is then simulated for each gyro-compass pair. The KF state vectors are initialised with the correct initial vehicle heading, but with zero gyro-bias estimates. At each sampling instant the SMA is calculated with $N = 30$, and threshold values for the crisp decision rules and fuzzy membership functions are given in Table 6.3:

Table 6. 3 Simulation Scenario 6.2: Threshold values for crisp decision rules and parameters of fuzzy membership functions

Parameter	$\mathbf{SMA_{max}}$	$\mathbf{SMA_{min}}$	**SMAN**	**SMAP**	**DWN**	**DWP**
Value	5	-5	-10	10	-0.1	0.1

The simulation runs for 1000 time steps. After one third of the total simulation time, Compass 2 ($R_2 = (5.5\ °)^2$) is made to fail so that the readings remain static at the last value before failure. The simulation results are shown in Figures 6.9 to 6.13.

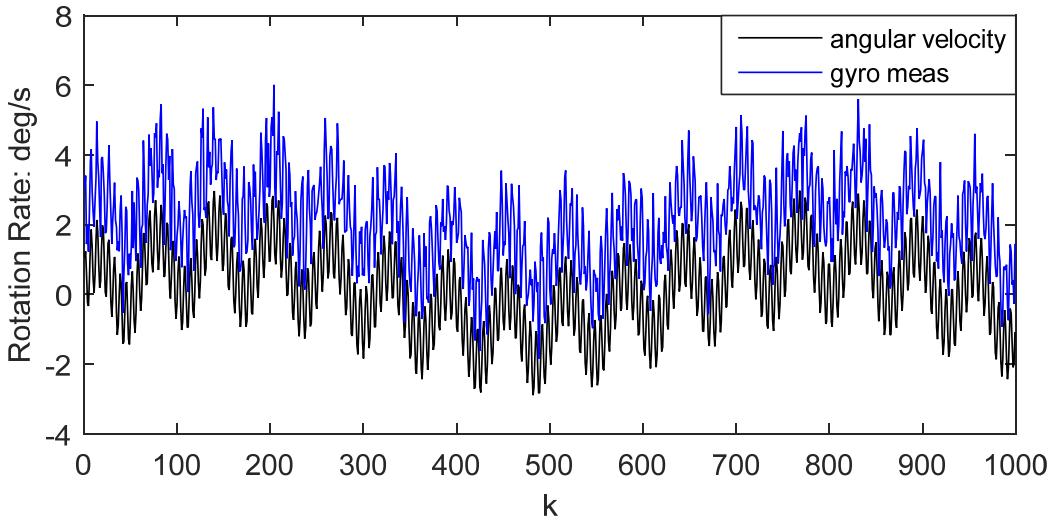

Figure 6. 9 Simulation Scenario 6.2: simulated actual USV change in rotation rate ω_i and gyroscope output ω_o

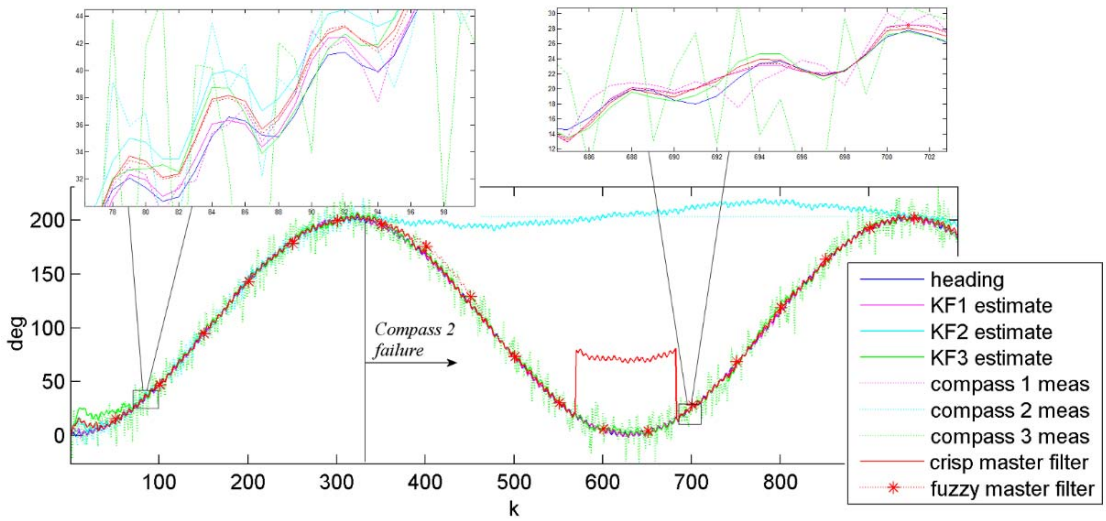

Figure 6. 10 Simulation Scenario 6.2: actual and KF estimates of the heading, compass measurements, and crisp and fuzzy data fusion estimates (Compass 2 fails at time step $k = 333$)

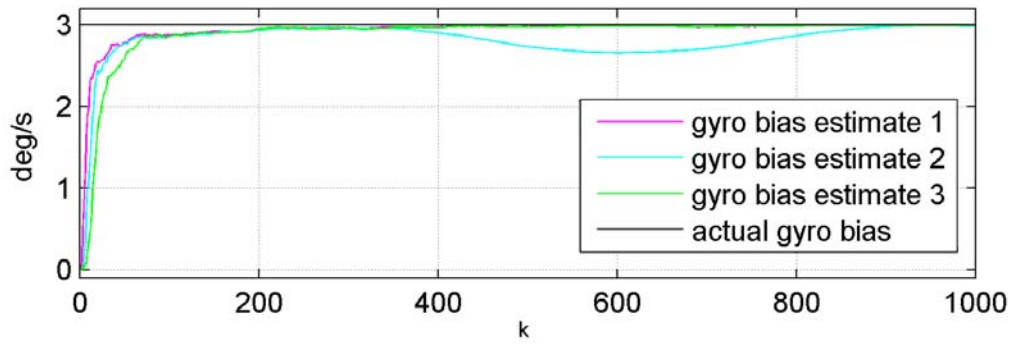

Figure 6. 11 Simulation Scenario 6.2: actual and KF estimates of the gyroscope bias (Compass 2 fails at time step $k = 333$)

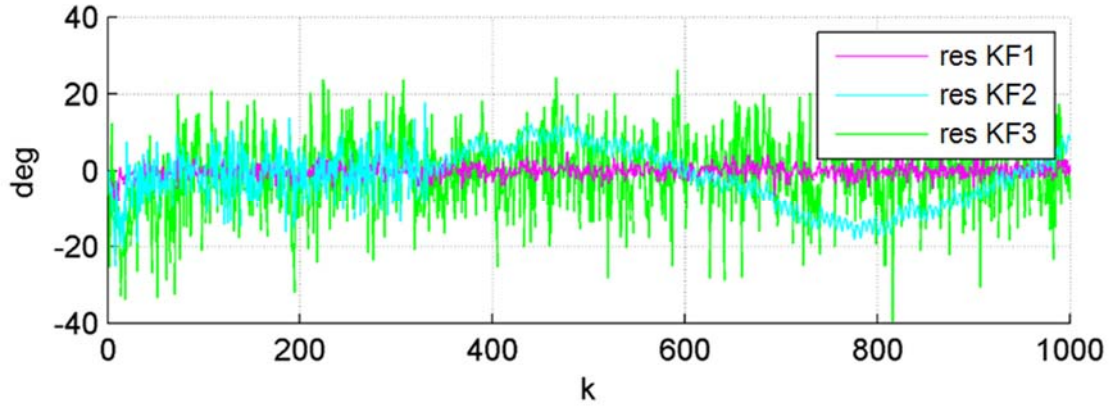

Figure 6. 12 Simulation Scenario 6.2: residual sequences of each KF (Compass 2 fails at time step *k* = *333*)

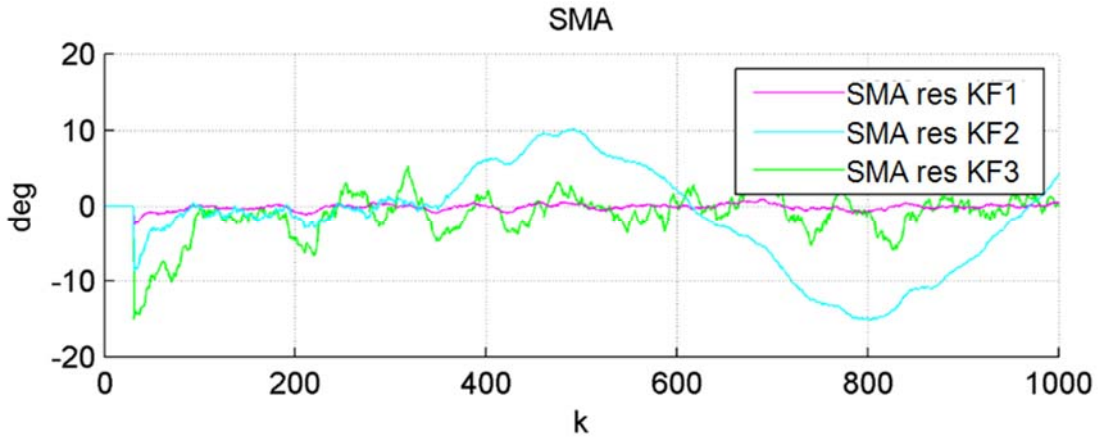

Figure 6. 13 Simulation Scenario 6.2: SMA of the residual sequence of each KF (Compass 2 fails at time step *k* = *333*)

It can be seen that each KF estimate improves upon the corresponding raw compass estimate, particularly for the two KFs that operate under the correct hypotheses in Figure 6.12. However, the KF associated with the failed compass cannot provide a reliable estimate. From Figure 6.11, it can also be observed how this KF's estimate of the gyroscope bias also starts deviating from the true bias from the moment the compass fails. From Figure 6.10, whilst both the crisp and the fuzzy logic fusion of the compass data are able to reject the KF associated with the failed compass, the crisp estimates immediately reincorporate this KF when the SMA falls back within the threshold limits, due purely to the change in turning rate, which results in an incorrect estimate. The fuzzy logic fusion is more cautious, and does not restore confidence to the failed compass KF so readily.

Table 6. 4 Simulation Scenario 6.2: RMSE results for the simulation of 1000 time-steps

Method	***RMSE (deg)***
KF1	0.71
KF2	9,995
KF3	17.67
Compass 1	2.02
Compass 2	9,688
Compass 3	99.17
Crisp decision fusion	502.18
Fuzzy decision fusion	11.62

Although from Table 6.4 the RMSE of the fuzzy logic fused data seems to be considerably larger than that of the best KF (KF1), this is because the initial transient period (bearing in mind that the fuzzy fusion algorithm does not start changing the weights until enough samples are obtained so that the SMA can be calculated), and furthermore, the changes in the weights are gradual. In fact, if the simulation time is increased, then the RMSE of the fuzzy algorithm estimate tends to that of the best KF, as can be seen in the results in Table 6.5, which corresponds to a simulation with a total time of 5000 time-steps.

Table 6. 5 Simulation Scenario 6.2: RMSE results for the simulation of 5000 time-steps

Method	***RMSE (deg)***
KF1	0.73
KF2	5,709
KF3	5.6
Compass 1	2.23
Compass 2	5,755
Compass 3	99.17
Crisp decision fusion	91.4
Fuzzy decision fusion	1.19

6.3.3. Practical trials

The stored experimental data, from the *Springer* USV trial that is described in detail in Section 5.3, are used to test the system's abilities on 1) determining navigation system reliability, 2) autonomous recovery of signal loss in the short term, and 3) autonomous fault detection and tolerance. Recall that earlier the *Springer* USV was assigned the mission to track three waypoints as shown in Figure 5.20. During the operation, GPS raw measurements were set to be blocked for two short time periods and the updated trajectory result is shown in Figure 6.14, where the two periods when the GPS signal is lost are highlighted by the green circles. At this time, the fused data of the data fusion algorithm developed in Section 6.2.1 recovers the trajectories (indicated by the reproduction of trajectory when GPS signal is unavailable) and provides continuous estimations of the position.

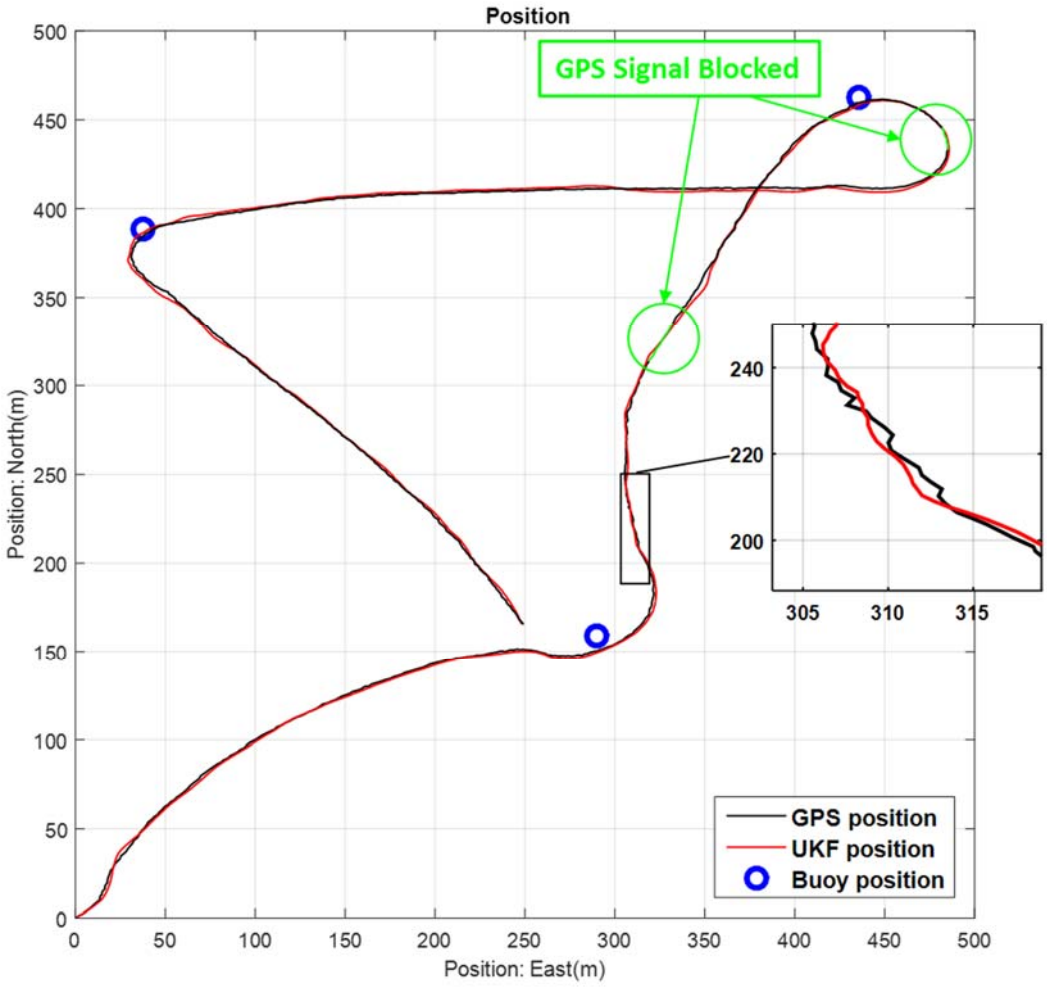

Figure 6. 14 *Springer* trial trajectory fusion results with two blockages of GPS signal

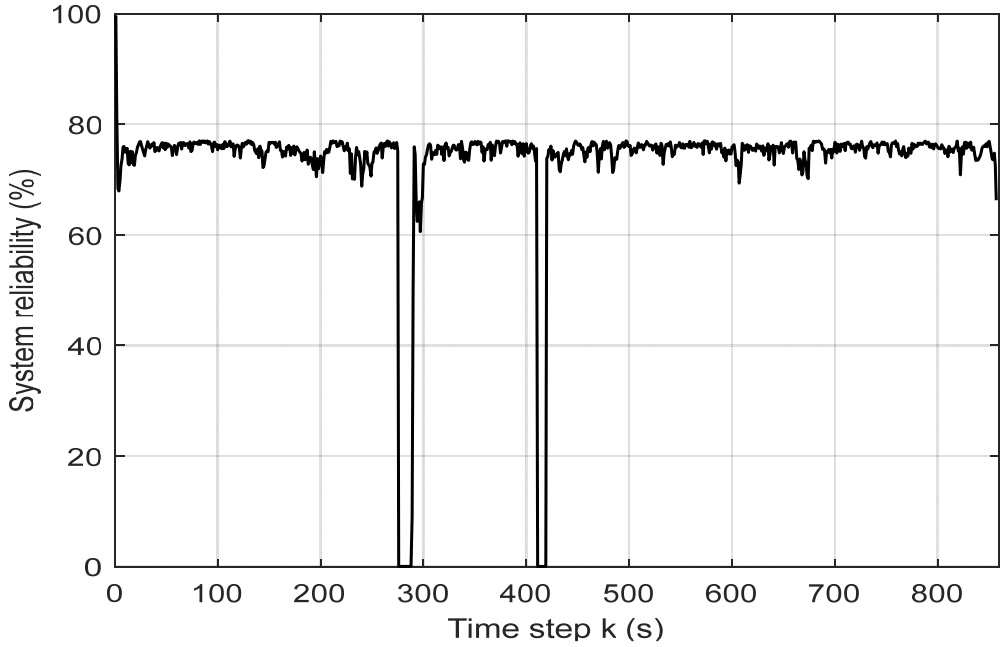

Figure 6. 15 Determined system reliability for *Springer* trial

Figure 6.15 illustrates the determined system reliability. Similar to the simulation, when the GPS signal is unavailable, the Reliability degrades to 0% as the measurement of the GPS cannot be trusted during that time. Apart from that, the reliability varies between 60% and 80%, which gives a reasonably high degree of confidence that the estimations of the navigation system are reliable.

According to the description in Chapter 3, *Springer* is equipped with three independent electronic compasses, TCM2, HMR3000 and KVH100 as well as a MEMS gyroscope. The HMR3000, which is labelled as Compass 2, is made to fail from time step $k = 180$ to the end. The raw measurements of the three different electronic compasses (magenta line denotes TCM2's measurements, cyan line represents HMR3000's measurements and the green line denotes KVH100's measurements) and the inferred headings (blue line) obtain by the gyroscope's raw measurements are demonstrated in Figure 6.16. It can be seen that Compass 2 stops providing measurements from $k = 180$ and the heading inferred by the gyroscope alone has a certain deviation from the compass measurements.

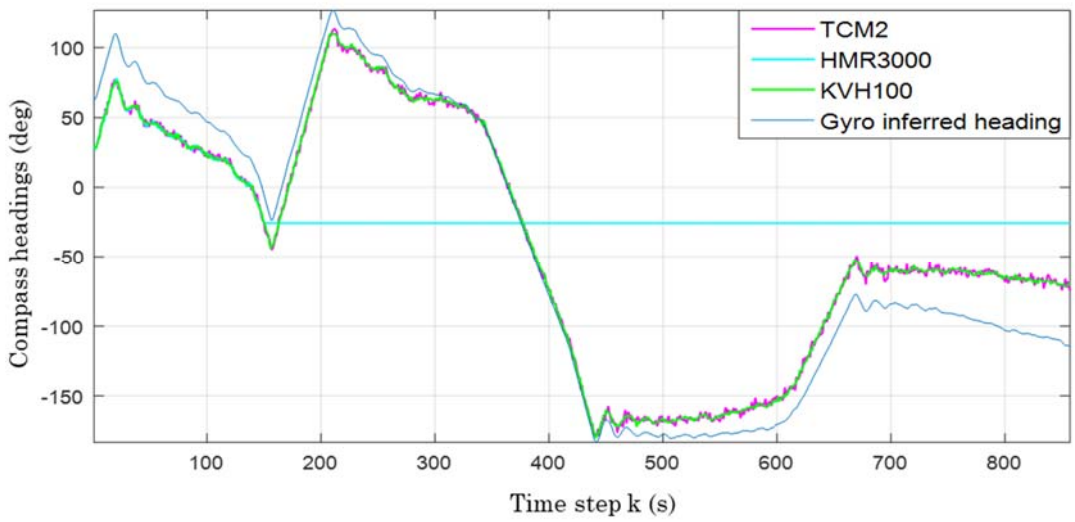

Figure 6. 16 raw measurements of each electronic compass in the trial, in which Compass 2 fails at time step $k = 180$

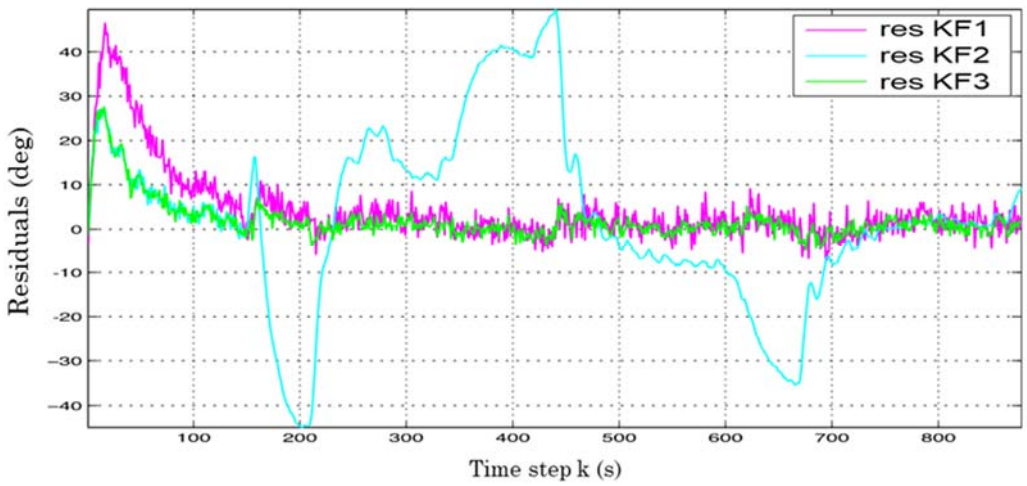

Figure 6. 17 Residual sequences of each KF

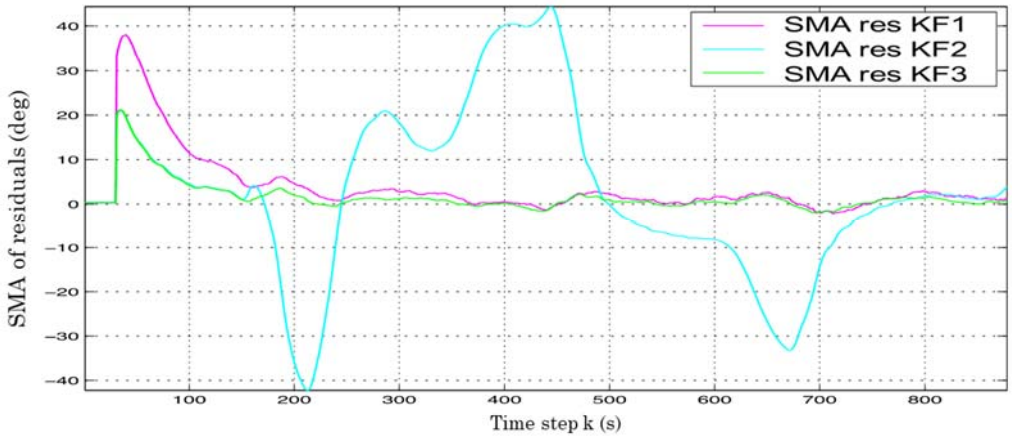

Figure 6. 18 SMA of the residual sequence of each KF

In the trial data analysis, the SMA values of the KF residuals are still calculated with sample size of $N = 30$ as they were for the Simulation 6.2, and the threshold for fuzzy membership functions are also set the same as those in the simulation. As a result of Compass 2's failure, the residuals and their SMA values of KF2 associated with Compass 2 start to deviate significantly from zero (Figure 6.17 and 6.18) at time step $k = 180$. It is noticeable that the KF residuals and their SMA values are also much larger than 0 at the beginning of the KF operation. The reason for this is, at the outset the error covariance is calculated based on initial settings, which are not very accurate. But this effect is reduced in the following stages.

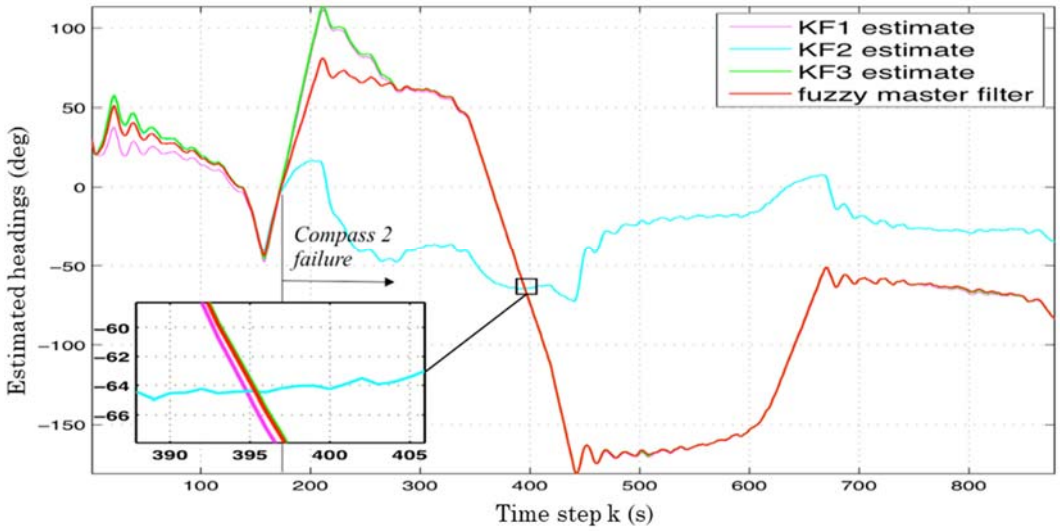

Figure 6. 19 KF estimates of the heading and fuzzy data fusion estimates

The fused heading results are demonstrated in Figure 6.19. The magenta line represents the fused headings of KF1, the cyan line denotes the fused headings of KF2, the green line shows the fused headings of KF3 and the red line denotes the master fusion results of the designed fuzzy multi-sensor data fusion algorithm. Although Compass 2 fails after $k = 180$ and its associated KF2 produces inaccurate estimations (cyan line), the fuzzy master filter can still provide a proper fused result and successfully mitigate against the failed sensor. As in the practical experiment, the actual headings of the USV are unpredictable. It cannot tell whether the fuzzy master filter provides better results than any of the KFs, whereas the results do confirm that the fuzzy master filter can aggregate different fuzzy inputs and discard sensor malfunctions. This fuzzy multi-sensor data fusion algorithm is

sufficient for practical operations since the failure of a navigation instrument cannot be predicted in advance.

6.4. Summary

The data fusion algorithms developed and proved earlier, although delivering accurate navigational data, were not capable of maintaining navigational accuracy in the event of signal, sensor or sub-system failure. It is a practical concern that such failures can occur and this would impact and reduce the level of confidence that the USV's position could be accurately determined to the degree required for safe navigation. In addition, level of confidence would influence the reliability of the leading path generated by path planning algorithms. With the simple system the navigation could default to the working sensor but this solution was only viable for short term loss of sensor performance but not prolonged failure or signal loss.

Using Gaussian techniques a methodology for providing a comparative measure of accuracy in terms of probability confidence was developed. Not only did this impact the actual navigation of the USV but would help inform the path planning in terms of degrees of error consideration that would have to be made in the path planning itself.

Multiple sensors or backup systems could be considered but it was determined that cold backup systems might fail to initiate and take over when required and this would have to be done manually, notwithstanding that such a system may itself be damaged while sitting idle. To achieve improved autonomous navigation management hot backup systems were considered but since the cost effectiveness of having such systems on line to take over just in case of primary system failure it was decided to exploit such systems to provide improved navigational system reliability by combining their operation with that of the primary system.

Multiple Kalman Filters were then considered. The outputs would then be combined and compared using fuzzy data fusion algorithms. Apart from delivering raw navigational data output this approach would allow the system to determine when a sensor or subsystem had failed through analysis of the KF outputs. The levels of confidence would cater for the loss of a subsystem by detecting the ridiculous (on unfeasible) measure and effectively determine that the output from that subsystem would remain unfeasible. This technique was applied to both the Crisp process and the Fuzzy logic process with the latter providing creditable results under simulation of a navigation with a failed sensor for a USV navigation system comprising three electronic compasses and a gyroscope.

Multi-sensor data fusion algorithms will also be investigated and applied to improve the USV's capability in perceiving surrounding environment in the next chapter.

Chapter 7. Multi-sensor Data Fusion for Moving Target Ship Detection in maritime environment

In order to increase the degree of autonomy and better ensure navigation safety, USVs should not only be able to acquire their own accurate and reliable navigational data, but to perceive the surrounding environment to avoid collision risks. Normally, static obstacles, such as small islands and coastlines, can be determined from commercial nautical charts with sufficient accuracy. Detecting dynamic obstacles, such as moving target ships (TS), provides a more complex challenge. Automatic Identification System (AIS) can provide reasonably accurate navigational data of TSs, and a simple AIS receiver can be powered at low voltage levels that are similar and also adequate for the navigation sensor system of an autonomous USV. However, AIS is not installed on-board every vessel or ship and there are also uncertainties associated with AIS signals. Therefore, marine Radar is employed as a complementary sensor to obtain more comprehensive detection of surrounding TSs. In this chapter, intelligent and reliable TS detection, prediction and tracking algorithms are developed to improve and fuse the measurements from AIS and marine Radar.

7.1. AIS aided target ship detection and prediction

The Automatic Identification System (AIS) is an automatic tracking system that is employed by both mariners and the vessel traffic services (VTS) for identifying and locating surrounding vessels to improve maritime safety and was developed over the last few decades (IMO, 2003; Pallotta, 2013). AIS messages contain the target ship's dynamic navigational data. AIS data is reasonably accurate as it transmits absolute navigational information of the TS obtained from its on-board navigational sensors such as the GPS and electronic compass (Robson, 2006). As marine electronic devices, common AIS transponders support the NMEA 0183 output format standard, but unlike the GPS or electronic compass that provide measurements in human readable ASCII characters, the AIS messages use 6-bit binary encoding for the bulk

of the sentences (Holm and Mellegard, 2018). The messages commonly contain static information, dynamic information, voyage related information and short safety information. Static information, such as the ship's call sign, name and its Maritime Mobile Service Identity (MMSI) is permanently stored in the on-board AIS transponder. Dynamic information that contains the ship's absolute position, speed and course, is collected from the TS's own navigational sensors, e.g. GPS receivers, electronic compasses, etc. Voyage related information that includes ship's destination, hazardous cargo type, etc. is set up at the beginning of the voyage (Harati-Mokhtari, et al. 2007). The AIS transponder autonomously transmits messages at different update rates depending on message type (Lin, et al. 2008), which are listed in Table 7.1. Speed and course alteration will cause different reporting intervals of the dynamic information; the more significant the change , the higher the frequency of message transmission. The information updating interval can be as short as 2 seconds when a high-speed ship is changing its course, while a three-minute interval would be generated for the ship at anchor.

Table 7. 1 Reporting intervals of AIS dynamic messages (1 knot ≈ 0.51444 m/s)

Ship Status	**Reporting Interval (s)**
Anchored	180
Speed at 0-14 knots	10
Speed at 0-14 knots & altering	4
Speed at 14-23 knots	6
Speed at 14-23 knots & altering	2
Speed > 23 knots	2
Speed > 23 knots & altering	2

The real time TS's position is essential to evaluate the risk of collision between the USV and the TS. With knowledge of an USV's own navigational data together with the real time TS's positions, the risk of collision with the TS can be assessed against the navigation path designed for the USV. As shown in Figure 7.1, the smallest distance between the two synchronised positions can be calculated. If this distance is less than the predefined safe distance between the two ships the possibility of a clash exists, hence appropriate collision avoidance manoeuvres are needed and a new path to ensure the USV's safety will be generated. A detailed path planning algorithm

based on this premise can be found in Liu et al, 2017. Therefore, predictions of TS positions during extended AIS updating intervals are valuable for the path planning algorithm to take actions to avoid collision risks.

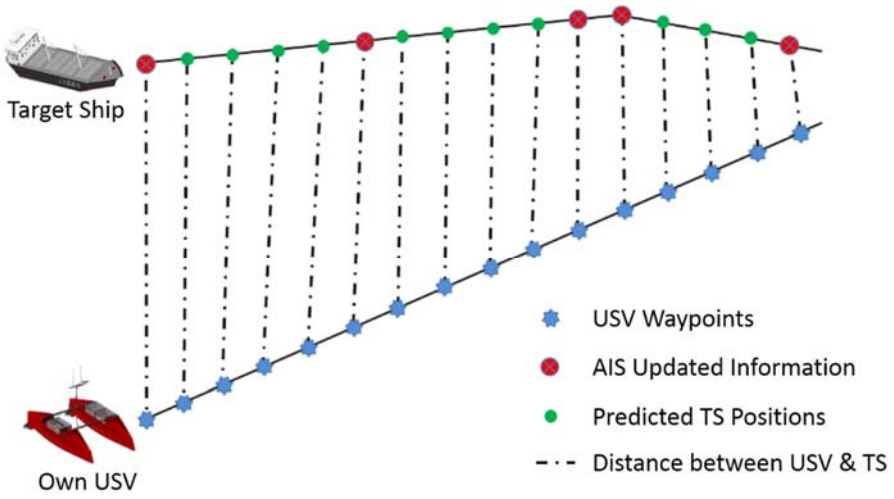

Figure 7. 1 Collision risk assessment

7.1.1. Target Ship detection and prediction

Prior to the consideration of a complex maritime environment, this section focuses on detecting and predicting the navigational data of a single target ship that is equipped with an AIS transponder to broadcast its own navigational data, i.e. position, speed over ground (SOG) and course over ground (COG). In general, the average seagoing vessel is not designed for both rapid and precise manoeuvring and its operation is associated with constant velocity and course unless manoeuvring is required to eliminate collision risks or correct trajectory drift. The rate of course change is often kept gradual to maintain the vessel on an even keel (Fossen, 2002). Therefore, a constant velocity (CV) model can be used to describe the state of the TS (Liu et al, 2017). The state vector is defined to include essential navigational data to assess the collision risk between the TS and USV.

$$\boldsymbol{x}_T = \begin{bmatrix} p_{Tx} & p_{Ty} & v_{Tx} & v_{Ty} & \varphi \end{bmatrix}^T \tag{7.1}$$

where p_{Tx} and p_{Ty} represent the TS's positions, v_{Tx} and v_{Ty} are the TS's SOG in the x and y directions, and φ is the COG of the TS. The system state equation based on a constant velocity model is denoted as below.

$$\boldsymbol{x}_T(k) = \begin{bmatrix} 1 & 0 & T & 0 & 0 \\ 0 & 1 & 0 & T & 0 \\ 0 & 0 & 1 & 0 & 0 \\ 0 & 0 & 0 & 1 & 0 \\ 0 & 0 & 0 & 0 & 1 \end{bmatrix} \boldsymbol{x}_T(k-1) + \boldsymbol{w}_T(k-1) \tag{7.2}$$

The observations are provided by the dynamic t6AIS messages, which give the absolute positions, SOG and COG of the detected TS. Therefore, the system measurement model can be defined as:

$$\boldsymbol{z}_A(k) = \begin{bmatrix} 1 & 0 & 0 & 0 & 0 \\ 0 & 1 & 0 & 0 & 0 \\ 0 & 0 & 1 & 0 & 0 \\ 0 & 0 & 0 & 1 & 0 \\ 0 & 0 & 0 & 0 & 1 \end{bmatrix} \boldsymbol{x}_T(k) + \boldsymbol{v}_T(k) \tag{7.3}$$

The Kalman Filter (Equations (7.4) to (7.9)) is then applied to reduce AIS signal noise and provide predicted navigational data during long AIS data-transmitting intervals. As shown in Figure 7.2, the algorithm first takes the prior states including TS's position, SOG and COG to make predictions of the navigational data for the next time step using Equations (7.4) and (7.5). It then calls the system to check whether there is an updated AIS message. If so, the system will enter the estimation stage using the updated data to correct the predicted TS's navigational data by Equations (7.6) to (7.8). Otherwise, the system will output the predicted navigational data and use it as the next state to enter the next prediction-estimation process.

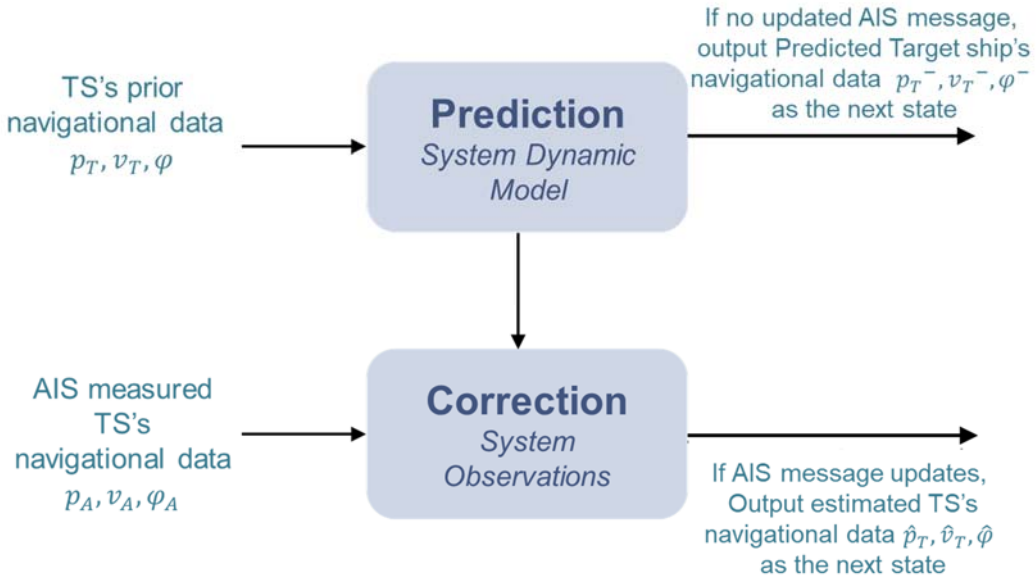

Figure 7.2 AIS data pre-process prediction & estimation

The predicted state of the TS's navigational data is computed by Equation (7.4) using the constant velocity model and the predicted error covariance $\boldsymbol{P}_T^-$ is defined in Equation (7.5), where $\boldsymbol{Q}_T$ is the processing error covariance.

$$\hat{\boldsymbol{x}}_T^-(k) = \begin{bmatrix} 1 & 0 & T & 0 & 0 \\ 0 & 1 & 0 & T & 0 \\ 0 & 0 & 1 & 0 & 0 \\ 0 & 0 & 0 & 1 & 0 \\ 0 & 0 & 0 & 0 & 1 \end{bmatrix} \hat{\boldsymbol{x}}_T(k-1) \tag{7.4}$$

$$\boldsymbol{P}_T^-(k) = \begin{bmatrix} 1 & 0 & T & 0 & 0 \\ 0 & 1 & 0 & T & 0 \\ 0 & 0 & 1 & 0 & 0 \\ 0 & 0 & 0 & 1 & 0 \\ 0 & 0 & 0 & 0 & 1 \end{bmatrix} \boldsymbol{P}_T(k-1) \begin{bmatrix} 1 & 0 & T & 0 & 0 \\ 0 & 1 & 0 & T & 0 \\ 0 & 0 & 1 & 0 & 0 \\ 0 & 0 & 0 & 1 & 0 \\ 0 & 0 & 0 & 0 & 1 \end{bmatrix}^T + \boldsymbol{Q}_T \tag{7.5}$$

The Kalman Filter gain $\boldsymbol{K}_T$ to correct the prior TS's navigational data by reducing the mean square error is computed by Equations (7.6) and (7.7):

$$\boldsymbol{K}_T(k) = \boldsymbol{P}_T^-(k) \begin{bmatrix} 1 & 0 & 0 & 0 & 0 \\ 0 & 1 & 0 & 0 & 0 \\ 0 & 0 & 1 & 0 & 0 \\ 0 & 0 & 0 & 1 & 0 \\ 0 & 0 & 0 & 0 & 1 \end{bmatrix}^T \boldsymbol{S}_T(k)^{-1} \tag{7.6}$$

$$\boldsymbol{S}_T(k) = \begin{bmatrix} 1 & 0 & 0 & 0 & 0 \\ 0 & 1 & 0 & 0 & 0 \\ 0 & 0 & 1 & 0 & 0 \\ 0 & 0 & 0 & 1 & 0 \\ 0 & 0 & 0 & 0 & 1 \end{bmatrix} \boldsymbol{P}_T{}^{-}(k) \begin{bmatrix} 1 & 0 & 0 & 0 & 0 \\ 0 & 1 & 0 & 0 & 0 \\ 0 & 0 & 1 & 0 & 0 \\ 0 & 0 & 0 & 1 & 0 \\ 0 & 0 & 0 & 0 & 1 \end{bmatrix}^T + \boldsymbol{R}_T \tag{7.7}$$

As demonstrated in Figure 7.2, if there is an updated AIS message with the observation $\boldsymbol{z}_A(k)$, the system state $\hat{\boldsymbol{x}}_T(k)$ can be computed by applying the calculated Kalman Filter gain $\boldsymbol{K}_T$ to the prior TS's navigational data as shown in Equations (7.8) and (7.9). If there is no updated AIS message, the predicted system state $\hat{\boldsymbol{x}}_T{}^{-}(k)$ will be treated as the current state of the TS to assess the collision risk.

$$\hat{\boldsymbol{x}}_T(k) = \hat{\boldsymbol{x}}_T{}^{-}(k) + \boldsymbol{K}_T(k) \left[\boldsymbol{z}_A(k) - \begin{bmatrix} 1 & 0 & 0 & 0 & 0 \\ 0 & 1 & 0 & 0 & 0 \\ 0 & 0 & 1 & 0 & 0 \\ 0 & 0 & 0 & 1 & 0 \\ 0 & 0 & 0 & 0 & 1 \end{bmatrix} \hat{\boldsymbol{x}}_T{}^{-}(k) \right] \tag{7.8}$$

$$\boldsymbol{P}_T(k) = \left(I - \boldsymbol{K}_T(k) \begin{bmatrix} 1 & 0 & 0 & 0 & 0 \\ 0 & 1 & 0 & 0 & 0 \\ 0 & 0 & 1 & 0 & 0 \\ 0 & 0 & 0 & 1 & 0 \\ 0 & 0 & 0 & 0 & 1 \end{bmatrix} \right) \boldsymbol{P}_T{}^{-}(k) \tag{7.9}$$

7.1.2. Manoeuvring target ship detection and prediction

In a maritime environment, although a vessel when conducting a mission usually adheres to straight line trajectories at a constant speed, the influences caused by water currents and winds would alter its trajectory. The vessel normally makes manoeuvres to correct its course to its destination or the next waypoint (Kazimierski, 2013). As a result, the system state equations, based on a constant velocity model are inaccurate and would generate inaccurate predictions when the TS is manoeuvring. Therefore, multiple models have been integrated into the system to describe the TS's motions with improved veracity to provide more accurate detection and prediction results.

7.1.2.1. Interacting multi-model based target ship detection

Interacting multi-model filtering has been widely used in manoeuvring TS detection (Kim and Hong, 2004; Wolejsza, 2012; Gao, et al, 2012; Zhang et al, 2014; Zhu et al, 2016; Sanchez-Ramirez et al, 2019) since it was first proposed by Blom (1984). According to the International Maritime Organization (IMO), 2002, vessels should maintain as steady a course as possible while operating over the sea. Turning at constant angular velocity is a common manoeuvre of vessels. Therefore, a coordinate turn (CT) model is normally used to model the TS's manoeuvre (Sanchez-Ramirez et al, 2019, Zhai et al, 2014). The transition matrix of a CT model is expressed in Equation (7.10) and the system dynamic equations are demonstrated in Equation (7.11).

$$\boldsymbol{A_{CT}} = \begin{bmatrix} 1 & 0 & \sin\omega T/\omega & -(1-\cos\omega T)/\omega \\ 0 & 1 & 1-\cos\omega T/\omega & \sin\omega T/\omega \\ 0 & 0 & \cos\omega T & -\sin\omega T \\ 0 & 0 & \sin\omega T & \cos\omega T \end{bmatrix} \tag{7.10}$$

$$f\big(x(k)\big) = \begin{cases} p_x(k-1) + \frac{\sin(\omega(k-1)T)}{\omega(k-1)} \times v_x(k-1) - \frac{(1-\cos(\omega(k-1)T))}{\omega(k-1)} \times v_y(k-1) \\ p_y(k-1) + \frac{1-\cos\omega((k-1)T)}{\omega(k-1)} \times v_x(k-1) + \frac{\sin(\omega(k-1)T)}{\omega(k-1)} \times v_y(k-1) \\ \cos(\omega(k-1)T) \times v_x(k-1) - \sin(\omega(k-1)T) \times v_y(k-1) \\ \sin(\omega(k-1)T) \times v_x(k-1) + \cos(\omega(k-1)T) \times v_y(k-1) \\ \theta(k-1) + \omega(k-1)T \end{cases} \tag{7.11}$$

The state of the TS can be predicted if the angular velocity is known. However, AIS cannot provide the measurement of the TS's angular velocity. Therefore, the angular velocity should be considered as a parameter rather than a variable to generate multiple models and an interacting multiple model estimator has been integrated to the KF based TS detection and prediction algorithm to model the TS's manoeuvres. The system state equation of the CT model can be then defined in Equation (7.12).

$$\boldsymbol{x}_T(k) = \begin{bmatrix} 1 & 0 & \frac{\sin\omega T}{\omega} & \frac{-(1-\cos\omega T)}{\omega} & 0 \\ 0 & 1 & \frac{1-\cos\omega T}{\omega} & \frac{\sin\omega T}{\omega} & 0 \\ 0 & 0 & \cos\omega T & -\sin\omega T & 0 \\ 0 & 0 & \sin\omega T & \cos\omega T & 0 \\ 0 & 0 & 0 & 0 & 1 \end{bmatrix} \boldsymbol{x}_T(k-1) + \begin{bmatrix} 0 \\ 0 \\ 0 \\ 0 \\ \omega T \end{bmatrix} + \boldsymbol{w}_T(k-1) \tag{7.12}$$

The Interacting Multiple Model Kalman Filter (IMMKF) has been proposed to calculate the possibilities of each of the predefined models and generate the fused navigational data accordingly. First, a set of fixed values of the angular velocities ($\omega 1, \omega 2, \omega 3, \dots, \omega j$) are defined to generate different coordinate turn models $CT1, CT2, CT3, \dots CTj$ as M using Equation (7.12).

$$M = \{CT1(\omega 1), CT2(\omega 2), CT3(\omega 3), \dots CTj(\omega j)\} \tag{7.13}$$

The model at each time step k can be expressed as:

$$m_j(k) \triangleq \{M(k) = m_j\} \tag{7.14}$$

Then the predicted probability $\mu_j{}^-$ of each model at time step k can be computed as in Equation (7.15).

$$\mu_j{}^-(k) \triangleq P\{m_j(k)|z(k-1)\} = \sum_i \pi_{ij}\, \mu_i(k-1) \tag{7.15}$$

The probabilities are then used to generate each model's mean $\hat{x}_{0j}$ and the spread of the means X_j and calculate and covariance P_{0j} of each model by Equations (7.16) to (7.19).

$$\mu_{i|j} \triangleq P\{m_i(k-1)\big|m_j(k), z(k-1)\} = \pi_{ij}\mu_i(k-1)/\mu_j{}^- \tag{7.16}$$

$$\hat{x}_{0j}(k-1) \triangleq E\big[x(k-1)|m_j(k), z(k-1)\big] = \sum_i \hat{x}_i(k-1)\, \mu_{i|j} \tag{7.17}$$

$$X_j \triangleq \sum_i \big[\hat{x}_i(k-1) - \hat{x}_{0j}(k-1)\big]\big[\hat{x}_i(k-1) - \hat{x}_{0j}(k-1)\big]^T \mu_{i|j} \tag{7.18}$$

$$P_{0j}(k-1) = \sum_i P_i(k-1)\mu_{i|j} + X_j \tag{7.19}$$

The predicted mean of system state $\hat{x}_j{}^-$ and covariance $P_j{}^-$ are computed using Equations (7.20) and (7.21).

$$\hat{x}_j{}^-(k) = A_{CTj}(k-1)\hat{x}_{0j}(k-1) \tag{7.20}$$

$$P_j{}^-(k) = A_j(k-1)P_{0j}(k-1)A_j(k-1)' + Q_j(k-1) \tag{7.21}$$

The measurement residual of each model is calculated as Equation (7.22) and gives the covariance of the residual in Equation (7.23).

$$v_j(k) = z(k) - H_j\hat{x}_i{}^-(k) \tag{7.22}$$

$$S_j(k) = H_j P_j^{-}(k) H_j' + R_j \tag{7.23}$$

The Kalman Filter gain can then be computed and the estimated state vectors $\hat{x}_j$ and error covariance P_j of each model are obtained by Equations (7.24) to (7.28).

$$K_j(k) = P_j^{-}(k) H_j' S_j(k)^{-1} \tag{7.24}$$

$$\hat{x}_j(k) = \hat{x}_j^{-}(k) + K_j(k) \nu_j(k) \tag{7.25}$$

$$P_j(k) = P_j^{-}(k) - K_j(k) S_j(k) K_j(k)' \tag{7.26}$$

$$L_j = \mathcal{N}\left[\nu_j; 0, S_j\right] = \frac{1}{\sqrt{2\pi S_j}} \times \exp\left(-\frac{1}{2} \nu_j^T S_j^{-1} \nu_j\right) \tag{7.27}$$

$$\mu_j = \frac{\mu_j^{-} L_j}{\sum_i \mu_i^{-} L_i} \tag{7.28}$$

The final estimation of the state vector and error covariance can be computed by combining all the data from each model based on its probability.

$$\hat{x}(k) \triangleq E[x(k)|z(k)] = \sum_j \hat{x}_j(k) \mu_j \tag{7.29}$$

$$P(k) \triangleq E\left[\left(x(k) - \hat{x}(k)\right)\left(x(k) - \hat{x}(k)\right)'|z(k)\right] = \sum_j P_j(k)\, \mu_j + X \tag{7.30}$$

$$X \triangleq \sum_i \left(\hat{x}_i(k) - \hat{x}(k)\right)\left(\hat{x}_i(k) - \hat{x}(k)\right)' \mu_i \tag{7.31}$$

This process is repeated in each iteration of the Kalman Filter based TS tracking algorithm and the most probable model is determined to express the TS's manoeuvre.

7.1.2.2. Multi-factor manoeuvre detector

The computational cost of multiple models becomes quite high with the increasing number of the models, which introduces a degree of non-practicability to real-time systems. Manoeuvres represent a change in the TS motion pattern, therefore detecting the manoeuvre of the TS first offers a solution to reduce such computational cost since the multiple model-based data fusion algorithm will only be employed when manoeuvring of the TS is detected. Chi-square based detectors are widely used in manoeuvring TS detection (Li and Jilkov, 2002). For an n dimensional Gaussian distributed vector $x \sim \mathcal{N}(\hat{x}, P)$, its covariance is Chi-square

distributed. Therefore, the proposed detector employs the covariance of system residuals in the proposed IMMKF TS detection and prediction algorithm to compare with the Chi-square defined thresholds (Equations (7.32) to (7.33)). The thresholds are listed in Table 7.2 (Lancaster, 1965), where α is the probability and $1-\alpha$ is the level of confidence, which is typically set at 95% or 99.5% by the system. The detector identifies whether the TS is making a manoeuvre by Equation (7.34). This procedure will save a significant amount of the computational cost generated by the multiple model filter.

$$\boldsymbol{\varepsilon}(k) = \boldsymbol{z}(k) - \boldsymbol{H}\hat{\boldsymbol{x}}(k) \tag{7.32}$$

$$dc(k) = \left|\boldsymbol{cov}\left(\boldsymbol{\varepsilon}(k)\right)\right| = \boldsymbol{\varepsilon}'(k)\,\boldsymbol{S}_T(k)^{-1}\boldsymbol{\varepsilon}(k) \tag{7.33}$$

$$dc(k) > \eta = {\chi_n}^2(\alpha) \tag{7.34}$$

Table 7. 2 Chi square distribution ${\chi_n}^2$

Confidence $(1-\alpha)$	**95%**	**99%**
Probability level (α)	3.84	0.01
$\boldsymbol{\eta^2}$ $(\boldsymbol{dof = 2})$	5.99	9.21
$\boldsymbol{\eta^2}$ $(\boldsymbol{dof = 3})$	7.81	11.345
$\boldsymbol{\eta^2}$ $(\boldsymbol{dof = 4})$	9.49	13.277
$\boldsymbol{\eta^2}$ $(\boldsymbol{dof = 5})$	11.07	15.086

Once the TS is detected as manoeuvring, the above interacting multiple model algorithm is applied to determine the system states.

7.1.3. Simulations of the AIS aided target ship detection and prediction algorithm

In this section, AIS measurements are simulated to determine a single dynamic TS's navigational data as well as to make predictions during the long AIS data-transmitting intervals. The target ship is treated as a single point without considering its actual size. Portsmouth Harbour (Figure 7.3(a)) is used to simulate a practical

environment for the TS. It has first been converted into a binary map (Figure 7.3(b)), which has the dimension of 800 pixels * 800 pixels representing a 1.2 km * 1.2 km area (1 pixel =1.5 m). The simulated TS is assumed to be operating at constant and initially adheres to a straight line trajectory. Additionally, a current vector with the speed of 0.3 m/s at 155° is simulated and this has the effect of pushing the TS towards the southeast. The trajectory of the TS is by this means affected and the TS has a constant angular velocity of 3 °/s when manoeuvring to correct its course, which is presented in Figure 7.3(b). The initial speed of the TS is 7 knots on a course of 160°, while the updating intervals of the AIS measurements are 10 seconds under normal conditions and 2 s when manoeuvring. The tracking start point is (450 m, 1200 m) and the end tracking point is (850 m, 64 m). The sampling time between each time step is 2 s. The TS starts to manoeuvre after time step $k = 140$. Eight angular velocities from -4 °/s to 4 °/s that cover the more frequently used angular velocities of a vessel are chosen to generate eight models.

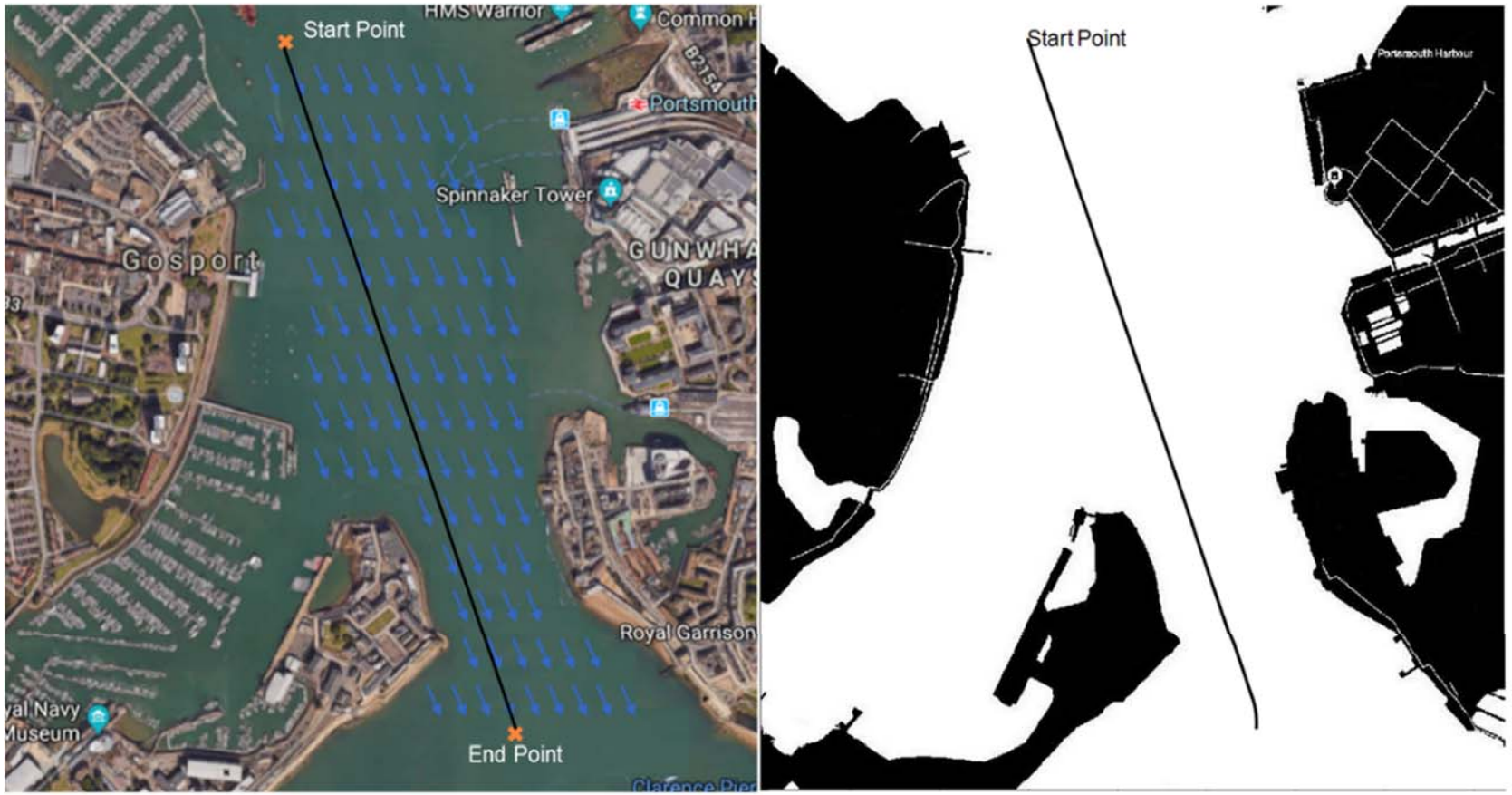

Figure 7. 3 Simulation Scenario 7.1: (a) testing environment in Portsmouth harbour with a constant current and the simulated straight trajectory of the TS; (b) the binary map and the altered true trajectory of the TS

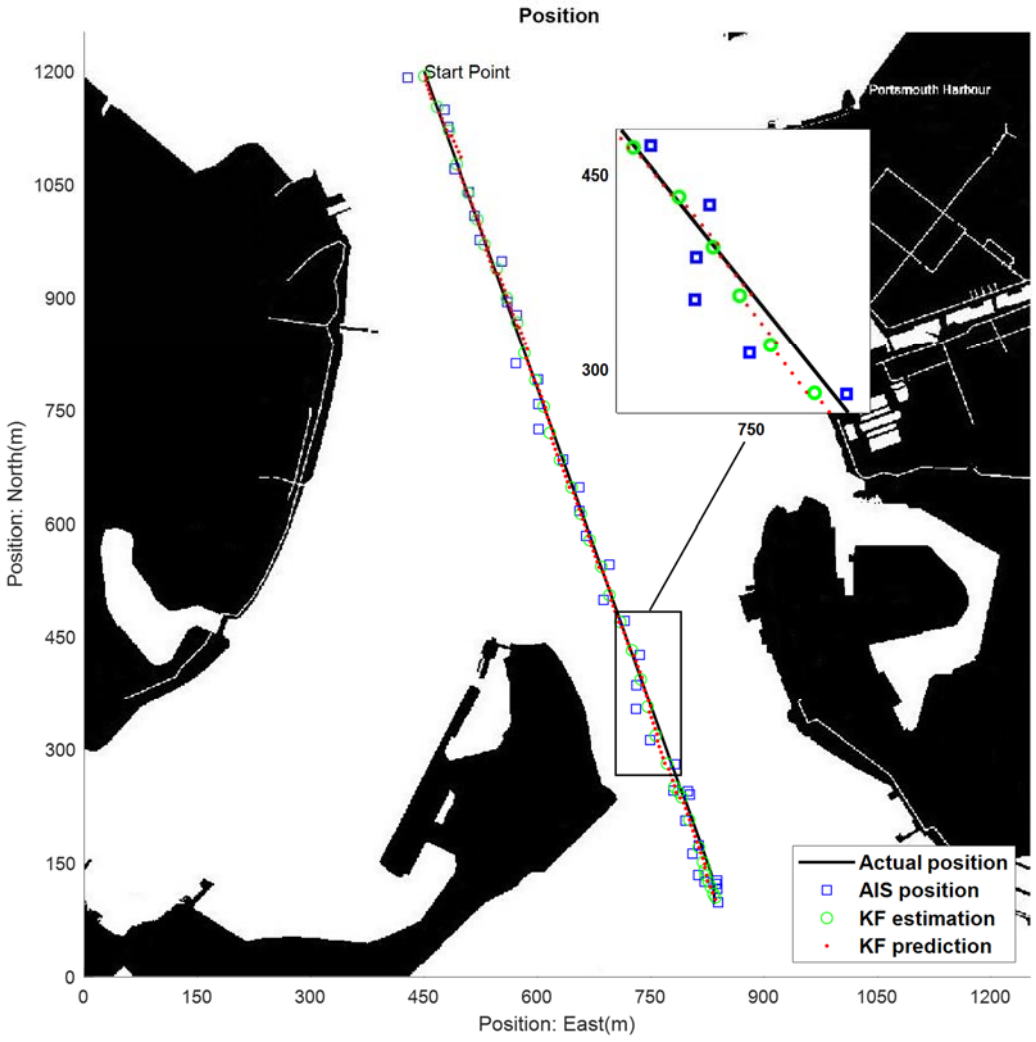

Figure 7. 4 Simulation Scenario 7.1: the simulation results of conventional KF based AIS aided TS detection and prediction algorithm

Figure 7.4 shows the simulation results of the conventional KF based AIS aided TS detection and prediction algorithm using the CV model. When the detected TS is following its trajectory, four possible positions (red dots) are predicted by the proposed algorithm during each AIS data update interval and all the predictions are along the simulated trajectory (black line), which proves that the algorithm is able to provide effective estimated positions without AIS measurement updates during the time period. From the enlarged inset in Figure 7.4, it is evident that the proposed algorithm performs creditably at improving AIS data accuracy since the estimated positions (green circles) are closer to the actual trajectory when the TS is operating along a straight line trajectory.

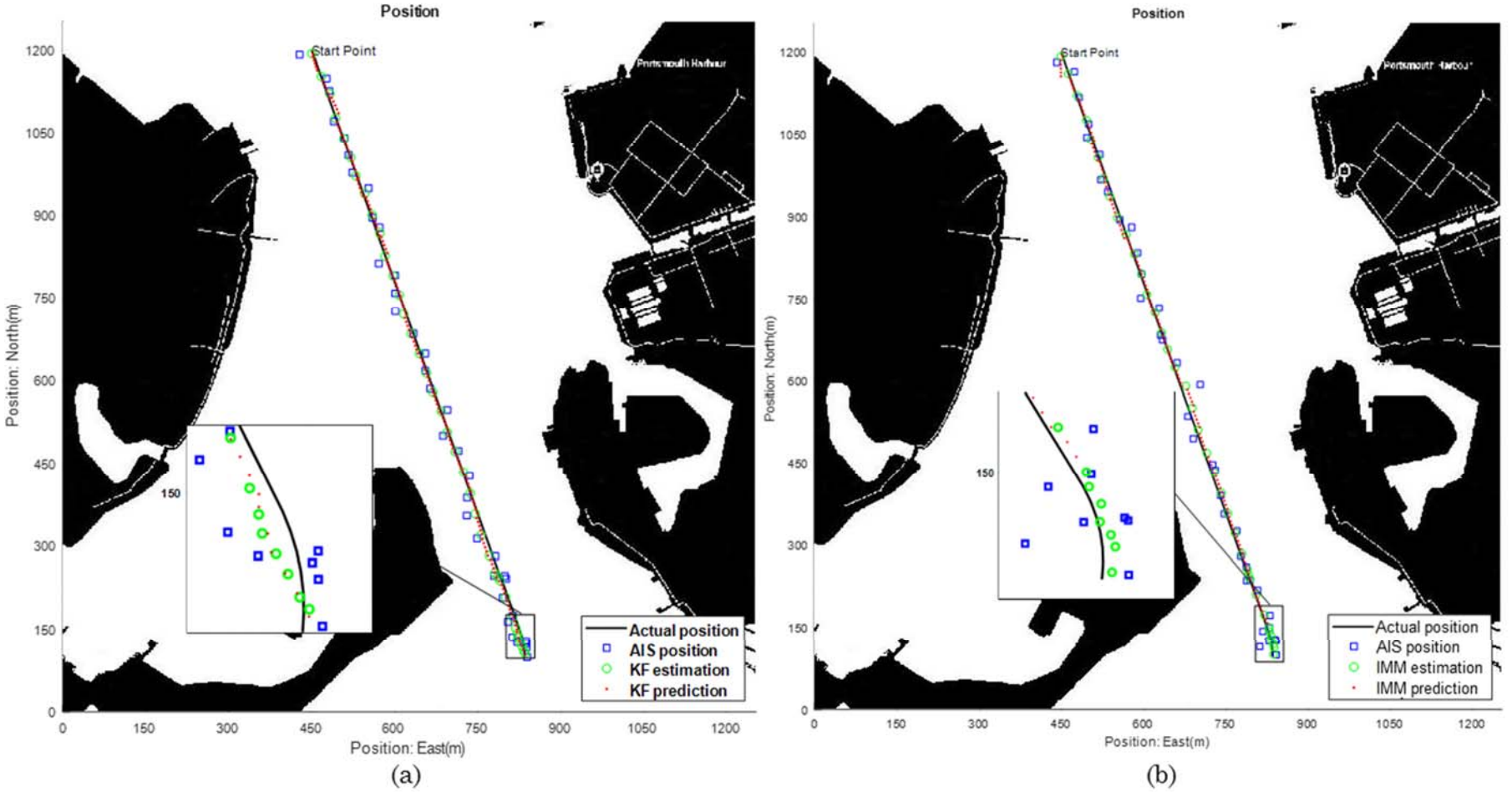

Figure 7. 5 Simulation Scenario 7.1: the simulated AIS measured positions and the predicted and estimated position results using standard KF and IMMKF algorithms

Figure 7.5(a) demonstrates the same simulation results as Figure 7.4 with an enlarged inset detailing the end of the trajectory, where the TS is conducting manoeuvres. It can be seen that the AIS data (blue squares) are updated more frequently when the TS is approaching the end of its trajectory since it is making frequent course corrections to get to its end point. However, the estimated positions (green circles) of the TS are driven to an incorrect direction when the TS is manoeuvring. The simulation results confirm the effectiveness of the constant velocity model based conventional KF TS detection and prediction algorithm when the TS is not manoeuvring, but it is incapable of estimating the correct course of the TS during manoeuvring, even though the AIS data updates more frequently. Figure 7.5(b) demonstrates the simulation results of the proposed IMMKF AIS aided manoeuvring TS detection and prediction algorithm. The manoeuvring TS detection algorithm performs better at estimating the positions and courses of the detected TS. It can be seen from the enlarged inset of Figure 7.5(b) that the estimated positions (green circles) adhere to the true trajectory (black line) while the TS is manoeuvring. Further numerical evidence is demonstrated in Figures 7.6 to 7.10.

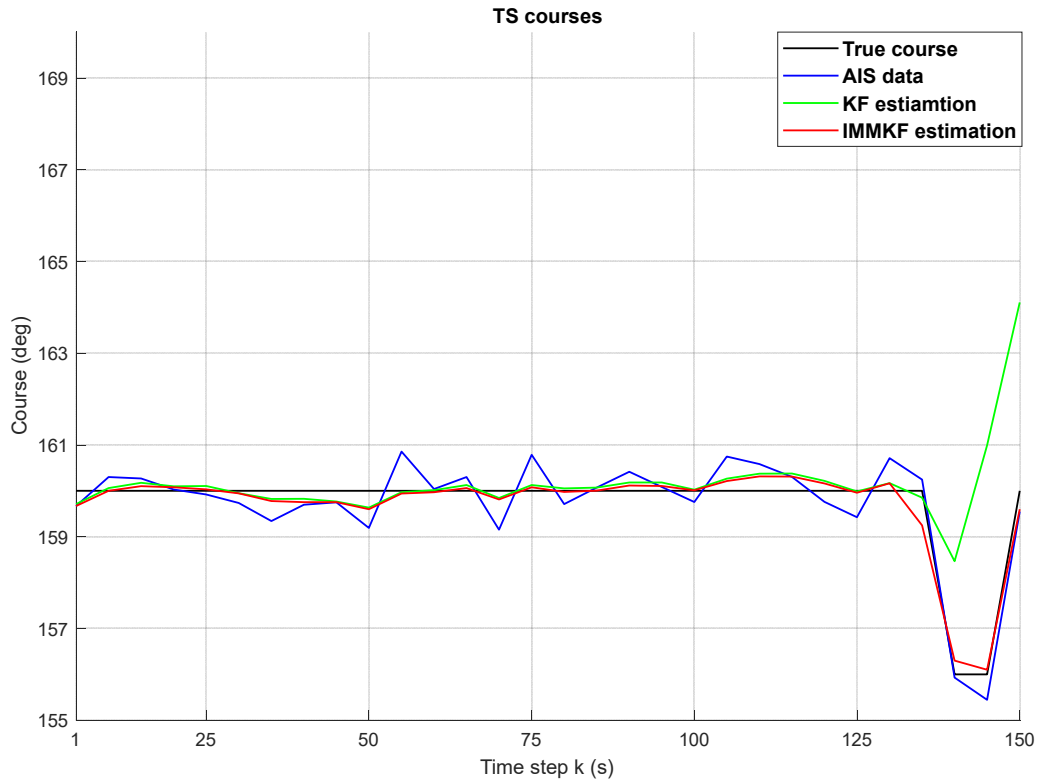

Figure 7. 6 Simulation Scenario 7.1: ideal course, AIS reported course, KF and IMMKF estmated course

Figure 7.6 provides a comparison of the estimated TS's courses by conventional KF based algorithm and the proposed IMMKF AIS aided manoeuvring TS detection and prediction algorithm. The actual course of the TS is denoted as the black line, the AIS reported course is shown as the blue line, the KF estimated course is presented as the green line and the IMMKF estimated course is denoted as the red line. This figure also supports the findings from Figures 7.4 and 7.5 since the green line and the red line are very similar and closer to the black line than the blue line before the TS starts manoeuvring around step $k = 140$, but the green line starts to deviate from the other three lines from that point while the red line is still close to the black line.

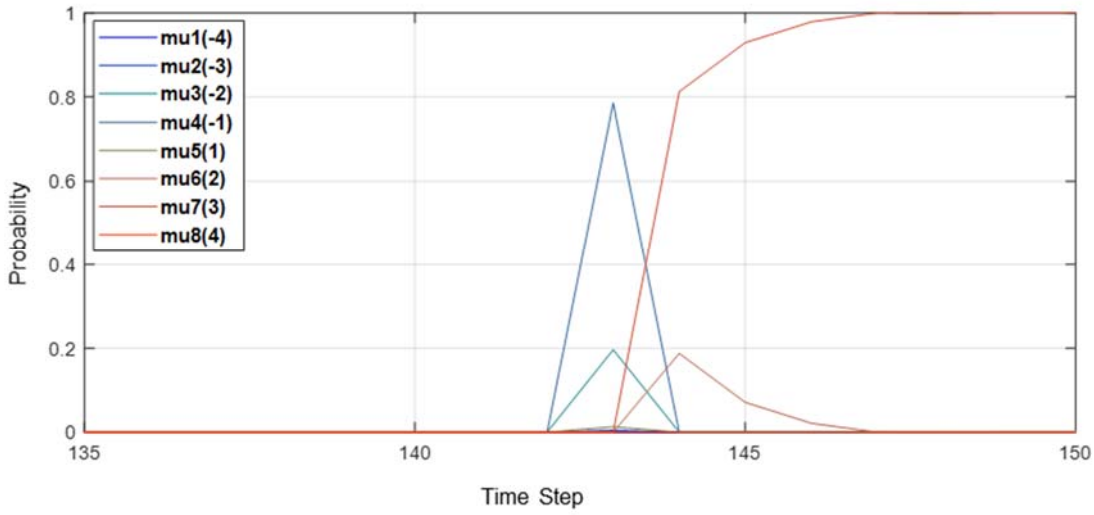

Figure 7. 7 Simulation Scenario 7.1: the probabilities of each manoeuvring model generated by the IMM filter

The probability of each model shown in Figure 7.7 expresses how the proposed IMMKF based algorithm determines which model is correct. Before time step $k = 140$ when the TS is not manoeuvring, all the probabilities of the 8 models (mu1, mu2, mu3, mu4, mu5, mu6, mu7 and mu8) remain at 0. It can be seen that at the beginning of the manoeuvring period, the probabilities of mu3, mu4 and mu6 peak and return to 0 in a short time. This is caused by insufficient data being obtained by the manoeuvre detector algorithm at the initial stage. After extracting enough data, the proposed algorithm determines the correct model (mu7) that represents the angular velocity of 3 °/s and its probability becomes the largest and tends to 1 during the TS's manoeuvring, which is the same as the TS's actual angular velocity. The results prove the effectiveness of the designed manoeuvre detector.

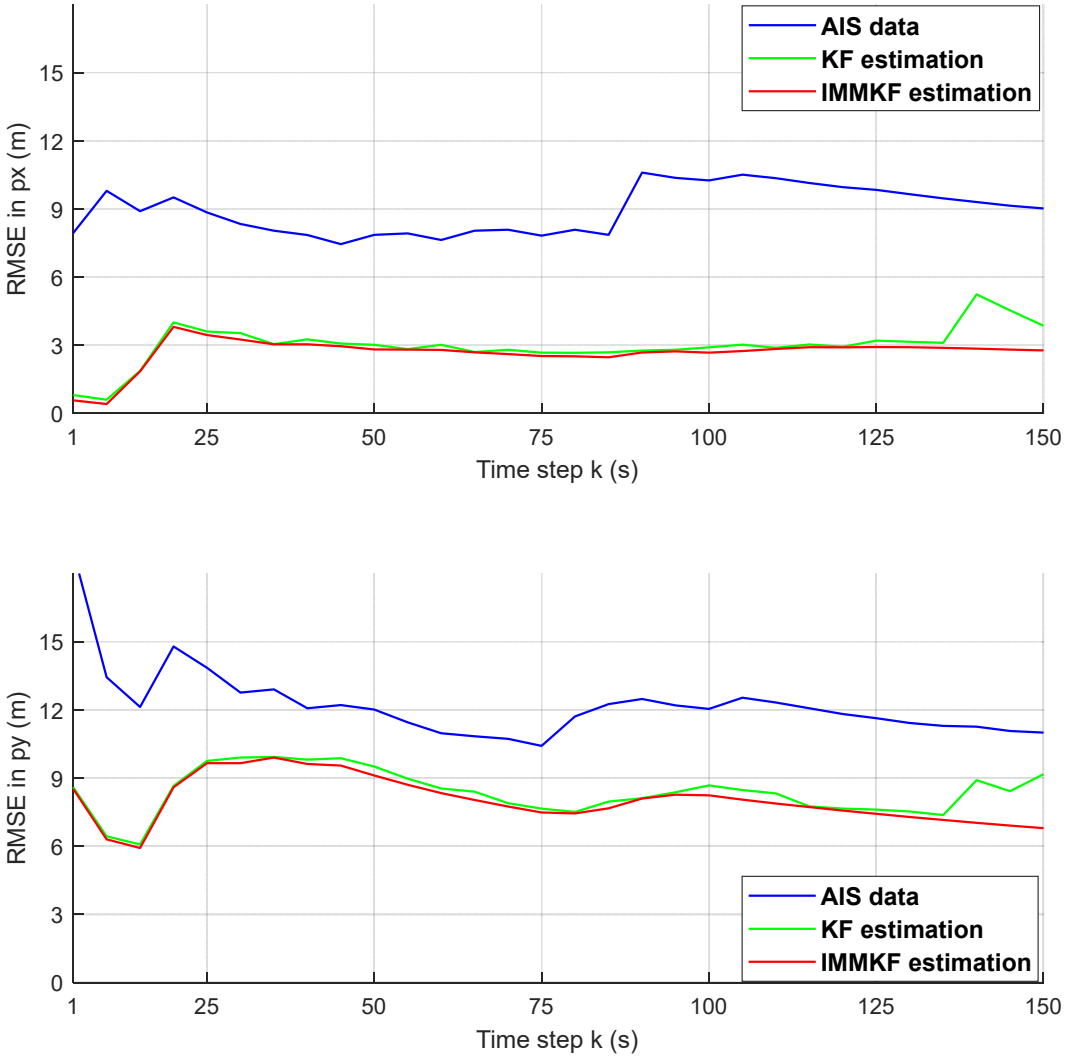

Figure 7. 8 Simulation Scenario 7.1: RMSEs of the TS's positions

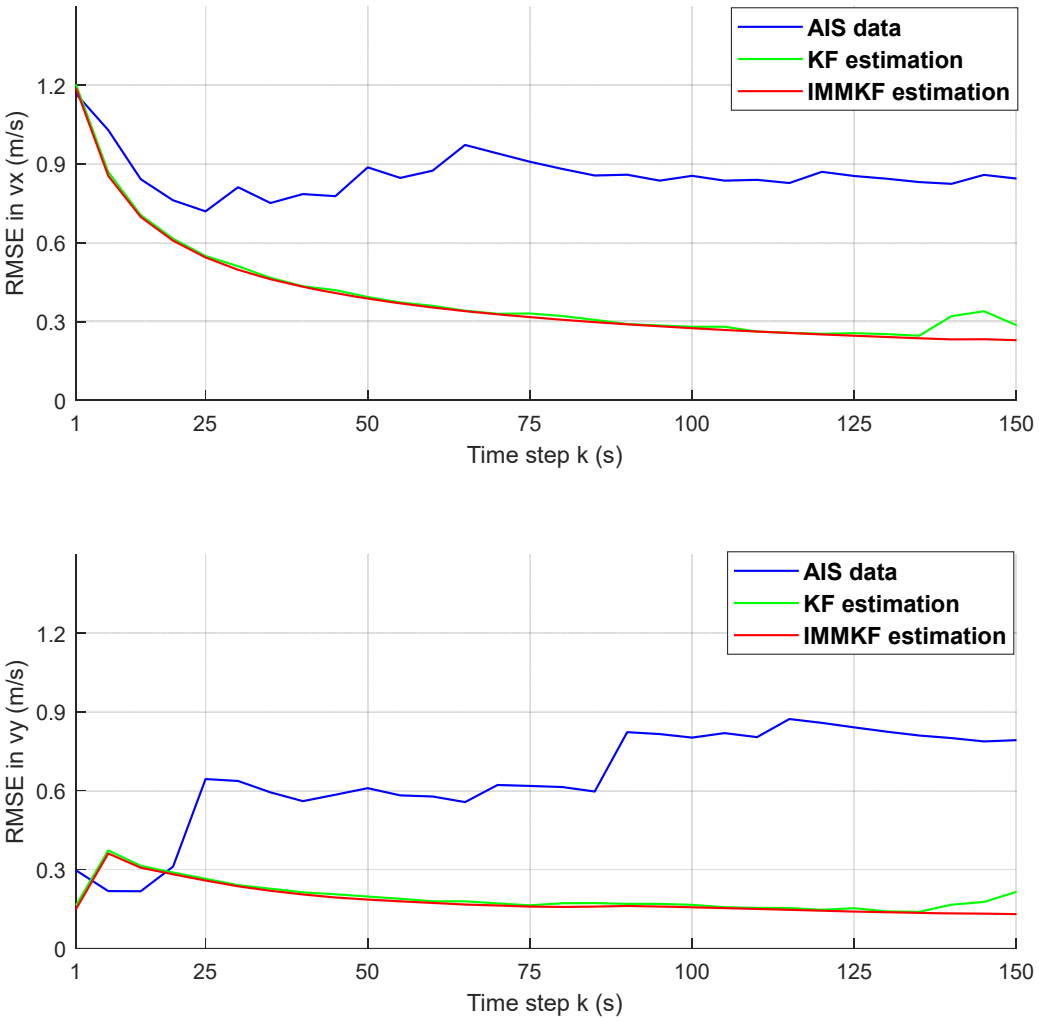

Figure 7. 9 Simulation Scenario 7.1: RMSEs of the TS's velocities

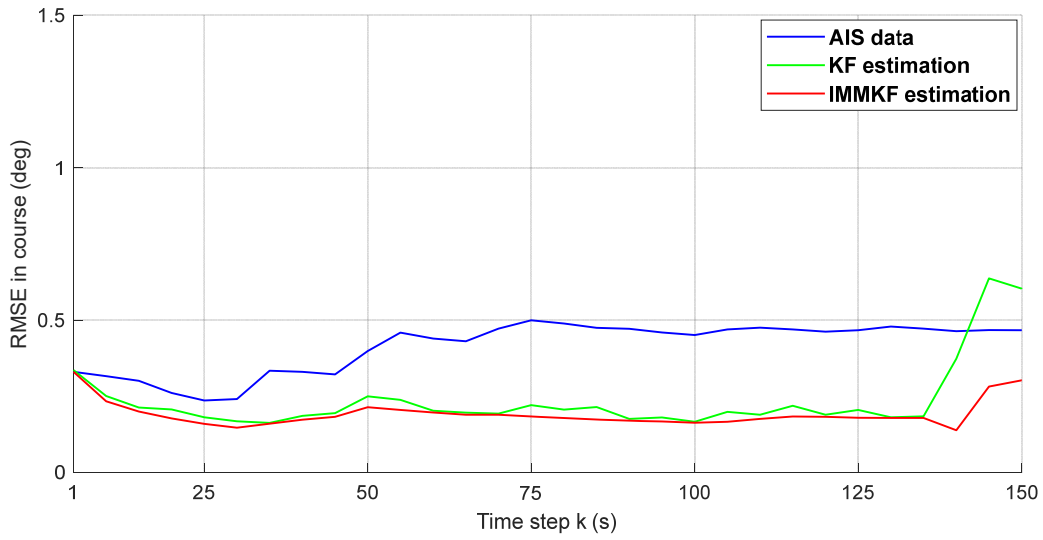

Figure 7. 10 Simulation Scenario 7.1: RMSEs of the TS's courses

The Rooted Mean Square Errors (RMSEs) of the TS's positions, velocities and courses, that are detailed in Figures 7.8 to 7.10, further support the improvement made by the proposed IMMKF AIS aided manoeuvring TS detection and prediction algorithm. In each figure, the blue line indicates the RMSE of the AIS raw measurements, the green line denotes the RMSE of the conventional KF based estimations and the red line represents the RMSE of the IMMKF based estimations. Around time step $k = 140$, the TS starts to manoeuvre and the RMSEs of the KF estimated positions, velocities and courses increase while the RMSEs of the proposed IMMKF estimations remain lower than those of both the KF estimations and AIS raw measurements. This is clearly evident in all the aspects of the TSs navigational data, especially the course in Figure 7.10. The RMSE of KF estimated courses steadily increases and eventually exceeds the error of the raw AIS measurement. The comparisons of RMSEs provide numerical evidence that estimation of the TS's positions in the x and y directions are improved by 4 meters and 3 meters respectively and the RMSE of the courses are reduced by approximately 50% by the IMMKF algorithm. All the evidence indicates the proposed IMMKF with manoeuvre detector TS detection and prediction algorithm based on AIS data is effective for both detecting the TS and predicting its positions and courses when the TS is manoeuvring.

7.2. Multi-sensor data fusion for target ship detection and tracking

While the USV is operating at sea, it could be within reasonably close proximity of multiple TSs. Tracking all the surrounding TSs to analyse the collision risks is essential to ensure its safety. Although, an increasing number of vessels are installing AIS devices, only large ships over 300 gross tonnage are mandated to install transponders (Maritime & Coastguard Agency, 2007; Lloyd's list intelligence, 2017). Smaller vessels are normally equipped with AIS receivers, so that they could only be aware of other TS's information while not sending their own information at the same time. In addition, AIS is broadcast on VHF radio waves that travel in straight lines. When a USV encounters a complex environment surrounded by multiple TSs,

especially in harbour, AIS data is prone to be lost due to the electromagnetic influence. The location of AIS transceivers or the types of the AIS transceivers and weather conditions could also affect the quality of the AIS signal. As a consequence, relying solely on AIS to detect TSs is unlikely to prove satisfactory for autonomous USV navigation. Marine Radar has been regarded as a prime solution to perceive the surrounding environment in maritime vessel navigation for many decades. It measures the relative distance and bearing by calculating the transmission time of the echo of an electromagnetic wave pulse. Details are presented in Chapter 2. This feature of a marine Radar could enable the USV to detect all the TSs surrounding the USV within Radar detection range, which is typically 48 nautical miles, but associated with a large degree of uncertainty. The TS detection can be difficult while using either the AIS or the marine Radar alone in harsh environments with an unknown number of TSs that varies with time. To improve system reliability, both sensors are employed as complementary devices to perceive the surrounding dynamic environment. A fusion algorithm is therefore required to merge the measurements from the two different sources. Most of the current studies on Radar and AIS data fusion are concerned with synchronising, associating and fusing the different measurements from each sensor (Habtemariam et al, 2014; Kalsen et al, 2015; Pelich et al, 2015;). In this research, raw Radar and AIS measurements will not be associated and fused directly. They will be associated with each detected TS track individually. The system states are then updated by the proposed manoeuvring TS detection and prediction algorithm from Section 7.1 using the associated sensor measurements respectively, and the final fusion algorithm generates the estimated TS's navigational data by fusing the updated estimations. The system structure is demonstrated in Figure 7.11.

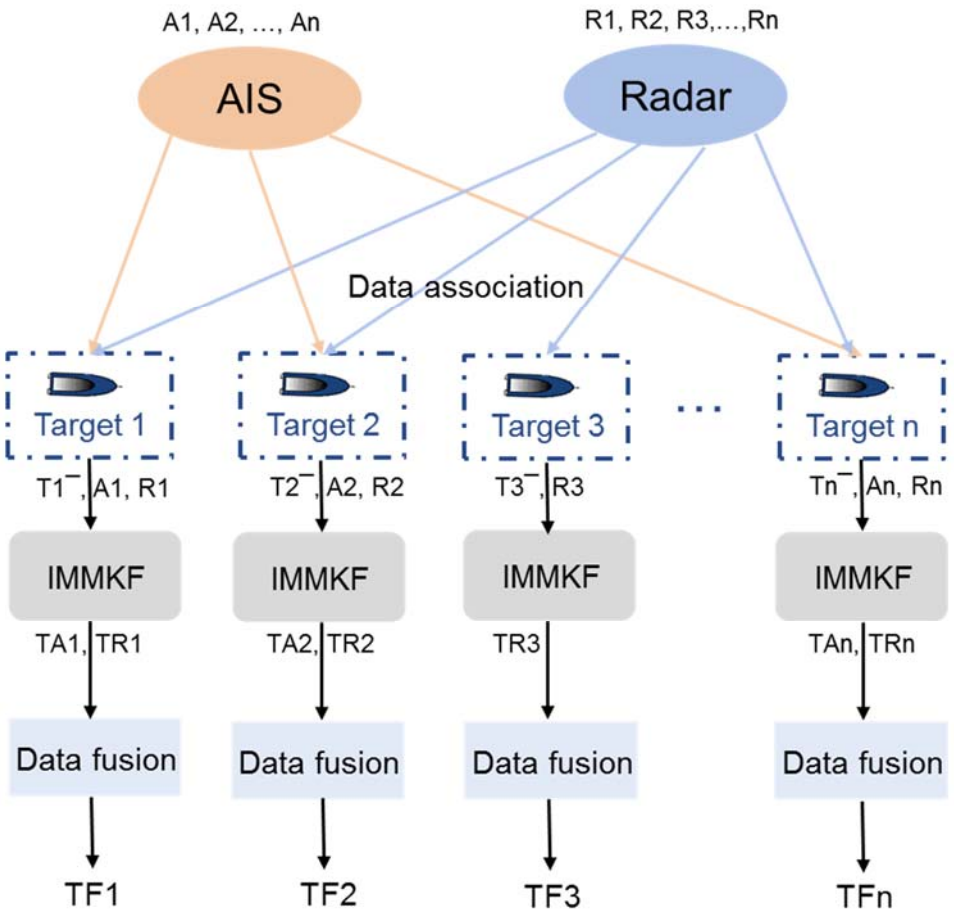

Figure 7. 11 System structure of multi-TS detection using AIS and Radar measurements

7.2.1. Multi-sensor data association algorithm

Generally, a complete marine Radar system comes with an automatic Radar plotting aid (ARPA) to provide a visual map for the mariner to identify the surrounding TSs. Most of the NMEA 0183 supported Radar systems also generate NMEA0183 sentences to provide the information of the detected TSs, which can be extracted by using the correct converter. In this research, the measurements obtained from NMEA0183 sentences are used. The main data obtained from a marine Radar is the dynamic information of the TS, such as the relative distance and bearing between Radar platform and the TS, as well as TS's true speed and course (Wolejsza, 2012; Lan et al, 2019).

After obtaining raw sensor data, a data association algorithm is then required for the autonomous system to determine the number of TSs and allocate each sensor

measurement to the related TS. In a real-time TS tracking system, the data collected from sensors should have some similar physical characteristics to the related TSs. Therefore, the data can be associated according to the designed rules that express their similarities. Figure 7.12 gives a simple approach of data association using the Nearest Neighbours. At each fusion time step, the green circle denotes the predicted TS generated by the IMMKF algorithm and the orange star represents a sensor measured TS (AIS or Radar). The sector formed within the dashed line gives the thresholds of both the position and bearing of the TS. If both TSs are inside the threshold, the sensor measured TS can be treated as related to the predicted TS.

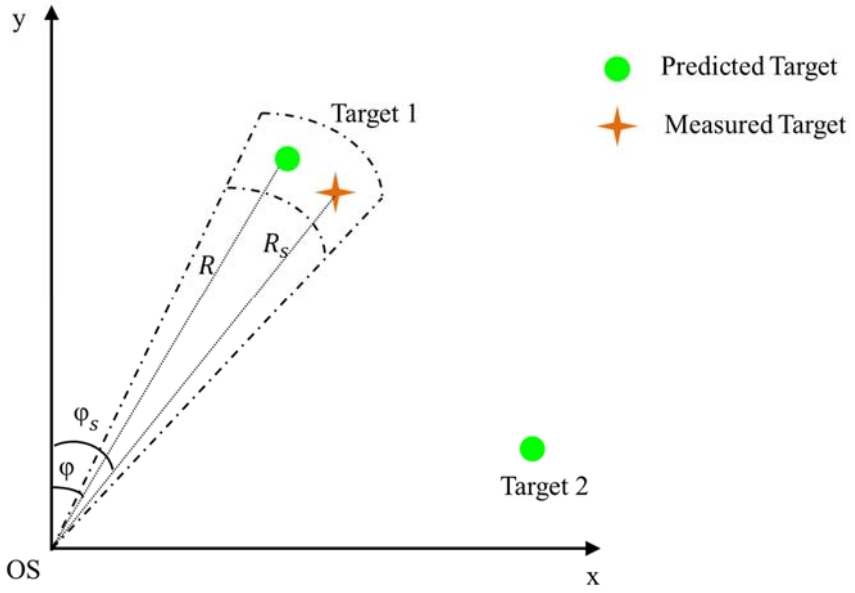

Figure 7. 12 TS Validation: measured TS and predicted TS

However, such a simple approach is not efficient and may generate error correlations when the number of TSs increases. Depending on the system complexity, other data association methods, such as the K-means or probabilistic data association are alternative solutions (Geller et al, 2015; Wang et al, 2017; Jilkov et al, 2017). These methods are based on statistical data association, the performance of which are not satisfactory for a practical and unpredictable dense environment (Xu, et al, 2017). In this study, a two stage multi-factor fuzzy integration decision-making algorithm has been proposed to associate measurements from AIS and Radar with detected TSs indirectly for real-time multiple TS tracking with the intention of reducing computational time. As mentioned before, a marine Radar can provide the relative

range, relative bearing, course and speed of the TS while AIS provides absolute position in latitude/longitude, course and speed. With the knowledge of the USV's own absolute position, the relative range and bearing can also be calculated from AIS measurements. Therefore, the four characters from Radar and AIS measurements can be compared with the detected TSs to determine whether the measurements are related to the same TS. As shown in Figure 7.13, at the first stage, the differences in the relative range and bearing to the USV between the sensor TS and system predicted TS are evaluated by the fuzzy decision making system to determine whether the TS detected by the sensor is in a similar location to that of the system predicted TS. However, it is yet to make a decision whether the two TSs are related at this stage, although the opposite fact that the sensor TS is related to a different TS is obvious if the differences in the range and bearing are large. The second stage that compares the course and speed of the two TSs will be enabled if the system requires further evaluation to make a final decision. Instead of inputting all the four characters of all sensor measurements, the proposed algorithm uses a two-stage structure that is able to reduce the computational cost significantly, especially in an environment with a large number of TSs.

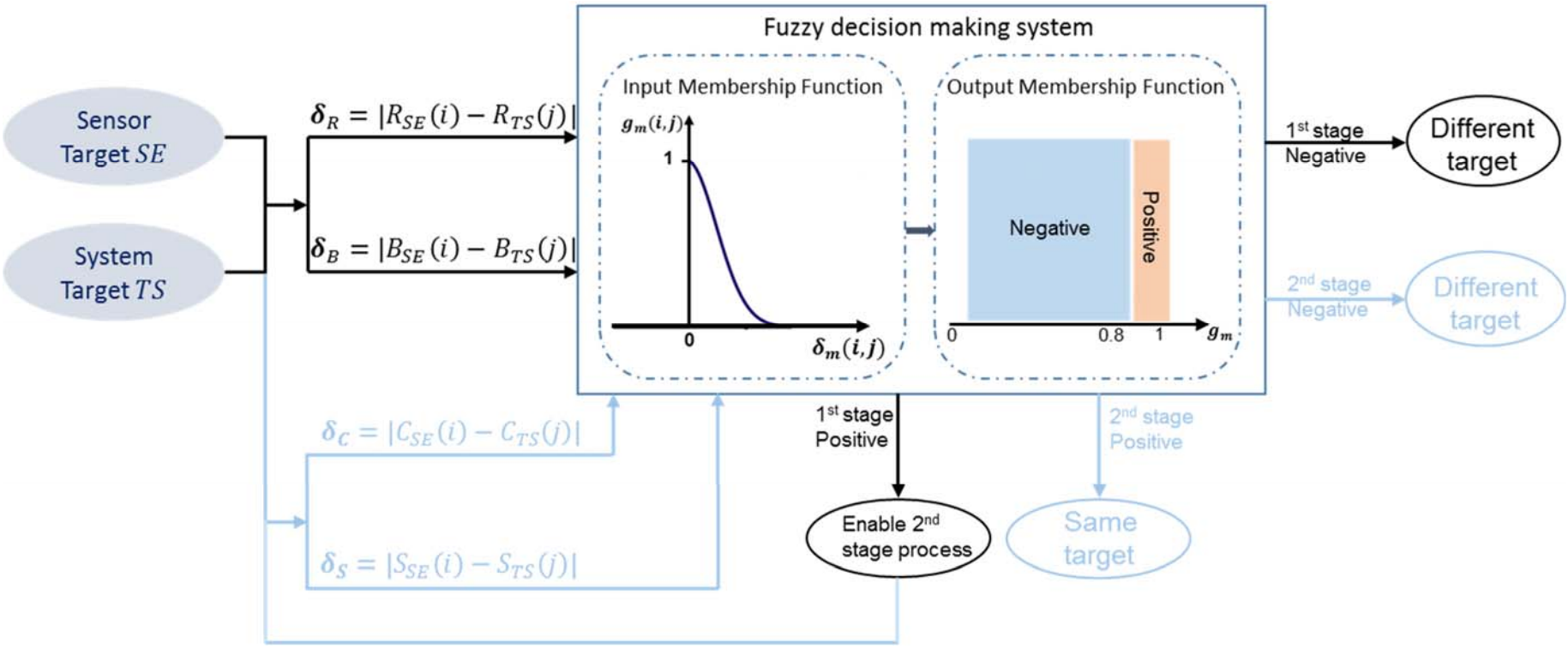

Figure 7. 13 Two-stage fuzzy multi-factor integration data association algorithm

Assume there are i measurements obtained by a sensor, denoted as $SE(i)$, and j system predicted TSs, denoted as $TS^{-}(j)$. The fuzzy set at the first stage is defined as the respective differences between the two TSs in the relative range $\boldsymbol{\delta}_R$ and bearing $\boldsymbol{\delta}_B$ to the USV.

$$\boldsymbol{\delta}_1(i,j) = \begin{bmatrix} \boldsymbol{\delta}_R \\ \boldsymbol{\delta}_B \end{bmatrix} = \begin{bmatrix} |R_{SE}(i) - R_{TS}(j)| \\ |B_{SE}(i) - B_{TS}(j)| \end{bmatrix} \tag{7.35}$$

where, R_{SE} and B_{SE} are the relative range and bearing obtained from the sensor measurements $SE(i)$; R_{TS} and B_{TS}, are from the system predicted states $TS^{-}(j)$.

A Guassian membership function is employed to compute the correlation grade of each input:

$$g_1(i,j) = \begin{bmatrix} g_R(i,j) \\ g_B(i,j) \end{bmatrix} = \begin{bmatrix} \exp(-\tau_R \boldsymbol{\delta}_R^2(i,j)/\sigma_R^2) \\ \exp(-\tau_B \boldsymbol{\delta}_B^2(i,j)/\sigma_B^2) \end{bmatrix} \tag{7.36}$$

where τ_R and τ_B are the predefined adjustment coefficients, σ_R and σ_B are the related sensor measurement errors that can be obtained from sensor specifications.

The integrated association grade $G_1(i,j)$ can then be computed by distributing the weight to each correlation grade of each character.

$$G_1(i,j) = [w_R \quad w_B] \times \begin{bmatrix} g_R(i,j) \\ g_B(i,j) \end{bmatrix} \tag{7.37}$$

A threshold is then designed and the initial decision as to whether the two TSs $SE(i)$ and $TS^{-}(j)$ are correlated can be made by comparing the integrated association grade $G_1(i,j)$ to the designed threshold according to the following rules:

- If $G_1(i,j) \geq threshold$, the two TSs $SE(i)$ and $TS^{-}(j)$ are related in the similar position and the second stage enables;
- If $G_1(i,j) < threshold$, the two TSs $SE(i)$ and $TS^{-}(j)$ are different.

Once the measurements of range and bearing are determined as being correlated, the algorithm then compares the course and speed of the two TSs $SE(i)$ and $TS^{-}(j)$ at the second stage to make the final decision whether the two TSs are correlated.

$$\boldsymbol{\delta}_2(i,j) = \begin{bmatrix} \boldsymbol{\delta}_C \\ \boldsymbol{\delta}_S \end{bmatrix} = \begin{bmatrix} |C_{SE}(i) - C_{TS}(j)| \\ |S_{SE}(i) - S_{TS}(j)| \end{bmatrix} \tag{7.38}$$

where $C_{SE}(i)$ and $S_{SE}(i)$ are the course and speed from the sensor measurements $SE(i)$; $C_{TS}(j)$ and $S_{TS}(j)$ are the Radar measurements in course and speed and belong to$TS^{-}(j)$.

The second stage association grade $G_2(i,j)$ is also computed using the fuzzy Guassian membership functions as below:

$$G_2(i,j) = [w_C \quad w_S] \times \begin{bmatrix} g_C(i,j) \\ g_S(i,j) \end{bmatrix} = [w_C \quad w_S] \times \begin{bmatrix} \exp(-\tau_C \boldsymbol{\delta}_C^2(i,j)/\sigma_C^2) \\ \exp(-\tau_S \boldsymbol{\delta}_S^2(i,j)/\sigma_S^2) \end{bmatrix} \tag{7.39}$$

Finally, it can be determined whether the TSs $SE(i)$ and $TS^{-}(j)$ are related to the same TS according to the following rules.

- If $G_2(i,j) \geq threshold$, the two TSs $SE(i)$ and $TS^{-}(j)$ are related to the same TS;
- If $G_2(i,j) < threshold$, the two TSs $SE(i)$ and $TS^{-}(j)$ are different.

7.2.2. Multi-sensor target ship detection and tracking algorithm

In order to detect multiple TSs in a maritime environment, moving tracks that are associated to each TS are formed to determine each TS's real time positions. Unlike the AIS, the sampling time of a marine Radar is fixed. It is about 1.25 s to 2.5 s as the rotation rate of its antenna is normally 24 or 48 rpm (revolutions per minute). The sampling time of the Radar is used as the system's sampling time. The proposed TS detection and prediction algorithm based on the IMMKF with manoeuvre detector from Section 7.1 is used to form the tracks of each TS. Therefore, the state vector of each TS is defined as follows:

$$\boldsymbol{TS}_m = [p_{xm} \quad p_{ym} \quad v_{xm} \quad v_{ym} \quad \varphi_m]^T \tag{7.40}$$

where m is the number of detected TSs.

When the TS is operating at a constant speed without manoeuvring, its motion model is

$$\boldsymbol{TS_m}(k) = \begin{bmatrix} 1 & 0 & T & 0 & 0 \\ 0 & 1 & 0 & T & 0 \\ 0 & 0 & 1 & 0 & 0 \\ 0 & 0 & 0 & 1 & 0 \\ 0 & 0 & 0 & 0 & 1 \end{bmatrix} \boldsymbol{TS_m}(k-1) + \boldsymbol{w}(k-1) \tag{7.41}$$

When its manoeuvre is detected, the motion model of the TS based on the coordinate turn model is described in Equation (7.42).

$$\boldsymbol{TS_m}(k) = \begin{bmatrix} 1 & 0 & \frac{\sin \omega T}{\omega} & \frac{-(1-\cos \omega T)}{\omega} & 0 \\ 0 & 1 & \frac{1-\cos \omega T}{\omega} & \frac{\sin \omega T}{\omega} & 0 \\ 0 & 0 & \cos \omega T & -\sin \omega T & 0 \\ 0 & 0 & \sin \omega T & \cos \omega T & 0 \\ 0 & 0 & 0 & 0 & 1 \end{bmatrix} \boldsymbol{TS_m}(k-1) + \begin{bmatrix} 0 \\ 0 \\ 0 \\ 0 \\ \omega T \end{bmatrix} + \boldsymbol{w}(k-1) \tag{7.42}$$

The Radar measurements are in a polar frame and have to be converted to a Cartesian frame. A debiased conversion algorithm has been employed to compensate for errors that might occur during the conversion as below. (Don and Yaakov, 1993).

$$p_{Rxm} = r_m \times cos\theta_m - \mu_{xm} \tag{7.43}$$

$$p_{Rym} = r_m \times sin\theta_m - \mu_{ym} \tag{7.44}$$

$$\mu_{xm} = E[\hat{p}_x | r_m, \theta_m] = \left[r_m \times cos\theta_m \times \left(e^{-\sigma^2_{\theta_m}} \right) - e^{-\sigma^2_{\theta_m}/2} \right] \tag{7.45}$$

$$\mu_{ym} = E\left[\hat{p}_y | r_m, \theta_m\right] = \left[r_m \times sin\theta_m \times \left(e^{-\sigma^2_{\theta_m}} \right) - e^{-\sigma^2_{\theta_m}/2} \right] \tag{7.46}$$

where p_{Rxm}, p_{Rym} are the position coordinates of the TS; r_m is the range from the mth TS to the USV; θ_m is the bearing of the TS; μ_{xm}, μ_{ym} are the estimated bias that will be removed during conversion.

The measurements obtained by Radar are converted to the following:

$$\boldsymbol{z}_{TSRm} = \left[p_{Rxm} \;\; p_{Rym} \;\; v_{Rxm} \;\; v_{Rym} \;\; \varphi_{Rm}\right]^T \tag{7.47}$$

And the measurements obtained by AIS are expressed as Equation (7.48).

$$\boldsymbol{z}_{TSAm} = \left[p_{Axm} \;\; p_{Aym} \;\; v_{Axm} \;\; v_{Aym} \;\; \varphi_{Rm}\right]^T \tag{7.48}$$

Unlike the single TS detection, all the measurements and predictions are associated from a known TS so that they can be used to form a moving track of the TS directly. For a multiple TSs problem, the proposed data fusion algorithm at each time step should first determine the number of the TSs and their relationships to those detected TSs from the previous time step. The following flow chart demonstrates the whole TS tracks formation and association and multi-sensor data fusion process. The system first predicts the next state of each of the detected TSs that are associated with m tracks from last time step k using system state models. The Radar measurements obtained are then investigated to determine how many target ships (j) are detected at this time step $k+1$. The predictions of each detected TS $\boldsymbol{TS}_m^{-}(k+1)$ are compared with the Radar measurements $\boldsymbol{R}_j(k+1)$ using the proposed two stage fuzzy association decision making algorithm to associate the Radar measurements with the known TSs' tracks. If $m < j$, then the Radar detects a new TS, a new track is then formed that makes $m = j$. The TSs' tracks can then be updated by the proposed data fusion algorithm to obtain Radar estimations $\widehat{\boldsymbol{TS}}_{RM}(k+1)$. The system then calls AIS measurements to check whether there is an update. If not, the system will make a new prediction $\boldsymbol{TS}_{Am}^{-}(k+1)$ based on the last AIS estimation that is also used as the updated AIS data $\widehat{\boldsymbol{TS}}_{Am}(k+1)$. Otherwise, the system will decode and convert new AIS measurements $\boldsymbol{A}_i(k+1)$ to associate them with known TS tracks using the two stage fuzzy association decision making algorithm. After associating the AIS measurements, the AIS prediction of each TS $\boldsymbol{TS}_{Am}^{-}(k+1)$ is equal to the system predicted states $\boldsymbol{TS}_m^{-}(k+1)$ and updated by the associated AIS measurements to generate AIS estimations $\widehat{\boldsymbol{TS}}_{AM}(k+1)$.

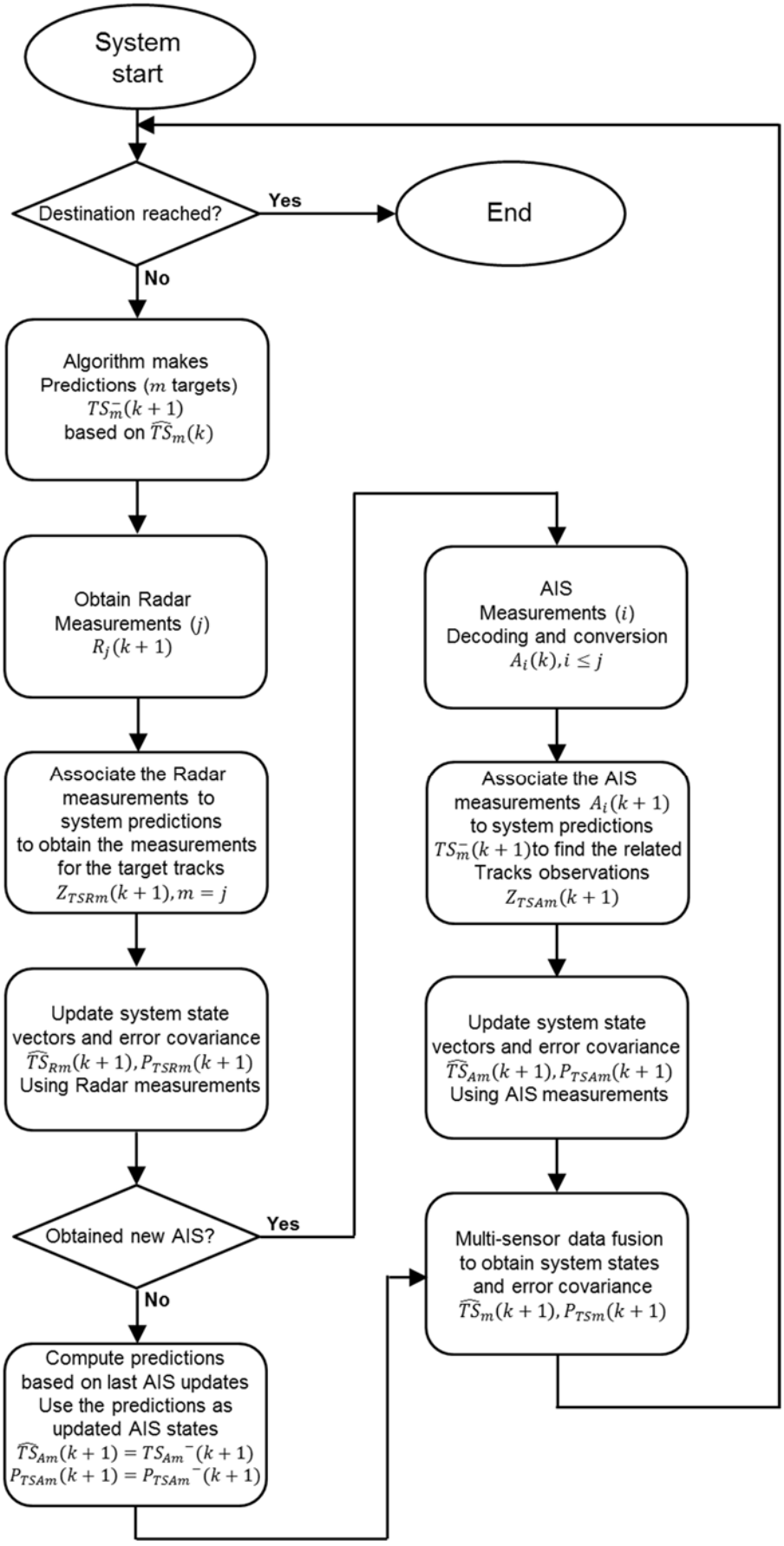

Figure 7. 14 Flow chart of the multi-sensor TS detection and tracking algorithm

After obtaining the system estimates $\widehat{\boldsymbol{TS}}_{Rm}(k+1)$ and $\widehat{\boldsymbol{TS}}_{Am}(k+1)$ by applying the Radar and AIS measurements respectively, these two estimations, rather than raw AIS and Radar measurements, are then fused to obtain the master fusion results. The Radar and AIS estimations belong to Gaussian distributions. Therefore, the two distributions for each TS track m can be fused by

$$P\left(x\middle|\widehat{\boldsymbol{TS}}_{Am},\widehat{\boldsymbol{TS}}_{Rm}\right) \propto P(\boldsymbol{TS})L\left(\boldsymbol{TS};\widehat{\boldsymbol{TS}}_{Am}\right)L\left(\boldsymbol{TS};\widehat{\boldsymbol{TS}}_{Rm}\right) = 1 \times exp\frac{1}{2}\left(\frac{\boldsymbol{TS}-\widehat{\boldsymbol{TS}}_{Am}}{\sigma_A}\right)^2 \times exp\frac{1}{2}\left(\frac{\boldsymbol{TS}-\widehat{\boldsymbol{TS}}_{Rm}}{\sigma_R}\right)^2 \tag{7.49}$$

$$\widehat{\boldsymbol{TS}}_{Fm}(k+1) = arg\max_x P\left(x\middle|\widehat{\boldsymbol{TS}}_{Am},\widehat{\boldsymbol{TS}}_{Rm}\right) = arg\min_{TS} -\log P\left(x\middle|\widehat{\boldsymbol{TS}}_{Am},\widehat{\boldsymbol{TS}}_{Rm}\right) = arg\min_x\left\{\frac{1}{2}\left(\frac{\boldsymbol{TS}-\widehat{\boldsymbol{TS}}_{Am}}{\sigma_A}\right)^2 + \frac{1}{2}\left(\frac{\boldsymbol{TS}-\widehat{\boldsymbol{TS}}_{Rm}}{\sigma_R}\right)^2\right\} \tag{7.50}$$

where $\widehat{\boldsymbol{TS}}_{Fm}$ expresses the fused data, σ_A and σ_R are the error covariance obtained from the estimation process with AIS and Radar updates respectively.

An improved weight distribution fusion algorithm has been proposed to deal with practical AIS sensor signal loss. It defines the relationship between the absence time of the AIS signal and the weights assigned to the AIS estimations. During the absence of AIS messages, the weight of AIS estimations reduces. A two-phase linear relationship is designed to describe the ratio of the weighting change and absence time as shown in Figure 7.15. $t1$ represents the safe time margin. If the duration of the loss of AIS signal is less than $t1$, the change of the weight of AIS estimation is relatively small. The weight then drops rapidly to zero at $t2$ since the AIS estimations are no longer reliable without AIS updated messages.

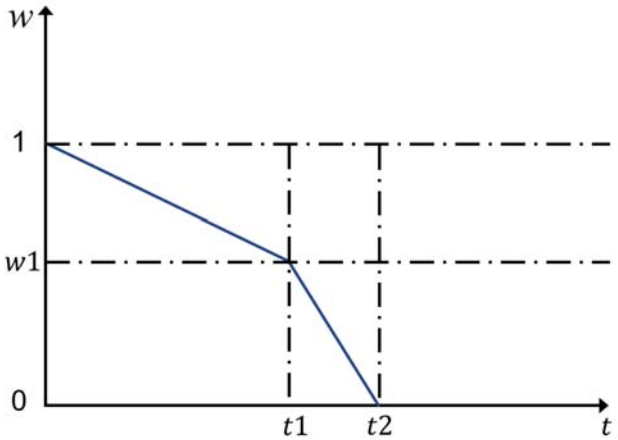

Figure 7. 15 Relationship between the weight of AIS estimations and the time without AIS update

7.2.3. Simulation of the multi-sensor target ship detection and tracking algorithm

The dynamic multiple TS detection system is implemented by simulating four TSs around the USV. Three of them are operating with both AIS and in marine Radar detection range and one of them can only be detected by Radar. The specific parameters of the simulated TSs are listed in Table 7.3.

Table 7. 3 Simulation Scenario 7.2: Simulated USV and TSs' initial position, speed and course

Vessels	Initial Position (nm)	Speed (kn)	Course (deg)	AIS equipped?	AIS signal lost
USV	(0, 0)	10	0	Yes	-
TS 1	(5, 13)	17	180	Yes	-
TS 2	(-16, 7)	13	75	Yes	$k = 100$ s to 120 s
TS 3	(-12, 2)	11(9)	30	Yes	$k = 300$ s to 450 s
TS 4	(1, 25)	11 (5)	100	No	-

Assuming the TSs 1 to 3 are equipped with AIS transponders and the USV can collect their AIS dynamic information at reporting interval $t_A = 10\,s$. TS 2 is set to be disabled for $k = 100$ s to 120 s and the AIS signal of TS 3 is lost during $k = 300$ s to 450 s. The sampling time of the USV's Radar is 2s, which is also used as the system's sampling time and the whole observation time is 900 time steps. During the observation, all the TSs are operating at constant speed and constant angular velocity when required, modelled as both CV model and CT model. The RMS error vectors for the AIS signals are 0.01 nautical miles in position, 0.007 knots in speed and 0.5 degree in course and for Radar are 0.08 nautical miles in relative range, 1.2 degree in relative bearing, 0.03 knots in speed and 1.0 degree in course. The parameters of the improved weight distribution fusion algorithm are defined as $w1 = 0.6, t1 = 60\,s$ and $t2 = 300\,s$. Figure 7.16 shows the simulated actual trajectories of the four TSs as magenta, blue, green and yellow lines respectively and the USV as the black line.

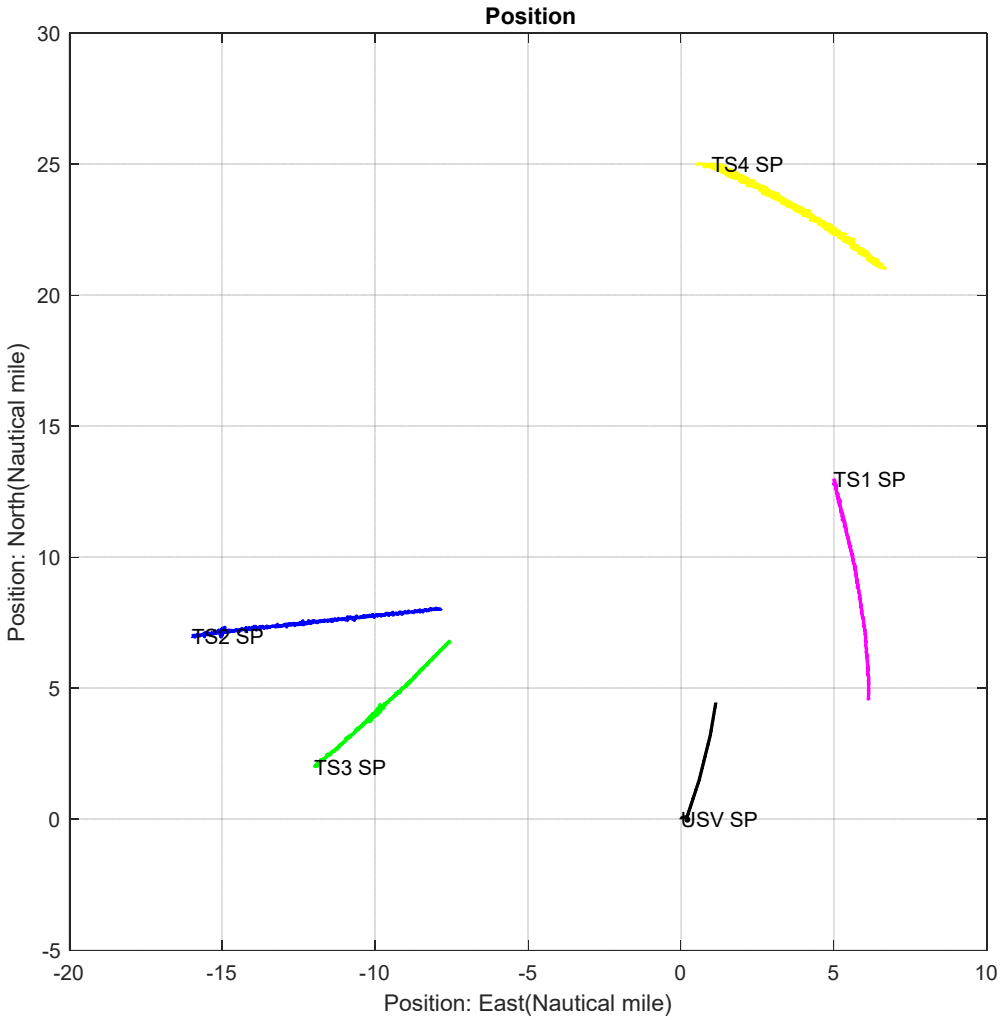

Figure 7. 16 Simulation Scenario 7.2: Simulated multiple TSs environment surrounding an USV

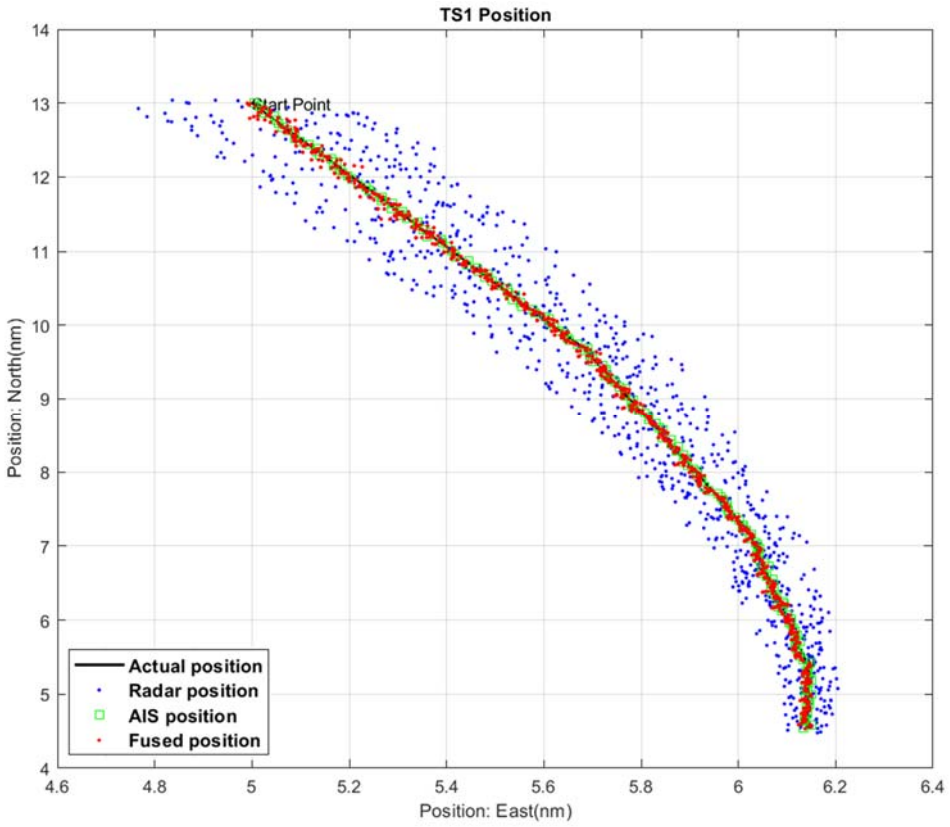

Figure 7. 17 Simulation Scenario 7.2: fused trajectories of target ship 1

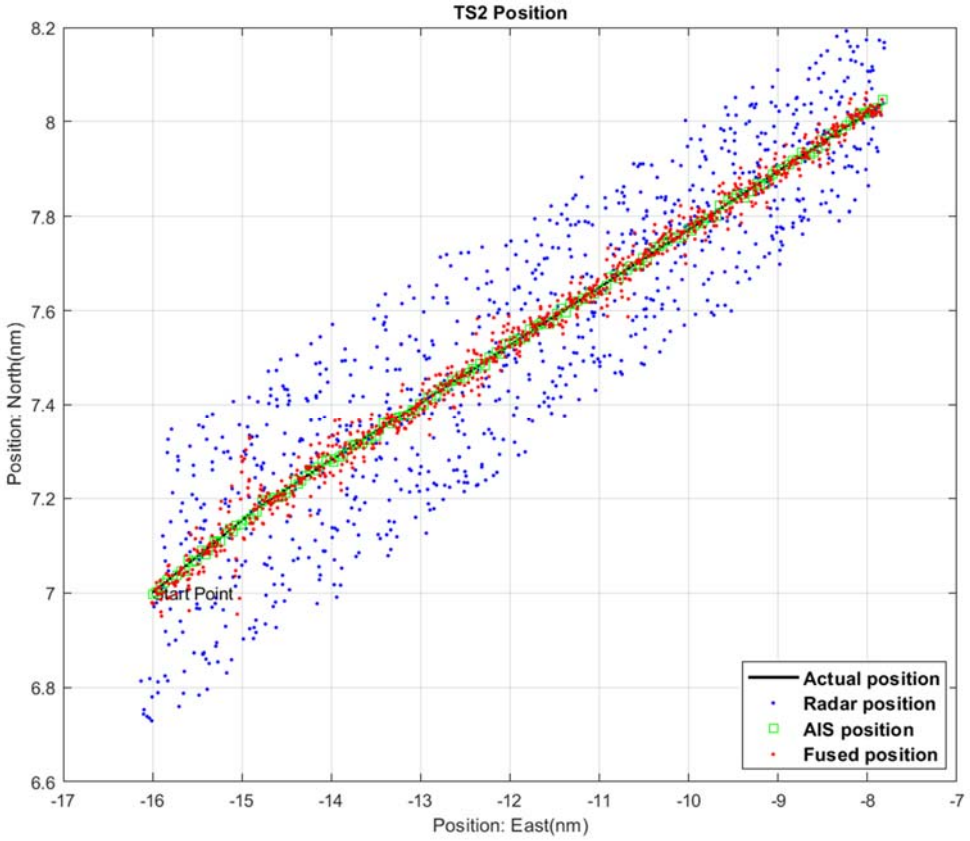

Figure 7. 18 Simulation Scenario 7.2: fused trajectories of Target ship 2

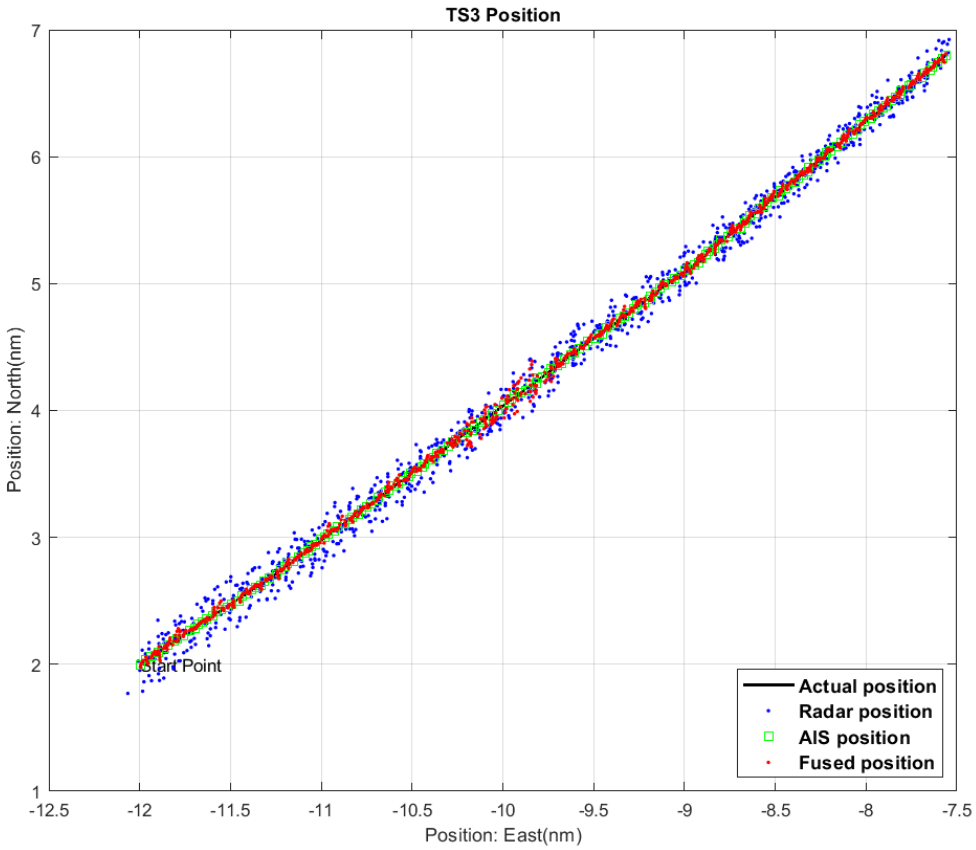

Figure 7. 19 Simulation Scenario 7.2: fused trajectories of Target ship 3

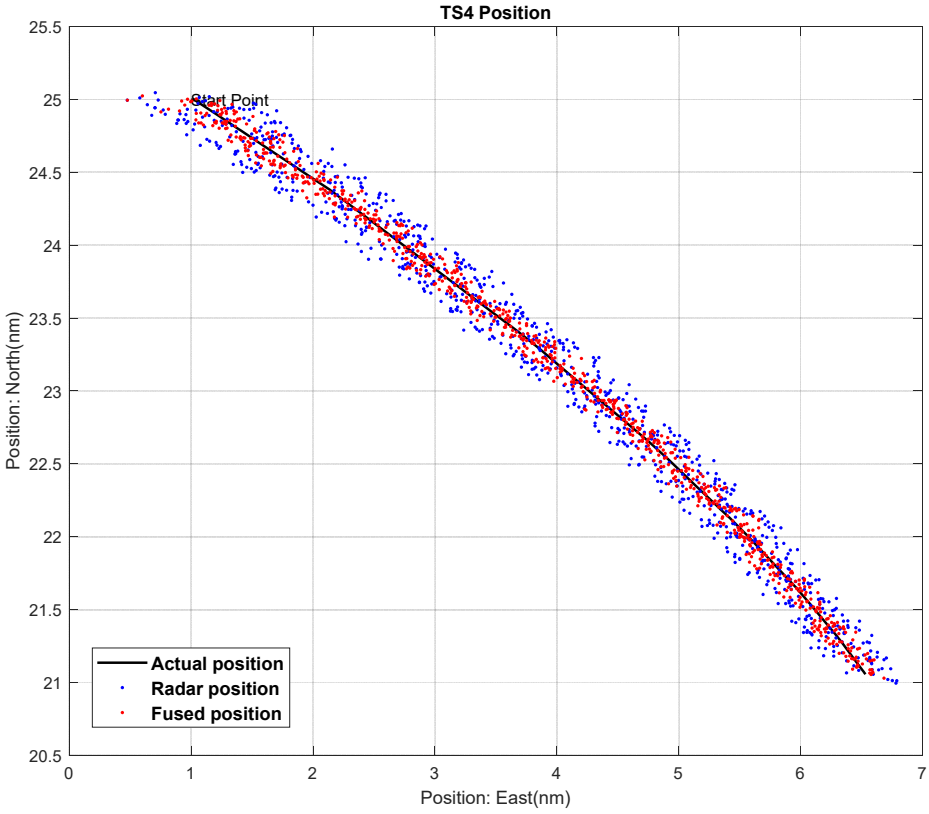

Figure 7. 20 Simulation Scenario 7.2: fused trajectories of Target ship 4

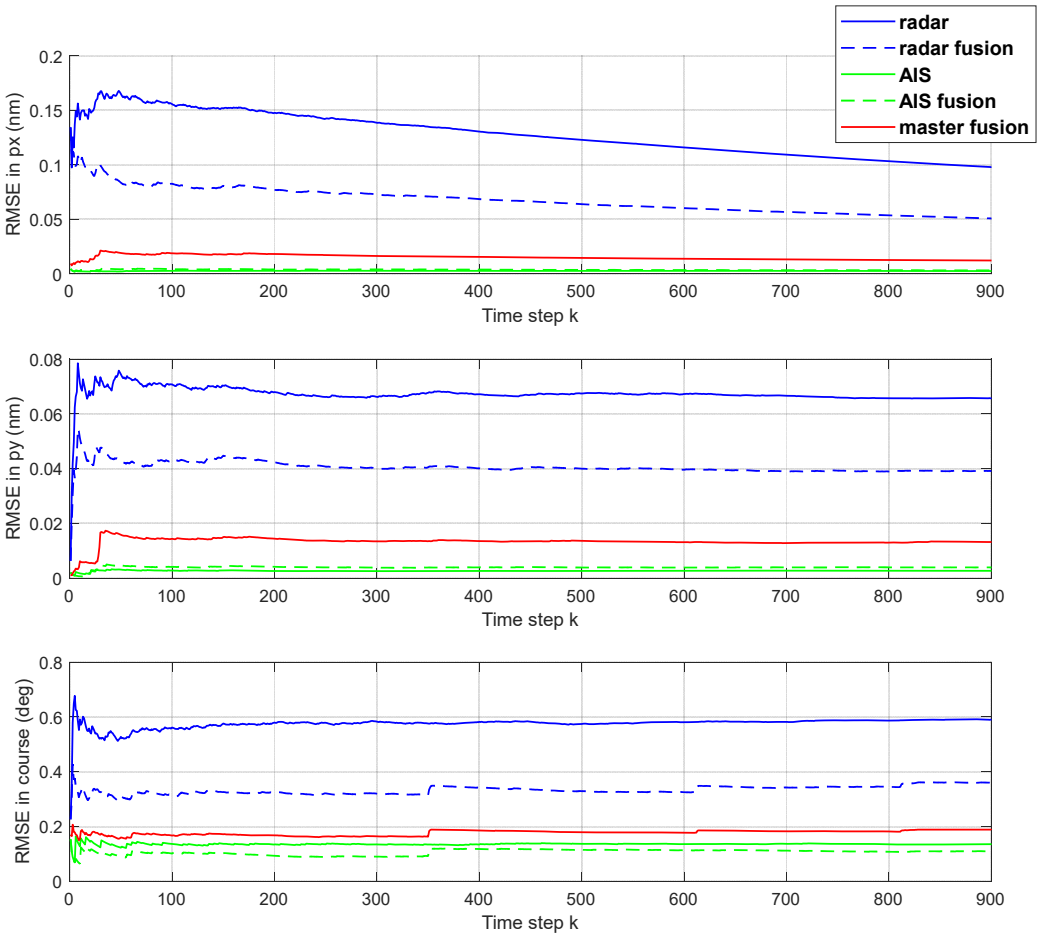

Figure 7. 21 Simulation Scenario 7.2: the RMSEs of Target Ship 1' positions and courses

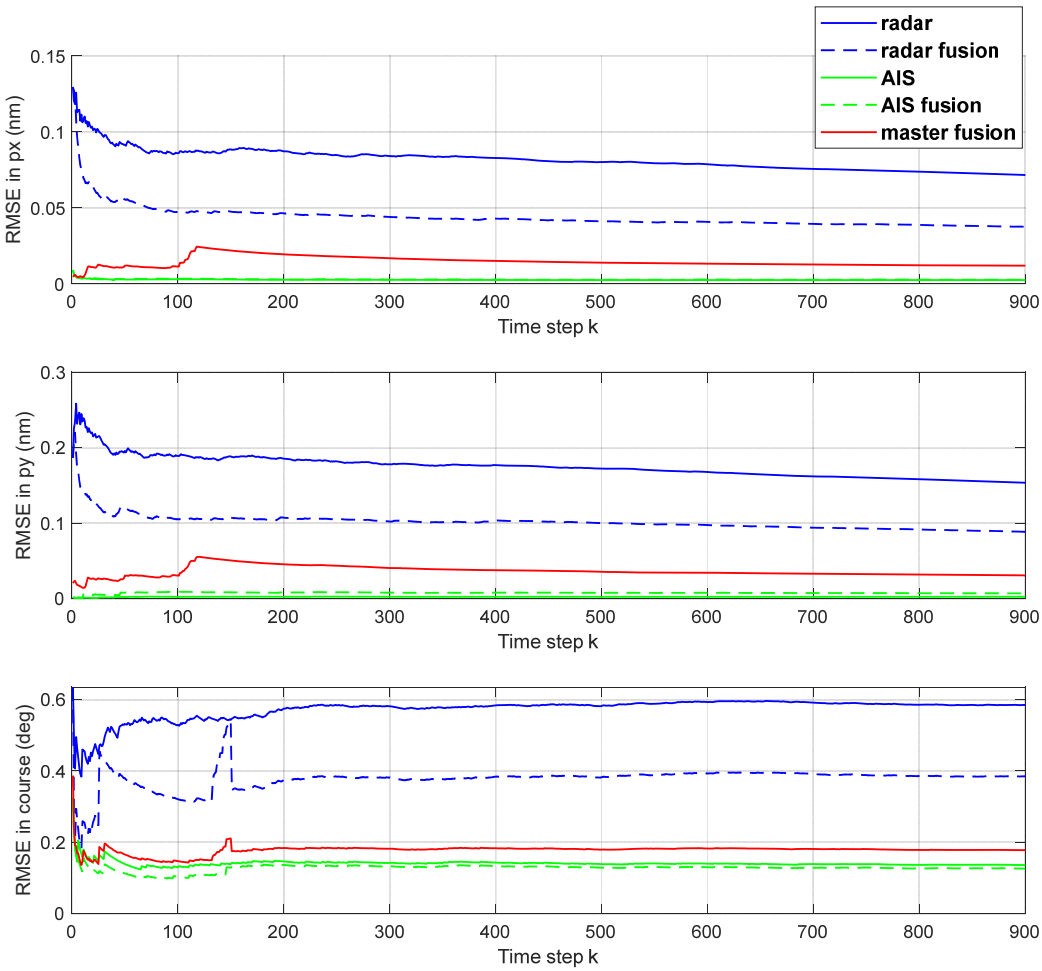

Figure 7. 22 Simulation Scenario 7.2: the RMSEs of Target Ship 2' positions and courses

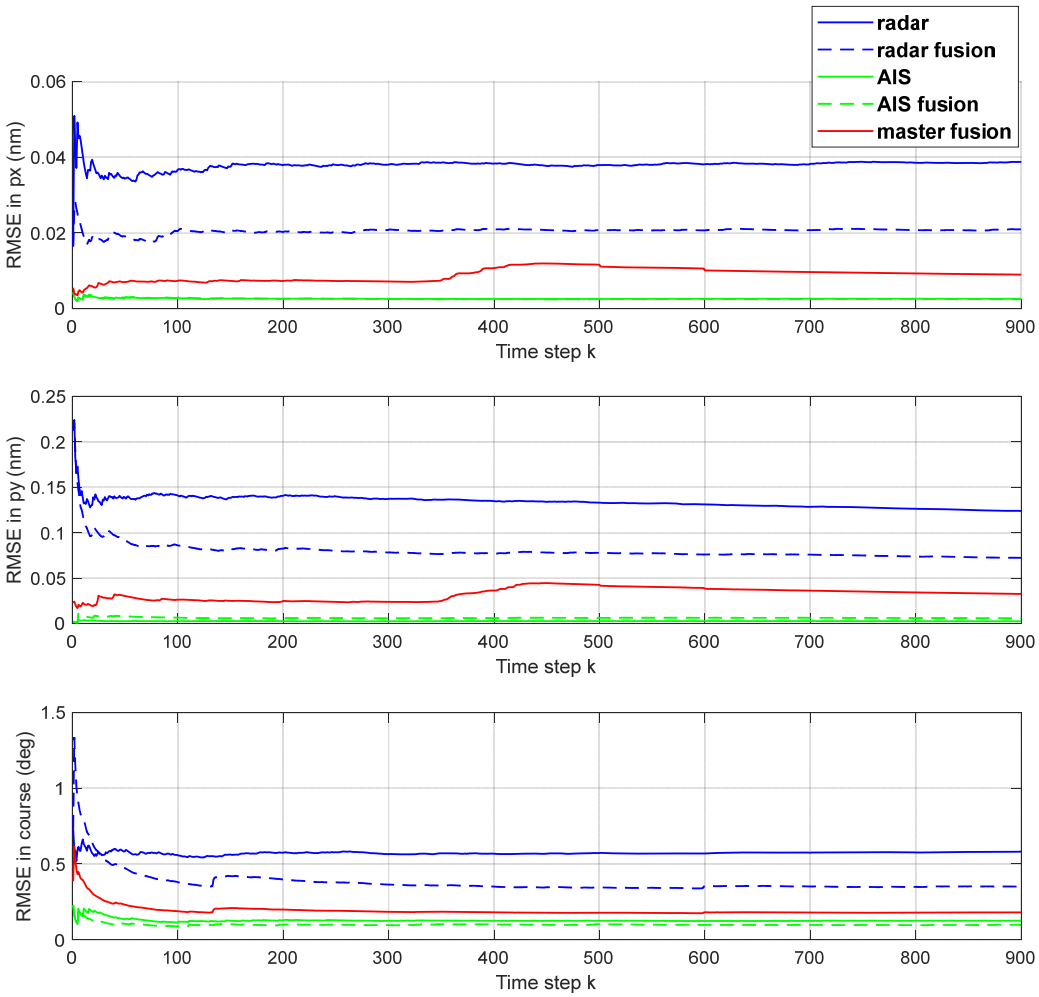

Figure 7. 23 Simulation Scenario 7.2: the RMSEs of Target Ship 3' positions and courses

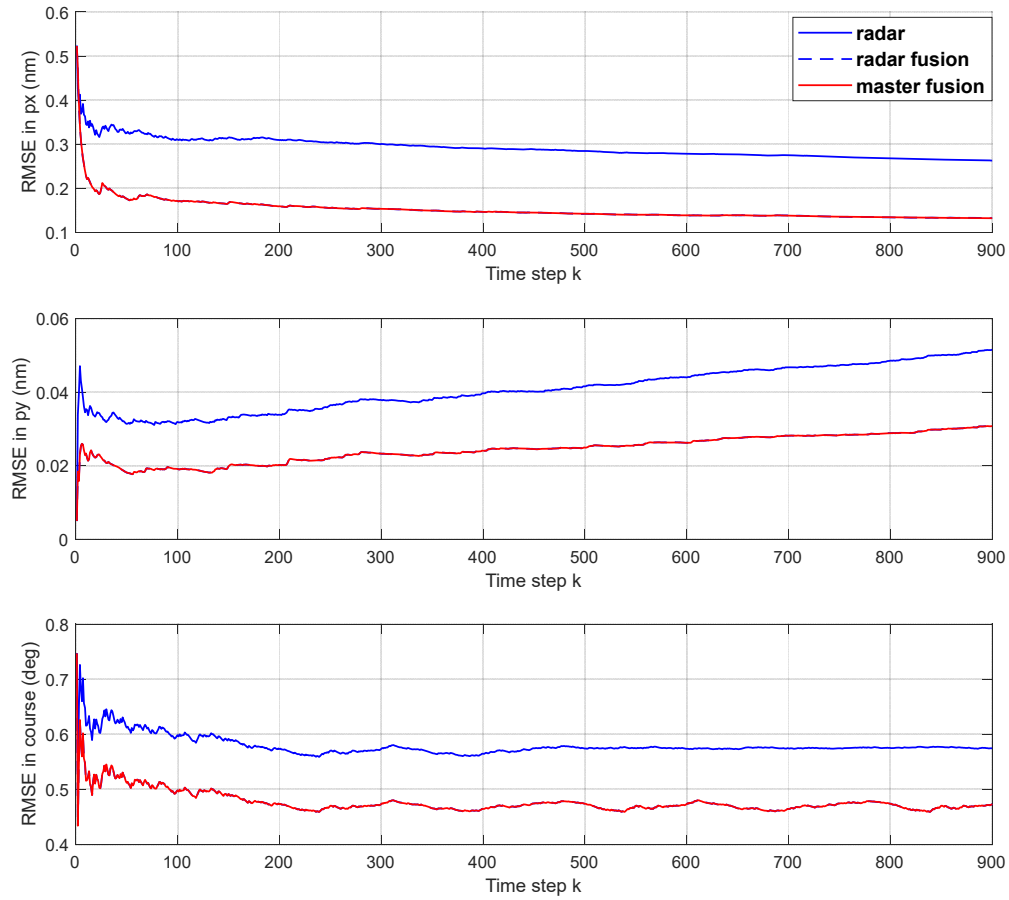

Figure 7. 24 Simulation Scenario 7.2: the RMSEs of Target Ship 4' positions and courses

Figure 7.16 demonstrates the master fusion results of the multiple TSs detection system, which are displayed in Figures 7.17 to 7.20. The actual positions, Radar measurements, possible AIS measurements and master fused positions are presented for each TS. It can be seen that TS 4 does not have AIS measurements and its fused results are generated from Radar based estimations. The trajectory results prove that the proposed multi-sensor TS detection and tracking algorithm can successfully and efficiently associate each AIS and Radar measurement to the related TS tracks using the two-stage fuzzy multi-factor integration data association algorithm. Figures 7.21 to 7.24 illustrate the RMSEs of the positions and courses for each TS. The blue solid line represents the RMSEs of raw Radar measurements, the blue dashed line denotes the RMSEs of Radar based estimations, the green solid line represents the RMSEs of raw AIS measurements, the green dashed line denotes the RMSEs of the AIS based estimations and the red line demonstrates the master fused results. In Figure 7.21, the AIS is updated every 10 s while the Radar provides continuous measurements at 2 s intervals. The master fusion results are much closer to the AIS

estimations than the Radar estimations due to the high accuracy of the AIS estimations. Two very small increases of the RMSEs of the fused course occur while TS 1 is manoeuvring. In Figure 7.22, the RMSEs of the master fusion results of all of TS 2's navigational data are increased from time step $k = 100$ s because of the absence of AIS measurements. This increase is then eliminated after the AIS measurements are restored after 20 s. A similar pattern occurs in Figure 7.23, where TS 3 is set to lose its AIS signal for 150 s. But the RMSEs of the master fusion results are more highly augmented due to the long duration of AIS signal absence. For TS 4, the proposed algorithm is still able to reduce the RMSEs of raw Radar measurements automatically without AIS integration. These results validate the performance of the proposed multi-sensor TS detection and tracking algorithm. Although the RMSE of the master fusion results are increased by a small amount when the TSs are making manoeuvres, the algorithm is able to compensate for such increases before the error increases to a magnitude greater than that of the error of raw Radar measurements, which confirms the effectiveness of the fusion algorithm.

7.3. Summary

When USVs are in operation there is the risk of two types of obstacles. Static obstacles, such as islands, coastal projections and topography and dynamic obstacles, such as other shipping, especially in busy and congested harbours and shipping lanes. The hazards posed by static obstacles are relatively easy to manage as the USV can be pre-programed with topographical data to assist path planning such as to avoid such hazards and reduce collision risks. As regards dynamic hazards, such as TSs, it is essential that the USV has knowledge of not just their position, but also their dynamic behaviour in terms of speed, course and any modifications to these parameters.

This chapter considered the viability of AIS as a data harvesting medium to inform the USV as regards this dynamic environment. Since AIS data transmission rates are dependent upon ship operations it was clear that an element of prediction-correction would be required to allow the USV to update its planned path during the intervals

when the AIS was not transmitting. The IMMKF was developed to provide highly accurate and reliable TS path prediction data. Both straight line and manoeuvring aspects of a TSs were captured by the improved algorithm that was verified by simulation.

However, not all shipping is equipped with AIS. When this obvious deficiency was further complicated by AIS itself not being 100% secure in operation another means of depicting the picture to the USV was required. Radar, although a mature, easily obtainable and viable technology, itself had shortcomings. In an effort to overcome these shortcomings a strategy of combining both AIS and Radar to improve applicability was developed.

The novelty of the approach was not to fuse the AIS and Radar data, as this would require an abundance of data processing capacity and also help the potential of marrying the wrong AIS data to Radar data, especially so when the number of TSs was significant. Instead a method of comparison and confirmation was developed such that USV could continue to assess the positions of TSs even though AIS updates were not being received. The ability to compare, confirm and then match AIS data with Radar data to differentiate between multiple targets with the two step fuzzy approach allowed not only the identification and tracking of multiple TSs, it also allowed enhanced prediction and correction of TS positional data with the IMMKF enhanced algorithm.

Chapter 8. Conclusion and future work

This research has developed, examined and tested multi-sensor data fusion algorithms for USV navigation, including self-localisation and target ship detection. The multi-sensor approach proved advantageous in the improvement of sensor accuracy as well as its adaptability to practical maritime applications. In addition, the algorithms were able to aid detection of faulted sensors, automatically discard faulty data and action sensors to function in complementary manner to minimise the impact of individual sensor error characteristics. The research findings and main contributions are summarised in this chapter followed by recommendations for future development of this research.

8.1. Discussions and conclusions

As referred to in the Introduction chapter, the aim of this research is the development of multiple sensor data acquisition and fusion algorithms that can function accurately, effectively, reliably and economically for an autonomous USV navigation system. In order to achieve this aim, this thesis details a complete solution for a practical USV to determine its own navigational data as well as detecting and tracking surrounding TS.

Chapter 3 has introduced the *Springer* USV and was followed by the hardware implementation of a practical navigation sensor system. The system employs an embedded Linux board as the main on-board navigation processor to extract and convert raw sensor measurements from a GPS receiver, an IMU module and an electronic magnetic compass as well as establishing the wireless communication with a control computer. The development includes the system hardware design and system software implementation using JAVA. The implemented compact navigation sensor system is able to obtain real-time navigational data when included in any practical USV platforms during operations.

Chapter 4 has developed a probabilistic approach underlying multiple sensor data

fusion and developed multi-sensor data fusion algorithms for autonomous USV. Kalman Filtering, a widely used data fusion technology, has been implemented to adapt the USV navigation in a quiet environment. However, since the conventional KF can only deal with linear systems, the performance of the developed KF based multi-sensor data fusion algorithm degraded from the moment the USV was required to manoeuvre. In addition, when considering the environment influences such as water currents that would introduce nonlinearity to the system, the performance of a KF based algorithm was found to be less satisfactory in a practical marine environment. An UKF based multi-sensor data fusion algorithm has then been developed to tackle the issue of non-linearities associated with the navigation system for practical USV applications. Simulations (4.3 and 4.4) have been carried out in environments with both constant and varying currents. In Simulation 4.3, three different speeds of water currents were simulated according to the real tidal currents data in Southampton water. In Simulation 4.4, three different planned trajectories were assigned for the USV to follow in the environment with varying water currents, which were also simulated based on real current data in Solent. The results have provided evidence that the developed UKF based multi-sensor data fusion algorithm demonstrates the ability to significantly reduce sensor noises in a practical environment.

Chapter 5 was dedicated to improving the robustness of the data fusion algorithms for the integrated GPS and inertial navigation system that was developed in Chapter 4. A fuzzy adaptive estimation method has been further developed to reduce the effect caused by unknown or unpredicted changes of sensor measurement noise on the system. The fuzzy logic based algorithm has been proposed to determine the adjustment coefficient to adapt the measurement covariance R based on the actual and theoretical innovation covariance matrices of the conventional UKF in real-time. Numerical simulations have been carried out and evaluated under different simulation conditions based upon practical maritime environments and the results illustrated the adaptive estimation based UKF algorithm does improve the accuracy of the conventional UKF. Although the results were quite similar when the system had accurate noise settings, the adaptive UKF significantly outperformed the conventional UKF with observably more accurate position estimations when the

system lacked *a priori* knowledge of the sensors' measurement noise, with the maximum improvement achieved being approximately 30%. The algorithms were then applied to the actual sensor measurements that were recorded from practical experiments. Results have demonstrated that the developed algorithm can deliver a more practical solution to solve the problem of the robust localisation of a USV.

Chapter 6 has focused on improving reliability of USV navigation, where probable types of sensor failure were taken into account along with solutions to mitigate against such failures. A method to calculate a numerical level of trust has been defined to quantify a measure to the reliability of the estimation obtained by the data fusion algorithms. The underlying concept of the methodology was to compare the same term obtained from two different sensors. If their consistency was high, the estimations based on the two sensor measurements were deemed to be more trustable. Three rules have been defined for the previously developed multi-sensor data fusion algorithms to recover their estimations when the GPS signal is unavailable for a short time period. A fuzzy logic based data fusion algorithm has been developed to detect the possible failure of the duplicated sensor by monitoring the residual vectors of associated KF and provides a feasible solution to avoid the failure sensor. Both simulations and the practical trial provide evident results that the reliability of the system can be improved by applying the developed algorithms.

Chapter 7 was dedicated to developing intelligent and reliable data fusion algorithms for both single and multiple TS detection, prediction and tracking. Instead of using the constant velocity model alone, a manoeuvring TS detection and prediction algorithm based on IMM filtering with different coordinate turn models has been developed to estimate the navigational data of the TS. Furthermore, a multi-senor data fusion algorithm for the AIS and marine radar measurements has been proposed to implement a multiple-TS detection and tracking system. The raw sensor measurements were pre-processed individually using the developed manoeuvring TS detection and prediction algorithm and both output were then being associated with related TSs to make further fusions. The multi-sensor data fusion algorithm increases system reliability by using two different sensors as the complementary devices. Simulations have been carried out to provide numerical evidence that the proposed

TS detection, prediction and tracking algorithms are effective in realising their designed purpose.

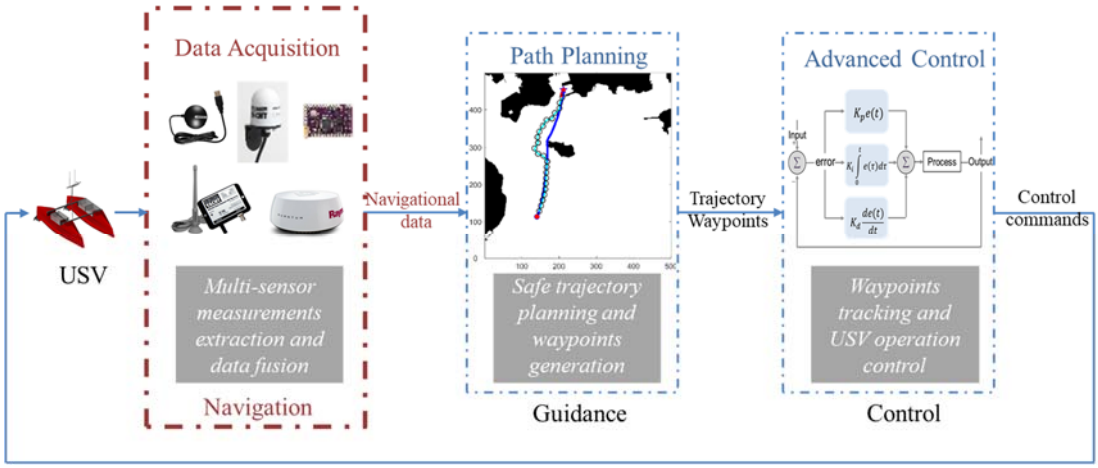

Figure 8. 1 Autonomous navigation system (NGC system) of an Unmanned Surface Vehicle using developed Kalman Filtering based multi-sensor data fusion algorithms

The Kalman Filtering based multi-sensor data fusion algorithms used throughout the research provided a complementary solution to autonomous navigation of an USV by improving raw sensor measurements, increasing system robustness as well as detecting malfunctions in practical environments. The developed navigation sensor system is recommended for the first step of the development of a USV's autonomous NGC system (Figure 8.1) for the following reasons: its capability to deal with practical environmental disturbances such as water current; being able to cope with the problems caused by unknown sensor error during practical operations; the facility to empirically express the reliability of the fused sensor information; the ability to detect and automatically recover from sensor malfunctions during operation; and the ability to allocate measurements from both AIS and radar to the associated TS's tracks and to generate more accurate fusion results of the TS's navigational data.

8.2. Future works

This research is part of an ongoing project in the marine group of the Mechanical Engineering Department of UCL. The following suggestions of future works are recommended for further investigation of the autonomous USV project.

- In Chapter 3, a practical hardware system has been implemented that employs an embedded Linux board as the hosting platform. It runs a General Purpose Operating System (GPOS) on which a Java program can be deployed. GPOS has certain disadvantages such as too much CPU occupations, potential system crashes, etc. Currently, the deployed Java program only has programmed sensor data extraction and conversion, and wireless communication that have been described in detail in Chapter 3. This GPOS has already encountered extended boot up time and slow response time. In the future, the data fusion and path planning computational algorithms will be ported to the embedded platform. In order to cope with such a large amount of calculations, a tailored, smaller sized operating system is required for smoother use and faster response. Real Time Operating System (RTOS) can be considered as a solution to this issue. RTOS is able to reduce the program occupation of the CPU by only processing dedicated tasks and adding time constraints to each assigned task, so that the system robustness and reliability can be enhanced. By integrating the RTOS, the system should then be able to assign those tasks in adjustable priority level and execute each task in a limited time.

- The multi-sensor data fusion algorithms developed to acquire accurate, robust and reliable navigational data for USVs were designed to deal with the operational issues that might occur in practice. However, the real world is more complex and the considerations through Chapter 4 to Chapter 6 are still limited. With regard to Chapter 4, water currents with a constant speed were considered as the main effect to USV's trajectory. Although the model used to express the currents is associated with varied directions, it is not changing continuously and that indicates an unrealistic model. Further research into investigating more practical models of water currents or even ocean currents is recommended to verify the effectiveness and make improvements of the developed UKF based multi-sensor data fusion algorithm. Chapter 5 improves the conventional UKF based data fusion algorithm by integrating a fuzzy adaptive estimation method to update the measurement noise covariance in real-time. The processing noise is not considered in the

algorithm since the raw sensor measurement noises have larger impact on system performance. Investigation into how the processing noise covariance would affect the performance of the developed UKF based data fusion algorithm and subsequently designing an improved mathematical method to update both processing noise covariance and measurement noise covariance in real time is recommended to further improve system robustness. In Chapter 6, although using redundant sensors is more suitable for an autonomous system to improve its fault tolerant ability than simply using a cold standby method, these two methods can be combined in future development to include more sensors and reduce operational cost at the same time. It is also recommended that more practical experiments are carried out to determine any possible problems and improve the developed data acquisition system.

- The results of dynamic TS detection algorithms implemented in Chapter 7 have demonstrated that the duration of time that the AIS signal is missing has a significant impact on the system performance. In this research, an improved weight distribution fusion algorithm was designed to describe the relationship between the absence duration of the AIS signal and the weights assigned to the system estimations based on the last AIS signal. Longer absence duration leads to the weight reducing more rapidly. It is a theoretical method to generally implement this relationship. In the future, a light-weight, low-cost AIS receiver such as AIS100 from Digital Yacht (Digital Yacht, 2019) can be integrated into the navigation sensor system implemented in Chapter 3. Further analysis on real AIS data may then be carried out to investigate the practical relationship between AIS signal absence duration and the weight of the system estimations based on inundated AIS data. In order to further improve the USV's situational awareness ability, static obstacles should also be taken into account. Incorporation of an electronic nautical chart has to gather more information about the surrounding environment in the ocean. Currently, various versions of electronic nautical charts exist in the market. NOAA produces two kinds of official electronic nautical chart, Raster Navigational Chart (RNC) and Electronic Navigational Chart (ENC). The RNC is a scanning version of the existing paper chart. The

UK Hydrographic Office (UKHO) provides RNCs as the ARCS, which is in HCRF format. It is supported by most Electronic Chart Display and Information Systems (ECDIS), but fewer computer chart plotting software products. ENC is a vector chart that digitises each feature's geometry into a specific object. Those navigational objects are maintained in a database, with additional information about their physical characteristics: geographic position, shape, colour, the age of the data, etc. The Admiralty Vector Chart Service (AVCS) provided by UKHO gives the ENCs in encrypted s63 format. Almost all the computer chart plotting software could show this format. There are some non-official electronic nautical charts from different companies available as well. However, these charts do not have a unified standard and will be replaced by the official charts. Hence, the official vector charts would be more useful in an autonomous navigation system. The tasks to incorporate the official vector charts include extracting required static information, such as position of coastlines, buoys etc. from the AVCS; integrating the dynamic overlay based on the developed multi-sensor data fusion system in this research; and displaying the integrated map using an appropriate application programming interface (API).

Reference

Allerton D.J. & Jia H. (2005). A Review of Multisensor Fusion Methodologies for Aircraft Navigation Systems. *Journal of Navigation,* 58, pp. 405-417.

Almagbile, A., Wang, J. & Ding, W. (2010). Evaluating the Performances of Adaptive Kalman Filter Methods in GPS/INS Integration. *Journal of Global Positioning Systems*. 9(1), p33-40.

Appriou A. (2014). *Uncertainty Theories and Multisensor Data Fusion*, London and Hoboken: ISTE Ltd and John Wiley and Sons, Inc.

Arduino (2014). *Arduino Mega 2560 Manual,* Available at: *http://arduino.cc/en/Main/ArduinoBoardMega2560* (Accessed: 12th April 2014).

Ardu-imu (2014). *Introduction to Arduimu V3,* Available at: https://code.google.com/p/ardu-imu/wiki/IntroductionPage (Accessed: 19th February 2014).

ASV Global (2018). *C-Sweep Multi-role MCM USV and Data Sheet,* Available at: http://www.asvglobal.com/military-and-security/c-sweep (Accessed: 17th August 2018).

ASV Global (2018). *UKs Maritime Autonomy Surface Testbed (MAST), An Unmanned Surface Vessel (USV) Based on the Innovative Bladerunner Hull Undergoing Trials on the Thames*. Available at: https://www.asvglobal.com/tag/mast/ (Accessed: 17th August 2018).

Baselga, S., Garcia-Asenjo, L., Garrigues, P. & Lerma, J. L. (2009). Inertial navigation system data filtering prior to GPS/INS integration. The Journal of Navigation, 62(4), pp. 711-720.

Bertolotti I.C. (2006). *Embedded Systems Handbook*, Kentucky: Taylor and Francis Group, LLC.

Bertram, V. (2008). *Unmanned surface vehicles-a survey*. Skibsteknisk Selskab / Danish Society for Naval Architecture and Marine Engineering Foundation, Copenhagen, Denmark, 1, pp.1-14.

Bezdek J.C., Ehrlich R. & Full W. (1984). FCM: The fuzzy c-means clustering algorithm. *Computers and Geosciences*, 10, pp. 191–203.

Bhattacharyya, S., Mute, D. L. & Gebre-Egziabher, D. (2019). Kalman Filter-Based Reliable GNSS Positioning for Aircraft Navigation. In *AIAA Scitech 2019 Forum*, pp. 0363.

Bijker J. & Steyn W. (2008). Kalman filter configurations for a low-cost loosely integrated inertial navigation system on an airship. *Control Engineering Practice*, 16(12), pp. 1509-1518.

Blackman S.S. (1990). *Multitarget-Multisensor: Tracking Advanced Applications*, Norwood: Artech House.

Blackman, S. (2004). Multiple hypothesis tracking for multiple target tracking. *IEEE Aerosp. Electron. Syst. Mag*. 19(1), pp. 5–18.

Blom, H. A. P. (1984). An efficient filter for abruptly changing systems. in *Proceedings of the 23rd IEEE Conference on Decision and Control*, pp. 656–658, Las Vegas, USA, December 1984.

Blom, H.A.P. & Bar-Shalom, Y. (1998). The interacting multiple model algorithm for systems with Markovian switching coefficients. *IEEE Trans. Autom. Control*. 33(8), pp. 780–783.

Bouzouraa M.E. & Hofmann U. (2010). Fusion of Occupancy Grid Mapping and Model Based Object Tracking for Driver Assistance System using Laser and Radar

Sensors. In: *Proceedings of IEEE Intelligent Vehicles Symposium*. San Diego, United States.

Brainerda J. & Pangb A. (2001). Interactive map projections and distortion. *Computers and Geosciences,* 27, pp. 299–314.

Brattebo, J. O. (2014). *Radar Detection, Tracking and Warning of Avian Targets at Airports-Reporting of potentially hazardous bird presence at airports using low cost magnetron Moving Target Detector (MTD) radar*. Masters thesis, NTNU, Norwegian University of Science and Technology.

Bremer, R. H., Cleophas, P. L., Fitski, H. J. & Keus, D. (2007). *Unmanned surface and underwater vehicles* (No. TNO-DV-2006-A455). TNO DEFENCE SECURITY AND SAFETY THE HAGUE (NETHERLANDS).

Briers, M, Maskell, S. R. & Wright, R., (2003). A Rao-Blackwellised Unscented Kalman Filter. In: *Proceedings of the 6th International Conference of Information Fusion*, Vol.1, 2003, pp. 55-61.

Caccia M., Bibuli M., Bono R. & Bruzzone G. (2008). Basic navigation, guidance and control of an Unmanned Surface Vehicle. Auton Robot, 25, pp. 349-365.

Carlson N.A. (1988). Federated filter for fault-tolerant integrated systems. In: *Proceedings of IEEE Position Location and Navigation (PLANS)*, pp. 110–119.

Carragher P., Hine G., LEgh-Simth P., Mayville J., Pai S., Parnum I., Shone P., Smith J. & Tichatschke C. (2013/2014). A New Platform for Offshore Exploration and Production. *Oilfield Review Winter*, 25(4), pp. 40-50.

Caruso M.J. (1997). Application of magnetoresistive sensors in navigation systems. *Sensors and Actuators*, SAE SP-1220, pp. 15-21.

Castanedo F. (2013). A Review of Data Fusion Techniques. *The Scientific World Journal*, 2013, pp. 1-19.

Ccolque-Churquipa, A., Cutipa-Luque, J. C. & Aco-Cardenas, D. Y. (2018). Implementation of a Measurement System for the Attitude, Heading and Position of a USV Using IMUs and GPS. In *2018 IEEE ANDESCON*, pp. 1-6.

CEE HydroSystems (2017). *CEE-USV*. Available at: http://www.ceehydrosystems.com/products/unmanned-survey-vessels/cee-usv/. (Accessed: 15th March 2017).

Charles, A. S. (2017). Kalman Filtering: A Bayesian Approach. *Princeton Neuroscience Institute.*

Chaturvedi, S. K. (2019). Study of synthetic aperture radar and automatic identification system for ship target detection. *Journal of Ocean Engineering and Science*, *4*(2), 173-182.

Choi, E.J., Yoon, J.C., Lee, B.S., Park, S.Y. & Choi, K.H. (2010). Onboard orbit determination using GPS observations based on the unscented Kalman filter. *Advances in Space Research*. 46, pp. 1440-1450.

Chong, T. J., Tang, X. J., Leng, C. H., Yogeswaran, M., Ng, O. E., & Chong, Y. Z. (2015). Sensor technologies and simultaneous localization and mapping (SLAM). *Procedia Computer Science*, 76, pp. 174-179.

Clearpath Robotics (2018). *HERON: Unmanned Surface Vessel*. Available at: https://clearpathrobotics.com/heron-unmanned-surface-vessel/. (Accessed: 11th August 2018).

Corfield S.J. & Young J.M. (2006). Unmanned surface vehicles – Game changing technology for naval operations. In Roberts G.N. & Sutton R. *Advances in Unmanned Marine Vehicles.* Herts: Institution of Engineering and Technology, pp. 311-328.

Croslow A. (2013). *The Beginners Guide to Different Satellite Navigation Systems*, Merlin: Linx Technologies.

Curcio, J., Leonard, J. & Patrikalakis, A. (2005). SCOUT-a low cost autonomous surface platform for research in cooperative autonomy. In Proceedings of OCEANS 2005 MTS/IEEE, pp. 725-729.

Dandrea, A. (2018). *Multi-Sensor Data Fusion Techniques for Autonomous Vehicles Navigation*. Masters dissertation, Politecnico di Torino.

Darrozes, J., Roussel, N. & Zribi, M. (2016). The reflected global navigation satellite system (GNSS-R): from theory to practice. In *Microwave Remote Sensing of Land Surface*, pp. 303-355, Elsevier.

Defence Science and Technology Laboratory (2016). MAST goes into action at Unmanned Warrior. Available at: https://www.gov.uk/government/news/mast-goes-into-action-at-unmanned-warrior (Accessed: 07 June, 2018).

Digital Yacht (2014). *HSC100 Compass: High Performance Electronic Fluxgate Sensor*, Available at: http://digitalyacht.co.uk/files/HSC100%20Brochure%20Eng.pdf (Accessed: 12th November 2014).

Digital Yacht (2019). *AIS100 AIS receiver*, Available at: https://digitalyacht.co.uk/product/ais100-receiver-nmea-0183/ (Accessed: 3rd May 2019).

EGSA (European Global Navigation Satellite Systems Agency (2019). *Galileo is the European global satellite-based navigation system*. Available at: https://www.gsa.europa.eu/european-gnss/galileo/galileo-european-global-satellite-based-navigation-system (Accessed: 30th May 2019).

EI-Rabbany A. (2002). *Introduction to GPS: The Global Positioning System,* Norwood: Artech House, INC.

Elfes A. (1989). Using Occupancy Grids for Mobile Robot Perception and Navigation. *IEEE Computer,* 22(6), pp.46-57.

Embention News, (2015). USV (Unmanned Surface Vehicle) Applications and Advantages. Available at: https://www.embention.com/en/news/usv-unmanned-surface-vehicle-applications-and-advantages/ (Accessed: 19th February 2018).

Faragher, R. (2012), Understanding the Basis of Kalman Filter via a Simple and Intuitive Derivation. IEEE Signal Processing Magazine.

Farnell (2014). *OMAP4460 Pandaboard ES System Reference Manual,* Available at: http://www.farnell.com/datasheets/1563613.pdf (Accessed: 17th April 2014).

Farrell, J.L. (2005). Inertial Instrument Error Characterisation. In: Proceedings of ION AM, Cambridge, MA, United States, pp.1020-1025.

Faulkner, N.M., Cooper S.J. & Jeary P.A. (2002). Integrated MEMS/GPS Navigation Systems. In: Proceedings of IEEE Position Location and Navigation Symposium, Palm Springs CA, United States.

Federal Aviation Administration (2014). *Satellite Navigation- GPS- Policy- Selective Availability,* Available at: http://www.faa.gov/about/office_org/headquarters_offices/ato/service_units/techops/navservices/gnss/gps/policy/availability/ (Accessed: 24th December 2014).

Feng, S. (2014). *Sensor Fusion with Gaussian Processes*, Thesis, University of Glasgow.

Fossen, T. I. (2002). Marine Control Systems: Guidance, Navigation and Control of Ships, Rigs and Underwater Vehicles. *Marine Cybernetics*, 2002.

Gain, N. (2019). *IMDEX 2019: Introducing Yunzhous Unmanned Solutions*. Available at: https://www.navalnews.com/event-news/imdex-asia-2019/2019/05/imdex-2019-introducing-yunzhous-unmanned-solutions/ (Accessed: 11th July 2019).

Ganesh, M. (2006). *Introduction to Fuzzy Sets and Fuzzy Logic*, New Delhi: Prentice-Hall of India Private Ltd.

Gao, B., Hu, G., Gao, S., Zhong, Y. & Gu, C. (2018). Multi-sensor optimal data fusion for INS/GNSS/CNS integration based on unscented Kalman filter. *International Journal of Control, Automation and Systems*, *16*(1), pp. 129-140.

Gao, L., Xing, J., Ma, Z., Sha, J. & Meng, X. (2012). Improved IMM algorithm for nonlinear maneuvering target tracking. *Procedia Engineering*, vol. 29, pp. 4117–4123.

Garmin Ltd. (2014). *What is GPS?* Available at: http://www8.garmin.com/aboutGPS/ (Accessed: 30th November 2014).

Gelb, A. (1974). *Applied Optimal Estimation*. Washington D.C.: The Analytic Science Corporation.

George, P. Kellaway (1970). *Map Projections,* London: Methuen.

Giorgi, G., Schmidt, T. D., Trainotti, C., Mata-Calvo, R., Fuchs, C., Hoque, M. M. & Sanjuan, J. (2019). Advanced technologies for satellite navigation and geodesy. *Advances in Space Research*, *64*(6), 1256-1273.

Glickman M. & Van Dyk D. (2007). Basic Bayesian Methods. In Walker J.M. *Methods in Molecular Biology*. Totowa: The Humana Press Inc.

Goyette, R. (2007). An Analysis and Description of the Inner Workings of the FreeRTOS Kernel. April 2007.

GPS Daily (2019). *China to complete BeiDou-3 satellite system by 2020*, Available at: http://www.gpsdaily.com/reports/China_to_complete_BeiDou_3_satellite_system_by_2020_999.html (Accessed: 10 Aug 2019).

Gregor, S., Pawel, B., Julian, H., Frank, H. (2017). Counteracting the effects of GNSS jamming in a maritime multi-target scenario by fusing AIS with radar data. In: *International Technical Meeting (ITM)*, Monterey, CA, USA.

Grewal M. S. & Andrews A. P. (2008). *Kalman Filtering: Theory and Practice Using Matlab*. 3rd edn, West Sussex: John Wiley and Sons, Ltd.

Grewal, M. S., Andrews, A. P. & Bartone, C. G. (2020). *Global navigation satellite systems, inertial navigation, and integration*. John Wiley and Sons.

Groves P. D. (2013). *Principles of GNSS, Inertial, and Multisensor Integrated Navigation Systems*, 2nd edn, Norwood: Artech House.

Guan, F., Peng, L., Perneel, L. & Timmerman, M., (2016). Open source FreeRTOS as a case study in real-time operating system evolution. *Journal of Systems and Software*, vol.118, pp. 20-35.

Gursoy, G., Prach, A. & Yavrucuk, I. (2013). Design of a Waypoint Tracking Control Algorithm for Parachute-Payload Systems. pp. 343-359.

Habtemariam, B., Tharmarasa, R., McDonald, M. & Kirbarajan, T. (2014). Measurement level AIS/radar fusion. *Signal Processing*, 106(2015), pp. 348–357, doi: 10.1016/j.sigpro.2014.07.029.

Hall, D. L. & Llinas, J. (1997). An introduction to multisensor data fusion. *Proceedings of the IEEE*, *85*(1), 6-23.

Han., J., Song, Q. & He, Y. (2009). Kalman Filter: Recent Adavances and Applications. Adaptive Unscented Kalman Filter and Its Applications in Nonlinear Control.

Han, J., Park, J., Kim, T. & Kim, J. (2015). Precision navigation and mapping under bridges with an unmanned surface vehicle. *Autonomous Robots*, *38*(4), 349-362.

Hanlon M. (2006). *The Protector Unmanned Surface Vehicle*, Available at: http://www.gizmag.com/go/6023/ (Accessed: 28th November 2014).

Hapgood, M. (2018). Societal and Economic Importance of Space Weather. In *Machine Learning Techniques for Space Weather.* pp. 3-26. Elsevier.

Harati-Mokhtari, A., Wall, A., Brooks, P. & Wang, J. (2007). Automatic Identification System (AIS): Data Reliability and Human Error Implications. *The Journal of Navigation*, 60, pp. 373-389.

Hermann, D., Galeazzi, R., Andersen, J. C., & Blanke, M. (2015). Smart sensor based obstacle detection for high-speed unmanned surface vehicle. *IFAC-PapersOnLine*, *48*(16), 190-197.

Hertzmann, A., Fleet, D. J. & Brubaker, M. (2015). Probability Density Functions (PDFs). University of Toronto, Lecture notes.

Hightower, P. & President, V. (2008). Motion Effects on GPS Receiver Time Accuracy. *Technical Descriptions, Instrumentation Technology Systems.*

Holm, H. & Mellegard, N. (2018). Fast Decoding of Automatic Identification Systems (AIS) Data. In: *International Conference on Computer Applications and Information Technology in the Maritime Industries*, Pavone, Italy.

Honeywell (2014). *Compass HMR3000 Manual*, Available at: http://web.arrownac.com/sites/default/files/pdfs/HMR3000.pdf (Accessed: 11th April 2014).

Howell E. (2013). *Navstar: GPS Satellite Network*, Available at: http://www.space.com/19794-navstar.html (Accessed: 10 November 2014).

Hu, C., Chen, W., Chen, Y. & Liu, D. (2003). Adaptive Kalman Filtering for Vehicle Navigation. *Journal of Global Positioning Systems*, 2(1), pp. 42-47.

Hu, X. & Lin, C. (2011). A Preliminary Study on Targets Association Algorithm of Radar and AIS Using BP Neural Network. *Procedia Engineering*, Vol 15, pp. 1441-1445.

Huang, B., Zhao, J., & Liu, J. (2019). A Survey of Simultaneous Localization and Mapping. *arXiv preprint arXiv:1909.05214*.

IEEE (2001). *Standard for Inertial Sensor Terminology*. IEEE Standard IS 528-2001.

International Maritime Organisation (IMO) (2003). *Guidelines for the installation of a shipborne automatic Identification System (AIS)*. SN/Circ.227.

International Maritime Organisation (IMO) (2002). *SOLAS convention*, Chapter V, Regulation 19.

International Maritime Organisation (IMO) (2019). *AIS transponders*, Available at: http://www.imo.org/en/OurWork/Safety/Navigation/Pages/AIS.aspx (Accessed: 15 April 2019).

Janes International Defence (2018). Sea sentinels: Chinese Unmanned Maritime Systems gain traction. *HIS Markit*.

Jan, S. & Kao, Y. (2013). Radar tracking with an Interacting Multiple Model and Probabilistic Data Association Filter for Civil Aviation Applications. *Sensors*, **13**, pp. 6636- 6650, doi: 10.3390/s130506636.

Jager, R. (1995). *Fuzzy Logic in Control*, Thesis, Delft University of Technology.

Jiang, G., Yin, L., Jin, S., Tian, C., Ma, X., & Ou, Y. (2019). A simultaneous localization and mapping (SLAM) framework for 2.5 D map building based on low-cost LiDAR and vision fusion. *Applied Sciences*, *9*(10), 2105.

Jin, M., Zhao, J., Jin, J., Yu, G. & Li, W. (2014). The adaptive Kalman filter based on fuzzy logic for inertial motion capture system. *Measurement*. 49, pp. 196-204.
Julier, S.J. & Uhlmann, J.K. (2004). Unscented filtering and nonlinear estimation. *Proceedings of the IEEE*, 92(3), pp. 401–422.

Jwo D.J. & Chang F.I. (2007). A Fuzzy Adaptive Fading Kalman Filter for GPS Navigation. in *Advanced Intelligent Computing Theories and Applications - with Aspects of theoretical and Methodological Issues*, Heidelberg: Springer-Verlag Berlin Heidelberg, 4681, pp.820-831.

Kamal R. (2003). *Embedded systems: architecture, programming and design*, Noida: Tata McGraw-Hill Education.

Kalsen, B. L., Nielsen, E. & Pedersen, M. T. (2015). Fusion of radar and secondary sensor data using kinematic models of multiple simultaneous targets. In *IEEE Sensor Signal Processing for Defence (SSPD)*, 9-10 Sept 2015, Edinburgh, UK, doi: 10.1109/SSPD.2015.7288504.

Kazimierski, W. (2013). Problems of data fusion of tracking radar and AIS for the needs of integrated navigation systems at sea. In *14th International Radar Symposium (IRS)*, Vol. 1, pp. 270-275.

Khamseh, H. B., Ghorbani, S. & Janabi-Sharifi, F. (2019). Unscented Kalman filter state estimation for manipulating unmanned aerial vehicles. *Aerospace Science and Technology*.

Kim, Y. S. & Hong, K. S. (2004). An IMM Algorithm for Tracking Maneuvering Vehicles in an Adaptive Cruise Control Environment. *International Journal of Control, Automation, and System*, Vol. 2, No. 3, pp. 310-318.

Klein, L.A. (2004). *Sensor and data fusion: a tool for information assessment and decision making* (Vol. 324). Bellingham, eWA WA: SPIE press.

Kobayashi, K., Cheok, K.C., Watanabe, K. & Munekata, F. (1998). Accurate Differential Global Positioning System via Fuzzy Logic Kalman Filter Sensor Fusion Technique. *IEEE Transactions on Industrial Electronics*, 45(3), pp. 510–518.

Kosko B. (1996). *Fuzzy Engineering*, Har/Dsk edn, New Jersey: Prentice Hall.

KVH (2014). *Compass KVH C100 Manual*, Available at: http://www.canalgeomatics.com/product_files/kvh-c100-compass_426.pdf (Accessed: 11th April 2014).

Lan, H., Sun, S., Wang, Z., Pan, Q. & Zhang, Z. (2019). Joint Target Detection and Tracking in Multipath Environment: A Variational Bayesian Approach. *IEEE Transactions on Aerospace and Electronic Systems*.

Lancaster, H. O. (1969). *The chi-squared distribution*, Wiley series in probability and mathematical statistics, Wiley, United Kingdom.

Langley R.B. (2003). The magnetic compass and GPS. *GPS World*, pp. 70-80.

Lee, D., Vukovich, G. & Lee, R. (2017). Robust unscented Kalman filter for nanosat attitude estimation. *International Journal of Control, Automation and Systems*, 15(5), pp. 2161-2173.

Li, X. R. & Jilkov, V. P. (2002). A survey of Manoeuvring Target Tracking – Part IV: Decision-Based Methods. In *Proceedings of SPIE Conference on Signal and Data Processing of Small Targets*, Prlando, FL, USA, April 2002, Paper 4728-60.

Li, W., Gong, D., Liu, M., Chen, J. & Duan, D. (2013). Adaptive robust Kalman filter for relative navigation using global position system. *IET radar, Sonar and Navigation.*

Lin, D., Dong, F., Lin, H., Le, L., Zhou, J. & Ou, Y. (2008). AIS Information Decoding and Fuzzy Fusion Processing with Marine Radar. *In: Proceedings of IEEE Wireless Communications, Networking and Mobile Computing Conference*, China.

Liquid Robotics (2014). *Wave Glider SV3 and spec sheet,* Available at: http://liquidr.com/technology/waveglider/sv3.html (Accessed: 15th August 2014).

Liu, M., Chen, J., Zhao, X., Wang, L. & Tian, Y. (2018). Dynamic obstacle detection based on multi-sensor information fusion. *IFAC-PapersOnLine*, *51*(17), 861-865.

Liu, W., Liu, Y., Gunawan, B. A. & Bucknall, R. (2020). Practical moving target detection in maritime environments using fuzzy multi-sensor data fusion. *International Journal of Fuzzy Systems*.

Liu, W., Liu, Y. & Bucknall, R. (2019). A Robust Localization Method for Unmanned Surface Vehicle (USV) Navigation Using Fuzzy Adaptive Kalman Filtering. *IEEE Access*, 7, pp. 46071-46083, DOI: 10.1109/ACCESS.2019.2909151.

Liu, W., Liu, Y., Song, R. & Bucknall, R. (2018). The Design of an Embedded Multi-Sensor Data Fusion System for Unmanned Surface Vehicle Navigation Based on Real Time Operating System. In: *Proceedings of the MTS/IEEE OCEANS'18 Kobe / Techno-Ocean Conferences*. 28-31 May, 2018, Kobe, Japan. DOI: 10.1109/OCEANSKOBE.2018.8559352.

Liu W., Liu Y., Song, R. & Bucknall, R. (2015). The design of an autonomous maritime navigation system for unmanned surface vehicles. In: *Proceedings of 14th International Conference on Computer and Information Technology Application in the Maritime Industries*. 11-13 May, 2015, Ulrichshusen, Germany. pp. 147-160.

Liu W., Liu Y., Song, R. & Bucknall, R. (2015). Towards the development of an autonomous navigation system for unmanned vessels. In: *Proceedings of 13th International Navigation Conference (INC) 2015*. 24-26 February, 2015, Manchester, UK.

Liu, Y., Song, R. & Bucknall, R. (2019). Intelligent tracking of moving ships in constrained maritime environments using AIS. *Cybern. Syst.* 50, 539–555.

Liu, Y., Liu, W., Song, R. & Bucknall, R. (2017). Predictive navigation of unmanned surface vehicles in a dynamic maritime environment when using the fast marching method. *International Journal of Adaptive Control and Signal Processing*. 31(4), pp. 464-488.

Liu Y., Song R., Liu, W. & Bucknall, R. (2014). Autonomous navigation system for unmanned surface vehicles. In: *Proceedings of 13th International Conference on Computer and Information Technology Application in the Maritime Industries*, 12-14 May, 2014, Redworth, UK. pp. 123-135.

Liu, W., Motwani, A., Sharma, S., Sutton, R. & Bucknall, R. (2014). Fault Tolerant Navigation of USV using Fuzzy Multi-sensor Fusion. *MIDAS technical report*. MIDAS.SMSE.2014.TR.010.

Liu, Z., Zhang, Y., Yu, X. & Yuan, C. (2016). Unmanned surface vehicles: An overview of developments and challenges. *Annual Reviews in Control*, 41, pp. 71-93.

Lloyds List Intelligence (2017). Understanding AIS: The technology, the limitations and how to overcome them with Lloyds List Intelligence. *Maritime Intelligence | informa.*

Loebis, D., Sutton, R., Chudley, J. & Naeem, W. (2004). Adaptive tuning of a Kalman filter via fuzzy logic for an intelligent AUV navigation system. *Control Engineering Practice*, 4(12), pp 1531–1539.

Ma, H., Ding N., Li, L. & Ma, Y. (2006). *Embedded System Design Tutorial*. Beijing: Publishing House of Electronics Industry.

Ma, Y., Fang, J., Wang, W. & Li, J. (2014). Decoupled Observability Analyses of Error States in INS/ GPS Integration. *The Journal of Navigation*. 67, pp. 473-494.

Maklouf, O., Ghila, A., Abdulla, A. & Yousef, A. (2013). Low Cost IMU\GPS Integration Using Kalman Filtering for Land Vehicle Navigation Application. *International Journal of Electrical, Computer, Energetic, Electronic and Communication Engineering*, 7(2), pp.184-190.

Manley, J. E. (2008). Unmanned Surface Vehicles, 15 Years of Development. In: *IEEE OCEANS*, Quebec, pp. 1-4.

Manley, J. E., (1997). Development of the autonomous surface craft “ACES”. In *Proceedings of Oceans97,* vol. 2, 1997, pp. 827–832.

Manley, J. E., Marsh, A., Cornforth, W. & Wiseman, C. (2000). Evolution of the autonomous surface craft AutoCat. In *Conference Proceedings of OCEANS 2000 MTS/IEEE Conference and Exhibition.* Vol. 1, pp. 403-408.

Marine Advanced Research INC. (2014). *Unmanned WAM-V*, Available at: http://www.wam-v.com/unmanned.html (Accessed: 15th August 2014).

Maritime and Coastguard Agency (MCA) (2007). Guidance on Chapter V – Safety of Navigation. *Safety of Life at Sea (SOLAS),* Regulation 19.

Matzka, S. & Altendorfer, R. (2008). A Comparison of Track-to Track Fusion Algorithms for Automotive Sensor Fusion. *In: Proceedings of IEEE International Conference on Multisensor Fusion and Integration for Intelligent Systems*, Seoul, Korea.

Maybeck, P. (1979). *Stochastic Models, Estimation, and Control*, Volume 1, London: Academic Press, Inc.

Maritime and Coastguard Agency (MCA) (1996). The Merchant Shipping (Distress Signals and Prevention of Collisions) Regulations 1996. MSN 1781 (M+F).

McWilliam, N., Teeuw, R., Whiteside, M. & Zukowskyj, P. (2005). *Field Techniques Manual: GIS, GPS and Remote Sensing*, Maidstone: Ordnance Survey, pp. 79-110.

Meng, Y., Gao, S., Zhong, Y., Hu, G. & Subic, A. (2016). Covariance matching based adaptive unscented Kalman filter for direct filtering in INS/GNSS integration. *Acta Astronautica*. V120, pp. 171-181.

MIDAS Group, Plymouth University. (2014). *Springer Unmanned Surface Vehicle,* Available at: http://www.tech.plymouth.ac.uk/sme/springerusv/ (Accessed: 11th May 2014).

Misra, P. & Enge, P. (2011). *Global Positioning System: Signals, Measurements and Performance*, 2nd edn, Lincoln: Ganga-Jamuna Press.

Morelle, R. (2014). *GPS back-up: World War Two technology employed,* Science Correspondent, BBC News, Available at: http://www.bbc.co.uk/news/science-environment-29758872 (Accessed: 24th December 2014).

Motwani, A., Liu, W., Sharma, S., Sutton, R. & Bucknall, R. (2016). An interval Kalman filter–based fuzzy multi-sensor fusion approach for fault-tolerant heading estimation of an autonomous surface vehicle. *Proceedings of the Institution of Mechanical Engineers, Part M: Journal of Engineering for the Maritime Environment*. 230(3), pp. 491-507. DOI: 10.1177/1475090215596180.

Motwani, A., Sharma, S.K., Sutton, R. & Culverhouse, P. (2014). Computation of stable Interval Kalman Filter bounds for their use in robust state estimation for an Uninhabitated Surface Vehicle with bounded indeterminate system dynamics. In: *Proceedings of IEEE Intelligen Vehicles Symposim (IV).* June 8-11, 2014, Dearborn, Michigan, USA.

Motwani, A., Sharma, S.K., Sutton, R. & Culverhouse, P. (2013). Interval Kalman Filtering in Navigation System Design for an Uninhabited Surface Vehicle. *Journal of Navigation*, 66, pp. 639-652.

Mousazadeh, H., Jafarbiglu, H., Abdolmaleki, H., Omrani, E., Monhaseri, F., Abdollahzadeh, M. R. & Makhsoos, A. (2018). Developing a navigation, guidance and obstacle avoidance algorithm for an Unmanned Surface Vehicle (USV) by algorithms fusion. *Ocean Engineering*, 159, 56-65.

National Coordination Office (2014). *Official U. S. Government information about the Global Positioning system (GPS) and related topics: Marine,* Available at: http://www.gps.gov/applications/marine/ (Accessed: 27th November 2014).

National Marine Electronics Association (2008). *NMEA 0183 Standard V4.10*, Available at: http://www.nmea.org/content/nmea_standards/nmea_0183_v_410.asp (Accessed: 21st November 2014).

Naval Technology (2014). *Protector Unmanned Surface Vehicle (USV), Israel.* Available at: http://www.naval-technology.com/projects/protector-unmanned-surface-vehicle/ (Accessed: 16th August 2014).

Ning, Q., Yan, S., Liu, L., Guo, B. (2016). Study on multiple manoeuvring targets tracking based on JPDA algorithm. *Meas. Sci. Instrum*. 7(1), pp. 30–34.

Noureldin A., Karamat T.B. & Georgy J. (2013). *Fundamentals of inertial navigation, satellite-based positioning and their integration*, Heidelberg: Springer-Verlag Berlin Heidelberg, pp.21-63.

Oceanα (2019). *Unmanned Surface Vehicles*. Available at: https://www.oceanalpha.com/ (Accessed: 03 Feburary 2019).

Osborne, J. & Rysdyk, R. (2005). Waypoint guidance for small UAVs in wind. *In Infotech@ Aerospace*, pp. 6951.

Pallotta, G., Vespe, M. & Bryan, K. (2013). Vessel Pattern Knowledge Discovery from AIS Data: A Framework for Anomaly Detection and Route Prediction. *Entropy*, **2013**(15), pp. 2218-2245, doi: 10.3390/e15062218.

Pang, B. (2011). Energy Consumption Analysis of ARM-based System. *Aalto University School of Science Degree Programme of Mobile Computing*, 68.

Patra, B. K., Launonen, R., Ollikainen, V. & Nandi, S. (2015). A new similarity measure using Bhattacharyya coefficient for collaborative filtering in sparse data. *Knowledge-Based Systems*, 82, pp. 163-177.

Paulino, A. D. C., Shiguemori, E. H. & Guimaraes, L. N. F. (2018). An Adaptive Neuro-Fuzzy-based Multisensor Data Fusion applied to real-time UAV autonomous navigation. In *Anais do XV Encontro Nacional de Inteligência Artificial e Computacional,* pp. 847-858.

Paulino, A. D. C., Guimaraes, L. N. F. & Shiguemori, E. H. (2019). Hybrid Adaptive Computational Intelligence-based Multisensor Data Fusion applied to real-time UAV autonomous navigation. *Inteligencia Artificial*, 22(63), pp. 162-195.

Pearson, D., An, E., Dhanak M., Ellenrieder, K.V. & Beaujean, P. (2014). High-Level Fuzzy Logic Guidance System for an Unmanned Surface Vehicle (USV) tasked to perform Autonomous Launch and Recovery (ALR) of an Autonomous Underwater Vehicle (AUV). In: *Proceedings of Autonomous Underwater Cehicles (AUV), IEEE/OES*, Oxford, MS.

Pelich, R., Longepe, N., Mercier, G., Hajduch, G. & Garello, R. (2015). AIS-based Evaluation of Target Detectors and SAR Sensors Characteristics for Maritime Surveillance. *IEEE Journal of Selected Topics in Applied Earth Observations and Remote Sensing*, Vol 8(8), pp. 3892-3901, doi: 10.1109/JSTARS.2014.2319195.

Penobscot marine museum, 2012. *Methods of Navigation*. Available at: https://penobscotmarinemuseum.org/pbho-1/history-of-navigation/history-navigation-introduction (Accessed: 08th June 2015).

PNI (2014). Compass TCM2 Manual. Available at: http://www.mil.ufl.edu/projects/gnuman/gnuman_pre2005/spec_sheets/tcm2_productsheet.pdf (Accessed: 11th April 2014).

Qiaohua, H. (2012). Development of Beidou navigation satellite system. In *Proceedings of the 5th Meeting of International Committee on GNSS (ICG-512)*.

QinetiQ, (2018). Blackfish Unmanned Surface Vehicle: Mission Overview. Available at: https://www.qinetiq-na.com/wp-content/uploads/MAC/Blackfish.pdf (Accessed: 3 May 2018).

Racz, R., Schott C. & Huber, S. (2004). Electronic Compass Sensor. In: *Proceedings of IEEE Sensors*, Vienna, Austria.

Rahimi, A., Kumar, K. D. & Alighanbari, H. (2015). Enhanced Adaptive Unscented Kalman Filter for Reaction Wheels. *IEEE Transactions on Aerospace and Electronic Systems*. **51**, (2), p1568-1575.

Ratsameethammawong, P. & Kasemsan, K. (2010). Mobile phone location tracking by the combination of GPS, Wi-Fi and cell location technology. *Communications of the IBIMA*.

Rios, J. A. & White, E. (2002). Fusion filter algorithm enhancements for a MEMS GPS/IMU. *Crossbow Technology, Inc*, 1-12.

Roberts, G.N. & Sutton, R. (2008). *Advances in Unmanned Marine Vehicles*, Herts: the Institution of Engineering and Technology.

Robson, J. K. (2006). Overview of Collision detection in the UKCS. *AEA Technology Plc*, Health and Safety Executive, Research report: RR514.

Rohde and Schwarz (2012). Introduction to Radar System and Component Tests. White paper.

Ross, T.J. (2010). *Fuzzy Logic with Engineering Applications*, 3rd edn, West Sussex: John Wiley and Sons, Ltd.

Roth, M. (2017). *Advanced Kalman filtering approaches to Bayesian state estimation*, Doctoral dissertation, Linköping University Electronic Press.

Sabatini, R., Moore, T. & Ramasamy, S. (2017). Global navigation satellite systems performance analysis and augmentation strategies in aviation. *Progress in Aerospace Sciences*, *95*, pp. 45-98.

Saderzadeh, A. (2010). Mobile Robot Navigation Error Handling Using an Extended Kalman Filter. *Journal of Advances in computer Research*, *1*(1), pp. 61-75

Sameena, N., Afshar, A. & Ranjit, B. (2011). Effect of different defuzzification methods in a fuzzy based load balancing application. *IJCSI International Journal of Computer Science Issues*, 8(5), No 1, pp. 261-267.

Sanchez-Ramirez, E. E., Rosales-Silva, A. J., Vianney-Kinani, J. M. & Alfara-Flores, R. A. (2019). A Four-Model Based IMM Algorithm for Real-Time Visual Tracking of High-Speed Manoeuvring Targets. *Journal of Intelligent and Robotic Systems*, **2019**(95), pp.761-775.

Saneifard, R. (2011). A Method for Defuzzification based on Centroid Point. *Turkish Journal of Fuzzy Systems (TJFS)*, 2(1), pp. 36-44, Doi: 10.1007:s10846-018-0926-1.

Sarkka, S. (2011). *Bayesian Estimation of Time-Varying Systems: Discrete-Time Systems*. Course booklet. Aalto University, Finland.

Sarkka, S. (2013). *Bayesian Filtering and Smoothing*, Cambridge: Cambridge University Press.

Shiau, J.K., Huang, C.X. & Chang, M.Y (2012). Noise Characteristics of MEMS Gyros Null Drift and Temperature Compensation. *Journal of Applied Science and Engineering*, 15 (3), pp. 239-246.

Shimkin, N. (2009). Derivations of the discrete-time Kalman filter. *Technion – Israel Institute of Technology, Estimation and identification in dynamical systems.*

Shurcliff, W. A. (1947). *Bombs at Bikini: The Official Report of Operation Crossroads*. WH Wise.

Siegert, G. (2017). Multi-Radar Multi-target Tracking in the Context of Cooperative Maritime Traffic Situation Assessment. *German Aerospace Center, Institute of Communications and Navigation.* Neustrelita, Germany.

Smith, S. G. (2000). The Global Positioning System and Inertial Navigation. JA Farrell and M. Barth. The McGraw-Hill Companies, McGraw-Hill House, Shoppenhangers Road, Maidenhead, SL6 2QL, UK. ISBN 0-07-022045-X. *The Aeronautical Journal*, *104*(1033), 162-162.

Sonnenburg, C. & Woolsey, C. A. (2012). An experimental comparison of two USV trajectory tracking control laws. In: *Proceedings of IEEE International Conference on OCEANS'12*. pp. 1-10.

Song, R., Liu, W., Liu, Y. & Bucknall, R. (2016). Aspect of a reliable autonomous navigation and guidance system for an unmanned surface vehicle. In: *Proceedings of MTS/IEEE OCEANS'16 Conferences*. 19-23 September, 2016, Monterey, USA. DOI: 10.1109/OCEANS.2016.7761415.

Song R., Liu, Y., Liu, W. & Bucknall, R. (2015). A two-layered fast marching path planning algorithm for an unmanned surface vehicle operating in a dynamic environment. In: *Proceedings of MTS/IEEE Oceans'15 Conferences*. 18-21 May, 2015, Genova/Italy. DOI: 10.1109/OCEANS- Genova.2015.7271405.

Stateczny, A. & Kazimierski, W. (2011). Multisensor Tracking of Marine Targets – Decentralized Fusion of Kalman and Neural Filters. *International Journal of Electronics and Telecommunications*, 57(1), pp. 65-70.

Stateczny, A. & Lisaj, A. (2006). Radar and AIS Data Fusion for the Needs of the Maritime Navigation. *In: Proceedings of Radar Symposium*, Krakow, Poland.

Subramanian, V., Burks, T.F. & Dixon, W.E. (2009). Sensor Fusion using Fuzzy Logic Enhanced Kalman Filter for Autonomous Vehicle Guidance in Citrus Groves. *American Society of Agricultural and Biological Engineers*, 52(5), pp. 1411-1422.

Subsea Tech (2019). USV CAT-Surveyor: USV for harbour and coastal areas. Available at: https://www.subsea-tech.com/cat-surveyor/ (Accessed: 7 May 2019).

Sutton, R., Sharma, S. & Xu, T. (2011). Adaptive navigation systems for an unmanned surface vehicle. *Proc IMarEST- Part A: Journal of Marine Engineering and Technology*, 10(3), pp. 3-20.

Svensson, L., Svensson, D., Guerriero, M. & Willett, P. (2011). Set JPDA filter for multitarget tracking. *IEEE Trans. Signal Process*. 59(10), pp. 4677–4691.

Tanaka H., Okuda T. & Asai K., (1976). A formulation of fuzzy decision problems and its application to an investment problem. *Kybenetes*, 5, pp. 23-30.

Tang, P., Zhang, R., Liu, D., Huang, L., Liu, G. & Deng, T. (2015). Local reactive obstacle avoidance approach for high-speed unmanned surface vehicle. *Ocean Engineering*. 106, pp. 128-140.

Tetley L. & Calcutt D. (2001). *Electronic Navigation System*, 3rd edn, Oxford: Butterworth-Heinemann.

TinkerKit (2014). *TinkerKit 4x Gyroscope Manual,* Available at: http://www.tinkerkit.com/gyroscope-4x/ (Accessed: 10th April 2014).

Titterton, D.H. & Weston J.L. (1997). *Strapdown Inertial Navigation Technology,* United Kingdom: Peter Peregrinus Ltd.

Trimble (2015). *User Guide: Welcome to Rangefinder*. Available at: https://www.neigps.com/wp-content/uploads/2014/06/Geo-7-Rangefinder-Utility-Version-1.20-User-Guide-DRAFT-English.pdf (Accessed: 24th May 2015).

Tronico (2015). *The NMEA 0183 Protocol*. Available at: http://www.tronico.fi/OH6NT/docs/NMEA0183.pdf (Accessed: 10th October 2014).

Tu, E., Zhang, G., Rachmawati, L., Rajabally, E. & Huang, G. (2018). Exploiting AIS Data for Intelligent Maritime Navigation: A Comprehensive Survey from Data to Methodology. *IEEE Transactions on Intelligent Transportation Systems*, 19(5), pp. 1559-158, DOI: 10.1109/TITS.2017.2724551.

Vadiee, N. & Jamshidi, M. (1993). Chapter 4: Fuzzy rule-based expert systems-I. In *Ross T.J. Fuzzy Logic and Control: Software and Hardware Applications,* Volume 2, New Jersey: Prentice Hall, pp. 51-85.

Van Der Merwe, R. (2004). *Sigma-point Kalman filters for probabilistic inference in dynamic state-space models*, Doctoral dissertation, OGI School of Science and Engineering at OHSU.

Vaneck, T. W., RODRIGUEZ-ORTIZ, C. D., Schmidt, M. C. & Manley, J. E. (1996). Automated bathymetry using an autonomous surface craft. *Navigation*, *43*(4), pp. 407-419.

Varshney P.K. (1997). Multisensor data fusion. *Electronics and Communication Engineering Journal*, pp. 245-253.

Vasilj, J., Stancic, I., Grujic, T. & Music, J. (2016). Development of Modular Unmanned Surface Vehicle for Research and Education. *2nd International Multidisciplinary Conference on Computer and Energy Science*, Split, Croatia.

Vasilj, J., Stancic, I., Grujic, T. & Music, J. (2017). Design, Development and Testing of the Modular Unmanned Surface Vehicle Platform for Marine Waste Detection. *Journal of Multimedia Information System*, Volume 4, No. 4, pp. 195-204

Veness C. (2015). *Calculate distance, bearing and more between Latitude/Longitude points*, Cambridge: Movable Type Ltd.

Viau C. (2013). Market Survey of Unmanned Surface Vehicles and Unmanned Aerial Vehicles for Maritime Application. *Defense Research and Development Canada.*

Wan, E. A. & Merwe, R. (2000). The Unscented Kalman Filter for Nonlinear Estimation. *Proceedings of the IEEE 2000 Adaptive System for Signal Processing, Communications, and Control Symposium*. Oct 4.

Wang, N., Gao, Y., Weng, Y., Zheng, Z. & Zhao, H. (2018). Implementation of an integrated navigation, guidance and control system for an unmanned surface vehicle. In *2018 Tenth International Conference on Advanced Computational Intelligence (ICACI)*, pp. 717-722.

Wang, X., You, Z. & Zhao, K. (2015). Inertial/celestial-based fuzzy adaptive unscented Kalman filter with Covariance Intersection algorithm for satellite attitude determination. *Aerospace Science and Technology*. **48** (2016), pp. 214-222.

Wang, Y. (2009). Centroid defuzzification and the maximizing set and minimizing set ranking based. *Computersand Industrial Engineering*, 57(1), pp. 228-236.

Whyte, H. D. (2006). Simultaneous localisation and mapping (SLAM): Part I the essential algorithms. *Robotics and Automation Magazine*.

Wolejsza P. (2012). Statistical analysis of real radar target course and speed changes for the needs of multiple model tracking filter. *Scientific Journals, Maritime University of Szczecin*, 20(102), pp. 166-169.

Woolfson. M. S. (1985). An Evaluation of Manoeuvre Detector Algorithms. *GEC J. of Research*, Chelmsford, England, 3(3), pp. 181–190.

Varshney, P. K. (1997). Multisensor data fusion. *Electronics and Communication Engineering Journal*, *9*(6), pp. 245-253.

Xia, G., Wang, G., Chen, X. & Xue, J. (2016). Low-cost MEMS-INS/GNSS integration using quaternion-based nonlinear filtering methods for USV. In *OCEANS16*, April, 2016, Shanghai, China, pp. 1-7.

Xie B. & Wan Y. (2011). Design of Multi-Sensor Integrated Navigation System for Land Vehicle. In: *Multi-Platform/ Multi-Sensor Remote Sensing and Mapping*, IEEE, Xiamen, China.

Xu J., Lu X., Wu H., Bian Y. & Zou D. (2008). Application of Data Fusion in Multi-sensor Integrated Navigation System. In: *Proceedings of 3rd IEEE Conference on Industrial Electronics and Applications*, Singapore.

Xu, Z., Li, J. & Chen, Y. (2017). Survey of track association of radar and AIS. In *2017 IEEE 2nd International Conference on Image, Vision and Computing (ICIVC)*, pp. 960-964.

Yan, R., Pang, S., Sun, H. & Pang Y., (2010). Development and missions of unmanned surface vehicle. *Journal of Marine Science and Application*, Volume 9, Issue 4, pp 451-457.

Yan, J., Park, J., Kim, T. & Kim, J. (2015). Precision navigation and mapping under bridges with an unmanned surface vehicle. *Autonomous Robots*, Volume 38, Issue 4, pp 349-362.

Yang, C., Shi, W. & Chen, W. (2018). Correlational inference-based adaptive unscented Kalman filter with application in GNSS/IMU-integrated navigation. *GPS solutions*, *22*(4), 100.

Yang, C., Kim, T., Hong, D. & Ahn, H. (2013). Design of integrated ship monitoring system using SAR, Radar and AIS. In: *Proceeding of SPIE, Ocean Sensing and Monitoring V.* Vol. 8724, doi: 10.1117/12.2018017.

Yuan X., Lian F. & Han C. (2014). Models and Algorithms for Tracking Target with Coordinated Turn Motion. *Mathematical Problems in Engineering*, 2014, Article ID 649276.

Zadeh, L.A. (1965). Fuzzy Sets. *Information and Control*, 8, pp. 338-353.

Zahra, S., Ghazanfar, M. A., Khalid, A., Azam, M. A. & Naeem, U. (2015). Novel Centroid Selection Approaches for KMeans-Clustering Based Recommender Systems. *Information Sciences*, Doi: 10.1016/j.ins.2015.03.062 Reference: INS 11488.

Zhai, G., Meng, H. & Wang, X. (2014). A Constant Speed Changing Rate and Constant Turn Rate Model for Manoeuvring Target Tracking. *Sensors*, 2014(11), pp. 5239-5253, doi: 10.3390/s140305239.

Zhang, Y.; Guo, C.; Hu, H.; Liu, S.; Chu, J. (2014). An Algorithm of the Adaptive Grid and Fuzzy Interacting Multiple Model. *Journal of Marine Science and* Application, **2014**(13), pp. 340–345.

Zhang, F., Li, S., Yuan, S., Sun, E., & Zhao, L. (2017). Algorithms analysis of mobile robot SLAM based on Kalman and particle filter. In: *9th International Conference on Modelling, Identification and Control (ICMIC)* (pp. 1050-1055). IEEE. July 10th – 12th, Kunming, China.

Zhang, P., Gu, J., Milios, E. E. & Huynh, P. (2005). Navigation with IMU/GPS/Digital Compass with Unscented Kalman Filter. In: *Proceedings of the IEEE International Conference on Mechatronics and Automation.* July. Niagara Falls, Canada.

Zhu, W., Wang, W. & Yuan, G. (2016). An Improved Interacting Multiple Model Filtering Algorithm Based on the Cubature Kalman Filter for Manoeuvring Target Tracking. *Sensors*, **2016**(16), 805, doi:10.3390/s16060805.

Appendix A: Basic Kalman Filter

Assume a discrete system state vector is $\boldsymbol{x}$ and it is governed by the following linear stochastic differential equation:

$$\boldsymbol{x}(k) = \boldsymbol{A}\boldsymbol{x}(k-1) + \boldsymbol{B}\boldsymbol{u}(k) + \boldsymbol{w}(k-1) \tag{A.1}$$

with a measurement:

$$\boldsymbol{z}(k) = \boldsymbol{H}\boldsymbol{x}(k) + \boldsymbol{\nu}(k) \tag{A.2}$$

where $\boldsymbol{u}(k)$ is the input, $\boldsymbol{w}(k)$ is the process noise and $\boldsymbol{\nu}(k)$ is the measurement noise. They are both white noise with normal probability distribution $p(\boldsymbol{w}) \sim N\ (0, \boldsymbol{Q})$ and $p(\boldsymbol{\nu}) \sim N\ (0, \boldsymbol{R})$.

The KF involves two steps, prediction and correction (Figure A.1). With the initial estimates for state vector $\boldsymbol{x}$ and its covariance matrix $\boldsymbol{P}$, the predicted next state of the system can be calculated by the system dynamic model. The system will then estimate the optimal next state by applying the KF gain to correct the measurement. After the optimal estimation, the system will update its covariance matrix $\boldsymbol{P}$ to iterate the system and the error covariance of the system will be reduced.

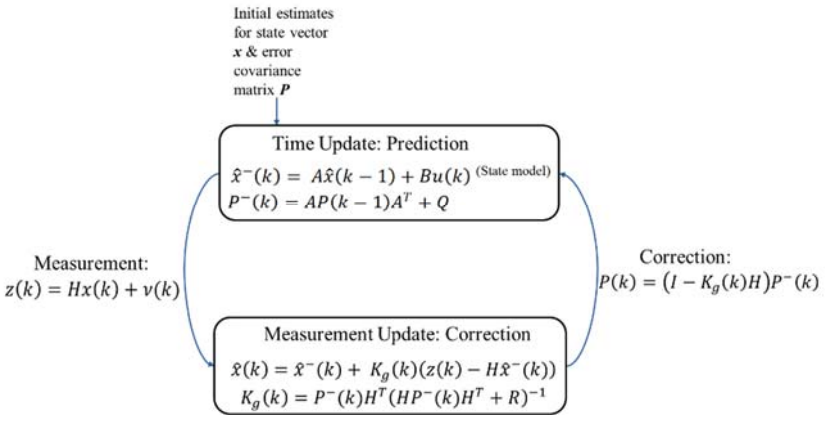

Figure A. 1 Kalman Filter (KF) prediction-correction process

Appendix B: Navigation sensors

Most marine electronic systems adhere to the NMEA (National Marine Electronics Association) 0183 standard, which is an electrical interface and data communication protocol for marine electronic devices (Tronico, 2015). Figure A.2 shows a typical asynchronous serial data segment as defined by the NMEA 0183 standard. Sensors transmit their measurements using an asynchronous serial method to the on-board hosting platform through common serial ports such as RS232 or USB. Serial communication is a form of I/O in which the bits of a byte being transferred appear one after the other in a timed sequence via a single path (BME, 2018).

Figure A. 2 Asynchronous Serial Data

This sensor supports several types of NMEA 0183 sentences and employs an asynchronous serial interface with a baud rate of 4800, 8 data bits, 1 stop bit and one parity bit.

B.1 GPS

A digital interface program is developed to extract the GPS measurements. It first sets up the serial connection and then reads the rx data bit by bit via the serial port. It distinguishes the start bit and stop bit to retrieve a whole sentence. After a complete and valid sentence has been received, it will parse the data to extract useful information in accordance with the data type. Each NMEA0183 GPS output sentence begins with a unique identifier, such as $GPRMC, $GPGLL, $GPGGA, etc. Discrete packets of information are provided in each sentence. Among them, the $GPRMC sentence is most widely used and includes the required information, such as the time, date and location. The following figure shows an example $GPRMC sentence as well as the explanation of each character (Tronico, 2015).

Example output sentence with raw GPS measurements:

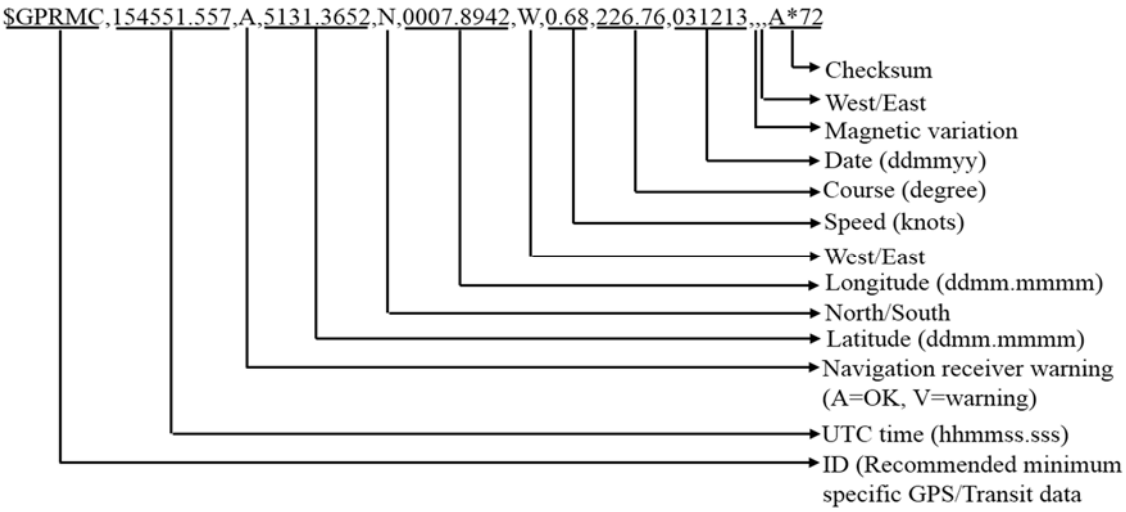

Figure A. 3 $GPRMC sentence and explanations

The core code to extract GPS data is shown as below:

```
int pos = msgStr.indexOf("RMC");
String gprmcStr = (pos > -1)? msgStr.substring(pos):null;
if(gprmcStr != null){
	gprmcStr =gprmcStr.substring(0); //GPRMC
}
return gprmcStr;

if(gprmcStr == null) return null;
GpsData gpsData =new GpsData();

for(int i=0; i<11;i++){
	String value=gprmcStr.substring(0,gprmcStr.indexOf(","));
	gprmcStr = gprmcStr.substring(gprmcStr.indexOf(",")+1);

	switch (i){
	case 0: gpsData.setType(value); break;
	case 1: gpsData.setTime(value); break;
	case 2: gpsData.setValid(value); break;
	case 3: gpsData.setLatitude(value); break;
	case 4: gpsData.setDirection1(value); break;
	case 5: gpsData.setLongitude(value); break;
	case 6: gpsData.setDirection2(value); break;
	case 7: gpsData.setSpeed(value); break;
	case 8: gpsData.setCourse(value); break;
	case 9: gpsData.setDate(value); break;
	case 10: gpsData.setMagneticDirection(value); break;
}
```

GPS provides absolute positions in longitude and latitude. The positional data in this format be converted to a two-axis coordinate system based on the predesigned

navigation frame, as mentioned in Chapter 2, in order to be applied to the algorithms. In this research, the Haversine formula, which is shown below, is employed to convert longitude and latitude to the related coordinates (Vaness, 2015).

The longitude/latitude conversion steps:

- Choose a point in the navigational frame as the reference, normally the start point of the USV's trajectory.
- Apply the Haversine Formula to calculate the bearing and distance between each position point and the reference point.
- Convert the distances to x-y coordinates using bearings.

Distance:

$$dlat = lat_2 - lat_1 \tag{B.1}$$

$$dlon = lon_2 - lon_1 \tag{B.2}$$

$$s = sin^2\left(\frac{dlat}{2}\right) + \cos(lat_1) * cos(lat_2) * sin^2(\frac{dlon}{2}) \tag{B.3}$$

$$c = 2 * atan2(\sqrt{s}, \sqrt{(1-s)}) \tag{B.4}$$

$$d = RE * c \tag{B.5}$$

Bearing:

$$\theta = atan2(\sin(dlon) * \cos(lat_2), \cos(lat_1) * \sin(lat_2) - \sin(lat_1) * \cos(lat_2) * \cos(dlon)) \tag{B.6}$$

where lat and lon are the latitude and longitude in radians, RE is the radius of the Earth. Here it is assumed that the Earth is a spherical model with an equatorial radius of 6378137 meters (Ratsameethammawong and Kasemsan, 2010).

B.2 Calibration of IMU

The following lists each step of the calibration.

- **Step 1**: put the IMU on a flat space, point its x axis to south, y axis to east and z axis downwards.
- **Step 2**: record the static data over 200 cycles and calculate the mean values of the acquired data, accx1, accy1 and gyroz1, which are the readings of the accelerometer in the x axis and y axis and the gyroscope in the z axis respectively.
- **Step 3**: rotate the IMU to make its x axis point to north, y axis to west and z axis downwards.
- **Step 4**: again record the static data over 200 cycles and calculate the mean values of the acquired data, accx2, accy2 and gyroz2,
- **Step 5**: calculate the bias. Ideally, the static data should be zero in a flat space. However, in practical conditions, the surface may not be ideally flat and the sensors will exhibit a constant bias. Therefore, the static data will be composed of the gravity deviation and the bias components.

$$accx1 = -g_x + b_{ax} \tag{B.7}$$

$$accy1 = g_y + b_{ay} \tag{B.8}$$

$$accx2 = g_x + b_{ax} \tag{B.9}$$

$$accy2 = -g_y + b_{ay} \tag{B.10}$$

Therefore the bias of the accelerometer can be determined as:

$$b_{ax} = (accx1 + accx2)/2 \tag{B.11}$$

$$b_{ay} = (accy1 + accy2)/2 \tag{B.12}$$

In the navigation frame, the Earth's rotation ω_e has three components in north, east and down as following:

$$\omega_{ie}^{n} = [\omega_e \cos(lat) \quad 0 \quad -\omega_e \sin(lat)] \tag{B.13}$$

So the bias of the gyroscope along the z axis can be determined by:

$$b_{gz} = (gyro1 + gyro2)/2 + \omega_e \sin(lat) \tag{B.14}$$